Journal of METALS

TRANSACTIONS
SECTION

Table of Contents Continued

Temperature Dependence of the Hardness of Secondary Phases Common in Turbine Bucket Alloys J. H. Westbrook **898**

Shear Along Grain Boundaries in Aluminum Bicrystals S. K. Tung and R. Maddin **905**

Intermetallic Compounds in Titanium-Hardened Alloys H. J. Beattie, Jr., and W. C. Hagel **911**

Hydrogen Distribution in Heat-Treated Titanium as Established by Autoradiography O. J. Huber, J. E. Gates, A. P. Young, M. Pobereskin, and P. D. Frost **918**

Blister Formation in Rolled Aluminum J. H. O'Dette **924**

Abrupt Yielding and the Ductile-to-Brittle Transition in Body-Centered Cubic Metals E. T. Wessel **930**

Diffusion of Magnesium, Silicon, and Molybdenum in Nickel R. A. Swalin, A. Martin, and R. Olson **936**

Determination of Orientation in Magnesium by Polarized Light Examination S. L. Couling and G. W. Pearsall **939**

The Transactions pages appearing in JOURNAL OF METALS *during 1957 will subsequently appear in AIME Transactions Volume* **209**, *and may be permanently referenced to that volume.*

Effects of Compression and Annealing on the Structure and Electrical Properties of Germanium

Germanium has been compressed under various conditions and has subsequently been annealed. These studies give direct evidence of the operation of the dislocation mechanism of plastic flow. No evidence of recrystallization has been found, but a domain structure composed of small angle boundaries is formed by large deformations at high temperatures. Annealable acceptor centers apparently due to point defects have been found and studied.

by E. S. Greiner, P. Breidt, Jr., J. N. Hobstetter, and W. C. Ellis

STUDY of the plasticity of germanium or other semiconductor crystals affords unusual opportunities to extend our knowledge of deformation mechanisms. Crystals are available having extraordinary perfection and very high purity. They deform by slip on the systems {111} <110>,[1-4] as do crystals of the simple face-centered-cubic structure. Dislocations generated in them during slip are easily revealed in the form of etch pits on either {111} or {100} surfaces.[1-3] This fact alone makes possible more detailed studies of mechanisms than is usually the case with metals but, even further, the effect of deformation on their electrical conductivity is very large compared with metals. This comes about not only because the mobility of the charge carriers is reduced, as in deformed metals, but also because the number of these carriers is greatly altered. This latter effect seems closely related to the formation of both line and point imperfections during deformation and thus provides a needed tool for the study of the kinds and distributions of these imperfections.

Other investigators have deformed germanium at elevated temperatures by bending,[1,4,5] compression,[6,7,10] tension,[2,8,9,11,12] torsion,[13] and indentation.[14] Wang and Alexander[15] have also reported successful indentation at room temperature. Dislocation etch pits consequent to deformation have been observed and studied.[1,2,10,11,14,16] The experiments to be described here include principally the compression and the subsequent annealing of germanium with concomitant studies of etch pits, microstructures, and electrical properties. Both single crystals and heavily twinned specimens were used. Some indentation studies are included.

E. S. GREINER, Member AIME, P. BREIDT, JR., J. N. HOBSTETTER, and W. C. ELLIS, Member AIME, are associated with Bell Telephone Laboratories, Inc., Murray Hill, N. J.

TP 4452E. Manuscript, June 16, 1956. New Orleans Meeting, February 1957.

Experimental Methods

Plastic compression was effected in the apparatus shown schematically in Fig. 1. It consists of two tantalum platens contained in a helium atmosphere and so arranged that pressure can be applied by a hydraulic press. The specimen between the platens is heated by the surrounding furnace. The specimen is usually a small crystal cube about 0.30 in. on an edge. A control specimen is always inserted so that it is subject to the same thermal cycle as the one being deformed. This serves to detect any impurity contamination that might accompany the thermal treatment. For high temperature work, where such impurity contamination often occurs, the specimens were first plated with gold whenever subsequent electrical properties were to be determined. This method[17] is effective in preventing significant contamination of germanium up to temperatures at least as high as 750°C, as evidenced by the constancy of the electrical conductivities of control specimens subjected to the same heat treatments. The total range of temperature used for deformation was from 375°C, the lowest at which significant flow was observed, up to 900°C.

Microscopic examination was made after mechanical and chemical polishing and etching. Dislocation pits were revealed with CP-4 etchant by the tech-

Copyright 1957 by American Institute of Mining, Metallurgical, and Petroleum Engineers, Inc. Printed in U. S. A.

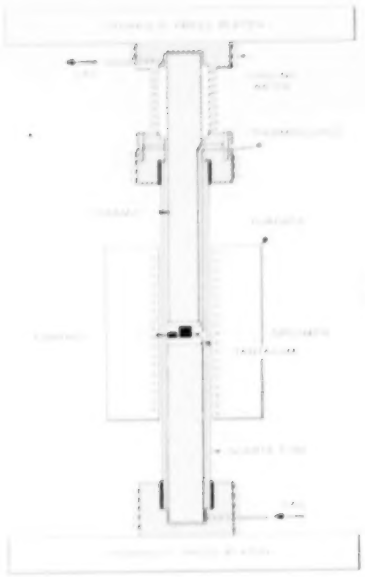

Fig. 1—Schematic drawing of compression apparatus

nique of Vogel, Pfann, Corey, and Thomas.[7] Examination for dislocations was made on surfaces parallel to {111} planes in most instances. Orientation relationships were established by the well-known Grenninger technique.[8] Electrical conductivity was measured at room temperature with a four-point probe as described by Valdes.[9] The type of conductivity—that is, whether *n* or *p*-type—was ascertained with a thermoelectric probe.[10]

Annealing of the compressed specimens was carried out in quartz tubes containing a helium atmosphere, and again gold plating was frequently used to avoid contamination.

To investigate the mechanism of flow in the lower temperature range of plasticity, single crystals of 0.2 (ohm-cm)$^{-1}$ *n*-type, antimony-doped germanium were deformed at 375°C by forcing the conical point of a tantalum indentor into polished surfaces parallel to {111} and {100} planes.[11] These planes were chosen so that etch pits associated with dislocations initially present and those produced in flow could be readily produced and observed.[4] A load of about 14 lb was applied in the same apparatus as shown in Fig. 1.

Dislocations in Indented Germanium

It was shown in a previous letter[6] that slip lines formed around an indentation, and that upon further etching with CP-4, the array of these lines was replaced by a parallel array consisting of rows of small pits. Indentation of {111} planes always produced triangular arrays of lines and rows of pits, while indentation on {100} planes produced orthogonal arrays. A typical etched {111} surface is shown in Fig. 2. The area is near an indentation made at 375°C. The few large circular markings are pits denoting dislocations in the crystal as grown; the many small pits are formed only after deformation and re-etching with CP-4. The latter are always aligned along the slip plane traces and their appearance on two planes of observation shows that they are associated with the {111} slip planes.

Fig. 3 shows a similar specimen that has undergone a gradient etch—that is, the etchant has been concentrated near the indentation (toward the lower right-hand corner), leaving the slip lines showing on the more remote, unetched surface. There is obviously a correspondence between slip lines and rows of etch pits. This figure offers conclusive evidence of the storage of dislocations in the active slip planes themselves. Patel and Alexander[12] have reached the same conclusion.

Recently S. G. Ellis[13] has described a new etchant (Ellis #7) which reveals not only the same pits as developed by CP-4, but numerous other pits on the surfaces of undeformed germanium. The present authors have also used this new etchant on indented specimens and find no significant difference from the results obtained with CP-4 in the deformed region. Figs. 4a and 4b show, respectively, an area near the indentation before and after using this etchant. Note again the correspondence between slip lines in the unetched specimen and rows of pits in the etched one. Although these two etchants do not produce the same results on undeformed crystals, it appears that they produce the same patterns on deformed ones. Compare Figs. 3 and 4b.

On heating the crystal indented on a {111} surface to about 800°C for 65 hr and re-etching, the triangular array of dislocation pits remained unchanged. The dislocations did not migrate into walls normal to slip planes, as they do in Vogel's[7] bent crystals. Possible reasons for this difference are that the dislocations from the complex stressing by indentation are not in pure edge orientation nor are they predominantly of one sign.

Dislocations in Lightly Compressed Germanium

Studies were made of the accumulation of dislocations during light compression of germanium and of changes in their density and distribution during subsequent annealing. Simultaneous studies were made of electrical conductivity changes. Single crystal specimens of *n*-type, antimony-doped germanium having a room temperature conductivity of 5.7 (ohm-cm)$^{-1}$ were used. These were cut into cubes bounded by pairs of (111), (110), and (112) planes and were compressed 2.5 pct in the [110] direction both at 525° and at 725°C. The electrical conductivity was then measured at room temperature and the dislocation pit density change was determined by counting pits on the (111) plane. The results are shown in Table I and in Fig. 5.

Table I. Changes of Conductivity and of Dislocation Density in Lightly Compressed and Annealed (*n* type) Germanium

Specimen	Condition	Conductivity, 25°C, (Ohm-Cm)$^{-1}$	Dislocation Density, Cm^{-2}
A	As grown	5.7	6x10^{6}
	As compressed 2.5 pct at 525°C	3.9	16x10^{6}
	Subsequently annealed at 725°C		
	for 15 min	4.5	13x10^{6}
	30 min	5.2	11.2x10^{6}
	60 min	5.1	11.6x10^{6}
B	As grown	5.7	4x10^{6}
	As compressed 2.5 pct at 725°C	5.1	14x10^{6}
	Subsequently annealed at 725°C		
	for 15 min	5.6	8.2x10^{6}
	30 min	5.1	7.6x10^{6}
	60 min	5.2	6.9x10^{6}

One of the chief results is the increase in dislocation density between two and three orders of magnitude brought about by the deformation, which is in agreement with the work of Patel and Alexander.[12] The increase is about the same at both temperatures of deformation. Fig. 5a shows that the dislocation pits have some tendency to align themselves

Fig. 2—Etch pits produced by CP-4 near indentation on a {111} plane. Note delineation of slip planes. X500. Reduced approximately 25 pct for reproduction.

Fig. 3—Gradient etch near indentation of a {111} plane showing how slip lines, when etched with CP-4, turn into rows of pits. X1000. Reduced approximately 25 pct for reproduction.

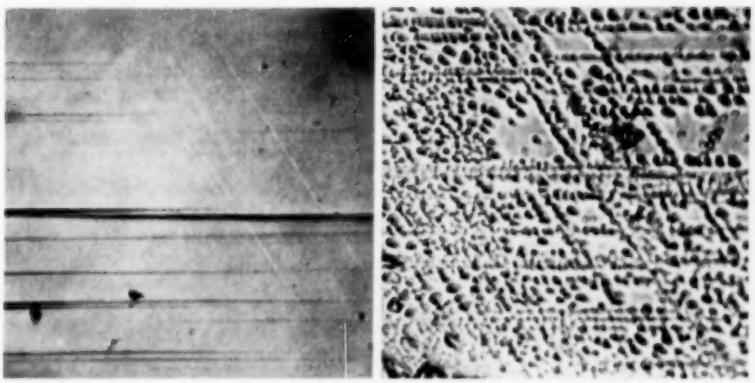

Fig. 4—a) LEFT: slip lines; and b) RIGHT: pits revealed by Ellis' etchant #7 near indentation on a {111} plane. X1000. Reduced approximately 25 pct for reproduction.

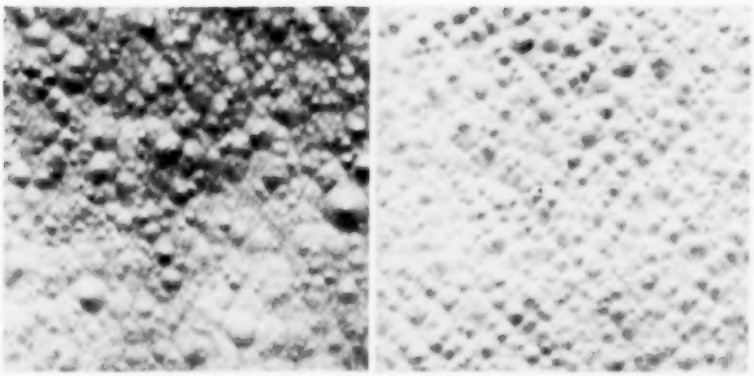

Fig. 5—a) LEFT: pits revealed on {111} plane by CP-4 after 2.5 pct compression at 525°C. b) RIGHT: Same after subsequent annealing for 60 min at 725°C. X1000. Reduced approximately 25 pct for reproduction.

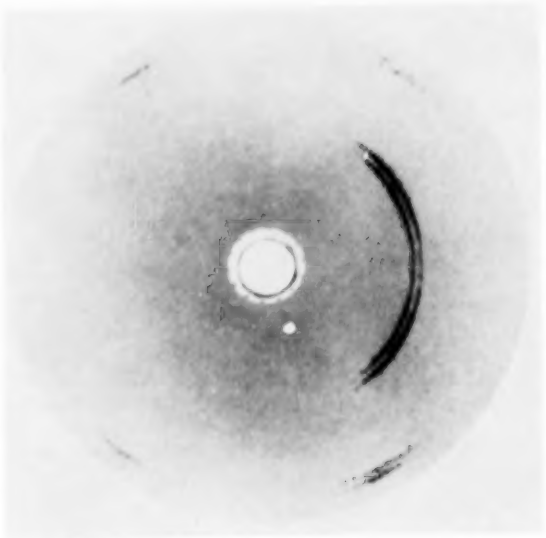

Fig. 6—X ray pattern from germanium, compressed 30 pct at 900°C in the [001] direction, shows discrete reflections in segments of the Debye ring. From the initial orientation of the crystal, the segments of the inner ring, each subtending about 10° of arc, are identified as 551 reflections. CuK radiation was used with the beam normal to the initial (110) surface.

along traces of the {111} slip planes, although this tendency is not so marked as in the case of Vogel's bent crystals or as in the present indented ones.

The specimens were finally annealed at 725°C and their conductivities and dislocation pit densities were determined after stated intervals at that temperature. These results are also shown in Table I. It is evident that a slow decrease in dislocation density occurs so that even after annealing for 60 min the dislocation density is still about two orders of magnitude larger than the initial density. The decrease seems to occur by internal cancellation of dislocations of opposite sign and leads to the formation of a more orderly microstructure, Fig. 5b, in which the dislocations appear more equally spaced. A tendency to align along the slip planes is still evident. Since these dislocations do not all necessarily contain edge components, they would not all be expected to migrate into walls normal to the slip planes as in bent crystals.

The conductivity changes accompanying deformation and annealing will be discussed in a later section. It suffices to note here that these changes are consistent with the view that deformation introduces acceptor centers.

Dislocations in Heavily Compressed Germanium

The microstructure of plastically deformed single crystals of germanium changes significantly with both degree and temperature of deformation. After small compressions at low temperatures only slip lines are seen on polished surfaces and a rather indistinct alignment of pits along slip plane traces on etched surfaces, Fig. 5a. Larger deformations at about 600°C produce intensified markings and, significantly, Laue spots are replaced by continuous-appearing segments of Debye rings. These segments indicate the formation of a range of orientations in a crystal. The same large deformations, 15 to 30 pct, brought about at high temperatures, 800° to 900°C, produce a definite domain type of microstructure and, at the same time, the segments of Debye rings become resolvable into a large number of discrete reflections, Fig. 6.

To study this domain structure in greater detail a single crystal cube of *n*-type, antimony-doped germanium with initial conductivity of about 0.1 (ohm-cm)$^{-1}$ was so cut as to have (111), (110), and (112) faces. It was compressed 23 pct at 875°C along [110]. The (111) face was then etched with CP-4 and examined at X500, Fig. 7.

Domain boundaries, consisting of dense rows of dislocation pits, appear in many instances to be parallel to the directions of the intersections of active slip planes with the surface of observation. Since such rows of dislocations are boundaries of disorientation, only local measurements of the angle between rows are meaningful. The local angles appear to be quite close to the expected 60°. It can be shown that if polygonization had occurred, a more complex pattern would have resulted. The order of the domain size is about 10^{-4} cm.

Annealing of Compressed Germanium

In none of the authors' studies of deformed and annealed germanium was recrystallization observed. Recovery was limited to a redistribution of dislocations, or to a reduction of their number. To investigate this subject further, single crystals and twinned crystals containing large angle boundaries were severely deformed and then annealed at high temperatures, as described in Table II.

Comparisons of Laue photographs before and after annealing of both lightly and heavily deformed single crystals showed that the annealing produced no new reflections and hence no recrystallization. These findings were supported by the results of microscopic examination using an etchant particularly effective in revealing new orientations (1 part HF, 1 part 30 pct H_2O_2, 4 parts H_2O. No new grains were found in either case.

X-ray and metallographic examinations of the heavily twinned germanium which had been compressed various amounts and annealed at high temperatures also revealed no new grains.

The failure of compressed germanium to recrystallize is not readily understood. The relatively small number of dislocations ($< 10^{9}$ cm^{-2}) stored in deformed material may be significant in this regard —after equivalent deformation metals are believed to store up to 10^{10} cm^{-2}. This fact suggests that the energy stored in germanium is less than in metals and is too low to induce the formation or growth of

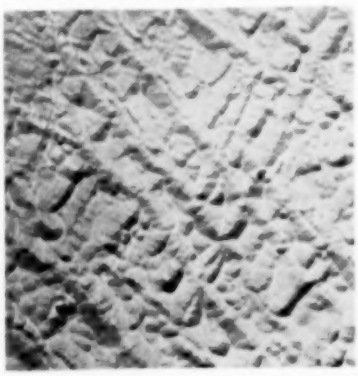

Fig. 7—Dense rows of pits forming domain boundaries revealed on a {111} plane by CP-4 after 23 pct compression at 875°C. X500. Reduced approximately 25 pct for reproduction.

strain-free grains. The reason for this small dislocation storage is not immediately evident.

Effects of Deformation on Electrical Properties

The structural changes produced by deformation of germanium are accompanied by large changes in electrical conductivity. A decrease in the conductivity of *n*-type[1,7] and a conversion of *n*-type to *p*-type[6,10,18] as a result of deformation have been reported. This conversion can only mean that acceptor centers having levels below the middle of the energy gap are introduced by deformation.

As an extension to an earlier report by two of the authors,[6] the effects of initial conductivity, type of conductivity, temperature of compression, amount of compression, and subsequent thermal treatments have been studied in detail. Measurements of conductivity were made at room temperature after removal of gold from the surface.

Consider first the conductivity changes accompanying the deformation and annealing of the lightly compressed specimens described above and in Table I. These data show that an annealable decrease in conductivity occurs upon low temperature deformation that does not occur upon high temperature deformation. This decrease results from acceptor centers stored in the deformed material after cooling to room temperature. Any such centers formed during the high temperature deformation have apparently annealed out before room temperature is regained. On the other hand, the pit density changes

Table II. Annealing of Compressed Germanium Crystals

Specimen	Temperature of Compression, °C	Compression, Pct	Annealing Treatment
Single crystal No. 1*	550	4.5	42 hr at 850°C
No. 2†	650	27	42 hr at 850°C
No. 3*	600	15	60 hr at 875°C
Twinned crystal No. 4‡	650	8.3	24 hr at 825°C plus 64 hr at 875°C
No. 5‡	650	14	24 hr at 825°C plus 64 hr at 875°C

* *n*-type germanium, ρ = 7-8 ohm-cm, antimony-doped.
† *p*-type germanium, ρ = 1.4 ohm-cm, indium-doped.
‡ *n*-type germanium, ρ = 8-9 ohm-cm, arsenic-doped.

are substantially the same during deformation and annealing in both tests. These results show clearly that the deformation-induced acceptor centers observed at room temperature are not the dislocations themselves. Otherwise, the same conductivity changes would be observed in both specimens just as the same dislocation density changes were observed in both. The results also show that these centers must occur in a form which is in part preserved at low temperatures but which anneals out about as rapidly as formed at 725°C. Tweet[18] has found similar centers which anneal in this way.

Consider secondly the accumulation of these acceptor centers as deformation proceeds. Fig. 8 shows conductivity curves as functions of percentage of compression near 550°C for germanium specimens of several different initial conductivities. Evidently electron conduction is decreased and hole conduction increased by deformation in all these specimens. It follows that the acceptor centers, even though they are not associated with stored dislocations, nevertheless increase with the amount of deformation at 550°C. Fig. 9 shows the effect of temperature during the deformation on the accumulation of these ac-

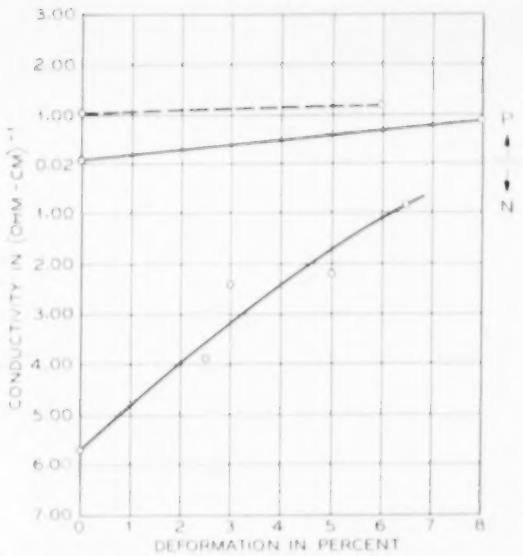

Fig. 8—Effect of compression near 550°C on room temperature conductivity of germanium specimens having different initial conductivities showing accumulation of acceptor centers. The origin of the conductivity scale is 0.02 (ohm-cm)⁻¹, the intrinsic conductivity of germanium at the temperature of measurement.

ceptors. At low temperatures the acceptors accumulate rapidly with deformation; at high temperatures they accumulate much less rapidly. This effect is the result of the rapid annealing out of the acceptors as the temperature is raised. In fact, as seen in Table I, in the case of small compression (2.5 pct), which introduces few acceptors, they anneal out so fast at 725°C that they are gone before the specimens cool from the compression temperature.

It is tempting to associate these new centers with vacancies[20] and interstitial atoms. Many such point defects must form during the observed increase of dislocation density.[7] The open network of atoms that constitutes the germanium (diamond) structure is such that, unlike more densely packed metals, interstitials should form about as easily as vacancies.[20] Furthermore, it is known that vacancy-interstitial pairs (Frenkel defects) formed in germanium by bombardment with various subatomic particles also act as acceptor centers.[21-23] Finally, it is known[20] that such pairs anneal out readily after times at temperature not inconsistent with those found for the deformation-induced centers which will now be described.

The specimens deformed at high and low temperatures were both annealed at 725°C and their room temperature conductivities and dislocation densities were determined at intervals. These results are also shown in Table I. In the low temperature specimen almost all of the deformation-induced acceptors annealed out rapidly in about 30 min. The conductivity of the high temperature specimen did not change. The dislocation densities decreased very slowly in both specimens and remained more than 100-fold above the original densities even after 60 min of annealing. These results reaffirm the view that the acceptor centers observed at room temperature are almost entirely independent of the number of dislocations themselves and that they are easily annealed out at high temperatures.

It may be pointed out that the residual decrease in conductivity observed in all fully annealed speci-

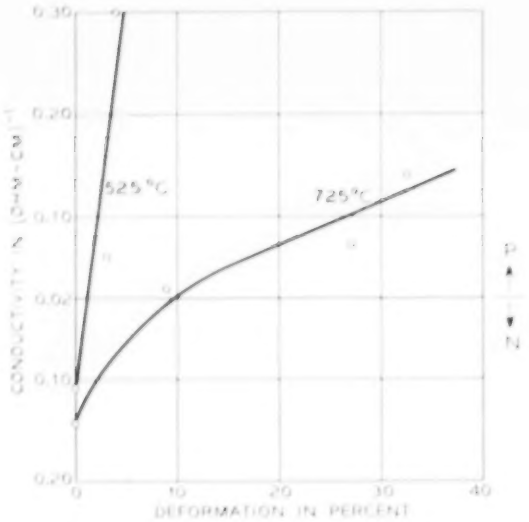

Fig. 9—Effect of compression at 525° and 725°C on the conductivity of germanium having initial conductivity of about 0.10 (ohm-cm)$^{-1}$ showing greater accumulation of acceptor centers at the lower temperature of compression.

mens probably reflects the decreased mobility of carriers in the presence of a 100-fold increase in dislocation density plus a quite small acceptor action of these dislocations. Pearson, Read, and Morin[7] have shown that dislocations do act as acceptor centers in *n*-type germanium, particularly at lower temperatures. Read[8,9] has elaborated a theory which ascribes this effect to an acceptor center associated with each dangling bond along any dislocation having an edge component. When these centers trap electrons from the conduction band, a row of negative charges, surrounded by a positive space charge region, forms. The resulting increase of electrostatic energy makes the trapping of all but a few electrons unfavorable. The number trapped in *n*-type germanium turns out to be negligible at room temperature unless the conductivity is very high. Only a very small effect should occur in the germanium used here.

The evidence presented here that room temperature conductivity measurements in germanium are very sensitive to the formation of vacancies and interstitials suggests that the method be developed as a tool to study these point imperfections. The work described is therefore being extended to elucidate the details of such a method.

Summary

Study of the deformation of germanium by indentation and compression has revealed in some detail the operation of the postulated dislocation mechanisms of plastic flow. Several new facts concerning the behavior of germanium itself have also been demonstrated. The general results of this study are:

1) Dislocations introduced by plastic flow and stored in the material have been shown to exist as an array on the active slip planes.

2) Annealing at high temperature after deformation slowly decreases the number of stored dislocations, apparently by internal cancellation.

3) Recrystallization does not occur in germanium even after compression of as much as 28 pct and long annealing near 900°C.

4) The heaviest of our compressions at high temperatures produce definite domain structures in which the domains are delineated by walls consisting of a high density of dislocations. These boundaries appear to be parallel to the active slip planes.

5) Electrical conductivity changes are consistent with the view that both dislocations and point defects are introduced by the deformation. At room temperature in *n*-type germanium having conductivity as low as 5.7 (ohm-cm)$^{-1}$, the dislocations seem to have very little effect; the point defects constitute substantially all the effective acceptor centers.

6) These acceptor centers increase in number with the amount of deformation at low temperatures such as 525°C, but are rapidly annealed out at higher temperatures such as 725°C.

7) Electrical conductivity measurements of germanium appear to provide an important tool for the study of point defects.

Acknowledgments

H. K. Birnbaum contributed to the early work on deformation of germanium in compression. H. N. Newton, J. A. Gutowski, and D. S. Blackford assisted in many experiments. Single crystals for study were furnished by W. G. Pfann, twinned crystals by H. C. Theuerer. Valuable discussion was had with D. F. Gibbons, W. T. Read, Jr., R. G. Treuting, and F. L. Vogel, Jr. during the course of the investigations and in the interpretation of results. The authors are also grateful to J. R. Patel and B. H. Alexander for letting them read the latters' paper before its publication.

References

[1] C. J. Gallagher: *Physical Review*, 1952, vol. 88, p. 721.
[2] R. G. Treuting: JOURNAL OF METALS, 1952, vol. 4, p. 1044.
[3] R. G. Treuting: *AIME Trans.*, 1955, vol. 203, p. 1027; JOURNAL OF METALS, October 1955.
[4] F. L. Vogel, W. G. Pfann, H. E. Corey, and E. E. Thomas: *Physical Review*, 1953, vol. 90, p. 489.
[5] F. L. Vogel, Jr.: *Acta Metallurgica*, 1955, vol. 3, p. 245.
[6] L. Graf, H. R. Lacour, and K. Seiler: *Ztsch. für Metallkunde*, 1953, vol. 44, p. 113.
[7] G. L. Pearson, W. T. Read, Jr., and F. J. Morin: *Physical Review*, 1954, vol. 93, p. 666.
[8] F. L. Vogel, Jr.: *Acta Metallurgica*, 1955, vol. 3, p. 95.
[9] W. C. Ellis and E. S. Greiner: *Physical Review*, 1953, vol. 92, p. 1061.
[10] J. R. Patel and B. H. Alexander: *Acta Metallurgica*, 1956, vol. 4, p. 385.
[11] R. P. Carreker, Jr.: *AIME Trans.*, 1956, vol. 206, p. 111; JOURNAL OF METALS, February 1956.
[12] F. D. Rosi: *Acta Metallurgica*, 1956, vol. 4, p. 26.
[13] E. S. Greiner: *AIME Trans.*, 1955, vol. 203, p. 203; JOURNAL OF METALS, January 1955.
[14] P. Breidt, Jr., E. S. Greiner, and W. C. Ellis: *Acta Metallurgica*, 1957, vol. 5, p. 60.
[15] C. C. Wang and B. H. Alexander: *Acta Metallurgica*, 1955, vol. 3, p. 515.
[16] C. J. Gallagher: *Physical Review*, 1953, vol. 92, p. 846.
[17] C. S. Fuller: Private communication. See also R. A. Logan and M. Schwartz: *Journal of Applied Physics*, 1955, vol. 26, p. 1287.
[18] A. B. Greninger: *AIME Trans.*, 1935, vol. 117, p. 61.
[19] L. B. Valdes: *Proceedings* I.R.E., 1954, vol. 42, p. 420.
[20] G. L. Pearson: Private communication. See also W. C. Dunlap, Jr.: *General Electric Review*, 1949, vol. 52, No. 2, p. 9.
[21] S. G. Ellis: *Journal of Applied Physics*, 1955, vol. 26, p. 1140.
[22] C. J. Gallagher and A. G. Tweet: *Physical Review*, 1954, vol. 96, p. 834.
[23] A. G. Tweet: *Physical Review*, 1955, vol. 99, p. 1245.
[24] F. Seitz: *Advances in Physics*, 1952, vol. 1, p. 43.
[25] J. N. Hobstetter: *Progress in Metal Physics*, vol. 7. To be published.
[26] H. Y. Fan and K. Lark-Horovitz: *Report of the Conference on Defects in Crystalline Solids*, July 1954, p. 232. Physical Soc. London, 1955.
[27] J. W. Cleland, J. H. Crawford, Jr., and J. C. Pigg: *Physical Review*, 1955, vol. 98, p. 1742.
[28] W. L. Brown, R. C. Fletcher, and K. A. Wright: *Physical Review*, 1953, vol. 92, p. 591.
[29] W. T. Read, Jr.: *Philosophical Magazine*, 1954, vol. 45, p. 775.
[30] W. T. Read, Jr.: *Philosophical Magazine*, 1954, vol. 45, p. 1119.
[31] W. T. Read, Jr.: *Philosophical Magazine*, 1955, vol. 46, p. 111.

Discussion of this paper sent (2 copies) to AIME by Sept. 1, 1957 will appear in AIME *Transactions* Vol. 212, 1958, and in JOURNAL OF METALS, April 1958.

Calculation of Diffusion Coefficients by the Matano-Boltzmann Method

Some aspects of Boltzmann's solution for one-dimensional diffusion in an infinite medium when the initial distribution is a step function are clarified. Thus, the fact that the concentration is a function of the single variable $x/t^{1/2}$ is established by a dimensional argument. The basis of the Matano-Boltzmann method for determining diffusion coefficients from concentration curves is discussed, and a new way of applying the method is derived and illustrated. As in the work of Hall, emphasis is placed on the curve obtained when (in effect) concentration is plotted against position on probability paper. This curve is approximated by a polynomial, and the diffusion coefficient is calculated by using an equation in which the coefficients of the polynomial appear as parameters. The new procedure makes the judgment of the effect of errors in concentration measurements easier than do the graphical methods frequently used.

by E. M. Baroody

MUCH information on intermetallic diffusion has been obtained in experiments in which two volumes, initially at different uniform concentrations, are maintained in contact at an interface which is plane, or nearly so. Concentration-distance curves are obtained after suitable times, and analyzed on the basis of a one-dimensional form of Fick's law

$$\frac{\partial c}{\partial t} = \frac{\partial}{\partial x}\left(D\frac{\partial c}{\partial x}\right). \qquad [1]$$

In early work the linear equation to which Eq. 1 reduces when D is independent of concentration was used. However, when the initial concentrations c_1 and c_2 are appreciably different this simplification is often unjustified, and the suggestion by Matano[1] in 1933 of a way of avoiding it was welcomed. Matano's paper was based on work done as early as 1882 by Boltzmann.[2,3]

In 1938 Rhines and Mehl[4] reported an extensive investigation of systems in which the diffusion coefficient depends strongly on concentration, and included a detailed description of the Matano-Boltzmann method. To a large degree, this description represents the formal method as it is understood and applied today, most later discussions having emphasized thermodynamic and mechanistic aspects of diffusion. Exceptions are the comments of R. V. Churchill, contained in a paper by Ham, Parke and Herzig,[5] and the papers by Hall[6] and by Kirkaldy.[7]

E. M. BARODY is associated with Battelle Memorial Institute, Columbus, Ohio.

TP 4429E. Manuscript, Nov. 14, 1955. New Orleans Meeting, February 1957.

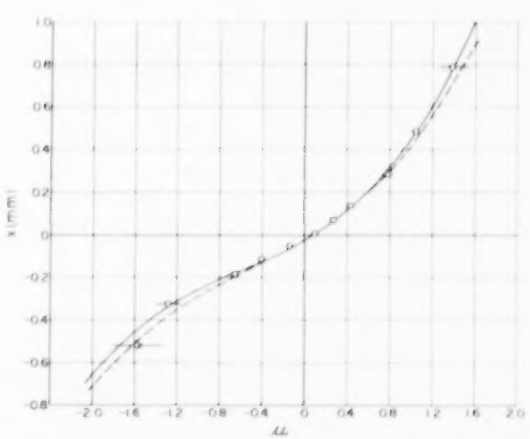

Fig. 1—Example of the relation between x and u. The points show experimental data of Rhines and Mehl for sample 2 of ref. 4. The solid curve was calculated from Eq. 30, and the dashed curve from Eq. 31.

More discussion appears necessary since some aspects of the problem remain obscure. Better computational procedures are also needed. The common method, involving graphical determination of slopes and areas, is inconvenient and makes the estimation of errors difficult.

Background of the Matano-Boltzmann Method

Eq. 1 is to be considered along with initial and boundary conditions. Take the origin of x at the

initial interface, let the distance over which measurable concentration changes occur be small compared with the dimensions of the system in the x direction, and introduce the notation

$$w = (c - c_i)/(c_s - c_i) \qquad [2]$$

$$g(w) = D(c)/B \qquad [3]$$

where B is a constant with the dimensions of a diffusion coefficient. The differential equation and the initial and boundary conditions then have the form

$$\frac{\partial w}{\partial t} = B \frac{\partial}{\partial x}\left[g(w) \frac{\partial w}{\partial x} \right] \qquad [4]$$

$$\begin{aligned} t = 0 \quad & x > 0 \quad w = 1 \\ & x < 0 \quad w = 0 \end{aligned} \qquad [5]$$

$$\begin{aligned} t > 0 \quad & x = \infty \quad w = 1 \\ & x = -\infty \quad w = 0. \end{aligned} \qquad [6]$$

Boltzmann saw that these equations have a solution which is a function of the single variable $\lambda = x/t^{1/2}$. He also realized that this solution is unique, but as Kirkaldy[1] has observed, a number of later workers have not understood this point. Kirkaldy has given two arguments for uniqueness, but the following statements seem to be more convincing, as well as simpler. Since w is dimensionless it must be a function of dimensionless groups. On the other hand, the only quantities with dimensions available for the formation of such groups are the variables x and t, and the constant B. In some problems the initial and boundary conditions would introduce quantities with dimensions, but not here, since no finite times or distances appear. Moreover, x^2/Bt is the only dimensionless combination of the available quantities. Hence, x and t enter w only in the combination $x/t^{1/2}$.

The solution of Eqs. 4 to 6 is now known to be of the form $w(\lambda)$. Eq. 4 reduces to the ordinary differential equation

$$2B \frac{d}{d\lambda}\left(g \frac{dw}{d\lambda} \right) + \lambda \frac{dw}{d\lambda} = 0 \qquad [7]$$

while Eqs. 5 and 6 become

$$w(\infty) = 1 \quad w(-\infty) = 0. \qquad [8]$$

Hausmaninger[2] tells how Boltzmann obtained these equations and how, making two integrations, he reached a result which (when D is a function of concentration) gives the concentration as the solution of an integral equation.* This result is of general interest, but not useful for the determination of $D(c)$ from an observed concentration curve. For this purpose, Boltzmann recommended a single, direct integration of Eq. 7, which yields

$$2D \frac{dw}{d\lambda} + \int_w^\infty \lambda \, dw' = \text{constant}. \qquad [9]$$

Eqs. 8 and 9 are consistent with finite values of D at the limiting concentrations only if the constant on the right of Eq. 9 is taken to be zero, and if

$$\int_0^1 \lambda \, dw = 0. \qquad [10]$$

If w is regarded as a function of x at a fixed time, Eqs. 9 and 10 take the form

$$2Dt \frac{dw}{dx} = -\int_w^\infty x \, dw' \qquad [11]$$

$$\int_0^1 x \, dw = 0. \qquad [12]$$

These equations have been used repeatedly for the calculation of D. In many cases, however, the meaning of Eq. 12 has been misrepresented, it being stated or implied that the origin may be freely chosen to satisfy the equation. Actually, $w(x/t^{1/2})$ will not be a solution of the given boundary value problem unless the origin of x is the initial interface. If this interface is known, and if its use as an origin leads to a violation of Eq. 12, the conclusion should be that Eqs. 4 to 6 have not been followed. Specific objections to measuring x from a plane differing from the initial interface were made earlier by R. V. Churchill (ref. 5, pp. 887–888). There also seems to be little evidence that Matano intended to introduce a new interface. It is more likely that he only meant that when D depends on concentration, the initial interface can be determined from Eq. 12, but not from $w = \frac{1}{2}$.

In recent years phenomena related to the Kirkendall effect have shown the need for generalizations of Eq. 1 which lead to Eq. 7, but with a new relation between λ and x. For example, if the quantity f in Eq. 87 of the review article by Seitz[3] is considered constant, and if

$$\lambda = (x/t^{1/2}) + 2f \qquad [13]$$

is written, Eq. 7 is obtained. Introducing $x_M = -2ft^{1/2}$ leads to†

$$2Dt \frac{dw}{dx} = \int_w^\infty (x_M - x) \, dw' \qquad [14]$$

$$x_M = \int_0^1 x \, dw. \qquad [15]$$

These equations replace Eqs. 11 and 12. Their form shows that in applying them it is not necessary to measure distances from the initial interface. The values of D which are obtained are independent of the choice of origin, while x_M locates the Matano interface relative to whatever origin is chosen.

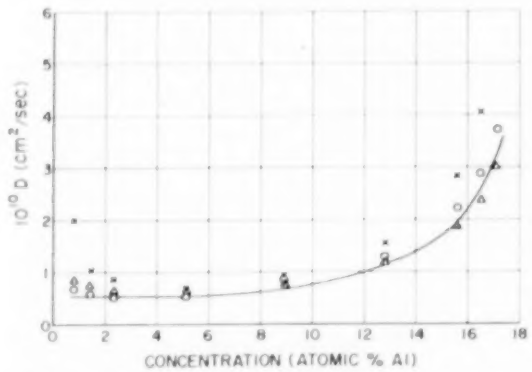

Fig. 2—Diffusion coefficient as a function of concentration. The circles and triangles were computed from Eq. 28, using Eqs. 30 and 31, respectively. The crosses show the effect of adding the term $0.003\,w^6$ to Eq. 30. The line shows the results computed by Rhines and Mehl.[4]

* Hausmaninger discussed diffusion out of a semi-infinite medium, but the problems are essentially the same.

† The dimensional proof that w is a function of $x/t^{1/2}$ still applies since the new constant f has the same dimensions as $B^{1/2}$.

Eqs. 14 and 15 are acceptable in the sense that they are consistent with finite values of $D(c_i)$ and $D(c_s)$, and with the approach of dc/dx to zero at large distances. However, the convergence and values of the integrals depend on the way in which dc/dx approaches zero. Actually, as Hausmaninger realized, $D(c)$ cannot be calculated at all without some assumption concerning its behavior near the limiting concentrations. The assumption that both D and dD/dc approach finite limits is reasonable, and its implications will now be considered.

There are advantages in emphasizing, as Hall[7] has done, not the concentration itself, but a function u defined by the equation‡

‡ Hausmaninger also used this transformation at one stage of his analysis.

$$w = \tfrac{1}{2}\,[1 + \phi(u)\,] \qquad [16]$$

where $\phi(u)$ is the error function. Differentiation of Eq. 16 gives

$$\frac{dw}{d\lambda} = \frac{1}{\sqrt{\pi}} \exp\,(-u^2)\,\frac{du}{d\lambda}. \qquad [17]$$

On the other hand, the assumption concerning the limiting behavior of $D(c)$ implies the following asymptotic form of Eq. 7

$$2D\,\frac{d^2w}{d\lambda^2} + \lambda\,\frac{dw}{d\lambda} = 0. \qquad [18]$$

Integration of Eq. 18 shows that $dw/d\lambda$ becomes proportional to exp $(-\lambda^2/4D)$. Comparing this with Eq. 17 leads to the conclusion that asymptotically

$$u = \frac{\lambda}{2D^{1/2}} = \frac{(x - x_s)}{2(Dt)^{1/2}} \qquad [19]$$

where it is understood that $D = D(c_i)$ for $\lambda = -\infty$, and $D = D(c_s)$ for $\lambda = +\infty$. That is, $u(\lambda)$ is asymptotic to two straight lines which intersect at $u = \lambda = 0$.§

§ The author is indebted to Martin N. Chase for calling attention to this fact.

Analytic Formulations of the Method

Hall[7] noted that for some data of da Silva and Mehl, a graph of $u(\lambda)$ is characterized by two linear portions joined by a region of rapidly changing slope. He suggested that a relation of the type $u = h\lambda + k$ be applied to each linear section of the curve, and derived corresponding expressions for the diffusion coefficient. For low concentrations (for which u is negative) he obtained

$$D(c) = \frac{1}{4h^2} + \frac{k\pi^{1/2}}{4h^2} \exp\,(u^2)\,[1 + \phi(u)\,]. \qquad [20]$$

The discussion of the asymptotic behavior of $u(\lambda)$ given above implies that Eq. 20 will not give finite limiting values of both D and dD/dc except for $k = 0$. In fact, using the asymptotic expansion of the error function

$$D(c) = \frac{1}{4h^2}\left(1 - \frac{k}{u}\right) \qquad [21]$$

$$\frac{dD}{dc} = \frac{k\pi^{1/2} \exp\,(u^2)}{4(c_s - c_i)\,h^2 u^2}. \qquad [22]$$

A finite limiting value is obtained for D, but not for dD/dc. Fig. 1 of Hall's paper shows that his value of k is significantly different from zero, which implies vertical tangents at the ends of the curve $D(c)$. Hall's Fig. 3 does not show this feature, possibly because it becomes apparent very near the limiting concentrations, and might easily be missed if not anticipated.

A reasonable conclusion is that the data of da Silva and Mehl do not reveal the behavior of $u(\lambda)$ in regions near the concentration limits, and that Eq. 20 is not a good representation of $D(c)$ very near these limits, although it may be a useful approximation over certain ranges of concentration.

A different analytic procedure has been studied in which experimental results are described by expressing x as a polynomial in u. It is desirable to use x rather than λ, because λ is not known until after x_s has been calculated. Representation of $x(u)$ by a polynomial is studied because it is likely to be convenient in a substantial fraction of the cases arising in practice.

Introducing the polynomial

$$x = \sum_{n=0}^{N} A_n u^n \qquad [23]$$

and Eq. 16 into Eqs. 14 and 15 leads to

$$2Dt \exp\,(-u^2)\,\frac{du}{dx} = x_s I_0(u) - \sum_{n=0}^{N} A_n I_n(u) \qquad [24]$$

$$\sqrt{\pi}\, x_s = \sum_{n=0}^{N} A_n I_n(\infty) \qquad [25]$$

where

$$I_n = \int_{-\infty}^{u} u'^n \exp\,(-u'^2)\,du'. \qquad [26]$$

Using these relations

$$x_s = A_0 + \sum_{n=2,4,6} \frac{(n-1)(n-3)\ldots 1}{2^{n/2}}\,A_n \qquad [27]$$

$$4Dt = (dx/du) \sum_{n=1}^{N} A_n F_n(u). \qquad [28]$$

The functions $F_n(u)$ are polynomials, the first few being

$$F_0 = 1 \qquad F_1 = u$$

$$F_2 = u^2 + 1 \qquad F_3 = \frac{u}{2}\,(2u^2 + 3).$$

All the even polynomials may be obtained from F_0 and all the odd ones from F_1 by the formula

$$F_n = \frac{1}{2}\,(n-1)\,F_{n-2} + u^{n+1}.$$

On reflection, Eq. 23 may appear unacceptable since, except for the special case $N = 1$, it disagrees with Eq. 19. Doubts are strengthened by a first examination of Eq. 28. This equation yields infinite values of $D(c_i)$ and $D(c_s)$, and also indicates possible difficulties at intermediate values of c. The functions $F_n(u)$ increase so rapidly with n that even for $u = 0$ any value of D may be obtained, without contradicting the experimental data, just by choosing an appropriate small value of some A_n, n being sufficiently large.

These consequences of Eq. 23 are undesirable, but the important question is whether or not the equa-

tion can be used in such a way that no errors are introduced into $D(c)$ which are not inherent in the experimental data. Considering the derivation of Eq. 28, it is noted that a term $A_n u^n$ in $x(u)$ introduces $A_n I_n(u)$ into Eq. 24 and that, according to Eq. 26, large contributions to $I_n(u)$ can only come from u' near $\pm\sqrt{\frac{n}{2}}$. Speaking roughly, Eq. 23 is inferred to be acceptable when the data can be adequately represented by a polynomial of degree N, where $\pm\sqrt{\frac{N}{2}}$ lies within the range of u which is well covered by the experimental data.

Application of the Polynomial Method

As an example, consider the results for sample 2 of Rhines and Mehl.[4] The initial components were copper and a Cu-Al alloy containing 8.5 wt pct Al, and the couple was held at 700°C for 38.40 days. After the data on pp. 189 and 193 of ref. 4 are converted to atomic pct Al, u can be obtained for various values of x. A plot of $x(u)$ is given in Fig. 1. The horizontal lines through the points indicate experimental uncertainties. They were obtained from the relation

$$du = \sqrt{\pi} \exp(u^2)\, dw \qquad [29]$$

and the assumption that the uncertainty in any measured concentration is about 1 pct of the maximum concentration, which is in reasonable accord with the authors' views regarding errors. Two approximations to the data are shown in Fig. 1

$$x = -0.02 + 0.29u + 0.115u^2 + 0.065u^3 \text{ (solid line)} \qquad [30]$$

$$x = -0.02 + 0.30u + 0.085u^2 + 0.055u^3 \text{ (dashed line).} \qquad [31]$$

The first of these gives a satisfactory approximation to the data and, roughly speaking, the deviation of the dashed curve from the solid one is as large as is permitted by experimental uncertainties. Carrying through calculations for both approximations permits some judgment of uncertainties in $D(c)$.

When Eq. 28 is applied to the two approximations, the results shown by circles and triangles in Fig. 2 are obtained, where D is plotted against concentration. The curve is well defined for about 80 pct of the concentration range (from 2 to 16 pct), the detailed results being more meaningful than might have been supposed. The results calculated by Rhines and Mehl from the same data are also shown (solid line), bringing out the good agreement between the two procedures in this case. The crosses show the effect of adding the unnecessary term $0.003u^5$ to the right side of Eq. 30. This point is discussed below.

Each of the approximations of Fig. 1 corresponds to a location for the Matano interface. Using $x_u = A_0 + \frac{A_1}{2}$, see Eq. 27, 0.038 mm is found for the solid line, and 0.022 mm for the dashed line. Rhines and Mehl give 0.04 mm.

Consider whether or not the use of polynomials is acceptable in this case. For this purpose, errors in $D(c)$ may be associated with: 1) limited accuracy of $x(u)$ within the range of the experiments, 2) uncertainty concerning $x(u)$ at large distances, and 3) deviations of the polynomials from reasonable behavior at large distances.

An estimate of the importance of the last item may now be made. Considering $u > 0$ and having in mind Eq. 19, from Fig. 1 it would be reasonable for $x(u)$ to follow Eq. 30 to $u = 1.6$, and then change gradually to a straight line cutting the x-axis at x_u. To estimate the difference between results based on such a curve and those based on Eq. 30, it may be supposed that the curve changes abruptly from the polynomial to a straight line at $u = 2$. From Eqs. 14, 15, and 17 it is evident that values of the integral

$$\int_0^\infty (x - x_u) \exp(-u^2)\, du$$

are needed. Use of the relation

$$x = \frac{u}{2}[x(2) - x_u] + x_u \qquad [32]$$

along with numerical values from Eq. 30 leads to 0.0069 mm. On the other hand, use of the polynomial leads to

$$\frac{1}{2} e^{-1} \sum_{n=1}^{8} A_n F_n(2) = 0.0077 \text{ mm.}$$

The small difference between these results may be compared with

$$\int_0^\infty (x - x_u) \exp(-u^2)\, du = \frac{1}{2e} \sum_{n=1}^{8} A_n F_n(1) = 0.098 \text{ mm.}$$

The comparison indicates that for $u = 1$ ($C = 16.5$ atomic pct), use of the polynomial introduces only about 1 pct error into D. On the other hand, Fig. 2 shows that the overall uncertainty in D at this concentration is about 20 pct.

The inclusion of unnecessary terms of high degree in the polynomial can completely change this situation. For example, addition of the term $0.003u^5$ to Eq. 30 does not lead to a contradiction of the experimental data, but greatly increases the difference between results based on the polynomial and those based on reasonable asymptotic behavior. Thus, the crosses in Fig. 2 illustrate an incorrect interpretation of the data. This agrees with the inference made at the end of the previous section. When $x(u)$ is cubic, the points $u = \pm\sqrt{N/2}$ lie well within the range covered by the experimental data, while for $N = 9$ these points lie beyond the range of the data.

Acknowledgments

The author has received a number of valuable suggestions from Martin N. Chase and Ralph J. Harrison, and has had helpful discussions with a number of other colleagues. He also wishes to thank Erwin Eichen of the Ohio State University for a careful reading of the manuscript.

References

[1] C. Matano: *Journal of Physics* Japan, 1933, vol. 8, p. 109.
[2] V. Hausmaninger: *Kaiserlichen Akad. Wiss. (Math.-Natur. Kl.)*, 1882, vol. 86, p. 1073.
[3] L. Boltzmann: *Annalen der Physik*, 1894, vol. 53, p. 959.
[4] F. N. Rhines and R. F. Mehl: *AIME Trans.*, 1938, vol. 128, p. 185.
[5] J. L. Ham, R. M. Parke, and A. J. Herzig: *ASM Trans.*, 1943, vol. 31, p. 877.
[6] L. D. Hall: *Journal of Chemical Physics*, 1953, vol. 21, p. 87.
[7] J. S. Kirkaldy: *Acta Metallurgica*, 1956, vol. 4, p. 92.
[8] R. Smoluchowski et al.: *Phase Transformations in Solids*, pp. 125-127. John Wiley & Sons, New York, 1951.

Discussion of this paper sent (2 copies) to AIME by June 1, 1957 will appear in AIME *Transactions* Vol. 209, 1957, and in JOURNAL OF METALS, October 1957.

Some Aspects of Alloying Onto Germanium Surfaces

Layers of *n*-type with thickness in the range of 0.0002 in. over areas of 0.006 sq in. have been produced on intrinsic germanium wafers by an alloy regrowth process as one stage in the fabrication of transistors. Experiments show that satisfactory alloying requires proper choice of solvent and doping impurity, good wetting of solvent to germanium, avoidance of contamination, good orientation of the germanium surface to the (111) plane, proper temperature cycle, and an inverted temperature distribution in the melt. Details are given of the process now in use in which lead is the solvent and antimony the doping impurity.

by J. W. Peterson, J. McGlasson, Jr., and W. C. Hittinger

THIS paper describes the result of an investigation of the production of thin alloyed layers on a thicker substrate of pure germanium as one step in the manufacture of transistors.[1] The technique of alloying materials with semiconductors is a means of introducing small amounts of impurity elements in the alloyed regions of the crystal lattice of the semiconductor, the presence of which make possible the junction type transistor.[2]

Impurity elements are added which will produce regions having differing electrical resistivities and means of carrying current. Impurities are of two types: those which produce an excess of electrons (negative or *n*-type), and those which produce a deficiency of electrons (positive or *p*-type) in comparison to the pure semiconductor. The boundary between two such regions is designated a *p-n* junction. Elements in Group V of the periodic table, having five valence electrons, give rise to an excess of electrons when present substitutionally in the semiconductor lattice (usually germanium or silicon from Group IV). Similarly, elements in Group III create a deficiency of electrons. Germanium and silicon which are substantially free of impurities of either *p* or *n*-type are designated intrinsic (*i*-type) semiconductors. The usual junction transistor has[3]

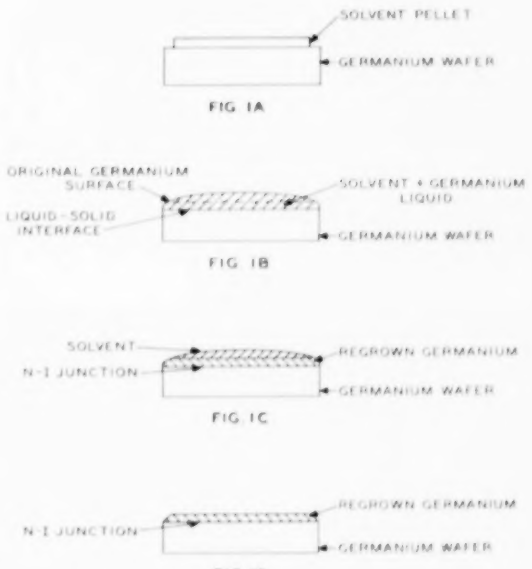

Fig. 1—Heating cycle for producing an N-I junction.

J. W. PETERSON, J. McGLASSON, JR., and W. C. HITTINGER are associated with the Bell Telephone Laboratories Inc., Murray Hill, N. J.

TP 4360E. Manuscript, Apr. 23, 1956. Cleveland Meeting, October 1956.

Fig. 2—Cross section of a type *n-p-n* transistor, showing inadequate wetting. X180. Reduced approximately 35 pct for reproduction.

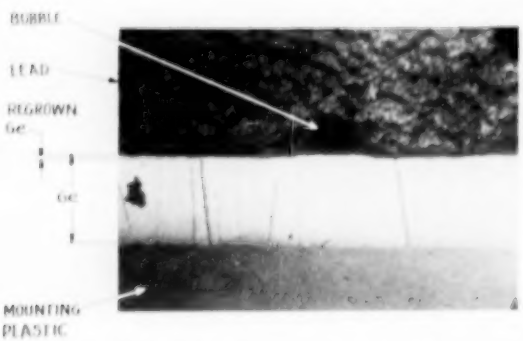

Fig. 3—Bubble formed by liberation of gases from decomposition of a lead oxide at a Pb-Ge interface. X180. Reduced approximately 35 pct for reproduction.

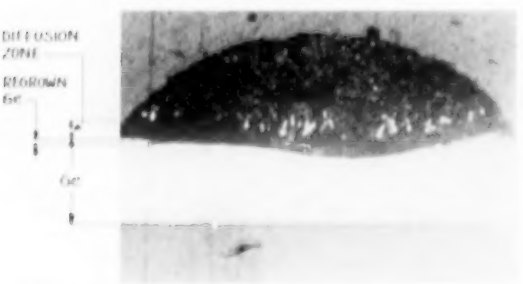

Fig. 4—A diffusion-controlled curved junction, the result of very rapid heating. X355. Reduced approximately 35 pct for reproduction.

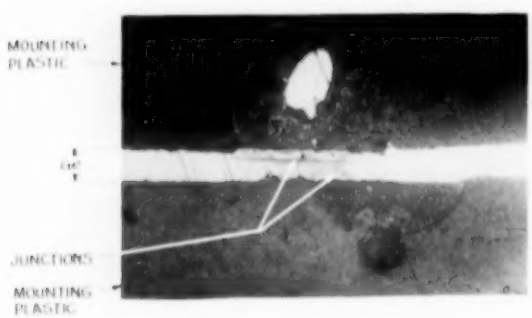

Fig. 5—Junction oriented to the (111) plane, as a result of very slow heating. X180. Reduced approximately 35 pct for reproduction.

two junctions (*p-n-p* or *n-p-n* transistors), while certain varieties may have more, such as the *p-n-i-p* transistor.[3]

In the alloy process to be described, a small wafer of solvent metal containing an *n*-type impurity is placed in contact with a wafer of germanium, Fig. 1A, after which the system is heated. As the temperature is raised above the solvent melting point, the solubility of germanium in the solvent increases, and a melt of solvent plus germanium is formed, Fig. 1B. During subsequent cooling the solubility of germanium decreases, causing crystallization of both germanium and impurity atoms out of the melt. In general, the crystallized atoms rebuild the previously dissolved germanium crystal structure, producing a *regrowth* layer which contains a certain concentration of impurity atoms, Fig. 1C. The impurity concentration in the regrown layer depends upon the distribution coefficient, which is the ratio, C_s/C_l, between concentration of the impurity element in the solid and in the liquid, at a given temperature. The objective of this investigation is to produce *n*-type regrowth layers on intrinsic (*i*-type) single-crystal germanium. Requirements placed on the regrowth layer were uniform and controlled thickness in the 0.00010 to 0.00014 in. range over an area of at least 0.002 sq in., and *n*-type impurity concentration of approximately 10^{17} atoms per cu cm with no inclusions of foreign material. Resistivity of the underlying intrinsic germanium was to remain substantially unchanged (35 ohm-cm minimum).

Upon completion of the alloying cycle the solvent material is removed by selective chemical etching, revealing the top surface of the regrowth layer, Fig. 1D. The *n-i* wafer is then ready for use in fabricating a *p-n-i-p* transistor.[4]

Materials

Crystal Orientation of Germanium Crystal—There is a well known[5] tendency for the solid-liquid interface during alloying to lie in the (111) crystallographic plane, and for germanium to regrow in (111)-oriented sheets. Therefore, the surface of the starting material must be accurately oriented to the (111) plane if a thin, uniform *n*-layer is to be produced. The accuracy of orientation required can be estimated by recognizing that in order for the *n-i* junction to lie in the (111) plane, a (111) plane must be completely exposed during the period of maximum solution of germanium in the alloying cycle. For example, to produce a 0.1-mil layer of 60 mil diam, the misorientation between the surface of the wafer and the (111) plane can at most be 0.2 mil in 60 mil, or about 11°.

Choice of Solvent—A *solvent* for our purposes is a metal (generally of low melting point) which together with germanium forms a system with a liquidus extending down to relatively low temperatures. Thus, an appreciable amount of germanium can be in the liquid phase at temperatures far below the germanium melting point.

The solvent material itself must not be a *p*-type or *n*-type impurity* and should contain as impurities no more than a few parts per million of elements having such properties. These requirements indicate the use of highly purified Group IV elements. Good wetting to germanium should take

* None of the *n*-type elements have a low enough distribution coefficient to allow a single element to be simultaneously solvent and *n*-type impurity in producing the desired value of impurity concentration in the regrowth layer.

place at a temperature well below that at which appreciable solution of germanium occurs, in order for solution to occur uniformly over the entire alloyed area. Adequate solubility of germanium must take place at a temperature which is reasonable from other considerations.† In order to avoid serious straining of the germanium during the cooling which follows solidification of the solvent, one of two requirements must be met. Either the yield strength of the solidified solvent must be low, or its thermal expansion coefficient must nearly match that of germanium. Finally, the solvent material should be easily removable after alloying, exposing the clean regrowth surface. Lead, tin, and various Pb-Sn alloys have been investigated. Lead had been found to be a more desirable solvent because of its lower yield strength and ease of chemical removal. The purity of Doe Run lead‡ is sufficient for most purposes; regrowth produced from undoped Doe Run lead has an *n*-type resistivity of the order of 5 ohm-cm.

† At first it was considered important to keep the alloying temperature at about 600°C or less, to avoid thermal conversion[5] of the intrinsic germanium. More recently, however, it has been demonstrated that no such conversion appears in a lead alloying process. Because of their high diffusion coefficient at alloying temperatures, the copper atoms responsible for conversion are swept into the melt, which acts as a sink because of the low distribution coefficient of copper in germanium. This fortunate attribute of an alloying process was first recognized by C. S. Fuller (private communication, July 1, 1952), and has recently been more fully investigated.[6, 7]

‡ Specially purified lead containing 30 ppm Bi, 12 ppm Cd, and 3 ppm or less of other elements.

Donor Impurity—It is desirable for the *n*-type impurity, of whose concentration in the regrowth material control is desired, to have a low vapor pressure at alloying temperatures. Thus the impurity concentration in the solvent will tend to remain constant throughout the alloying process and contamination of the graphite boat will be minimized. Such contamination would be undesirable, since it would tend to increase the doping in subsequent alloying runs. Two donor impurities, antimony and arsenic, have been investigated. Of the two, antimony has the lower vapor pressure, and appears to be the more generally satisfactory. A concentration of about 0.01 pct Sb in Doe Run lead produces regrowth of about the desired resistivity (approximately 0.05 ohm-cm).

Procedure

Equipment—In the present technique pellets of antimony-doped lead and wafers of nearly intrinsic germanium, held in a carbon boat, are heated in a resistance-type oven. The oven is a Nichrome tube of rectangular cross section, with its ends closed by removable plates. During an alloying cycle, the tube is first evacuated, after which deoxidized and dried hydrogen is passed through it. After the alloying cycle has been completed, the solidified lead is removed chemically§ and the *n-i* wafer is ready for evaluation and fabrication into a transistor.

§ The lead is dissolved in a solution of 2 parts H_2O_2 (30 pct), 2 parts glacial acetic acid, and 5 parts distilled H_2O.

Wetting—Obtaining good wetting over the entire area to be alloyed has been a serious and continuing problem. The critical requirement is that the germanium and solvent pellet surfaces be as clean and oxide-free as possible. Best results have come from cleaning both lead and germanium chemically, then heating them separately to about 650°C before combining them, inside the furnace, to initiate the alloying process. This technique avoids exposing the

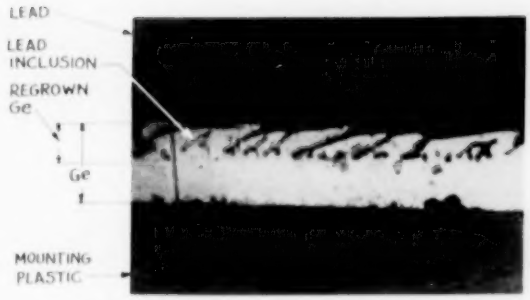

Fig. 6—Jagged regrowth surface with inclusions of lead, the result of intermediate regrowth rates. X180. Reduced approximately 35 pct for reproduction.

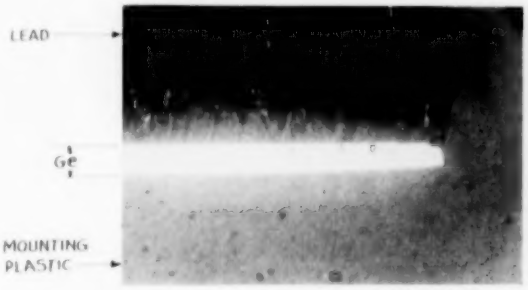

Fig. 7—Regrowth rates slower than used for Fig. 6 produce a cleaner interface, but some lead inclusions are still visible. X180. Reduced approximately 35 pct for reproduction.

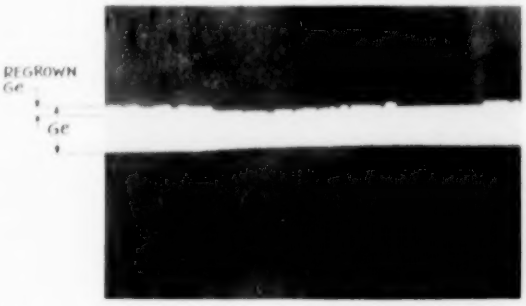

Fig. 8—Pits and columns are shown at the interface, the result of an unfavorable temperature gradient caused by heating the wafer from below. X106. Reduced approximately 35 pct for reproduction.

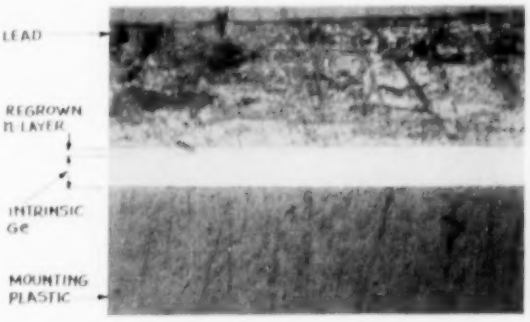

Fig. 9—Cross section of a typical regrowth layer 0.35 mil thick, made with a controlled temperature gradient. X135. Reduced approximately 35 pct for reproduction.

Fig. 10—Top surface of a regrowth layer, after lead removal. The surface was flat within a variation of 10^{-5} in.

clean surfaces to air before alloying takes place. These procedures have eliminated the necessity for using a flux, which is to be avoided wherever possible because of the danger of contamination.

Fig. 2 shows the cross section of an example of inadequate wetting in an *n-p-n* transistor. While the lead has spread over both germanium surfaces, a region on each side shows no solution and therefore poor wetting at this point. Occasionally bubbles appear at the Pb-Ge interface, probably caused by gases liberated by decomposition of a lead oxide. Such bubbles very effectively prevent wetting, as shown in Fig. 3. (In Figs. 2 to 5 and 9 the regrowth region lies between the dark, narrow line marking the junction,# and the surface of the wafer.)

It is difficult, in general, to reveal the *n-i* junction by the use of a chemical etch, particularly where the impurity concentration in the regrowth is relatively low, as it must be in satisfactory *n-i* material.

Temperature Cycle—A proper temperature cycle, consisting of heating and cooling periods, is essential to satisfactory alloying. In general, the shape of the *n-i* junction is determined by the heating period, and the shape and quality of the regrowth layer are determined by the cooling period.

If all dissolved germanium regrows during the cooling period, the thickness of the *n*-layer is determined by the amount of solvent and maximum temperature during the heating period. Assuming good wetting over its entire area, a layer of solvent¶ will

¶ Assuming that a negligible amount of solvent is incorporated in the regrowth germanium.

dissolve a thickness x of germanium given by

$$x = \frac{f}{1-f}\,\frac{M_{Ge}\,d_s}{M_s\,d_{Ge}}\,t$$

where t is the thickness of solvent layer; M_{Ge} and M_s are the atomic weights of germanium and solvent, respectively; d_{Ge} and d_s are the densities of germanium and solvent, respectively; and f is the atom fraction of germanium in solution at a given temperature. For the Pb-Ge system

$$x = 0.742\,\frac{f}{1-f}\,t.$$

In addition to providing good wetting during its initial portion, the heating period should maintain a planar solid-liquid interface as solution of germanium takes place. This is best accomplished by heating in such a manner that diffusion maintains a nearly uniform distribution of germanium in the melt. Since a low rate of solution is desirable, a heating period of given length is most effectively used when the rate of solution is kept constant. A constant rate of solution of germanium can be provided by use of the Ge-Pb phase diagram. If $df/dt = K$ (constant), then $f = Kt$;** and the abscissa of the phase diagram need only be multiplied by a suitable numerical factor to obtain a temperature-time curve which produces a constant rate of solution. It has been found that a heating period of 20 to 30 min to 700°C is satisfactory. To achieve steady state temperature conditions and uniform germanium concentration in the melt, 5 to 10 min at 700°C is ordinarily sufficient.

** More accurately, $f/1\text{-}f = Kt$. However, since in most alloying work $f << 1$, the approximation $f = Kt$ is generally a good one.

Very rapid heating, where diffusion controls the shape of the liquid-solid interface, produces curved junctions such as that of Fig. 4. Progressively slower heating rates produce progressively flatter interfaces. Fig. 5 shows a *p-n-p* cross section in which heating was so slow that the junctions are (111) planes (the wafer had obviously not been oriented to this plane). Too rapid heating also tends to produce pits in the junction surface, which promote the formation of the lead inclusions described below.

The cooling period should produce thin, uniform regrowth layers. This has been accomplished both by very rapid and by very slow cooling, while intermediate rates produce ragged regrowth which often contains inclusions of lead. In rapid cooling, regrowth takes place so quickly that preferential directions for crystal growth are unimportant. Instead, a thin uniform layer is built by those germanium atoms which are swept out by diffusion from the suddenly oversaturated melt. Fig. 4 illustrates this case, showing how the diffusion zone is bounded at the top by nucleated crystals of germanium. The regrowth layer thickness is determined by the diffusion zone width and original concentration of germanium in the melt.

As regrowth rate decreases from the very rapid case, the diffusion zone increases in width, and finally nucleation disappears. At these intermediate rates of regrowth the interaction between diffusion and preferential regrowth produces a jagged regrowth surface and inclusions of lead within the regrowth layer, as shown in Fig. 6. Fig. 7 shows the results of a still lower rate of regrowth, in which the regrowth is quite uniform, but inclusions of lead (in the small dark spots) are still present. The presence of such inclusions near the *n-i* junction appears to short out the junction and produce abnormally high reverse currents when the material is fabricated into a *p-i-n* diode for evaluation.

In slow cooling, diffusion maintains nearly uniform germanium concentration in the melt, and the form of the regrowth is determined by the preferential growth in (111)-oriented sheets. Since a low regrowth rate is desirable, a cooling period of given length is most effectively used when the rate of regrowth is kept constant.

Temperature Distribution in Melt—Even at low rates of regrowth the surface is generally not as flat as would be expected from the close approach to equilibrium. In addition to stepped (111) sheets, low columns and pits frequently are produced. The formation of stepped sheets is attributed to the presence of curved isothermal surfaces which result in faster regrowth in cooler regions, and therefore a net transport of germanium atoms from hot to cool regions. The occurrence of columns and pits is attributed to the unfavorable temperature gradient which results from heating the wafer from below,

with the upper part of the melt coolest. Thus an unstable condition exists, where a higher region tends to grow faster and a low region slower than the surrounding regrowth surface. This effect is illustrated in Fig. 8. It is believed that the improved flatness resulting from very slow cooling results principally from the reduction of temperature gradients, rather than from a closer approach to equilibrium. The use of auxiliary heaters to reverse the usual temperature gradient improves the flatness, and in particular nearly eliminates the formation of columns and pits.

Fig. 9 is a cross section of a typical regrowth layer 0.35 mil thick, made with a controlled temperature gradient. The portion of the wafer shown is 230 mil long. A photograph of the top surface of a regrowth layer made in the same fashion as the previous specimen is shown in Fig. 10 after lead removal. This surface, made on a 0.075x0.075 in. wafer, was flat within one fringe of sodium light, corresponding to a maximum variation of 10^{-5} in.

Summary

Thin, uniform *n*-type alloy regrowth layers have been produced as the result of careful attention to the following metallurgical aspects: crystallographic orientation of starting material, wetting of the solvent, constitution of the solvent, heating and cooling cycles, and temperature distribution in the melt. Layer thickness has been controlled to a value of 0.2 +0.1, −0.05 mil for a particular application, and layers of less than 0.1 mil have been produced for exploratory use.

Acknowledgments

Thanks are due to many of the authors' colleagues at the Bell Telephone Laboratories for valuable assistance and discussion; particular thanks are due J. M. Early and J. A. Wenger.

References

[1] W. Shockley: *Electrons and Holes in Semiconductors*. D. Van Nostrand Co. Inc. New York, 1950.

[2] W. Shockley: The Theory of p-n Junctions in Semiconductors and p-n Junction Transistors. *Bell System Technical Journal*, 1949, vol. 28, p. 435.

[3] J. M. Early: P-N-I-P and N-P-I-N Junction Transistor Triodes. *Bell System Technical Journal*, 1954, vol. 33, p. 517.

[4] S. H. Barnes and J. N. Carman: Regrown Regions in Silicon Fused Junctions. IRE-AIEE Semiconductor Device Research Conference, 1953.

[5] C. S. Fuller and J. D. Struthers: Copper as an Acceptor Element in Germanium. *Physical Review*, 1952, vol. 87, p. 526.

[6] H. Kromer: An Explanation of the Failure to Observe Thermal Conversion in Alloy Transistor Base Material. IRE-AIEE Semiconductor Device Research Conference, 1955.

[7] R. A. Logan: Restoration of Resistivity and Lifetime in Germanium. *Journal of Applied Physics*, 1955, vol. 26, p. 1287.

[8] M. Hansen: *Aufbau der Zweistofflegierungen*. Springer, Berlin, 1936.

Discussion of this paper sent (2 copies) to AIME by June 1, 1957 will appear in AIME *Transactions* Vol. 209, 1957, and in JOURNAL OF METALS, October 1957.

Technical Note

Further Contribution to the Crystallographic Angles for Bismuth and Antimony

by W. Vickers

SALKOVITZ[1] has given a number of useful angles between planes for use with the Laue method in determining the orientation of bismuth single crystals. Bismuth is usually considered as having a face-centered-rhombohedral structure with its axial angle 87°34′, Fig. 1. A similar figure given by Salkovitz appears to be in error in that the angle there marked as 87°34′ should be 92°26′. The primitive cell is a single rhombohedron of axial angle 57°14′. The structure is almost face-centered-cubic and hence high accuracy in measurements is essential if there is to be no confusion in indexing poles or zone axes.

It is easier to get this accuracy if zone axes are plotted on the stereogram because they will lie near the basic circle where the net has a more open scale. The zone axes can be read from the film, using a Greninger chart, and can be plotted more accurately than poles. Also, the angles between points near the basic circle can be read more accurately than those between poles near the center.

In order to use the zone axes the angles between directions have been calculated from a formula given by Niggli,[2] and are given in Table I. Miller indices

W. VICKERS, Student Associate AIME, is with the University of Sheffield, Sheffield, England.

TN 386E. Manuscript, June 26, 1956.

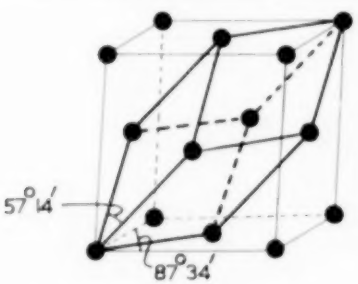

Fig. 1—Crystal structure of bismuth, showing simple rhombohedron and face-centered-rhombohedron.

Fig. 2—Standard [111] stereographic projection for bismuth and antimony.

Table I. Angles Between Directions

Directions	Angles	Directions	Angles	Directions	Angles	Directions	Angles	Directions	Angles	Directions	Angles	Directions	Angles
101		101		101		101		211		211		211	
	19°19'		33°6'		31°24'		19°52'		18°9'		20°37'		30°00'
102		113		112		212		212		111		101	
	6°22'		19°24'		29°58'		15°59'		48°18'		16°21'		30°00'
103		012		011		111		001		122		112	
	18°40'		57°29'		28°38'		19°28'		47°6'		19°27'		30°00'
001		111		121		121		212		011		011	
	18°12'		37°29'		28°38'		9°55'		17°52'		33°36'		30°00'
103		210		110		131		211		111		121	
	7°52'		19°24'		29°58'		24°46'		24°17'		18°22'		30°00'
102		311		211		010		210		211		110	
	17°43'		33°6'		31°24'		24°46'		24°39'		9°38'		30°00'
101		101		101		131		211		311		211	
	17°43'						9°55'				25°2'		
201						121				100			
	7°52'						19°28'				25°59'		
301						111				311			
	18°12'						15°59'				10°59'		
100						212				211			
	18°40'						19°52'						
301						101							
	6°22'												
201													
	19°19'												
101													

Table II. Angles Between Planes

Normals to Planes	Angles	Normals to Planes	Angles	Normals to Planes	Angles	Normals to Planes	Angles	Normals to Planes	Angles	Normals to Planes	Angles	Normals to Planes	Angles
101		101		101		101		211		211		211	
	17°45'		20°59'		28°39'		19°7'		17°19'		18°22'		30°00'
102		214		112		212		212		111		101	
	7°54'		8°56'		29°57'		15°36'		18°44'		15°13'		30°00'
103		113		011		111		214		122		112	
	18°11'		19°5'		31°23'		19°28'		29°21'		19°26'		30°00'
001		012		121		121		001		011		011	
	18°49'		41°00'		31°23'		10°7'		29°51'		36°58'		30°00'
103		111		110		131		214		111		121	
	8°21'		41°00'		29°57'		25°41'		19°22'		20°37'		30°00'
102		210		211		010		212		211		110	
	19°8'		19°5'		28°39'		25°41'		17°53'		10°25'		30°00'
101		311		101		131		211		311		211	
	19°6'		8°56'				10°7'		11°28'		25°21'		
201		412				121		421		100			
	8°21'		20°59'				19°28'		12°28'		24°9'		
301		101				111		210		311			
	18°49'						15°36'		23°35'		9°24'		
100						212		211		211			
	18°11'						19°7'						
301						101							
	7°54'												
201													
	17°45'												
101													

are used throughout and refer to the large face-centered-rhombohedron.

For checking or indexing spots, more angles between planes are needed than are given by Salkovitz. Therefore, some angles between planes have been calculated from another expression,[3] and are given in Table II. The angles between adjacent directions or adjacent normals to planes lying on prominent great circles are to be found in these tables. This way is more convenient than the conventional form.

Since bismuth is almost face-centered-cubic, a rough orientation can be obtained by considering it as such.[1] The zone axes can now be identified uniquely by accurately measuring the angles between them, and by using Table I in conjunction with the *cubic* indices and the standard [111] projection, Fig. 2.

Although the axial angle for bismuth is nearly 90°, it is not sufficiently accurate for this purpose to assume that angles between directions are the same as the angles between normals to planes with the same indices. After correctly indexing the zone axes the stereogram is rotated to the standard projection shown in Fig. 2, and the orientation is deduced.

As a check, the angles between one or two pairs of poles corresponding to prominent spots may be measured and compared with angles between planes given in Table II. The indices of the spots can be calculated from those of any two zone axes whose zones pass through them.[2] The angles in Tables I and II for bismuth can be used for antimony because its axial angle in the face-centered-rhombohedron is only 10' less than that of bismuth.

Acknowledgments

The author's thanks are due to G. B. Greenough for many helpful suggestions and criticisms, and to the University of Sheffield for the award of the Goodwin Fellowship for the course of work of which this is a part.

References

[1] E. I. Salkovitz: *AIME Trans.*, 1956, vol. 206, p. 176; JOURNAL OF METALS, February 1956.

[2] P. Niggli: *Handbuch der Experimental Physik*, 1928, vol. 7, part 1, p. 151.

[3] C. S. Barrett: *Structure of Metals*, pp. 189, 632. 2nd Ed. McGraw-Hill Pub. Co. Ltd. London, 1953.

On A Mechanism Of High Temperature Intercrystalline Cracking

An experimental investigation was made to ascertain the factors responsible for the nucleation and growth of intercrystalline voids in specimens subjected to high temperature and stress. It was determined that void nuclei are developed as a consequence of grain boundary slip. These voids, once nucleated, grow either by vacancy condensation or plastic yielding or both. A theory for the development of void nuclei by grain boundary slip is presented.

by C. W. Chen and E. S. Machlin

THIS investigation is concerned with the origin of the intercrystalline voids and cracks formed in metals and alloys subjected to stress at elevated temperature. There have been many suggestions in the recent literature relating to this problem. Greenwood[1] suggested that the voids may be produced by vacancy condensation. Zener[2] has stated that shear-stress relaxation across grain boundaries could initiate high tensile stresses at the regions blocking grain boundary slip and thereby cause the formation of cracks. Chang and Grant[3] have described the formation of cracks at grain boundary triple points and have experimentally verified Zener's mechanism for the grain boundary regions in the vicinity of a triple point.

Subsequent to the completion of this investigation, Gifkins[4] developed a model which made use of Stroh's[5] mechanism of fracturing to produce submicroscopic fractures that subsequently grow by grain boundary slip. Chen and Machlin,[6] in answer to Gifkins, described a model deduced from the present investigation, in which grain boundary slip provides both the stress to fracture at grain boundary jogs and the deformation required to separate fractured jog surfaces. The possibility of gas condensation to form intercrystalline voids and cracks is eliminated as a basic mechanism because such voids and cracks are developed in vacuum melted material containing minute amounts, if any, of gaseous impurities.

C. W. CHEN, Member AIME, formerly with the School of Mines, Columbia University, is now with the Magnetics Dept., Research Laboratory, Westinghouse Electric Corp., Pittsburgh. E. S. MACHLIN, Member AIME, is with the School of Mines, Columbia University, New York.

TP 4420E. Manuscript, Sept. 17, 1956. New Orleans Meeting, February 1957.

In a theoretical evaluation of this problem, Machlin[7] concluded that void nucleation by vacancy condensation during creep-rupture is improbable but that vacancy condensation on supercritical sized voids to produce growth is probable. This investigation was begun to evaluate the suggested mechanisms for intercrystalline fracture. In particular, in order to correlate vacancy supersaturation ratios produced in creep with those determined by Balluffi and Seigle[8] as critical for the nucleation of voids, specimens were obtained from the same heat of brass as used by the latter authors, through the courtesy of Dr. Seigle.

The experiments conducted in this investigation fall into the following categories:

1) Brass—observation of voids produced under a variety of conditions, including creep under compression, to evaluate the mechanisms of void nucleation and growth.

2) Bicrystal experiments to check the mechanism of void nucleation deduced in this investigation.

3) Morphology of intercrystalline voids produced in a variety of metals.

Each set of experiments will be described and discussed separately.

Experimental Techniques

A special creep-rupture test rack was constructed which made it possible to apply the stress to the specimen in a controlled atmosphere of inert gas, reducing gas, or vacuum. All the creep-rupture tests on α-brass (30 pct Zn) were conducted in nitrogen under a pressure slightly above atmospheric. Either dead weight loading or constant elongation rate loading could be applied with the load measured by means of a strain gage dynamometer. In order to obtain a coarse-grained crystal structure stable at

lower temperatures, all specimens were annealed in nitrogen 16 hr at 800°C. During the grain-coarsening anneal, α-brass chips surrounded the specimen to minimize dezincification. The average grain size developed was 0.5 to 1.0 mm diam.

Voids in α-Brass

Vacancy Supersaturation Limit in Grains—According to the latest diffusion experiments of Resnick and Seigle,[7] who used the same heat of brass in their experiments, the smallest vacancy supersaturation ratio at which voids are developed within the grains in this brass lies between 1.04 and 1.7. In the present investigation, many creep-rupture tests have been conducted at 482°C at a strain rate of 1 pct per hr with the same brass. In *no* case in over 20 specimens examined were voids found within the grains. From these experiments and observations it appears that the vacancy supersaturation ratio developed by this creep rate within the grains is less than 1.7. Inasmuch as this creep rate is much larger than that which exists in normal creep-rupture tests and inasmuch as theory predicts that for a given creep rate the vacancy supersaturation ratio should decrease with increasing temperature, it may be concluded that in α-brass, at least, the vacancy supersaturation ratio within the grains will be less than 1.7 under creep conditions that yield intercrystalline fracture. (The tendency to have intercrystalline fracture increases the lower the creep rate and the higher the temperature.)

Voids at Grain Boundaries—In all the specimens subjected to a strain rate of 1 pct per hr at 482°C for more than 1½ hr, voids and cracks were developed at grain boundaries. These voids and cracks were definitely not produced by dezincification at grain boundaries because identically prepared specimens never produced voids outside the dezincified zone after being annealed prolongedly at 482° or even 800°C in the absence of stress or prior creep strain. In view of the fact that grain boundaries are good sinks for vacancies and that in thin specimens Balluffi and Seigle never observed porosity along grain boundaries in dezincified brass of the same heat, even when porosity had developed within the grains, it implies that the creep rupture test conditions had either decreased the critical supersaturation required to develop voids along grain boundaries, that the actual vacancy supersaturation at the grain boundaries is higher than within the grains, or that the cracks and voids were formed by a mechanism not involving vacancy condensation.

A simple test was conducted as follows to evaluate the first possibility. Specimens of 0.357 in. diam were subjected to ½ pct strain at a strain rate of 1 pct per hr, at 482°C. They were then stretched another 5½ pct at −196°C and annealed in nitrogen 6 hr at 482°C. Thin dezincified zones developed. In these zones it was found that voids had developed along grain boundaries as well as elsewhere, see Fig. 1a. In equivalent specimens, not previously subjected to stress, but similarly annealed, no voids were found at the grain boundaries in the dezincified zone, see Fig. 1b. Other specimens subjected to 6 pct strain at −196°C, then annealed at 482°C for 6 hr, did not develop voids along grain boundaries in the dezincified zone. Also, if the specimens were annealed for 20 hr at 800°C just subsequent to the ½ pct strain at 482°C, then *no grain boundary voids were produced in the dezincified zone* that appeared after the further sequence of 5½ pct at −196°C and 6 hr in nitrogen at 482°C. In other words, a sintering anneal subsequent to the high temperature (482°C) strain of ½ pct removed the effect of such strain in the production of voids in the presence of excess vacancies pumped in by the dezincification process. It is therefore concluded that the critical supersaturation ratio of vacancies required to form* voids at grain boundaries is reduced by the prior application of sufficient strain at relatively high temperatures (above the *equicohesive* temperature) but not at relatively low temperatures. That is, for the same vacancy supersaturation produced *by dezincification* under identical conditions voids developed at grain boundaries in specimens previously deformed at high temperature, but did not develop in specimens previously deformed at or below room temperature only.

* Either by heterogeneous nucleation and growth or by growth of supercritical sized nuclei.

Void Growth—Although the previous sequence of experiments demonstrates that high temperature strain has produced more potent heterogeneous void embryos or nuclei (submicroscopic cracks) and thereby lowered the critical supersaturation ratio of vacancies for void formation, it says nothing about the actual supersaturation ratio of vacancies at grain boundaries under the creep-rupture conditions or about whether the voids or cracks developed at grain boundaries during creep would have appeared in the absence of vacancy condensation.

It is difficult to conceive of an experiment which can reveal information about the relative importance of these two concepts. On the other hand, it is possible to devise, on the basis of certain premises, some experiments which might shed light on the question of whether or not excess vacancies exist under creep-rupture conditions. If excess vacancies do exist, then certain results might be expected. The results obtained from these experiments will serve to test the validity of these premises. Two such sets of experiments have been devised. In the first, the premise is made that if heterogeneous void nuclei are present, then it should be possible by cold deformation to produce an excess vacancy concentration and by a subsequent anneal to enable the vacancies to condense on the heterogeneous void nuclei present to produce visible voids. In the second set of experiments, the premise is made that if voids obtained under creep-rupture conditions are grown out to visible size by vacancy condensation, then such voids should be observed under compression creep conditions.

In an attempt to evaluate these possibilities, brass tensile specimens were first deformed ½ pct at 482°C at a rate of 1 pct per hr, to produce submicroscopic cracks; further deformed 18½ pct at −196°C, to open out these cracks so they can act as nuclei and to produce excess vacancies; examined at room temperature; annealed at 482°C for 20 hr in nitrogen to provide mobility for vacancy migration and an opportunity for the vacancies, if there, to condense on the nuclei to grow out voids; and then examined again. Typical results are presented in Fig. 2. It is shown there that additional isolated voids are produced during the 482°C anneal.

The formation of these additional isolated voids is probably not a dezincification effect, because then the voids would be expected to be much more uniformly distributed. Also, no such voids are observed after a cycle of 18½ pct strain at −196°C and an

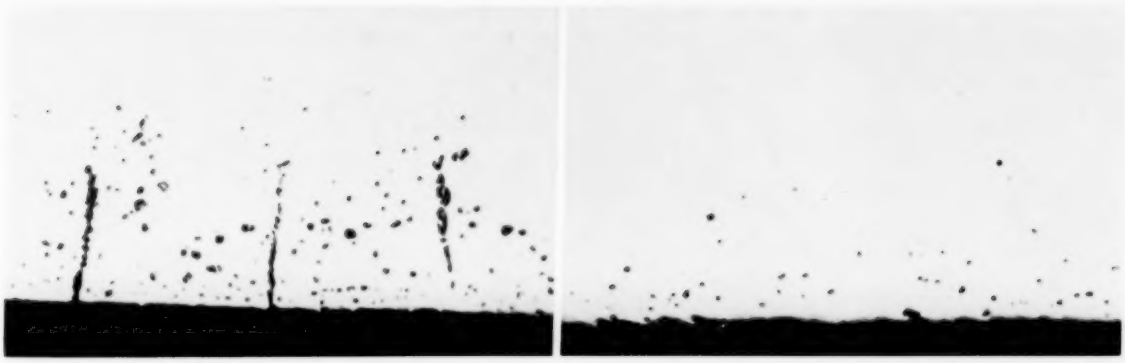

Fig. 1—Voids formed in thin dezincified zone of α-brass specimens. a) LEFT: Specimen was annealed 16 hr at 800°, strained ½ pct at 482° and 5½ pct at —196°, and annealed 6 hr at 482°C. Notice that voids are formed at grain boundaries. b) RIGHT: Specimen was annealed only; not previously strained. Diffusion voids are formed only within grains by the Kirkendall effect. X150. Reduced approximately 30 pct for reproduction.

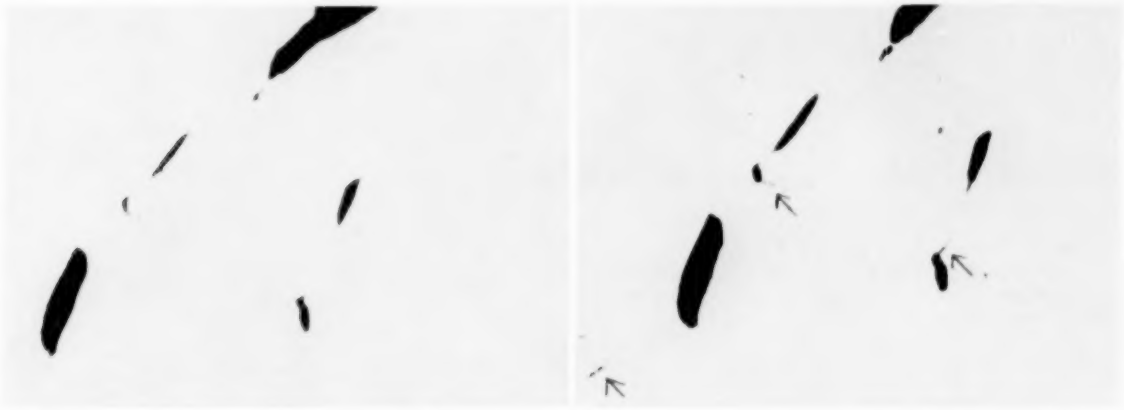

Fig. 2—a) LEFT: Intercrystalline voids and cracks are developed in an α brass specimen strained ½ pct at 482° and 18½ pct at —196°C. b) RIGHT: Additional voids (indicated by arrows) are produced after specimen shown in Fig. 2a was annealed 20 hr at 482°C. X50. Reduced approximately 15 pct for reproduction.

Fig. 3—Typical intercrystalline voids formed in compression creep specimens of α-brass. Test conditions: strain rate of 5 pct per hr at 1000°F for 1 5/6 hr in nitrogen. Transverse section. X50. Reduced approximately 15 pct for reproduction.

Fig. 4—Typical intercrystalline voids and cracks formed in creep of α-brass specimens under compression. Test conditions: strain rate of 5 pct per hr at 1000°F for 1 5/6 hr in nitrogen. Transverse section. X50. Reduced approximately 15 pct for reproduction.

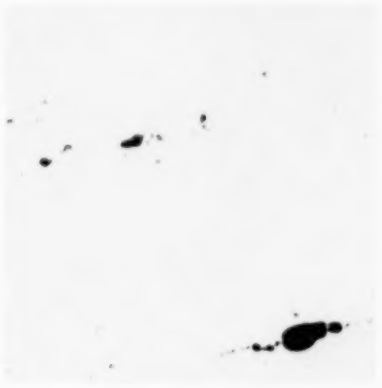

Fig. 5—Typical intercrystalline voids formed in compression creep of high purity copper (99.999 pct). Test conditions: strain rate of 1 pct per hr at 1200°F for 22 hr in a vacuum of 10^{-4} mm Hg. Large voids are about three times actual size as a result of etching. X75. Reduced approximately 30 pct for reproduction.

Fig. 6—Voids and cracks developed along a copper bicrystal boundary by grain boundary shear, diamond dust polished and unetched. Test conditions: 600 psi and 482°C for 20 hr in hydrogen. X150. Reduced approximately 35 pct for reproduction.

anneal for 20 hr at 482°C, without the prior high temperature strain. The effect might be due to the relaxation of internal tensile stress distributions near the spearheads of the existing cracks. It also might be due to the condensation of vacancies on supercritical void nuclei that exist near cracks produced during the previous deformation cycle. Consequently, it can be deduced that the possibility of vacancy production during deformation and condensation of said vacancies on void nuclei are consistent with the experimental results, although they have by no means been proven.

In a test of the second suggestion, compression specimens of α-brass were subjected to a compressive strain rate of 5 pct per hr at 1000°F in an atmosphere of nitrogen. Colloidal graphite was used between the specimen and load plates to minimize barrelling. After a total strain of 9 pct, the specimens were sectioned both transversely and longitudinally. Many intercrystalline voids were found with about the same number per unit area at the center of the specimen as near the outside surfaces (beneath the thin dezincified zone). In general, more voids were distributed along longitudinal boundaries than along transverse grain boundaries. Also, in the transverse section, there was a noticeable tendency for the voids to surround certain grains rather than to be equally distributed along the longitudinal boundaries. Typical examples of the voids that were found are presented in Figs. 3 and 4.* These results are eminently consistent with the theory of void growth by vacancy condensation. Although it is possible to account for the growth of the voids by submicroscopic tensile stresses induced at the edges of the submicroscopic cracks, this mechanism for void growth is not as attractive as that of vacancy condensation. The facts that the voids tend to be spherical and isolated support the hypothesis of vacancy condensation as the source of the void volume as compared to a plastic flow mechanism of void growth. It should be pointed out, however, that very high strain rates localized about the grain boundaries would be necessary to account for the total volume of voids found.[7] The measured strain rate for the specimens as a whole is too small by at least a factor of 100 to account for the vacancies generated unless for some unknown reason the vacancy generating power of the dislocations moving in the vicinity of grain boundaries is many times that for dislocations moving within the grains.

Similar compression creep tests have also been conducted on high purity copper and silver specimens with very similar results, see Fig. 5, except that the number of isolated voids in copper and silver is noticeably less than that found in α-brass.

From the above sequence of experiments, it can be concluded that the vacancy condensation mechanism cannot yet be ruled out as the responsible mode of void growth. On the other hand, the results obtained are consistent with this hypothesis. The same statements can also be made for a mechanism of isolated void growth by plastic flow under a local tension field of stress. However, it is difficult to visualize the operation of the latter mechanism in detail.

Void Nucleation—In view of the results described in a previous section on the nucleation of voids at grain boundaries, it appeared desirable to evaluate the role of the high temperature strain in the process of void nucleation. In the absence of prior high temperature strain it was found that no voids or intercrystalline cracks could be developed either by a deformation of 6, 20, or 50 pct at −196°C. However, the sequence ½ pct strain at 482°C (at a rate of 1 pct per hr), and a subsequent deformation of 18½ pct at −196°C, produced a multiplicity of intercrystalline cracks, see Fig. 2a. If specimens are annealed at 800°C for 20 hr subsequent to the ½ pct strain at 482°C but prior to the low temperature strain, then no cracks or voids are observed either after the 18½ pct strain at −196°C or after annealing at 482°C for 20 hr subsequent to the 18½ pct strain. These results and the other results described previously using α-brass specimens are summarized in Table I. It is indicated from this set of experiments that small submicroscopic cracks are developed at grain boundaries during the ½ pct strain at 482°C, that these cracks are sufficiently small so that they can be sintered out in 20 hr at 800°C, that these cracks are sufficiently large to affect the low temperature fracture stress, and that these submicroscopic cracks at grain boundaries are not produced as effectively or at all by deformation at low tem-

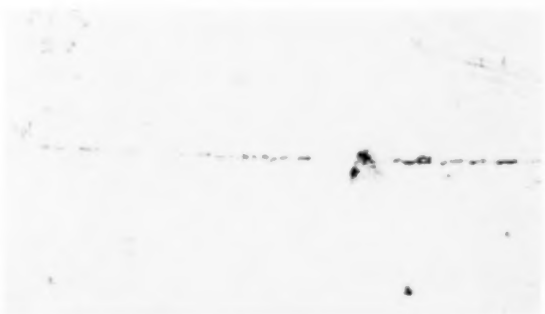

Fig. 7—By the application of tensile stress of 1200 psi at 1200°F for 20 hr, voids and cracks seen in Fig. 4 are grown to form elongated cracks. New voids and cracks are also observed. Specimen surface is the same in both Figs. 6 and 7. The poor micrographic appearance is due to the fact that the surface has been subjected to 1200°F in hydrogen (some oxidation has taken place) and is shown without additional polishing for comparison of the voids relative to their appearance in Fig. 6. X150. Reduced approximately 35 pct for reproduction.

* Control specimens, both annealed and cold-worked, never developed voids when polished and etched by the technique used on these specimens.

peratures in these specimens. Further, if these submicroscopic cracks are made sufficiently large, they act as void nuclei to condense vacancies in the presence of an excess concentration of vacancies. The observed effect of temperature of deformation strongly implies that grain boundary shear, which exists at high temperature but not at low temperature, is involved in the formation of the submicroscopic cracks. A direct experimental check of this implication was devised and is described in the next section.

Bicrystal Experiments

As indicated in the previous section, it appears probable that grain boundary shear is required to form the submicroscopic cracks which act as nuclei for voids grown by vacancy condensation and provide the stress concentrators in subsequent low temperature tensile tests. In order to provide a direct test of this implied result, bicrystals were grown, using 99.999 pct Cu according to the technique of Chalmers.[9] Sections were carefully cut normal to the bicrystal boundary to produce many

Table I. Experimental Results

Experiment No.	Treatment	Observation in Microscopic Examination*
1	6 pct strain at 482°C	Specimen failed in the mode of intercrystalline rupture. Voids at grain boundaries everywhere.
2	6, 20, 50 pct strain at −196°C	No voids.
3	6 pct strain at −196°C, 6 hr anneal at 482°C	No voids.
4	½ pct strain at 482°C, 5½ pct strain at −196°C	No voids.
5	½ pct strain at 482°C, 5½ pct strain at −196°C, 6 hr anneal at 482°C	Voids at many grain boundaries in the dezincified zone at the surface. No voids elsewhere, see Fig. 1a.
6	½ pct strain at 482°C, 6 hr anneal at 482°C	No voids even along grain boundaries of dezincified zone.
7	½ pct strain at 482°C, 18½ pct strain at −196°C	Voids at grain boundaries all over the entire surface of the specimen.
8	½ pct strain at 482°C, 18½ pct strain at −196°C, 20 hr anneal at 482°C	Additional (with respect to experiment No. 7) round voids at grain boundaries, see Fig. 2.
9	½ pct strain at 482°C, 20 hr anneal at 800°C, 18 pct strain at −196°C	No voids.
10	½ pct strain at 482°C, 20 hr anneal at 800°C, 18 pct strain at −196°C, 20 hr anneal at 482°C	No voids.

* In no case were voids found within the grains outside the dezincified zone.

bicrystal specimens having the same relative grain and boundary orientations. The final dimensions of each specimen were about 1 x ½ x 0.080 in. A clamping mechanism was constructed which made possible the application of a shear traction parallel to the boundary. Another set of clamps was used in order to apply a tension force normal to the grain boundary. At first, the tests were conducted in nitrogen at 1200°F. It was found that the oxide produced along the grain boundary obscured the results. Consequently, subsequent tests were performed in low dew point hydrogen.

It was found that visible voids appeared along the grain boundary, as revealed by diamond polishing alone or in conjunction with subsequent etching,* after grain boundary shear. Voids never appeared when tension normal to the boundary was the sole

* Etchant was 5 parts NH_4OH, 5 parts H_2O, and 2 parts H_2O_2 (3 pct).

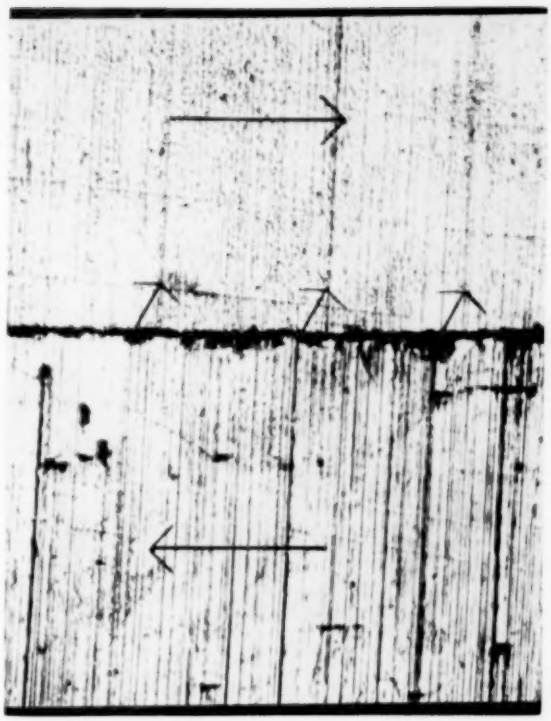

Fig. 8—Grain boundary shear along copper bicrystal boundary indicated by the displacement of scratches. Amount of displacement is about 30 μ; shear stress, 600 psi; temperature, 1200°C; time, 20 hr. The bicrystal boundary runs horizontally. X150. Reduced approximately 10 pct for reproduction.

stress history. In other words, application of a tensile stress, as for example 1200 psi, normal to the boundary for a period of 20 hr at 1200°F *never produced visible voids*. On the other hand, application of a shear stress of about 600 psi at 1200°F, parallel to the boundary, for a period of 20 hr always resulted in visible voids. See, for example, Fig. 6, which shows a line of voids along the grain boundary in a bicrystal specimen after the latter was subjected at 1200°F to shear stress parallel to the grain boundary, as revealed by diamond polishing alone. Similar diamond polishing of nonstressed bicrystal specimens never produced voids along the boundary. If tensile stress normal to the grain boundary was applied subsequent to a prior application of parallel shear, then the number and size of voids observed along the boundary increased. See, for example, Fig. 7. However, as previously mentioned, no voids were ever observed after application of a tensile stress alone normal to the boundary. One specimen, in which the boundary was not ideally plane, illustrated this result strikingly. The sections of the boundary normal to the applied force developed *no* visible voids. The sections of the boundary having a resolved shear component (about 45° to the force direction) developed visible voids. The results of this section were reproducible over five sets of identical experiments.

By observation of fiducial lines crossing the boundary, see Fig. 8, it was observed that the grain boundary shear resulted in slip along the grain boundary. An average value of the relative translation of grains in these experiments in which grain boundary voids were observed is about 25 to 30 μ. It can be

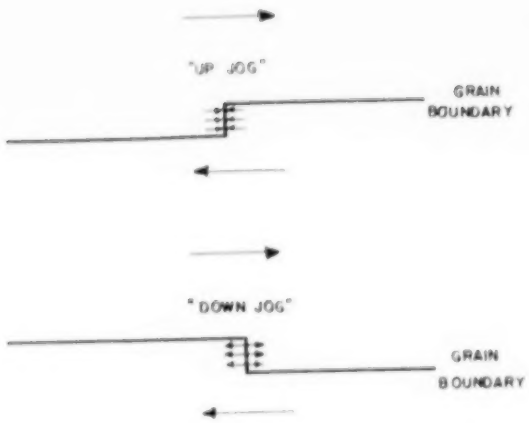

Fig. 9—Stresses induced by boundary sliding in the direction shown at jogs.

concluded from these experiments that relative translation of the grains along the boundary, hereafter called grain boundary slip, is a necessary condition for the development of intercrystalline voids and cracks under creep-rupture conditions. It can also be concluded that the model of void nucleation[7] based on the Stroh mechanism of dislocation pile up to develop high tensile stresses and fracture at the grain boundary is not real under the conditions of the previously described experiments.

A model that is consistent with experiment is as follows. At high temperature, grain boundaries have negligible resistance to shear traction. As a consequence of grain boundary slip accompanying shear traction, stresses are developed wherever grain boundary slip cannot occur. One such region is a triple point and Chang and Grant[7] have adequately shown that the stresses developed at such regions can lead to the development of intercrystalline cracks. Another region where grain boundary slip is blocked is at a jog along the boundary. Fig. 9 illustrates that tensile or compressive stresses can be developed at a *down* jog or *up* jog, respectively. The magnitude of this stress at a particular jog increases as the area of the jog decreases and the shear relaxation length between the adjacent jogs increases. The tensile stress at a *down* jog may therefore exceed the fracture stress. Thereafter, the role of grain boundary slip is to separate the fractured jog surfaces, as illustrated in Fig. 10. Once the submicroscopic crack thus formed exceeds a critical length, either vacancies may condense on the crack and thereby form a visible void; or the tensile stress normal to the boundary that is concentrated at the crack edges may induce plastic deformation that will enlarge the crack; or both.

Development of Macroscopic Intercrystalline Cracks

It is believed that the linking together of isolated intercrystalline voids is responsible for the formation of the macroscopic intercrystalline cracks. As a check, many intercrystalline cracks have been examined in a large variety of metals, e.g., silver, nickel, copper, and α-brass. Some of these cracks are shown in Fig. 11. It is apparent that the crack outline invariably appears to be in the form of isolated semicircles connected by straight lines. Also, isolated voids are usually found at the spearheads of the macroscopic cracks, see Figs. 2b, 4, and 11. It appears, therefore, that there is good evidence for the assertion that the many macroscopic intercrystalline cracks are a result of linking together of the isolated intercrystalline voids.

Discussion

As a consequence of this investigation there is no doubt that grain boundary slip is a necessary condition for the development of intercrystalline void nuclei. Further, it has been demonstrated that such void nuclei can be grown out to visible size in the presence of a supersaturation of lattice vacancies and that plastic deformation probably produces such a supersaturation of lattice vacancies.

It is of practical, as well as scientific, interest to speculate about the factors that affect the resistance to grain boundary slip and the fracture stress of the grain boundary jogs. As Gifkins[9] pointed out, slip that intersects the grain boundary produces grain boundary jogs. Jogs will usually be associated with inclusions along the boundaries. Wrong jogs instead of fracturing will act to lock grain boundary slip and undoubtedly are responsible for the observed effect[10] that grain boundary shear displacement is often distributed over the volume adjacent to the boundary rather than localized at the boundary itself. Right jogs for fracturing, if present alone, must have sufficient area to resist the shear traction. A simple calculation on the assumption of a fracture stress of about 100,000 psi and a creep stress of about 10,000 psi reveals that a plastic strain larger than $(10{,}000/4 \times 10{,}000) \times 100 = 2.5$ pct would be required to produce sufficient slip intersection jogs along grain boundaries to prevent jog fracture. It is now apparent that if particle hardening were to be used to block grain boundary slip, an extensive distribution of particles along the boundary would be required.

In normal single phase alloys and metals, there would not normally be any resistance to jog fracture* except in the case of marked grain boundary migration under the creep-rupture conditions. Consequently, in these materials the rupture life of the part would depend upon the rate of growth of the voids. One such theory has already been given.[7] Because the amount of grain boundary slip has been shown by previous investigators[10, 10] to be uniquely related to the total deformation, it is possible that

* It is assumed that, for most of the jogs, the grain material adjacent to the jog is *relatively hard*; that is, the stress across the jog cannot be relieved by plastic flow because of the smallness of the jog dimension, 10^{-6} cm or less.

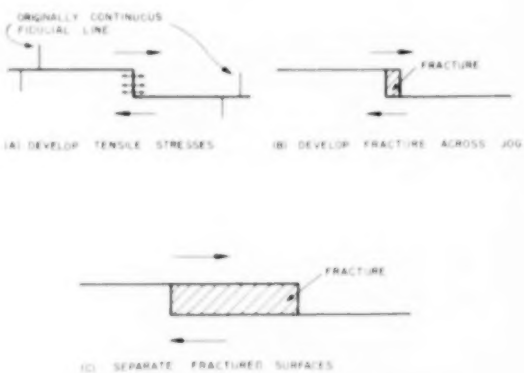

Fig. 10—Steps in the development of intercrystalline cracks due to increasing boundary slip according to the proposed mechanism.

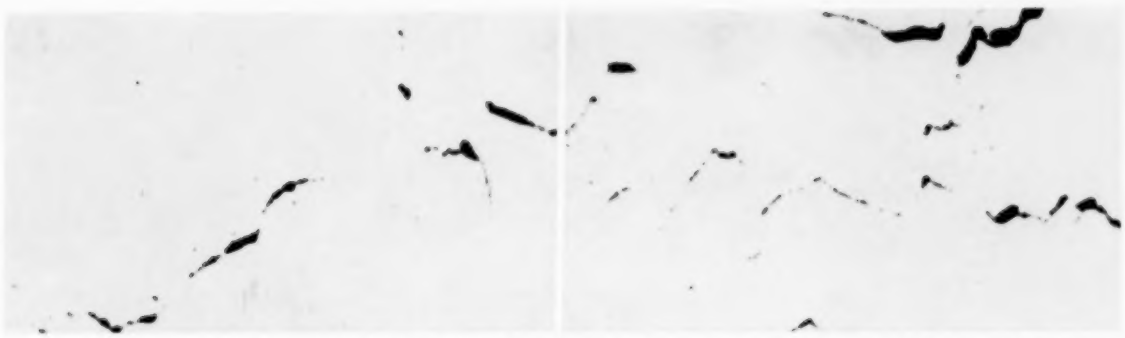

Fig. 11—Micrographs illustrate that voids link together to form cracks. Notice the semicircular outline of cracks. a) LEFT: Transverse section of α-brass specimen subjected to creep under compression. b) RIGHT: Longitudinal section of nickel specimen subjected to creep-rupture test under tension. X50. Reduced approximately 25 pct for reproduction.

the time to produce the critical size of submicroscopic crack by slip, required before growth by vacancy condensation or plastic flow can take place, may be an appreciable fraction of the total rupture life. Observations revealed that at 1 pct strain per hr at 482°C no voids were observed until about 25 pct of the total rupture life or strain (6 pct) had been achieved. Further, ½ pct strain at 482°C alone was not sufficient to induce void formation along grain boundaries in the dezincified zone. Consequently, under the stated conditions it is apparent that the time to produce the critical size of submicroscopic crack is less than 25 pct but more than 8.5 pct of the rupture life. Surface active elements introduced as impurities or via the atmosphere may appreciably lower the surface energy of these void embryos and cause vacancy condensation and fracture to occur sooner. Also, the particular surface active element, oxygen, may cause an increase in the insufficient number of jogs at the boundary through the formation of oxides, and thereby hasten rupture.

In the special case where there are insufficient jogs to prevent jog fracture, the smaller the number of jogs the longer will be the rupture life(the more each jog must grow before macroscopic intercrystalline cracking can be achieved). It should be possible to achieve high strength against intercrystalline cracking by distributing sufficient particles along grain boundaries to anchor the grain boundary slip and migration adequately. It is believed that the SAP materials achieve their strength in this manner.

Conclusions

As a result of the present investigation, a mechanism of high temperature intercrystalline cracking in metals has been proposed. The formation of voids at grain boundaries is considered to be primarily responsible for the brittle failure of metals at elevated temperature. Voids are nucleated at jogs and grain corners along grain boundaries as a consequence of grain boundary slip and grown either by vacancy condensation or plastic yielding or both.* Macroscopic intercrystalline cracks are formed by the linking together of isolated voids.

The results of a series of α-brass tension creep experiments indicate that a sufficient amount of high temperature strain is required to produce void nuclei. The observation of void formation in the single grain boundaries of bicrystals with the application of shear traction parallel to the boundaries reveals that grain boundary slip is necessary to form void nuclei. A model illustrating the development of void nuclei by grain boundary slip is presented.

The probable mechanism of void growth by vacancy condensation has been demonstrated by the formation of spherical voids along grain boundaries in compression creep specimens and also by the development of isolated voids after annealing cold worked specimens that have contained void nuclei. However, this does not rule out the other growth mechanism, viz., by plastic yielding.

Evidence for the linking together of isolated voids to form macroscopic intercrystalline cracks has been obtained for a variety of metals and typical examples are presented.

Acknowledgments

This research was supported by the United States Air Force through the Wright Air Development Center. The authors also gratefully acknowledge the help of Hiizu Kuzuu, Robert Duncan, and David Kramer during part of the experimental investigation and the encouragement of James Poynter of the Wright Air Development Center.

References

[1] J. N. Greenwood, D. R. Miller, and J. W. Suiter: Intergranular Cavitation in Stressed Metals. *Acta Metallurgica*, 1954, vol. 2, No. 2, pp. 250–258.

[2] C. Zener: The Micro-Mechanism of Fracture. *Fracturing of Metals*, pp. 7–8. American Soc. for Metals, Cleveland, 1948.

[3] H. C. Chang and N. J. Grant: Mechanism of Intercrystalline Fracture. *AIME Trans.*, 1956, vol. 206, pp. 544–551; JOURNAL OF METALS, May 1956.

[4] R. D. Gifkins: A Mechanism for the Formation of Intergranular Cracks When Boundary Sliding Occurs. *Acta Metallurgica*, 1956, vol. 4, pp. 98–99.

[5] A. N. Stroh: The Formation of Cracks as a Result of Plastic Flow. *Proceedings* Royal Soc. of London, 1954, series A, vol. 223, No. 1154, pp. 404–414.

[6] C. W. Chen and E. S. Machlin: On the Mechanism of Intercrystalline Cracking. *Acta Metallurgica*, 1956, vol. 4, pp. 655–656.

[7] E. S. Machlin: Creep Rupture by Vacancy Condensation. *AIME Trans.*, 1956, vol. 206, pp. 106–111; JOURNAL OF METALS, February 1956.

[8] R. W. Balluffi and L. L. Seigle: Effect of Grain Boundaries Upon Pore Formation and Dimensional Changes During Diffusion. *Acta Metallurgica*, 1955, vol. 3, No. 2, pp. 170–177.

[9] R. Resnick and L. L. Seigle: Nucleation of Voids in Metals During Diffusion and Creep. *AIME Trans.*, 1957, vol. 209, pp. 87–94; JOURNAL OF METALS, February 1957.

[10] B. Chalmers: Crystal Growth and Crystal Boundary Techniques. *Modern Research Techniques in Physical Metallurgy*, pp. 181–182. American Soc. for Metals, Cleveland, 1953.

[11] F. N. Rhines, W. E. Bond, and M. A. Kissel: Grain Boundary Creep in Aluminum Bicrystals. *ASM Trans.*, 1956, vol. 48.

[12] B. Fazen, O. D. Sherby, and J. E. Dorn: Some Observations on Grain Boundary Shearing During Creep. *AIME Trans.*, 1954, vol. 6, pp. 919–922; JOURNAL OF METALS, August 1954.

[13] D. McLean: Grain Boundary Slip During Creep of Aluminum. *Journal* Institute of Metals, 1953, vol. 81, pp. 293–300.

Discussion of this paper sent (2 copies) to AIME by Sept. 1, 1957 will appear in AIME *Transactions* Vol. 212, 1958, and in JOURNAL OF METALS, April 1958.

* After this paper was submitted, D. Kramer at Columbia University obtained striking evidence that the crack area per unit grain boundary area was proportional to the amount of grain boundary sliding. Hence, the latter is controlling not only in void nucleation but in the important aspect of void growth, that is, the area of the voids across which there is a lack of cohesion. These results will be reported shortly.

Cube Texture in Copper

Copper single crystals of initial (358) [523] orientation, after being cold rolled to 98 pct reduction in thickness, were observed to retain essentially their original orientation. The operating mechanism previously suggested[1] for this component of deformation texture in face-centered-cubic metals during recrystallization was experimentally observed to be valid to a certain extent.

by Y. C. Liu

IN the study of the rolling recrystallization of face-centered-cubic metals, a most unusual observation is the frequent occurrence of a sharp recrystallization texture of cube orientation. Although the general conditions under which this texture occurs are known,[2,3] its origin is still not well understood.

Based on the observed relationship between the {110}<112> deformation texture and the {113}<211> recrystallization texture, regardless of the effect of alloying elements[2,4,5] or the symmetry of the deformation texture,[6] there is a strong indication that a specific component of the deformation texture is related to a specific component of the recrystallization texture. Using the rotational reorientation relationship as a means of correlating the deformation and recrystallization textures, it was proposed that the deformation component which related the cube texture has {358}<523> indices.[1]

* The exact indices of the modified (358)[523] indices are (358)[40 16 25]. Throughout this paper the {358}<523> indices will signify the modified {358}<523> indices, the word modified being omitted for convenience. The four {358}<523> components, (358)[523], (358)[523], (358)[523], and (358)[523] are designated by Roman numerals I, II, III, and IV, respectively, as shown in Fig. 1, and are referred to in this way in the text.

The investigation reported here was undertaken to seek experimental evidence for the validity of this proposition.

Experimental Procedure

Two copper single crystals having an initial orientation within 2° of (358)[523] indices were prepared in the manner described in Ref. 5. The purity of the copper was between 99.94 and 99.97 pct. The original dimensions of the crystals were as follows: specimen A, 0.465 in. thickness, 0.844 in. width, and 0.955 in. length; specimen B, 0.535 in. thickness, 1.120 in. width, and 1.36 in. length. Rolling was done on a laboratory rolling mill according to the following schedule: 0.010 in. per pass to 50 pct reduction in thickness, 0.005 in. per pass to 70 pct reduction in thickness, 0.002 in. per pass to 85 pct reduction in

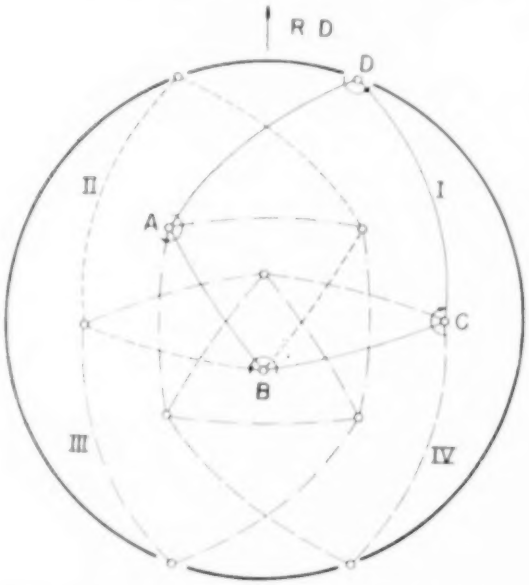

Fig. 1—Operation mechanism of (358) [523] deformation texture after annealing. Angle of rotation is 44°.

Y. C. LIU, Junior Member AIME, formerly Associate Engineering Scientist, Research Div., New York University, is now with Ford Motor Co., Detroit.

TP 4467E. Manuscript, May 28, 1956. New Orleans Meeting, February 1957.

Fig. 2—{111} pole figure after 95 pct reduction in thickness.

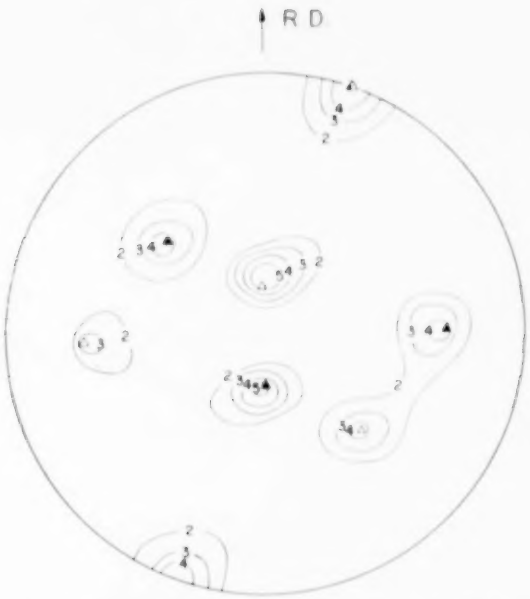

Fig. 3—{111} pole figure after 98 pct reduction in thickness (surface texture).

thickness, and 0.001 in. per pass to any reduction above 85 pct. All annealing was done in a muffle furnace with temperature control to ±5°C. A Pb-Sn bath with temperature controlled to within ±2°C was used for the isothermal anneal prior to hardness determination. All textures were determined by X-ray diffraction using a special Geiger-counter device adapted from the Schulz method.[6] The pole figure plotted was the surface texture. Since the device does not have an integrating mechanism, anneals were restricted to conditions which would keep grain size relatively small.

Experimental Data

Deformation Textures—The deformation textures for the two copper single crystals were found to retain the original $(35\bar{8})[523]$ orientation, with a reasonable degree of scatter, after being cold rolled to 80, 85, 90, and 95 pct reduction in thickness, Fig. 2. Of the two rolled strips, specimen B showed more scatter, but in the subsequent investigation of recrystallization textures, no appreciable difference was noticed between them.

On rolling to 98 pct reduction, two $\{358\}\langle\bar{5}23\rangle$ components, I and III, were observed, Fig. 3. Fig. 4 shows the deformation texture of the center part of the strip; it is very similar to the texture of cold-rolled polycrystalline material. This difference between the surface and center textures in the strip reduced 98 pct is not observed in the strip reduced 95 pct. In the latter, the only difference is a little more scatter in the center texture than in the surface texture.

Recrystallization Textures—Since the $(35\bar{8})[523]$ deformation texture may yield another $\{358\}\langle\bar{5}23\rangle$ recrystallization component, the exact position of this deformation texture with respect to a fixed-reference rolling plane and rolling direction was determined before the specimens were annealed.*

* In all the pole figures presented in this paper, the $(35\bar{8})[\bar{5}23]$ orientation, component I, was plotted as the deformation texture.

This precaution would avoid any ambiguity as to whether the $\{358\}\langle\bar{5}23\rangle$ recrystallization component was derived by the *recrystallization in situ* mechanism[7] or by the rotational reorientation mechanism.[8,9] During the course of this investigation, efforts were also extended to study the effect of a second anneal on the recrystallization texture of the specimens.* The second anneal was carried out either at a higher temperature or at the same temperature with longer annealing time.

* It was observed that, in all cases, the specimen after the first anneal has shown a completely recrystallized structure and its recrystallization pole figure was not much different from that after the second anneal. This indicated that only limited grain growth had taken place during the described conditions of the second anneal.

A specimen given an 80 pct reduction showed only scattered signs of recrystallization after being annealed 17 hr at 200°C. A recrystallization texture having four components, two in twin relationship with the other two, was observed after an additional anneal of 19 hr at 300°C. This is shown in Fig. 5, which is the recrystallization pole figure of the same specimen after further annealing for 1 hr at 400°C. One of the components in this figure is very close to a cube orientation and is present in almost all of the subsequent recrystallization pole figures plotted. For simplicity, this component is named the *off-cube* component. In Fig. 1, a 44° rotation about pole *A* yields a cube orientation; the off-cube orientation is related by a 38° rotation. This off-cube component is always accompanied by its twin component across the plane of the octahedral pole around which the rotational reorientation relationship is imposed. The other component has no common octahedral pole with the $(35\bar{8})[\bar{5}23]$ orientation and is referred to here as component *X*.

Fig. 4—{111} pole figure after 98 pct reduction in thickness (inside texture).

Fig. 6—{111} pole figure after 90 pct reduction and anneal at 400°C for 1 hr. Closed triangle represents the off-cube orientation and its twin; open square represents Y orientation.

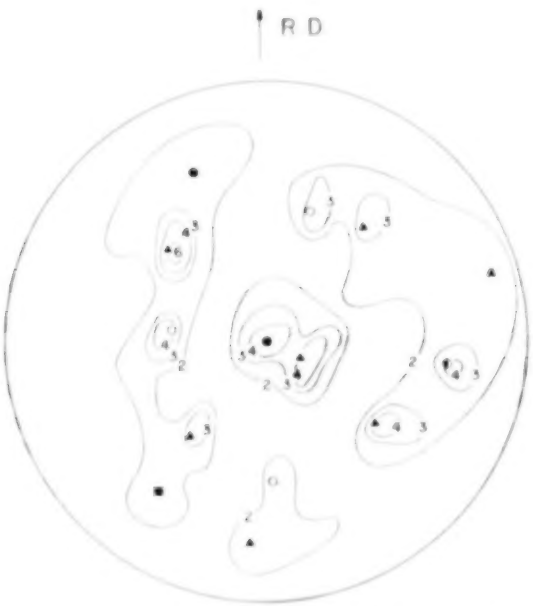

Fig. 5—{111} pole figure after 80 pct reduction and anneal at 200°C for 17 hr, at 300°C for 19 hr, and at 400°C for 1 hr. Closed triangle represents the off-cube orientation and its twin; open circle, X orientation; and closed circle, twin orientation of orientation X.

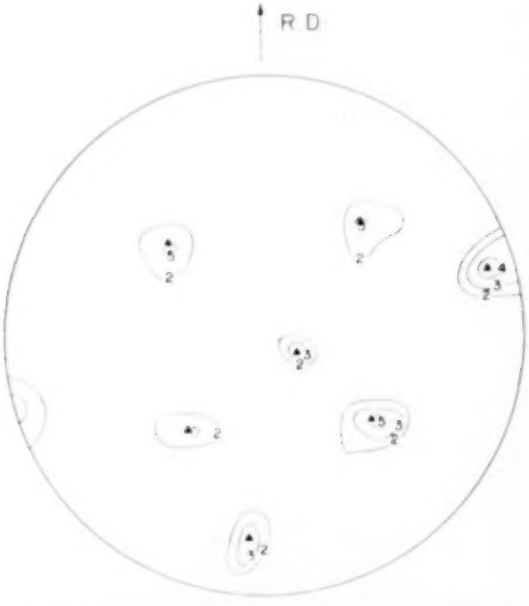

Fig. 7—{111} pole figure after 90 pct reduction and anneal at 500°C for 1 hr. Closed triangle represents the off-cube orientation and its twin.

Direct annealing of the specimen (80 pct reduction) either at 300°C for 65 hr or 500°C for 1 hr exhibited no major change in the recrystallization texture shown in Fig. 5, except that the intensities are somewhat consolidated.

A specimen of 85 pct reduction, after being annealed either at 400°C for 1 hr or an additional 15 min at 500°C, showed a recrystallization pole figure similar to that shown in Fig. 5, except that the twin orientation of component X disappears.

Fig. 8—<111> pole figure after 95 pct reduction and anneal at 400°C for 30 min and at 500°C for 15 min. Closed triangle represents cube orientation and its twin; open triangle, (358) [523] orientation; and open square, Y orientation.

Fig. 9—{111} pole figure after 98 pct reduction and anneal at 300°C for 1 hr and at 400°C for 30 min. Closed triangle represents cube orientation and its twins; open triangle, {358}<352> orientations.

Fig. 6 is the recrystallization pole figure of a specimen reduced 90 pct and annealed 1 hr at 400°C. In addition to the off-cube component, there is a second component, Y, which might be a second order twin of the off-cube orientation. Direct anneal of a specimen of the same reduction at 500°C for 1 hr removes this component, as shown in Fig. 7.

Fig. 8 is the recrystallization pole figure of a specimen reduced 95 pct and annealed 30 min at 400°C plus 15 min at 500°C. It is not clear whether a cube or an off-cube orientation should be assigned to one of the recrystallization components. Besides this component, a weak $(\bar{3}58)[523]$ component (component III) is observed.

Fig. 9 shows the recrystallization pole figure of a specimen reduced 98 pct and annealed 1 hr at 300°C plus 30 min at 400°C. A similar pole figure, but with much stronger intensities around the <111> poles of the cube orientation, was obtained by directly annealing the specimen for 30 min at 400°C. A stereographic analysis (the twin components are not indicated) of Fig. 9 is shown in Fig. 10.

Lowering the annealing temperature to 250°C for 30 min, followed by a 15 min anneal at 300°C, produced a slightly different pole figure, Fig. 11, for the specimen of 98 pct reduction. The ideal orientations shown in Fig. 1 seem to fit the data quite well. However, there is an indication that an off-cube rather than a cube orientation might be assigned to one of the components.

Discussion of Results

Deformation Texture—Hibbard and Yen[5] defined the *stable end orientations* or *ideal texture orientations* as the orientations of the grains which are suitable for deformation flow without a change in orientation. Once the grains rotate to these orientations, they remain there without further rotation during subsequent deformation. Barrett and Steadmann[7] concluded that the ideal orientation for the deformation texture of cold-rolled polycrystalline copper could be either {234}<323> or {135}<211> or, more precisely, {358}<835> indices. In a later study on the deformation texture of cold-rolled polycrystalline copper,[10] slightly different indices, {358}<523>,* were used. Together with the observations made in the present study, there is little doubt that the {358}<523> orientation is a texture orientation in cold-rolled polycrystalline copper.

* Indices of {6, 13, 21}<433> were also recently suggested for cold-rolled 2S aluminum of 83 pct reduction.[11]

The formation of a second {358}<523> deformation component is explained here on the basis of the zig-zag movement of <110> slip.[12] Mathewson[12] postulated that slip in the <110> direction on the {111} plane in face-centered-cubic metals could be resolved into two consecutive movements in the <112> directions. The first <112> movement results in a stacking fault of a twin orientation with respect to the matrix, and the second restores it to the matrix orientation. By assuming this process for slip, the first <112> movement on the (111) *D* yields materials of twin orientation across this (111), Fig. 13. Since this twin orientation is unstable with respect to the rolling process, two possibilities might occur; either the second <112> movement continues or lattice rotation through a small angle occurs to a stable orientation. This would depend on the relationship between the resultant twin orientation and rolling process. In the present case, a lattice rotation of only 16° from the twin orientation is needed to yield a {358}<523> orientation which is

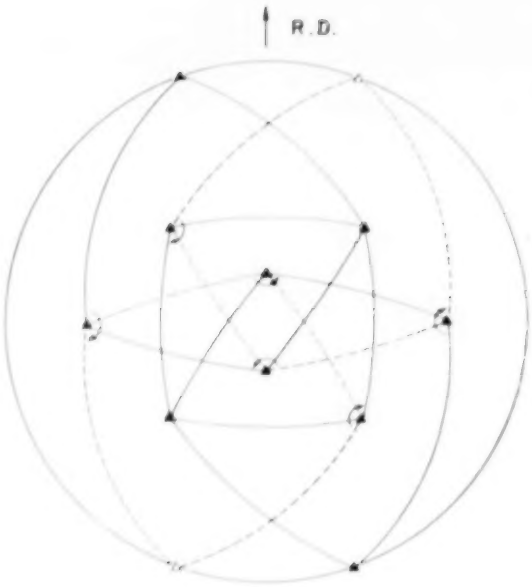

Fig. 10—Stereographic analysis of Fig. 9. Deformation texture is shown by broken lines and recrystallization texture is shown by solid lines.

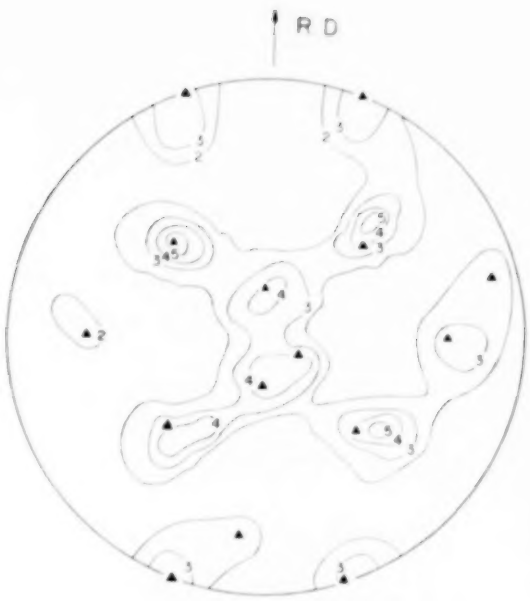

Fig. 11—{111} pole figure after 98 pct reduction and anneal at 250°C for 30 min and at 300°C for 15 min. Ideal orientations correspond to Fig. 1.

stable to the rolling process. The other two {358}<523> components (their orientations are not indicated) in Fig. 4 could also be explained on this basis by assuming stacking faults on {111} *B* and *C*, Fig. 1. The stacking fault formed on (111) *A* has an orientation quite remote from any which is stable to the rolling process. Instead, a second <112> movement might take place to reestablish the original {358}<523> orientation. A small portion of material might be expected to remain in this twin orientation and serve as the origin of the secondary recrystallization texture in copper.[4]

Recrystallization Textures—The consistent appearance of the off-cube recrystallization component might lead to a better understanding of the cube recrystallization texture in face-centered-cubic metals. It could be that the cube recrystallization texture is not of cube orientation, but is composed of off-cube orientations under the guise of symmetry. In a matrix of double {358}<523> component, by allowing two octahedral poles (pole type *A* in Fig. 1) to operate to yield two off-cube components, the center of the high intensity areas in the pole figure would shift and locate at the cube orientation. This effect is more pronounced in a matrix of quadruple {358}<523> deformation component,* such as in cold-rolled polycrystalline material. As shown in Fig. 14, the dots represent the octahedral poles of off-cube orientations resulting from each of four {358}<523> deformation components. The broken circles are of 8° radius. The proposed scatter of the cube texture is of approximately the same order as observed experimentally.

The other possibility could be that the amount of rotation for a given deformation component varies with the appearance of this component. In other words, when the {358}<523> deformation component appears as single-component deformation texture, it exhibits a 38° rotation, whereas the same component appearing in the form of either a double component, as in the specimen of 98 pct reduction in the present investigation, or a quadruple component, as in the polycrystalline materials, would exhibit a 44° rotation. This difference is conceivable, since the stress pattern on different slip planes varies with the development of the deformation components, which in turn influences the nucleation mechanism. The failure of the appearance of the {110}<112> recrystallization component from the {358}<523> deformation component[1] might also be attributed to this cause.

Figs. 9 and 11 confirm the belief that the {358}<523> deformation component is capable of generating a {358}<523> recrystallization component upon recrystallization. As shown in Fig. 9, there seems to be little doubt that recrystallization by the rotational reorientation mechanism, not by a *recrystallization in situ* mechanism, is responsible for the occurrence of this recrystallization component.

There is an unambiguous indication that the {358}<523> deformation component recrystallizes at a lower temperature than does the {110}<112> deformation component, as suggested previously.[5] Specimens of (110)[112] deformation texture, after 99.5 pct reduction, showed no sign of recrystallization after being annealed 5 min at 300°C, but specimens of the same purity copper possessing a (358)[523] deformation texture were almost completely recrystallized after the same heat treatment with only 95 pct reduction, Fig. 12.

* The terminology quadruple component here denotes four components of the same multiplicity of Miller indices distributed in such a way that they are in mirror image about both the rolling and transverse directions.

As observed previously, all equivalent recrystallization components* are more likely to appear when annealed at low temperatures.[5] This characteristic of recrystallization behavior was also observed in the present investigation. In addition, the higher the rolling reduction, the more likely the occurrence of all equivalent components. If the latter observation made on the single crystal could be extended to the polycrystalline materials, this would imply that at a given annealing temperature the sharp cube texture could only be obtained in a certain range of rolling reductions. At a higher reduction, its recrystallization texture would comprise both the cube and its equivalent components. Since the equivalent components of cube orientation, {358}<523>, have an orientation the same as the components in the deformation texture, this phenomenon might be mistakenly observed as the retention of the deformation texture after recrystallization.

An increase in the amount of cube or off-cube recrystallization component could be achieved either by a second anneal of the specimen that had been completely recrystallized or by a direct anneal at high temperatures. The same phenomenon was also observed recently by Merlini in polycrystalline copper.[14] It is worthwhile to discuss this phenomenon in terms of the *oriented growth* and *oriented nucleation* hypotheses.

In an isolated situation where only two grains exist, the orientation relationship can be defined in terms of either grain. This relationship alone would not determine which grain would grow at the expense of the other. The *oriented growth* hypothesis only suggests the likely event after the grains start to grow, but does not determine which grain should grow. This hypothesis therefore accounts only for the secondary (growth) but not the primary (origination) cause of the occurrence of the recrystallization texture in general.

It may be suggested that, under the assumption that the recrystallization of cold-rolled polycrystalline copper comprises five components, one cube and four {358}<523> components, Fig. 1, as observed by Merlini,[14] the cube component would grow favorably at the expense of not one but of all four of the {358}<523> matrix components.[7, 14] Since the *oriented growth* hypothesis does not specify which component should grow, the cube component would have the same probability of being *consumed* not by one but by all four of the {358}<523> components. In order to circumvent this situation the argument could be advanced that since grain growth ought to occur during the recrystallization process, once the grains of all orientations start to grow, the cube grains would grow faster in such a matrix than grains of other orientations. Based only on the orientation relationship, this explanation is also not true. The cube component is not *the* fastest growing component in such a matrix. As shown in Fig. 1, the orientation relationship between any one of the four {358}<523> components and a matrix of one cube and the other three {358}<523> components is the same as that of the cube component and a matrix of four {358}<523> components. The rate of grain growth would be the same no matter which component is growing. Thus, interpretation based on the *oriented growth* hypothesis would not determine which component would grow but explains the observation no matter whether the cube grains grow or do not grow. An interpretation based on the *oriented nucleation* hypothesis is therefore sought.

One of the factors likely to cause the growth of cube grains is their relatively large grains. These large cube grains occur under the assumption that the activation energy for recrystallization of cube grains is less than of grains of other orientations so that they are nucleated earlier. For example, in the case of two equivalent components, *A* and *B*, appearing from a single-component deformation texture after recrystallization, and the activation energy for recrystallization of component *A* being less than that of component B, upon isothermal annealing, grains in *A* orientation would appear first. At low annealing temperatures, both rate of nucleation and rate of growth of grains in *A* orientation are relatively low. During the time interval Δt_1, Fig. 15, grains in *A* orientation would be the only growing inhabitants in a surrounding deformed matrix. Since the size of recrystallized grains is a function

* The *equivalent (recrystallization) components* are the components of the recrystallization texture, which may or may not have the same Miller indices and are related, through the rotational reorientation relationship of same amount of rotation but about different octahedral poles, to the same component of deformation texture.

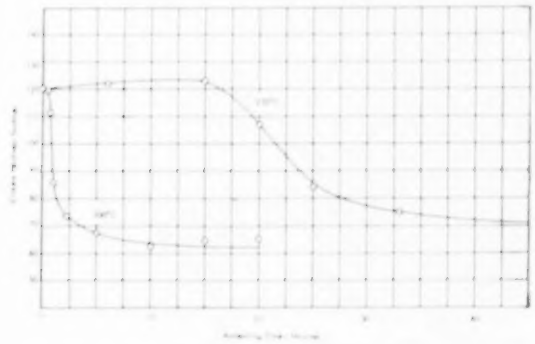

Fig. 12—Isothermal hardness curve of 95 pct rolled strip at designated annealing temperatures. Specimen thickness, 0.027 in.; load, 0.3 kg.

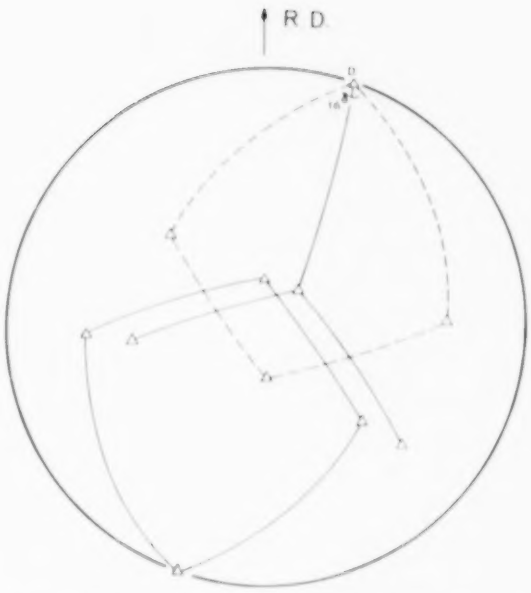

Fig. 13—Suggested mechanism for the appearance of the second (358) [352] component of the deformation texture.

of both rate of growth and the time interval during which this growth takes place, grains in *A* orientation would therefore be larger than any grains which are nucleated later. At time T_a, the specimen has already recrystallized, say, 30 pct. The remaining deformed matrix will then recrystallize through the nucleation and growth mechanism of grains in both *A* and *B* orientations and also by the growth of grains in *A* orientation which appeared before T_a. After complete recrystallization, the specimen would exhibit relatively uniform grains of components *A* and *B* and few but large grains in *A* orientation. Reannealing the specimen at higher temperature would cause these large grains in *A* orientation to grow at the expense of small matrix grains. In the meantime, some small grains in *A* and *B* orientations would also grow at the expense of each other, depending on the local situations. Since grains in *B* orientation can only be consumed by large grains of *A* orientation and have the same probability of survival when competing with small grains of *A* orientations, a reasonable amount of grains in *B* orientation are expected to remain. Thus, the amount of material in *B* orientation would depend on both the first and second annealing temperatures under stepwise annealing conditions.

If the specimen is annealed directly at high temperature, the rate of nucleation of component *A* should increase many times, and so should its rate of growth. The deformed matrix recrystallized before T_a would transform into numerous fine grains in *A* orientation due to its high rate of nucleation and the shortening of time interval Δt, at high annealing temperature. At time T_a, say, only 40 pct of the deformed matrix remains, which then recrystallizes into component *B* as well as into component *A*. The amount of deformed matrix actually recrystallizing into component *B* would be a small fraction of the total volume. Thus, the higher the annealing temperature, the less the material available to be converted into *B* orientation and the sharper the component *A*. The above analysis based on the concept of *oriented nucleation* hypothesis is in agreement with the observation that all equivalent recrystallization components are more likely to occur when recrystallization takes place at a low temperature.

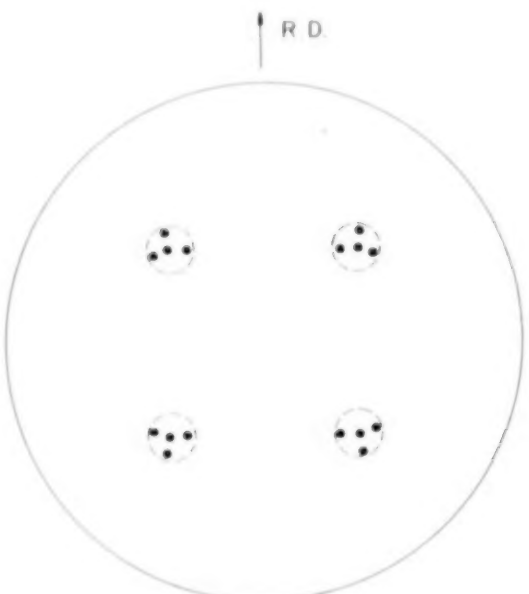

Fig. 14—Superimposition of four off-cube orientations to form the cube orientation.

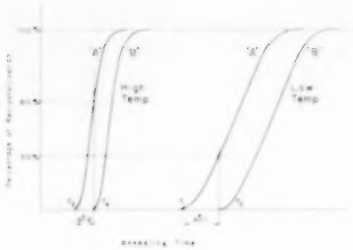

Fig. 15—Schematic drawing of isothermal recrystallization curves of components *A* and *B* if they recrystallized independently.

Summary

1) Copper single crystals of (358)[523] initial orientation retain their orientation up to 95 pct reduction thickness. Further cold rolling generates a multiplicity of this orientation.

2) After annealed at different temperatures, a component of the recrystallization texture of either a cube or an off-cube orientation was observed.

3) In a deformed matrix of the same orientation, the occurrence of recrystallization texture depends on both annealing temperature and rolling reduction. The lower the annealing temperature, the higher the rolling reduction, the more likely the exhibition of all equivalent recrystallization components.

Acknowledgments

This paper is based on an investigation sponsored by the National Science Foundation, Washington, D. C., Grant No. G-0471. Figs. 2, 4, and 7 were taken from the Master's thesis submitted by David J. Barnette to the faculty of the College of Engineering, New York University, 1954. The author wishes to express his gratitude to H. Margolin and R. F. Bunshah of the Research Div., New York University, and W. R. Hibbard, Jr. of General Electric Co., for their helpful reading of the manuscript.

References

[1] Y. C. Liu and W. R. Hibbard, Jr.: *AIME Trans.*, 1955, vol. 203, p. 381; JOURNAL OF METALS, February 1955.

[2] C. S. Barrett: *Structure of Metals*, McGraw-Hill Book Co. Inc. New York, 1952.

[3] W. M. Baldwin, Jr.: *AIME Trans.*, 1946, vol. 166, p. 591; METALS TECHNOLOGY, April 1942.

[4] B. M. Brick and M. A. Williamson: *AIME Trans.*, 1941, vol. 143, p. 84; METALS TECHNOLOGY, February 1941.

[5] Y. C. Liu and W. R. Hibbard, Jr.: *AIME Trans.*, 1953, vol. 197, p. 672; JOURNAL OF METALS, May 1953.

[6] P. A. Albert: Report to Watertown Arsenal, Watertown, Mass., on Contract No. DA-30-069-ORD-869, Oct. 15, 1954.

[7] P. A. Beck and H. Hu: *AIME Trans.*, 1952, vol. 194, p. 83; JOURNAL OF METALS, January 1952.

[8] W. R. Hibbard, Jr. and M. K. Yen: *AIME Trans.*, 1948, vol. 175, p. 126; METALS TECHNOLOGY, February 1948.

[9] C. S. Barrett and F. W. Steadman: *AIME Trans.*, 1942, vol. 147, p. 57; METALS TECHNOLOGY, February 1942.

[10] H. Hu, P. R. Sperry, and P. A. Beck: *AIME Trans.*, 1952, vol. 194, p. 76; JOURNAL OF METALS, January 1952.

[11] L. K. Jetter, C. J. McHargue, and R. O. Williams: *Journal of Applied Physics*, 1956, vol. 27, No. 4, p. 368.

[12] W. R. Hibbard, Jr.: Private communication.

[13] C. H. Mathewson: *ASM Trans.*, 1944, vol. 32, p. 38.

[14] A. Merlini: *AIME Trans.*, 1956, vol. 206, p. 987; JOURNAL OF METALS, August 1956.

Discussion of this paper sent (2 copies) to AIME by Sept. 1, 1957 will appear in AIME *Transactions* Vol. 212, 1958, and in JOURNAL OF METALS, April 1958.

Grain Growth in Dilute Alloys of Copper

An experimental study of grain growth in dilute binary alloys of copper was performed. It was found that the grain growth law $D = Kt^n$ fit most of the data. The grain growth exponent n decreased with solute content until a saturation value was obtained at slightly under 0.2 for both silicon and aluminum solutes. It is concluded that the grain growth exponent n depends upon solute adsorption at the grain boundaries. An estimate of the activation energy was made and it was found that the activation energy decreased with temperature. The activation energies for grain boundary migration compare well with values obtained from internal friction studies on identical alloys. This contributes strong experimental support for the two-step mechanism for complete grain boundary stress relaxation.

by S. Weinig and E. S. Machlin

IN a previous study of the grain boundary stress relaxation phenomenon,[1] the authors had arrived at the conclusion that two successive steps were involved in the *complete* relaxation of stress at a grain boundary. These two steps were grain boundary migration and grain boundary slip. It was further suggested that the slower of these two processes is rate controlling. In an attempt to ascertain the validity of the above, a study of grain growth kinetics on the same alloys used for the previous study was undertaken.

Separate wire specimens, 0.030 in. diam, in the same as-deformed state (99 pct reduction in area) as in the previous investigation were heated to the various temperatures for a sequence of times. The compositions used and the temperatures of testing are summarized in Table I. A statistical determination of grain size was then made on each specimen, using the average length of traverse between boundaries as a measure of the grain size. Examples of typical results obtained are shown in Figs. 1 and 2. The grain growth law $D = kt^n$ was found to fit most of the data. Using this relation, values of the grain growth exponent n were calculated and the interesting dependence of n on solute content shown in Figs. 3 and 4 was then obtained. Also, it was found that the constant K which was obtained from extrapolation is roughly independent of solute content. (K is uncertain to within ±25 pct.)

An estimate of the activation energy for grain growth was made using the technique of Burke.[2] This method utilizes the plot of the reciprocal of time necessary for the grain size to increase from a definite starting size D_o to a final size D, for each isothermal heat treatment. The slope of this curve corresponds to the heat of activation for the process. In Fig. 5 the rate of grain growth is plotted against the reciprocal of absolute temperature. The activation energies were obtained from these curves and are summarized in Fig. 6.

Discussion

It is interesting to note that the same saturation in the variability with concentration has been found for the grain growth exponent n in this research as was found in the previous researches on both grain boundary stress relaxation[1] and internal friction of dislocation origin.[4] The significant feature is that saturation in the variation of these properties has been found to occur at about the same level of solute concentration, namely, between 0.1 and 0.5 atomic pct. The only characteristic common to these different quantities is that solute adsorption at grain boundaries and dislocation can take place and affect these values in a similar fashion. Thus, it is concluded that the grain growth exponent n depends upon solute adsorption at the grain boundaries. It appears, therefore, that theoretical considerations leading to the contrary conclusions[5, 6] have not treated the real process by which solute atoms exert their effect on grain growth.

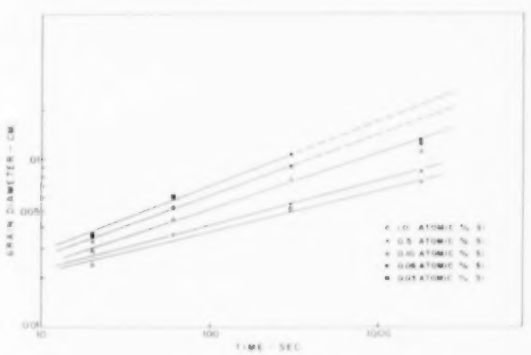

Fig. 1—Average grain diameter as a function of time at 600°C.

Prior to the analysis of the observed activation energies, certain of the aspects of the aforementioned grain boundary stress relaxation investigation will be briefly reviewed. It was found that with the addition of solute atoms the grain boundary stress relaxation peak (internal friction vs temperature) decreased in intensity. Simultaneously a second peak was observed which increased with increasing solute atoms. Both of these peaks were shown to be the result of grain boundary stress relaxation. They have been termed, respectively, *pure* peak and *solute* peak. It was suggested that the *solute* peak was dependent upon grain boundary migration, whereas the *pure* peak was a manifestation of grain boundary slip. Activation energies for both peaks were obtained as a function of solute content.

The value of the activation energy in the temperature range corresponding to the *solute* peak was

S. WEINIG, Junior Member AIME, is Assistant Professor of Metallurgy, College of Engineering, New York University, New York. E. S. MACHLIN, Member AIME, is Associate Professor of Metallurgy, Columbia University, New York.

TP 4470E. Manuscript, Aug. 24, 1956. New Orleans Meeting, February 1957.

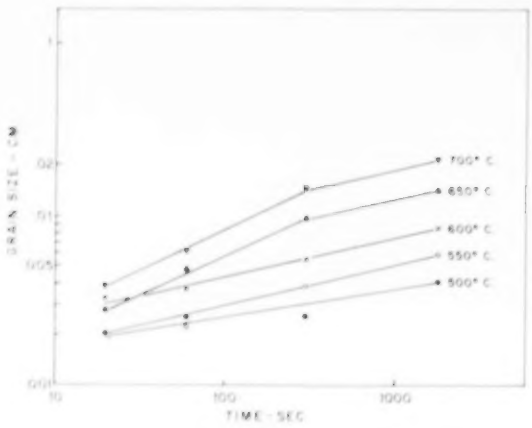

Fig. 2—Average grain diameter as a function of time for a 0.5 atomic pct Cu-Si alloy.

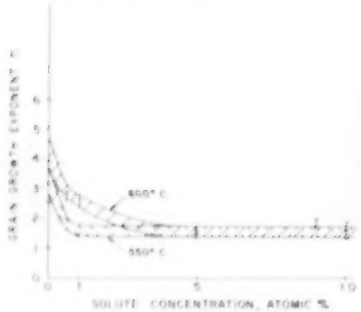

Fig. 3—Grain growth exponent *n* as a function of the solute concentration; copper base alloy containing aluminum solute.

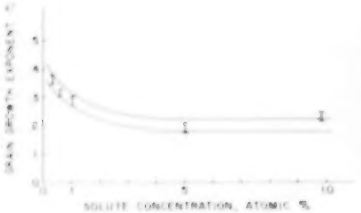

Fig. 4—Grain growth exponent *n* as a function of the solute concentration; copper base alloy containing silicon solute; 600°C.

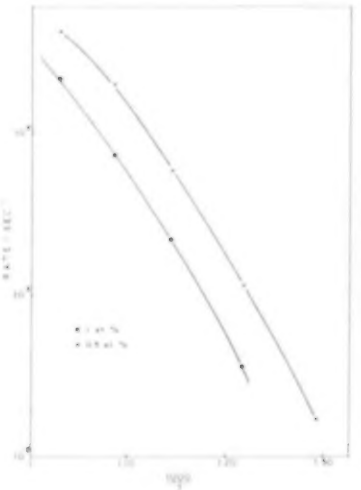

Fig. 5—Rate of grain growth as a function of the absolute temperature for binary alloys of copper in Cu-Si.

about 50,000 to 55,000 cal per mol. The same batch of wires used in the internal friction study was then used in the present grain growth investigation. In the same temperature range at which the *solute* peak appeared, the extrapolated values of the activation energy for grain growth are 51,000 and 58,000 cal per mol for the 0.5 and 1 atomic pct Si alloys, respectively. In the temperature range corresponding to the *pure* grain boundary stress relaxation peak found in the previous study the internal friction measurements yield values for the activation energy *in excess* of 80,000 cal per mol. This is in comparison to the extrapolated values of 61,000 to 78,000 cal per mol for boundary migration occurring during grain growth in the present experiments on identical specimens. It is apparent

Table I. Compositions of Copper Binary Alloys Studied in This Investigation*

Alloy	Composition, Atomic Pct
Cu-Al	0.03
	0.06
	0.10
	0.50
	1.00
Cu-Si	0.03
	0.06
	0.10
	0.50
	1.00

* Copper was of 99.999 pct purity. All specimens were tested at 550° and 600°C. The 0.5 and 1.0 atomic pct specimens were tested at 500°, 550°, 600°, 650°, and 700°C.

that the energy of activation for grain boundary migration is in much better agreement with that for the *solute* peak than for the *pure* peak. This result is consistent with the prediction made in the previous paper.[1] It supports the theory developed there that complete grain boundary stress relaxation involves two successive steps, namely, boundary migration and boundary slip. The former is believed controlling in dilute alloys and the latter in pure metals. The existence of the two grain boundary stress relaxation peaks in an alloy is believed to be the result of a distribution in solute adsorbability for the grain boundaries present. A fraction of the boundaries have sufficient solute to limit their ability to migrate. The migration rate controls the rate of stress relaxation along these boundaries. The remaining boundaries, which have not adsorbed sufficient solute, can migrate faster than grain boundary slip can occur along them. Hence, the latter step controls the rate of shear stress relaxation along these relatively solute-free boundaries.

The temperature dependence of the activation energy found in this research is not new. Similar results have been found by other investigators, as, for example, in the secondary recrystallization of copper.[7] An explanation of this behavior as well as of the solute dependence of the grain growth exponent is still desired. Because of the discontinuous nature of boundary migration during grain growth (long periods of stability followed by very rapid migration), it is believed that the explanation must involve the concept of a fluctuation in which a boundary is able to depart from its atmosphere of adsorbed solute or vice versa.

Conclusions

1) The grain growth law $D^n = kt$ was found to describe satisfactorily the data for dilute binary alloys of copper.

2) The grain growth exponent n is a function of solute content up to approximately 0.2 atomic pct.

3) Activation energies for grain migration compare well with values obtained from internal fric-

tion studies on identical alloys. This contributes strong experimental support for the two-step mechanism for complete grain boundary shear stress relaxation.

Acknowledgments

The authors gratefully acknowledge the assistance of Gerald Pincus in this investigation. This research was supported by the United States Air Force, through the Office of Scientific Research of the Air Research and Development Command.

References

[1] E. S. Machlin and S. Weinig: A Theory for the Grain Boundary Stress Relaxation Peak. *Journal of Applied Physics*. To be published.

[2] J. E. Burke: Some Factors Affecting the Rate of Grain Growth in Metals. *AIME Trans.*, 1949, vol. 185, p. 73; JOURNAL OF METALS, February 1949.

[3] S. Weinig and E. S. Machlin: The Effect of Solute Additions on Grain Boundary Stress Relaxation. *AIME Trans.*, 1957, vol. 209, p. 32; JOURNAL OF METALS, January 1957.

[4] S. Weinig and E. S. Machlin: Low Frequency Studies of Dislocation Interactions with Solute Atoms. *Acta Metallurgica*, 1956, vol. 4, p. 262.

[5] R. Fullman: Boundary Migration During Grain Growth. *Metal Interfaces*. ASM, Cleveland, 1952.

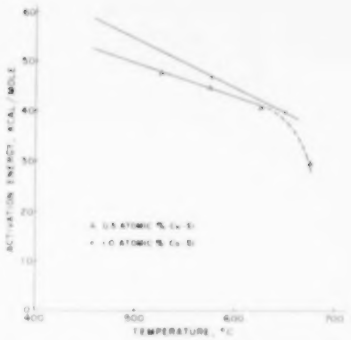

Fig. 6—The activation energy for grain boundary migration as a function of temperature.

[6] R. Fullman: Discussion of Some Applications of the Thermodynamic Theory of Irreversible Processes to Physical Metallurgy. *AIME Trans.*, 1954, vol. 200, p. 668; JOURNAL OF METALS, May 1954.

[7] J. E. Burke and D. Turnbull: Recrystallization and Grain Growth. *Progress in Metal Physics*, vol. 3, p. 235. Interscience Publishers Inc. New York, 1952.

Discussion of this paper sent (2 copies) to AIME by Sept. 1, 1957 will appear in AIME *Transactions* Vol. 212, 1958, and in JOURNAL OF METALS, April 1958.

Technical Note

Concerning an Order-Disorder Transition in the Ni-Cr System

by B. W. Roberts and R. A. Swalin

CONSIDERABLE controversy has centered about the existence of an order-disorder transformation in alloys in the composition vicinity of 75 atomic pct Ni and 25 atomic pct Cr. All the evidence to date for such a transformation is of a rather indirect nature, since direct X-ray confirmation is difficult to obtain as a result of the small difference in X-ray scattering factors between nickel and chromium. As a result, superlattice lines would be very faint if present. Several investigators[1-3] have observed anomalies in the electrical resistivity vs temperature curves of alloys in the vicinity of 25 atomic pct Cr. The observed change is characterized by a rather broad resistivity peak at about 540°C. A discontinuous drop in resistivity is normally associated with ordering. However, Taylor and Hinton[1] have rationalized that the discrepancy could conceivably be caused by changes in the Brillouin zones upon ordering. The same investigators measured the specific heat as a function of temperature and have also observed anomalies in the vicinity of 540°C. Nordheim and Grant[3] have proposed, because of the absence of superlattice lines and the absence of a discontinuity in the resistivity vs temperature curve, that long-range order is improbable and that the results could be better explained by short-range ordering. To date, however, the question has not been resolved satisfactorily.

Neutron diffraction techniques provide a method for partially resolving the question since nickel and chromium have considerably different atomic scattering factors in the case of neutrons and, therefore, superlattice peaks, if ordering occurs, should be readily discernable. The results of a neutron diffraction investigation* coupled with a dilatometric investigation are reported here.

B. W. ROBERTS, Member AIME, is associated with Research Laboratory, General Electric Co., Schenectady. R. A. SWALIN, Junior Member AIME, formerly with Research Laboratory, General Electric Co., is associated with the Dept. of Metallurgy, University of Minnesota, Minneapolis.

TN 392E. Manuscript, Apr. 10, 1956.

* Neutron diffraction studies were carried out at the reactor of Brookhaven National Laboratory, Upton, N. Y.

An alloy containing 28.0 atomic pct Cr was prepared from carbonyl nickel and electrolytic chromium in the form of a 1-in. diam x 10-in. ingot. Melting was done in an alumina crucible and casting in a graphite mold. The ingot was homogenized at 1250°C for seven days, after which a 5-in. long piece was cut into shavings in order to obtain a suitable neutron diffraction sample. Hardness samples and samples suitable for dilatometric analysis (⅛ in. diam x 2 in.) were prepared from the remaining piece. The neutron diffraction sample, along with a hardness sample, was annealed at 501°C for seven days, at which time the temperature was lowered to 479°C and held at this temperature for twenty-four more days. The hardness was observed to increase from 133 to 147 Vhn during the course of the annealing treatment, in qualitative agreement with Nordheim and Grant.[3]

Neutron diffraction traces taken at room temperature and at 4.2°K are shown in Fig. 1. The insert shows the trace taken at room temperature with short counting times and thus only fair statistical accuracy. No evidence for superstructure reflections of Cu$_3$Au-type ordering is observed. The statistical accuracy of the 4.2°K trace was improved by using longer counting periods. Several weak intensities are observed at small angles, including an aluminum reflection from the cryostat assembly and a very

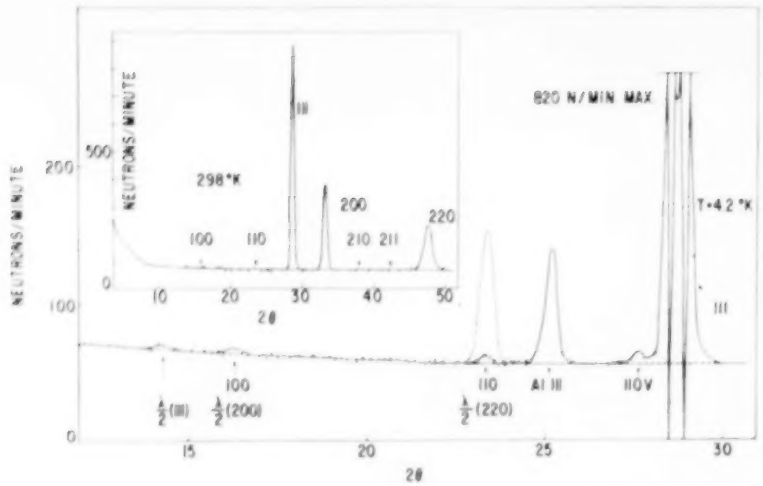

Fig. 1—Neutron diffraction data taken at 4.2°K. Insert shows data taken at 298°K. Environmental background included.

weak reflection near the (111) peak which is attributed to the vanadium sample holder. The 111 $\left(\frac{\lambda}{2}\right)$ reflection is observed as well as two very weak reflections at (100) and (110) positions which are at the proper angles to coincide with 200 $\left(\frac{\lambda}{2}\right)$ and 220 $\left(\frac{\lambda}{2}\right)$ second-order reflections. The three second-order intensities have the ratio to the first-order reflections expected at the wave length used.

Relative intensities have been calculated[4] for a cylindrical specimen utilizing the following constants: $\lambda = 1.018$A, $\mu r = 0.593$, density = 1.9 g per cu cm, $b_{Ni} = 0.352 \times 10^{-12}$ cm, $b_{Cr} = 1.033 \times 10^{-12}$ cm, the temperature factor $2M = 1.435 \times 10^{-16}$ cm sq, and $a_o = 3.54$A. In Table I the observed intensities may be compared with calculated intensities for zero long-range order ($S = 0$) and perfect long-range order ($S = 1$). Perfect long-range order is immediately ruled out since no unexpected intensity is observed at the (100) and (110) superstructure reflection positions and the calculated intensities are high, being roughly one tenth of the (111) fundamental reflection as indicated by the dashed reflection in Fig. 1. If a small amount of long-range order were present and in evidence in the (100) and (110) reflections to the extent of one or two intensity units, the neutron data would appear inconsistent, since no evidence of diffuse maxima is present to suggest a high state of short-range order. If ordering forces induce a small amount of long-range order, the remaining atoms will be expected to have a high degree of short-range order.[7,8]

Table I. Calculated and Observed Neutron Intensities at 4.2°K

hkl	$P_{obs.}$	$P_{calc.}, S = 0$	$P_{calc.}, S = 1$
111 $\left(\frac{\lambda}{2}\right)$	2.2		
100 or 200 $\left(\frac{\lambda}{2}\right)$	2.0	0	38.2
110 or 220 $\left(\frac{\lambda}{2}\right)$	2.0	0	36.9
111	415	414.9	414.9
200	(231)*	228	228
210	(Ni)*	0	28
211	(Ni)*	0	23
220	(213)*	214	214

* Parentheses denote room temperature measurements.

A dilatometric sample was annealed at about 980°C for 12 hr and water-quenched to room temperature, after which the sample was isothermally annealed at 510°C for six days in a dial gage quartz dilatometer. No volume change occurred. Similarly, no volume change was observed upon annealing at 473°C for six days. An alloy sample containing 24.9 pct Cr and 75.1 pct Ni was also obtained. Isothermally annealing a quenched sample at 510°C for eleven days yielded no volume change either. The fact that no volume change occurred suggests that long-range order is not important, since all known order-disorder transitions are associated with significant volume changes. It is significant that the resistivity of a 25 atomic pct Cr alloy was observed to begin changing almost immediately upon isothermally annealing at 479°C.[6]

The neutron diffraction and dilatometric results reported here indicate that long-range order of the classical Cu_3Au type is not produced by annealing sequences which result in the observed resistivity and specific heat anomalies. The lack of diffuse short-range order maxima suggests that a high degree of short-range order is absent. If long-range order and pronounced short-range order are not considered as the cause of the resistivity change observed near Ni_3Cr composition, what physical processes remain? Changes in a low degree of short-range order are possible. A precipitation process by ordinary diffusion might cause the resistivity change, but this appears unlikely, since the resistivity was found to begin changing almost immediately upon isothermal annealing at temperatures as low as 479°C and to reach a maximum in a few hours. An antiferromagnetic transition as a nondiffusion controlled process is to be considered, but no evidence exists for a transition in the vicinity of 540°C (813°K).

References

1. J. H. Thomas and R. M. Davies: *Philosophical Magazine*, 1936, vol. 22, No. 7, p. 681.
2. Z. Yano: *Japan Nickel Review*, 1941, vol. 9, p. 17.
3. H. Grover and J. Hutzenlaut: *Physical Review*, 1939, vol. 56, p. 212.
4. A. Taylor and K. G. Hinton: *Journal* Institute of Metals, 1952, vol. 81, p. 169.
5. R. Nordheim and N. J. Grant: *Journal* Institute of Metals, 1953, vol. 82, p. 440.
6. G. E. Bacon: *Neutron Diffraction*. Clarendon Press, Oxford, 1955.
7. D. R. Chipman: *Journal of Applied Physics*, 1956, vol. 27, p. 739.
8. B. W. Roberts and G. H. Vineyard: *Journal of Applied Physics*, 1956, vol. 27, p. 203.

Preferred Growth Direction of Metals

A theory is developed for face-centered-cubic metals which predicts that the preferred orientation formed during solidification of the columnar zone of an ingot is: 1) the <111> direction for pure metals, 2) no preferred direction for slightly impure metals, and 3) the <100> direction for impure metals and alloys. The theory predicts the direction of formation of boundaries between substructures and the occurrence of stray crystal formation as a function of the orientation of the solid-liquid interface and the degree of constitutional supercooling existing in the liquid.

by William A. Tiller

SEVERAL authors[1-6] have shown that, during solidification from the melt, the direction of formation of substructure boundaries depends upon the direction of heat flow and the rate of solidification of the metal. The most prominent of these observations was that a preferred orientation developed during the solidification of the columnar zone of an ingot which for face-centered-cubic metals was the <100> direction. Previous explanations[1-4] given to account for this preferred orientation and the other boundary phenomena are all based on the premise that the phenomena are characteristics of the pure element. However, recent experiments by Rosenberg and Tiller[7] have demonstrated that the preferred orientation in pure lead is the <111> orientation, and that the heretofore observed <100> orientation is due to the effect of solute on the mode of solidification of the metal.

Teghtsoonian and Chalmers,[4] studying *striation* boundaries in tin, and Chalmers and Rutter,[5] studying *corrugation* boundaries in tin, showed that these substructure boundaries were aligned parallel to the axis of heat flow for slow rates of growth, and that the alignment varied from this direction as a function of the rate of growth to approach the dendrite direction at high rates. Chalmers,[6] studying the direction of formation of a grain boundary separating two crystals of different orientation, showed that at slow growth rates the boundary is parallel to the axis of heat flow, while at higher speeds it will deviate from this direction, sloping into the crystal whose dendrite orientation departs the most from the axis of heat flow. It is this phenomenon that allows certain crystallites in the chill zone region of an ingot to encroach on their neighbors and ultimately produce the preferred orientation of the columnar zone of the ingot. Since the previous explanations of this preferred orientation are unable to account for the recent observations,[7] a new mechanism will be considered. This will lead to an explanation of the other substructure boundary phenomena as well.

Investigations by Graf,[8] Billig,[9] Rosenberg,[10] and others have demonstrated in a striking fashion that crystal growth takes place by the deposition of individual layers oriented along the close-packed planes of the material considered. This lamellar or

W. A. TILLER is associated with Westinghouse Research Laboratories, Pittsburgh.

TP 4450E. Manuscript, Aug. 14, 1956. New Orleans Meeting, February 1957.

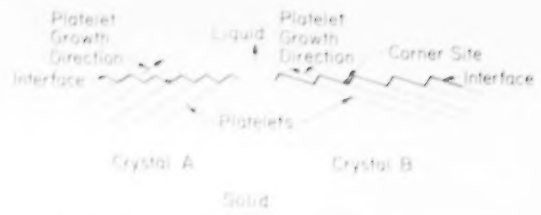

Fig. 1—Trace of the solid-liquid interface on a horizontal section through the crystal representing the edgewise growth of (111) platelets.

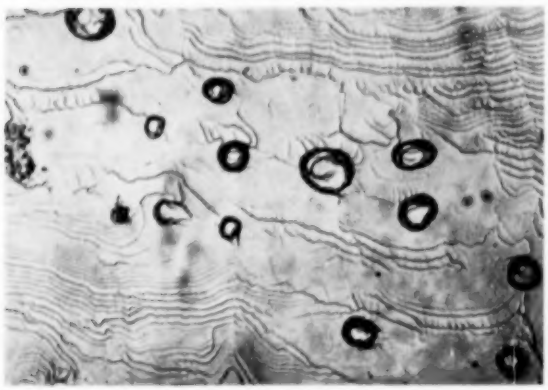

Fig. 2—Micrograph of a (111) interface in lead showing the nucleating centers of the (111) platelets. X300. Reduced approximately 15 pct for reproduction.

Fig. 3—Micrograph of an (*hkl*) interface in lead showing the traces of the (111) platelets. X300. Reduced approximately 15 pct for reproduction.

plate-like structure is found not only on typical layer crystals or crystals of low symmetry, such as hexagonal crystals, but also on crystals with highest symmetry, such as face-centered-cubic crystals. The step height of a lamella, which is visible both on the exposed surface of the crystal and on a decanted interface, is generally between 10^{-7} and 10^{-6} cm. Rosenberg[3] has shown cinematographically that the solidification of lead does not occur by the advancement of a smooth interface normal to itself, but occurs by the edgewise growth of these platelets, which produces a corrugated interface as shown in Fig. 1. Fig. 1 represents two crystals cut to reveal the platelet outlined in a horizontal section. The individual platelets are shown extending back into the solid to facilitate visualizing the direction in which they grow. In general, the plane separating the platelets is a {111} plane. However, platelets of the {100}, {110}, and {311} types have also been observed on rare occasions. Fig. 2 shows a (111) interface of lead on which the platelets appear to be nucleating. The mounds in the micrograph are considered to be nucleation centers. Fig. 3 shows an interface of the (*hkl*) type, the (111) platelets making an angle with the interface.

By considering the edgewise growth of the {111} platelets on interfaces of (*hkl*) orientation, it is possible to account for the preferred orientation in pure and impure metals and the other boundary phenomena. The present paper is a theoretical examination of these boundary phenomena and the development of a preferred growth direction in metals under the following main headings: 1) preferred growth direction for an ultra-pure metal; 2) lack of preferred growth direction for a metal containing a small amount of impurity, and solidified slowly; and 3) development of preferred growth direction in an alloy as a function of the growth conditions.

The treatment to follow concerns itself with face-centered-cubic metals and, specifically, lead. It will be assumed that the particular {111} platelet system that operates is the one most nearly parallel to the interface. Experiments on lead appear to support this assumption. Metals of other crystal types solidify by a fundamental platelet mechanism and, if the platelet plane is known, a similar analysis can be carried out.

Theoretical Considerations

Pure Metal—In this section it will be shown how the growth of the (111) platelets can produce a preferred [111] orientation in a casting of pure lead. Previous treatments of preferred orientation have assumed that it is necessary to produce an interface step between two adjacent crystals of different orientation in order to have one encroach on the other. A simpler approach is to determine if it is possible to produce such an interface step in a pure metal, and this approach will be considered.

From the viewpoint of the *thermodynamics of phase equilibrium*, the free energy per unit volume in the two crystals of different orientation would have to be different in order to make the liquid-solid transformation temperatures different. In the pure metal this would only be possible if there were different degrees of imperfections introduced into the two crystals. This is very unlikely since for any orientation the atoms of the liquid become a part of the solid by being accommodated at a corner site, as represented in Fig. 1.

If the kinetics of the transformation are considered, the treatment of Chalmers[2] may lead to an interface step, but one which would produce a <100> preferred orientation for pure lead.

Since both thermodynamic and kinetic considerations are unable to predict the existence of an interface step which could account for the preferred <111> orientation in lead, the conception of an interface step between adjacent crystals being a necessary prerequisite to a preferred growth direction must be discarded. A more fruitful approach is developed by considering the properties of the grain boundary groove formed at the interface between

the crystals. It may be assumed that such a groove exists.

Fig. 4 illustrates a grain boundary groove formed between crystal A having a <111> orientation, and crystal B having an <hkl> orientation. During growth the crystals are growing independently, the lateral component of growth causing them to meet at the boundary region. The portion of solid which forms to provide intimate contact between A and B must contain the grain boundary surface, thereby having a greater free energy per unit volume than the solid some distance from the boundary. The liquid-solid transformation temperature of this intercrystalline material is therefore lowered, causing the point of junction of the two crystals and the liquid to occur a certain distance behind the rest of the interface. This distance will depend on the temperature gradients in both the liquid and the solid, and on the misorientation between the crystals.

The platelet edge is assumed to make some angle ϕ with the platelet face. If it is also assumed that one platelet cannot project over the edge of the platelet beneath, and from nucleation considerations this appears reasonable, then the maximum slope of the groove walls is determined by the angle that the {111} platelet plane makes with the interface. The lower the angle the platelet plane makes with the interface the steeper the groove can be. Therefore, for any ϕ, the {111} interface shown in Fig. 4 will produce the steepest slope.

Fig. 5 illustrates the possible shapes of the grain boundary grooves for bicrystals having the interface orientations shown. The crystals comprising the bicrystal in both cases are misoriented from each other by an angle Ψ due to a symmetrical rotation about the specimen axis. It is quite apparent, however, that if Fig. 5 represents the grain boundary groove existing between the crystals, then the liquid in this groove will be supercooled, since a positive temperature gradient exists in the liquid ahead of the interface. Under these conditions it is possible for a conjugate (111) platelet system to provide solidification in the groove. It is not known at this time if there is any nucleation problem involved in the formation of this conjugate (111) platelet system. However, the nucleation of the conjugate platelet system will be easiest if the walls of the boundary grooves are {111} planes. This type of boundary groove will be considered, and it will be assumed that there is no nucleation problem associated with the operation of the conjugate (111) platelet systems shown in Fig. 6. More will be said about this nucleation problem later.

If both bicrystals of Fig. 6 are growing under the same heat flow conditions, i.e., same temperature gradient in the liquid and solid, they are both advancing at the same rate, R_x, along the specimen axis. If the conjugate platelet systems are nucleating at the centers of the groove walls as shown, then these platelets must grow edgewise at different net rates in the two bicrystals in order to advance the solid a distance $R_x\Delta t$ in time Δt. As discussed by Chalmers,[4] the net rate of attachment of atoms onto the interface is a function of the supercooling ΔT. Therefore, in order for a platelet to advance edgewise at a certain rate R', it must be supercooled by an increment of temperature $\Delta T'$. In order for the boundary grooves in Fig. 6 to advance the same distance in unit time, and they must under identical heat flow conditions, the conjugate platelets of the bicrystal with the <hkl>interface must grow faster

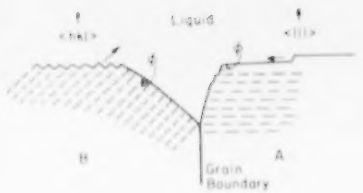

Fig. 4—Representation of a grain boundary groove between a crystal having a <111> orientation, and a crystal having an <hkl> orientation.

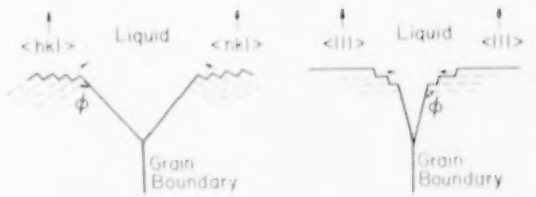

Fig. 5—Bicrystals, each misoriented by an angle Ψ due to a rotation about the specimen axis. a) LEFT: crystals having {hkl} interfaces, and b) RIGHT: crystals having {111} interfaces.

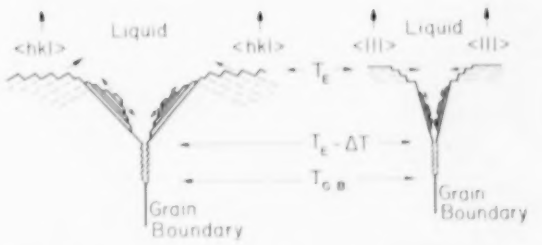

Fig. 6—Grain boundary cusps if conjugate (111) platelet systems are operating.

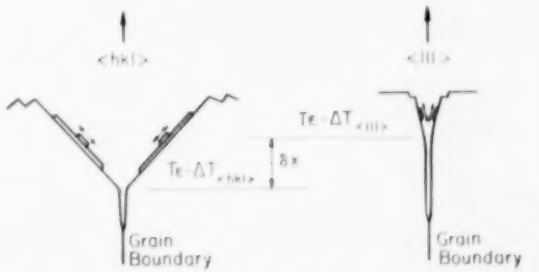

Fig. 7—Relative shapes of the grain boundary cusps under similar growth conditions for a <111> bicrystal and an <hkl> bicrystal.

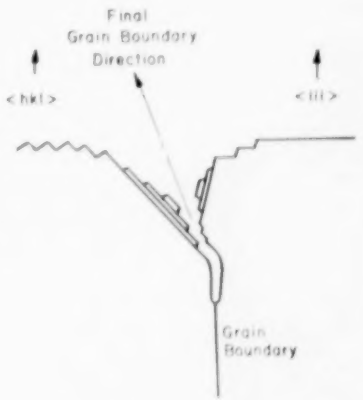

Fig. 8—Bicrystal of (<hkl>, <111>) type under actual growth conditions showing that the <111> crystal will encroach on the <hkl> crystal.

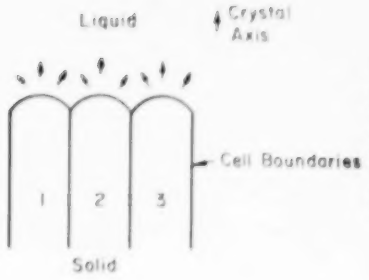

Fig. 9—Horizontal section of the crystal illustrating the fiber structure of the corrugations and the normal growth component at the interface.

than the conjugate platelets of the <111> bicrystal. This can only occur if the average temperature at the platelet edge for the <*hkl*> bicrystal is lower than for the <111> bicrystal and the relative shapes of the grain boundary grooves for the two bicrystals will therefore be as shown in Fig. 7.

The above discussion has not considered any change in the isotherms of the liquid near the groove due to the presence of the solid. If this fact is taken into consideration it will be immediately obvious that the steeper the groove, the greater will be the departure of the temperature gradient in the groove from the macroscopic temperature gradient in the liquid, G_l, toward the macroscopic temperature gradient in the solid, G_s. For reasonable rates of growth $G_s > G_l$ and, therefore, at the same distance Δx behind the main interface, a platelet on the steeper groove wall of the <111> bicrystal can grow edgewise at a faster rate than a platelet on the groove wall of the <*hkl*> bicrystal. This enhances the effect discussed above.

From the foregoing considerations it can be seen that when an <*hkl*> crystal and a <111> crystal form a bicrystal the grain boundary groove will be unsymmetrical in shape. This boundary groove will be very much like that produced by taking half of each of the two bicrystals in Fig. 7 and joining them at the boundary. The normal growth of the conjugate platelets on the groove walls will lead to an overhang of the <*hkl*> crystal by the <111> crystal as shown in Fig. 8. Thus, the <111> crystal will encroach on the <*hkl*> crystal. This leads to the development of a preferred <111> direction of growth in the columnar zone of an ingot of pure lead.

If the growth of a (<111>, <111>) bicrystal where the boundary is not a symmetrical one is considered, then one of the crystals might be found to encroach upon the other during growth, since one may have less difficulty in nucleating the conjugate (111) platelet system on the groove wall than the other. Consider the <111> bicrystal in Fig. 6 as being unsymmetrical with respect to the boundary. Let the right-hand crystal have a <110> direction in the plane of the paper pointing toward the boundary. Let the left-hand crystal have a <211> direction in the plane of the paper pointing toward the boundary. Then, if the boundary groove is perpendicular to the paper, the groove wall of the right-hand crystal may be a {111} plane and the conjugate (111) platelet system has little difficulty in nucleating. However, the groove wall of the left-hand crystal cannot be a {111} plane, and there will be a nucleation problem associated with the formation of the conjugate platelet system on this wall. Thus, the right-hand crystal would be expected to encroach on the left-hand crystal. An experiment carried out by Shewmon[11] on bycrystals of zone refined copper having the orientations described above verified the prediction that the crystal with a <110> direction pointing toward the boundary always encroached on the crystal with the <211> direction pointing toward the boundary.

Small Alloy Additions—In this section it will be shown how the presence of a small amount of solute hinders the growth of the {111} platelets to such an extent that a preferred <111> direction of growth does not develop. Under these conditions no preferred direction of growth develops. To account for this phenomenon let us again consider if an interface step can develop between two crystals of different orientation.

From the thermodynamic point of view there may be a difference in equilibrium temperature of the two crystal faces if the melt contains a small amount of solute. Theoretical considerations, which will be discussed in a subsequent publication, support the presence of edge dislocation arrays on the (111) planes between platelets. The density of the dislocations will be a maximum for a crystal of [111] orientation. This may lead to an interface step between crystals.

From the kinetic viewpoint an interface step may again be produced. As the platelet advances edgewise it rejects solute from its edge, and this solute must diffuse away from the edge for growth to proceed at the initial edge temperature. If a (111) plane is in the plane of the interface, a platelet cannot grow rapidly across the interface, since it is building up a solute distribution at this edge which will not be able to diffuse away at as fast a rate as it is being rejected. This diffusion problem will be considered in a subsequent publication. However, qualitative results indicate that the temperature of a (111) interface is lower than the temperature of an (*hkl*) interface.

The above effects, which may produce a small interface step between crystals, only account in part for the loss of the <111> preferred orientation. The major cause is located at the grain boundary groove. Because of the existence of solute in the liquid, Tiller et al.[12] have shown that a nonequilibrium solute distribution will exist in the liquid adjacent to the advancing interface. Tiller and Winegard[13] have shown that under these conditions the grain boundary groove will act as a sink and, if the distribution coefficient[12] is less than unity for the solute, a greater solute concentration will exist in this region than on the rest of the interface. There will therefore be no supercooling in the liquid of the groove region as long as the conjugate platelet systems operate.

It will be immediately apparent that the edgewise growth of the conjugate (111) platelets in the groove region of an (<*hkl*>, <111>) bicrystal will tend to trap solute near the base of the groove, which will restrict further growth of the platelets. Thus, the platelets in this region are constrained to grow more slowly because the solute cannot readily diffuse out into the bulk liquid. The main part of the crystal is still advancing at its normal rate, and this will lead to a deep boundary groove. The conjugate platelets of the <111> crystal are growing at a steeper angle than the conjugate platelets of the <*hkl*> crystal and, because of the solute diffusion restriction, must advance more slowly. The presence of the solute passivates the platelet growth in the groove region. Therefore, there will be no overhang of the <*hkl*> crystal by the <111> crystal as for

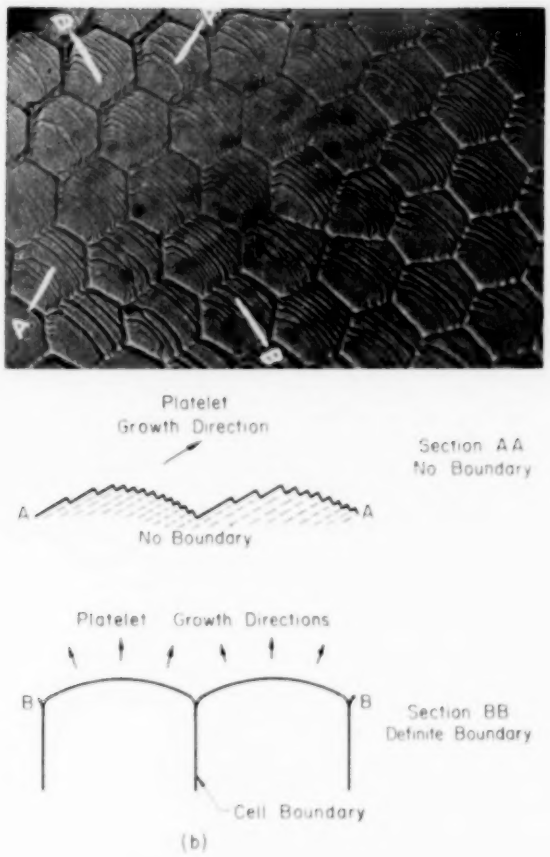

Fig. 10—Cellular interface composed of (111) platelets advancing at some angle to the interface normal. a) Micrograph. X250. Reduced approximately 25 pct for reproduction. b) Schematic representation. Section *A-A* shows no solute trapping at the cell boundary; section *B-B* shows definite solute trapping at the boundary.

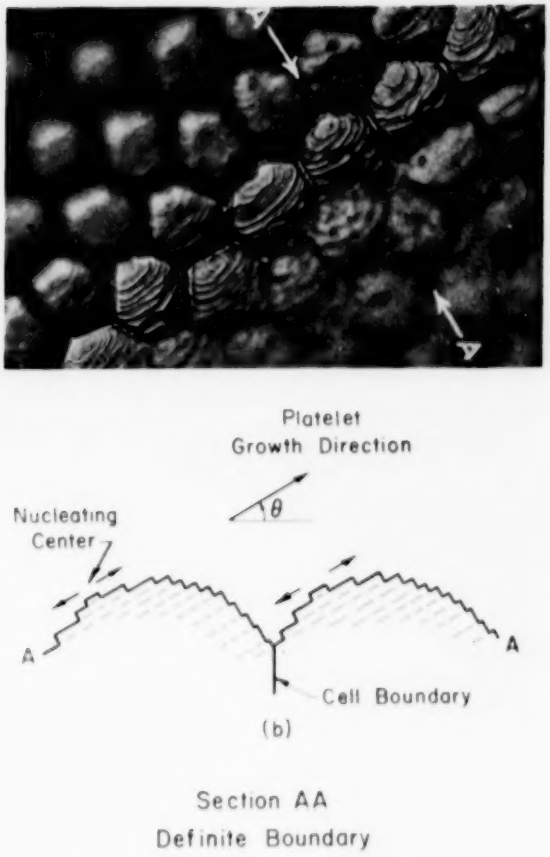

Fig. 11—Cellular interface, each cell containing its own nucleating center. a) Micrograph. X250. Reduced approximately 25 pct for reproduction. b) Schematic representation of platelet growth.

pure lead, Fig. 8, and the <111> crystal will no longer be able to encroach on the <*hkl*> crystal.

The above considerations appear to be adequate to account for the loss of the <111> preferred orientation by the influence of a small amount of solute. These considerations apply when the solute concentration and the growth conditions are such that no constitutional supercooling exists in the liquid adjacent to the interface.

Alloys—This section differs from the last in that the effect of constitutional supercooling on the development of preferred orientation will now be considered.

When a crystal is grown from a melt containing solute, the layer of liquid adjacent to the interface becomes enriched in solutes having distribution coefficients less than 1. The quantitative features of this solute distribution have been calculated for a smooth plane interface by Tiller et al.[10] They have shown that for a critical set of growth conditions the smooth interface will break down into an interface consisting of a network of cellular projections. Rutter and Chalmers[5] postulated that these cells form to relieve the constitutional supercooling in the zone of liquid immediately adjacent to the interface. Tiller and Rutter[11] have verified this hypothesis and have shown that as the amount of constitutional supercooling is increased the cellular caps project further into the liquid to relieve the instability.

It is necessary to consider in what way the cells are able to relieve the constitutional supercooling. From Fig. 9, which represents a longitudinal section of the crystal to show the fiber structure of the corrugations, it will be apparent that the growth at the tip of the projection will be normal to the surface of the solid, so that there is not only growth down the axis of the crystal, but there is some growth in a lateral direction also. This lateral growth traps solute between the cells which cannot diffuse out into the bulk liquid. Because of this high solute concentration at the cell boundaries this liquid cannot freeze until a lower temperature is reached. The way in which the cells relieve the constitutional supercooling is that they trap solute at the cell boundaries that would otherwise reside in the solute-rich layer of liquid at the interface. In effect, then, they lower the solute concentration at the interface and thus the constitutional supercooling.

Fig. 10a shows a cellular interface composed of (111) platelets advancing at some angle to the interface normal; this is the initial stage of cellular

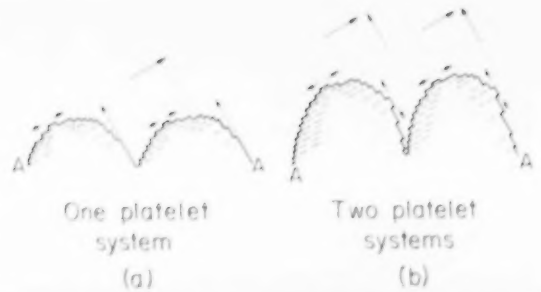

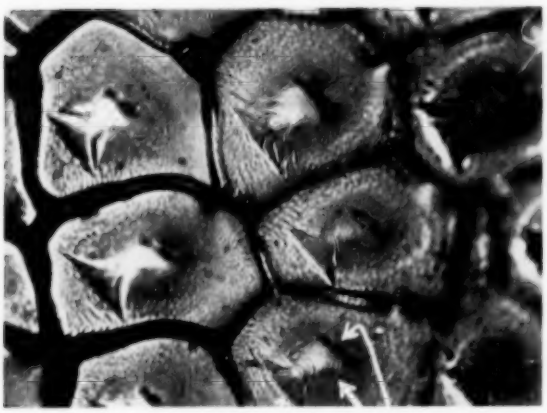

(c)

Fig. 12—a) Shape of cell at which instability of single platelet system occurs. b) Two conjugate (111) platelet systems operating to provide solidification on cell. c) Micrograph of cellular interface on which three conjugate (111) platelet systems are operating. X500. Reduced approximately 30 pct for reproduction.

development. A schematic section of the cellular interface is given in Fig. 10b. For the *A-A* section the platelets are all growing to the right in the direction shown, so that there will be a drift of these cells to the right. Thus, no solute will be trapped at the base of the cells, and no pronounced cell boundary segregation will be formed in the solid. On section *B-B* there is a lateral growth of the platelet edge in the groove regions, which tends to trap solute in these regions. This, in turn, forms deep boundary grooves and a pronounced cell boundary segregation in the solid. Thus, although the interface of Fig. 10a presents a cellular morphology, if the crystal was sectioned parallel to the interface and etched to show the solute distribution only a line array of solute segregations should be observed. This would come from segregation to the *B-B* boundaries. Fig. 11a shows a cellular interface consisting of a single platelet system with deep grooves between the cells. In this case, each cell is growing like an independent crystal, with the (111) platelets nucleating on each cell. This is represented schematically in Fig. 11b. From the schematic drawing it can be seen that the platelet, by advancing edgewise, is not only rejecting solute into the bulk liquid but is rejecting solute into the cell boundary region, i.e., it is pushing solute into the region where it can be trapped. The steeper the platelet plane with respect to the average interface plane, the more effectively it will be able to trap solute in the boundary region. If a crystal presenting the interface morphology of Fig. 11a were sectioned parallel to the interface and etched to show the solute distribution, a cellular array of solute segregation should be observed.

It will be readily appreciated that, as the contour of the cell necessary to relieve the instability is changed, a point is reached at which the platelets begin to push solute into the surface of the adjacent cell, as shown in Fig. 12a. When this happens, this side of the cell cannot grow as fast as the center of the cell, and an instability will arise here. At this point, the edge of the platelet will become the face and the platelet will begin growing outward, as shown by the dotted arrows. When the slope of this surface is appropriate, the instability is relieved by the operation of a conjugate platelet system which pushes the solute out into the liquid rather than against the adjacent cell. At this stage all of the cells will have conjugate platelet systems operating on two of their sides, as shown in Fig. 12b. The condition will eventually be reached in which the other sides of the cell encounter the same solute problem in the intercell region and, if it is possible, the other two conjugate platelet systems will nucleate to relieve this instability. The above applies to the development of a cell for a (100) interface. Here, there are four conjugate platelet systems that can operate. Three are shown in Fig. 12c.

For an interface of the (*hkl*) orientation which lies somewhere near the center of the stereographic triangle, one of the {111} planes makes an angle of about 25° with this high index interface, whereas the conjugate (111) planes make angles of about 50°, 70°, and 90°. A cellular interface of this type must become very unsymmetrical as the conjugate platelet systems operate to bound the cell and, for a given projection length of the cell, the cell width for an (*hkl*) interface must be larger than the cell width for a (100) interface. This is illustrated by Fig. 13. The angles between the conjugate platelets on the two cells are different because the platelets are not normal to the section drawn. This is a section through the center of the cells.

If the growth of an (*hkl*) interface is considered, it can be demonstrated how the transition from one to two, then three, and four operating platelet systems occurs to change the direction of the corrugation axis from the axis of the specimen when only one platelet system is operating toward the dendrite axis and when the multiple platelet systems are operating. Fig. 14 shows the development of this type of cell. It only shows the development of one cross section, as it is very difficult to represent the three-dimensional development. This, however, will serve to illustrate the point. The platelets on the cells 1 and 2 are growing in the θ direction as shown, where θ is the angle between the (111) plane and the average macroscopic interface, and they produce the surface *ABC*. At this stage there are no platelets of the same system growing in the $(\theta + \pi)$ directions. The growth on cell 2 in the $(\theta + \pi)$ direction will be pushing solute toward cell 1 at *B*. This will trap solute at *B*, thus forming a boundary there, and it will also inhibit the growth of cell 1 at *B* in the θ direction. Cell 1 will then begin to become asymmetrical. When the asymmetry is sufficient to produce a face of the proper slope on the *B* side of cell 1, a conjugate (111) platelet system will nucleate and begin to provide growth.

As this second platelet system begins to grow normal to itself, it greatly increases the asymmetry. Up to this point the cell boundary has been constrained

to form along the axis of the crystal because the trapping of the solute occurs at *B*. However, now cell 1 begins to overhang *B*, so that the boundary must deviate into cell 2. The boundary will deviate more and more as the cell continues to develop this second platelet system. The boundary will finally lie along that axis about which the diffusion of solute is symmetrical; i.e., along the axis which is the bisector of the angle between the two platelet systems. When, finally, the four platelet systems are operating, the corrugations will be pointing and growing in the <100> direction for face-centered-cubic metals, since this is the direction bounded by four conjugate (111) platelets. This accounts for the variation in the direction of formation of corrugations as a function of the rate of growth. Increasing the rate of growth increases the amount of constitutional supercooling to be eliminated by the cellular interface, forcing the cell to be more well developed. As the length to width ratio of the cellular caps increases, more platelet systems must be operating and, therefore, the head of the cell is more closely aligned toward the dendrite direction. The corrugation boundaries are then growing in this direction.

The above considered the development of cells on single crystals having (*hkl*) interfaces. Let us now consider the growth of a bicrystal. Under conditions of constitutional supercooling, cellular projections form on the interface of each crystal. As already mentioned, the steeper the platelet planes with respect to the average interface plane, the more the solute can be trapped in the boundary region. The more solute there is in the boundary, the less solute there is in the solute-rich layer of liquid and, therefore, the lower the solute concentration at the interface. The lower the solute concentration at the interface, the higher the freezing temperature. Therefore, the (100) interface is able to grow at a higher temperature than an (*hkl*) interface, since the platelets make a steeper angle with the interface, and there are four conjugate systems that can bound this type of cell.

The cell size is determined by the growth conditions and the amount of constitutional supercooling to be relieved; i.e., there must be enough cell boundary to receive the extra solute and there must be time for diffusion and platelet growth to get it there. It is obvious that the smaller the cell width, the less time it will take for the diffusion of the solute to the cell boundary. Therefore, if the cell widths in adjacent grains differ, then the grain with the enlarged cell size cannot diffuse the necessary amount of solute to the cell boundary in the time allowed, and so will have a higher concentration of solute at its interface than the other grain. Rosenberg and Tiller[7] have shown that, for crystals with well developed

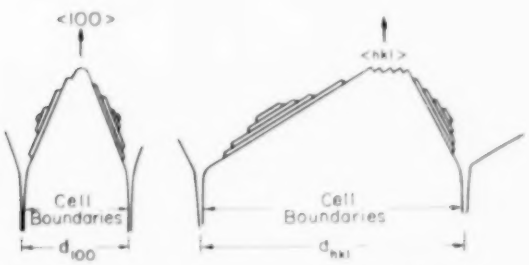

Fig. 13—Relative cell widths on an (*hkl*) and a (111) interface for a given projection length of cell.

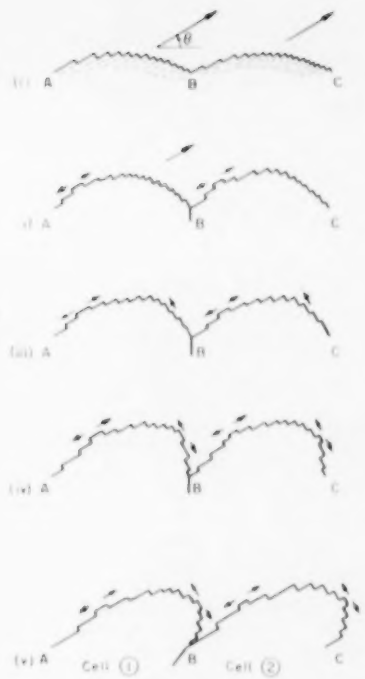

Fig. 14—Development of a cell on an (*hkl*) interface as the constitutional supercooling is increased.

cells, an interface step between adjacent grains is found to occur when the two grains have cells of different size. The large cell size is found on grains of high index orientation, as predicted earlier, and the small cells on crystals of low index orientation. The interface with the smaller cells is always in advance.

The significant difference in cell size as a function of orientation has been discussed by Tiller and Rutter,[4] and can be accounted for by the inability of {111} platelet systems to form a bounded cell of the appropriate size and contour for interfaces of high index orientations.

It can be seen from the foregoing that the presence of solute allows the interface of one crystallite to be stable at a higher temperature than another interface of less favorable orientation. Because of the interface step the crystal in advance will encroach upon the depressed crystallite and eventually grow it out of the specimen. The crystal in advance is the crystal closest to the {100} orientation, so that the boundary in a bicrystal will deviate into the crystal which departs the most from having its <100> direction along the axis of heat flow. The boundary will deviate the most at high rates when the cells are well developed and the interface step is the greatest.

The trend toward a preferred orientation is found to occur in the early stages of cell development.[7] This may be due to the breakdown to cells of a (100) interface before an (*hkl*) interface. If it requires some nominal gradient of constitutional supercooling in the liquid ahead of the interface to make the interface become unstable, the (100) interface will become unstable before an (*hkl*) interface. The instability will be shown by projections forming on the interface and extending ahead of the main interface into the liquid.[4] The projections will be on the edges of the (111) platelets and will be growing in this direction. Thus, it is the nominal gradient of constitutional supercooling in the direc-

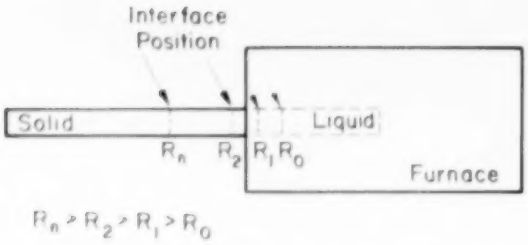

Fig. 15—Interface position relative to the furnace as a function of the freezing rate *R*.

tion of (111) platelet advance that is important. Since the (111) platelets make a steeper angle with a (100) interface than with a (*hkl*) interface, during the growth of an ([*hkl*], [100]) bicrystal there will be a greater gradient of constitutional supercooling ahead of the (100) interface in the [111] direction than ahead of the (*hkl*) interface in the [111] direction. Thus, the (100) interface will become unstable first, and an interface step will develop between it and the (*hkl*) interface such that the (100) can encroach on the (*hkl*).

It has been possible to account for the variation in the direction of formation of corrugation boundaries and grain boundaries as a function of constitutional supercooling. It is possible now to incorporate the observations made on the striations as a function of constitutional supercooling. The answer to this question leads back to the direction of formation of corrugation boundaries. Whenever corrugations and striations are found to coexist, it is observed that a striation boundary never cuts across a corrugation boundary, but rather follows its outlines. This implies that the striation boundary is tied to the corrugation boundary and, therefore, the direction of formation of the striation boundary varies with the constitutional supercooling in the same manner as the direction of formation of corrugation boundaries.

Discussion

The foregoing treatment has dealt with the effect of constitutional supercooling on the direction of formation of grain boundaries and subboundaries. It is now necessary to show that the observations made by Chalmers and his collaborators were made under conditions such that the constitutional supercooling would increase considerably as the rate of growth increased.

All of the observations on corrugation boundaries, striation boundaries, and grain boundaries have been made on crystals grown using the modified Bridgman technique described by Chalmers.[5] This method essentially consists of moving a furnace away from a cylinder of molten metal at a controlled rate so that solidification begins at one end and proceeds along the cylinder at a rate that corresponds closely to the rate of movement of the furnace.

The position of the interface between solid and liquid relative to the edge of the furnace is determined by the temperature of the furnace and the cooling arrangement on the end of the boat. However, the faster the crystal is solidified, the more latent heat there is to be conducted away per unit time. This necessitates a steepening of the temperature gradient in the solid or a flattening of the temperature gradient in the liquid. For this to happen, the interface must be further away from the edge of the furnace, as shown in Fig. 15, so that there is a zone of liquid between the interface and the furnace from which heat can be lost laterally by radiation to the surroundings. The important point to consider is that the faster the crystal is made to solidify using this technique, the further the solid-liquid interface is outside of the furnace. Thus, more heat can be lost laterally from this zone of liquid as the speed of solidification increases.

Since the temperature gradient in the solid decreases as more solid is formed, it is the temperature gradient in the liquid that must decrease in order to grow at a greater rate. This can only be done by lateral heat loss from the region of liquid ahead of the interface. Fig. 16 represents the temperature gradient in the liquid as a function of rate. For low rates of growth the gradient is constant. As lateral heat losses occur the temperature distribution curves become flatter at the interface. The greater the lateral losses, the flatter the temperature gradient will become; the lateral losses can increase to the point where a zone of supercooling is created ahead of the interface. For growth under a temperature distribution of type c the solid will form faster than for type *a* or *b*, since extra latent heat can be liberated to flow down this gradient in the liquid. In some cases, the extra heat may be enough to eliminate this temperature inversion. However, the lateral heat losses may be so great as to maintain this condition in spite of the extra heat supplied from the solidification of the solid at the increased rate. This type of temperature distribution has been reported by Goss.[6]

From the above it can be seen that, as the rate of furnace travel increases, the temperature gradient in the liquid decreases, and the rate of solidification increases. Therefore, at some critical rate of furnace travel, constitutional supercooling will be initiated in the zone of liquid adjacent to the interface, and the amount of constitutional supercooling will increase as the rate of furnace travel increases. Therefore, the effects ascribed to the difference in growth rate are probably caused by the amount of constitutional supercooling in the liquid adjacent to the interface.

Nucleation of Stray Crystals—It has been observed in many laboratories that the tendency for stray crystal formation in single crystal growth increases as the rate of growth increases, and as the dendrite orientation of the crystal departs from the direction of heat flow. This has been considered by

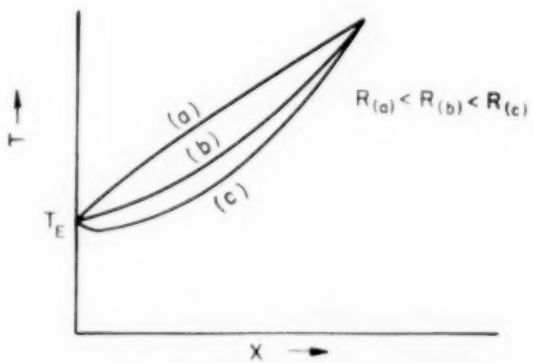

Fig. 16—Temperature distribution in the liquid as a function of the freezing rate *R*.

Chalmers,[4] and may be explained by the previous analysis. Since the degree of constitutional supercooling increases as the rate of growth increases, the development of a cellular interface increases. The cells are unable to eliminate all of the constitutional supercooling and, since the probability of stray nuclei forming in this zone of liquid increases as the degree of supercooling increases, the rate of formation of stray crystals will also increase with the rate of growth. If the crystals are grown by a horizontal travelling furnace as in the study of Goss,[15] it is also possible to produce a temperature distribution of the type in Fig. 16c so that stray nuclei will have an even greater probability of formation.

For a crystal of high index orientation, the rate of growth at which the crystal can no longer relieve all of the constitutional supercooling is less than for a crystal of low index orientation. Therefore, the degree of constitutional supercooling in the liquid adjacent to a high index orientation crystal will be greater than in front of a crystal of low index orientation for the same rate of growth, and the probability of stray formation will also be greater.

In this way both the orientation dependence and the rate of growth dependence of the frequency of stray formation have been accounted for.

Conclusions

The foregoing treatment shows that the preferred orientation in face-centered-cubic metals is caused by the interaction between the three important variables of growth: 1) K, the crystallographic features of the growing crystal where these are manifest in the anisotropic growth characteristics of the platelets; 2) T, the temperature distribution in the metal; and 3) S, the solute distribution in the metal. It has been shown that the direction of formation of grain boundaries and substructure boundaries during solidification from the melt is not a characteristic attributable to the nature of the pure metal, but is due to the effect of the growth conditions on the mode of solidification.

A theory is developed for face-centered-cubic metals which predicts that the preferred orientation during solidification of the columnar zone of an ingot is: 1) the <111> direction for pure metals; 2) no preferred direction for slightly impure metals; and 3) the <100> direction for impure metals and alloys. The theory predicts that the direction of formation of boundaries between substructures for slightly impure metals is a) along the axis of heat flow if there is no constitutional supercooling in the melt, and b) deviated toward the axis of dendritic growth in the specimen as the constitutional supercooling increases in the melt. The theory also predicts that the frequency of stray crystal formation during the growth of single crystals will increase as the constitutional supercooling is increased and as the orientation of the solid-liquid interface departs from the (100).

This once again illustrates the magnitude of effect that the existence of constitutional supercooling has on the mode of solidification.

References

[1] G. Tammann: *States of Aggregation*. D. Van Nostrand Co. New York, 1925.
[2] B. Chalmers: *AIME Trans.*, 1954, vol. 200, p. 520; JOURNAL OF METALS, May 1954.
[3] R. F. Mehl: *Solidification of Metals and Alloys*. AIME. New York, 1951.
[4] E. Teghtsoonian and B. Chalmers: *Canadian Journal of Physics*, 1951, vol. 29, p. 370; also 1952, vol. 30, p. 388.
[5] J. W. Rutter and B. Chalmers: *Canadian Journal of Physics*, 1953, vol. 31, p. 15.
[6] B. Chalmers: *Canadian Journal of Physics*, 1953, vol. 31, p. 132.
[7] A. Rosenberg and W. A. Tiller: *Acta Metallurgica*. To be published.
[8] L. Graf: *Ztsch. für Metallkunde*, 1951, vol. 42, p. 336.
[9] E. Billig: *Proceedings* Royal Soc., London, 1955, vol. 229 A, p. 346.
[10] A. Rosenberg: Ph.D. Thesis, University of Toronto, 1956.
[11] P. G. Shewmon: Private communication.
[12] W. A. Tiller, K. A. Jackson, J. W. Rutter, and B. Chalmers: *Acta Metallurgica*, 1953, vol. 1, p. 428.
[13] W. A. Tiller and W. C. Winegard: *Acta Metallurgica*, 1955, vol. 3, p. 208.
[14] W. A. Tiller and J. W. Rutter: *Canadian Journal of Physics*, 1956, vol. 34, p. 96.
[15] A. J. Goss: *Proceedings* Physical Soc., London, 1953, vol. 66B, p. 65.

Discussion of this paper sent (2 copies) to AIME by Sept. 1, 1957 will appear in AIME *Transactions* Vol. 212, 1958, and in JOURNAL OF METALS, April 1958.

Technical Note

Nucleation Sites of Bainitic Carbides in Alloy Steels

by S. M. Kaufman, G. M. Pound, and H. I. Aaronson

WHETHER the carbides associated with bainite precipitate from the ferritic component of bainite, as originally suggested by Davenport and Bain,[1] or from the adjacent austenite at austenite:ferrite boundaries, as proposed by Hultgren,[2] remains in dispute.[3,4] A recent metallographic investigation in this laboratory has shown that the bainitic carbides formed in a plain carbon hypoeutectoid steel nucleate entirely within ferrite at higher reaction temperatures[5] and in both ferrite and austenite at lower temperatures.[5] The present investigation was undertaken to ascertain the effects of alloying elements on the nucleation sites selected by bainitic carbides.

The compositions of the steels studied were as shown in Table I. Specimens of these steels were

S. M. KAUFMAN, Student Member AIME, and G. M. POUND, Member AIME, are Graduate Student and Associate Professor, respectively, Dept. of Metallurgical Engineering, and H. I. AARONSON, Junior Member AIME, is Research Metallurgist, Metals Research Laboratory, Carnegie Institute of Technology, Pittsburgh.

TN 391E. Manuscript, July 19, 1956.

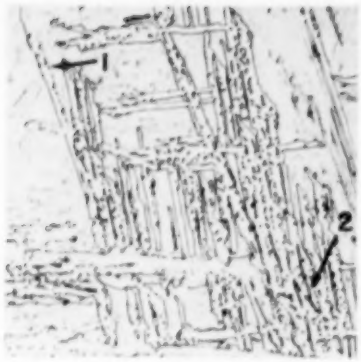

Fig. 1—Carbide protruding into austenite from austenite-ferrite boundary (arrowhead No. 1) and carbide consuming sliver of entrapped austenite (arrowhead No. 2) in manganese steel. Reacted for 35 sec at 475°C. Etched in 2 pct nital. X1000. Enlarged approximately 1.8 times for reproduction.

austenitized for 30 min at 1300°C and isothermally reacted at temperatures found to yield moderate amounts of relatively large carbides in partially reacted specimens. Such structures developed within the range 450° to 550°C in most steels. In the chromium steel, however, the range was narrowly centered about 600°C, while in the silicon steel no reaction temperature was found which fulfilled this specification.

The basic results obtained were substantially independent of both composition and reaction temperature. Arrowhead No. 1 in Fig. 1 points out a carbide which can be seen, upon careful examination, to protrude appreciably into the adjacent austenite. The frequency with which such presumably austenite-nucleated carbides were found at the austenite:ferrite boundaries of well separated ferrite plates, however, did not appear to be sufficient to account for the density of carbides in a number of these plates. Some of the carbides thus appear to have precipitated from the ferrite plates, rather than from the surrounding austenite. In areas of the type indicated by arrowhead No. 2, where adjacent ferrite plates have closely approached impingement, on the other hand, carbides were rather frequently observed to have partially consumed the remaining slivers of austenite. Schrader and Wever[4] and Ko[5] have previously discussed the later type of process, but considered it to be the only mechanism through which bainitic carbides are precipitated.

Evidence of the type cited above for the precipitation of carbides from ferrite is indirect in nature and cannot be appreciably improved without a quantitative analysis of the distribution of carbides about and within the bainitic areas. An analysis of this type, however, does not appear feasible in view of the complex shapes which the ferritic component of bainite normally develops. In the chromium steel, however, unequivocal evidence was obtained for the formation of substantial numbers of ferrite-nucleated carbides. Specimens of this steel which were reacted at 600°C initially contained bainite plates*

* This reaction temperature is above the top of the lower C-curve of the *TTT* diagram for this steel and is accordingly above the presently accepted *bainite-start* temperature. The present authors, however, accept as bainite any aggregate structure formed by nucleation and growth during the decomposition of austenite, which fulfills the original Davenport-Bain description of ferrite and ferrite-nucleated carbides. The failure of the lower C-curve to delimit completely the temperature region within which clearly bainitic microstructures develop is currently being investigated in this and other 3 pct Cr steels.

in which appreciable areas of ferrite were unblemished by carbides. These plates were quickly surrounded by masses of dark-etching *aborescent pearlite*.[3] At later reaction times, however, the entire areas of the bainite plates etched more rapidly than the pearlite. The additional carbide precipitation necessarily occurred entirely *within* the bainite plates. This observation and the basically similar observations made by Davenport[6] on a Cr-Mn-Mo steel and by later investigators on Ni-Mn-Mo[7] and Si[8] steels* provide direct proof of the precipitation of bainitic carbides within ferrite in a diversified group of alloy steels.

* In these steels, carbides did not appear within ferrite plates until substantial amounts of carbide-free ferrite had formed. The ferritic origin of these carbides is accordingly certain. The low temperatures at which the (temporarily) carbide-free ferrite was formed and the comparatively long interval of time between the formation of ferrite and the formation of carbide resulted in the application of the name *X-constituent*[6] to structures of this type in order to distinguish them from bainite, in which the *isothermal delay time* between the two reactions is normally quite small. As Davenport[6] tentatively recognized originally, however, this distinction appears to be unnecessary, inasmuch as the difference between X-constituent and bainite is one of degree, rather than of kind.

On the basis of the observations made during the present and previous investigations, it is concluded that the carbides associated with bainite in alloy steels can nucleate both in austenite and in ferrite. This is in marked contrast to the behavior of a plain carbon steel over an appreciable range of temperature.[9] A satisfactory explanation for this difference has not yet been found.

Table I. Composition of Steels Studied

Designation	Pct C	Pct Mn	Pct Si	Pct Ni	Pct Mo	Pct Cr	Pct S	Pct P
Cr	0.39	0.25	0.19	—	—	2.96	0.007	0.008
Mn	0.34	1.87	0.09	0.02	0.02	0.01	0.032	0.011
Ni	0.33	0.08	0.02	3.65	0.02	0.01	0.020	0.020
Mo	0.33	0.06	0.01	0.02	0.80	0.00	0.010	0.010
Si	0.37	0.14	3.53	0.02	0.02	0.02	0.012	0.007
4340*	0.39	0.73	0.27	1.80	0.26	0.77	0.020	0.014

* Alloy strongly banded.

Although the carbide precipitate in the bainite ranges in both plain carbon and alloy steels can have dual origins, especially at lower temperatures, it seems advisable to retain the original definition of bainite given by Davenport and Bain[1] (ferrite-nucleated carbides only). This practice permits recognition that two distinctly different reaction mechanisms are often involved, i.e., one precipitate nucleates within another precipitate in the case of ferrite-nucleated carbides, whereas both precipitates nucleate in the matrix in the case of austenite-nucleated carbides.

Acknowledgments

The authors express their appreciation to the Office of Naval Research for sponsoring this investigation, to R. F. Mehl for valuable discussions, and to G. A. Roberts and the Vanadium-Alloys Steel Co. for the gift of the ternary steels. This paper is based on a portion of a thesis by Sydney M. Kaufman submitted to the Dept. of Metallurgical Engineering, Carnegie Institute of Technology, in partial fulfillment of the requirements for the degree of Bachelor of Science.

References

[1] E. S. Davenport and E. C. Bain: *AIME Trans.*, 1930, vol. 90, p. 117.
[2] A. Hultgren: *ASM Trans.*, 1947, vol. 39, p. 915.
[3] H. I. Aaronson and C. Wells: *AIME Trans.*, 1955, vol. 203, p. 1002; JOURNAL OF METALS, September 1955.
[4] A. Schrader and F. Wever: *Archiv Für Eisenhüttenwesen*, 1952, vol. 23, p. 489.
[5] T. Ko: *Journal* Iron and Steel Institute, 1953, vol. 175, p. 16.
[6] H. I. Aaronson and C. Wells: Unpublished research.
[7] T. Lyman and A. R. Troiano: *ASM Trans.*, 1946, vol. 37, p. 402.
[8] E. S. Davenport: *ASM Trans.*, 1939, vol. 27, p. 837.
[9] J. R. Cruciger and J. R. Vilella: *ASM Trans.*, 1944, vol. 32, p. 195.

Tensile Properties of Zone Refined Iron in The Temperature Range from 298° to 4.2°K

The tensile properties of zone refined iron have been evaluated in the temperature range from 298° to 4.2°K. It has been found that the higher the purity, the lower the flow stresses and the better the low temperature ductility. Yield stresses as low as 3,800 psi have been observed at room temperature and elongations of 10 pct have been observed at 4.2°K. The major portion of the ductility at 4.2°K arises from twinning. Deformation by twinning at 4.2°K is not suppressed by prestraining at room temperature and the twins occur all through the test. Slip traces were observed to initiate at the ends of previously formed twin traces.

by R. L. Smith and J. L. Rutherford

ALTHOUGH considerable effort has been devoted toward the determination of the mechanical properties of pure metals, it is extremely difficult to compare the results of such work. This is because of differences in method and type of test, grain size, heat treatment, and purity of material. There is very little information on the properties of most of the high melting point reactive metals with purities greater than 99.9 pct.

Previous evidence concerning the tensile properties of unalloyed metals show that: body-centered-cubic metals are brittle at low temperatures; face-centered-cubic metals remain ductile; some hexagonal metals remain ductile, others become brittle. It may be that traces of impurities decrease the low temperature ductility of the body-centered-cubic lattice. This would suppose that a body-centered-cubic lattice free from impurities would exhibit nearly the same ductility as a face-centered-cubic structure. The present investigation has been an evaluation of the tensile properties of zone refined iron in order to determine whether higher purity material than that previously evaluated behaves differently.

Experimental Procedure

In this investigation, high purity iron was zone purified using the floating zone method.[1] The starting stock was obtained from two sources. The first,

R. L. SMITH, Member AIME, and J. L. RUTHERFORD, Junior Member AIME, are associated with the Solid State Physics Div., Franklin Institute Laboratories for Research and Development, Philadelphia.

TP 4479E. Manuscript, Aug. 16, 1956. New Orleans Meeting, February 1957.

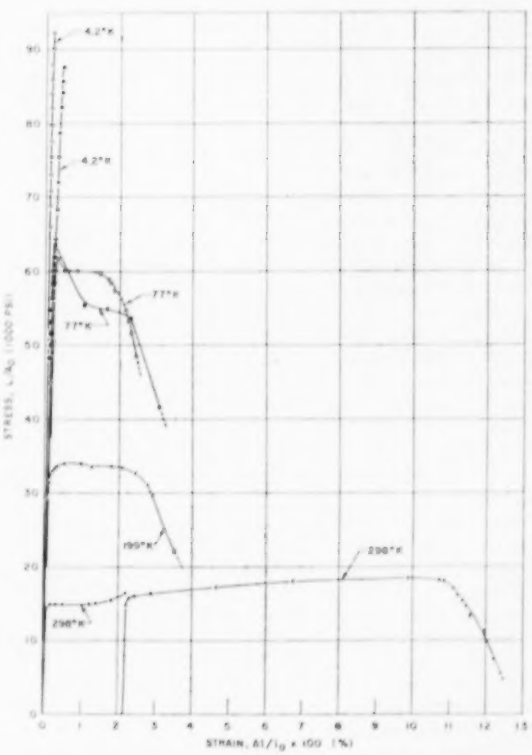

Fig. 1—Tensile properties of vacuum melted iron, grain size ASTM No. 8.

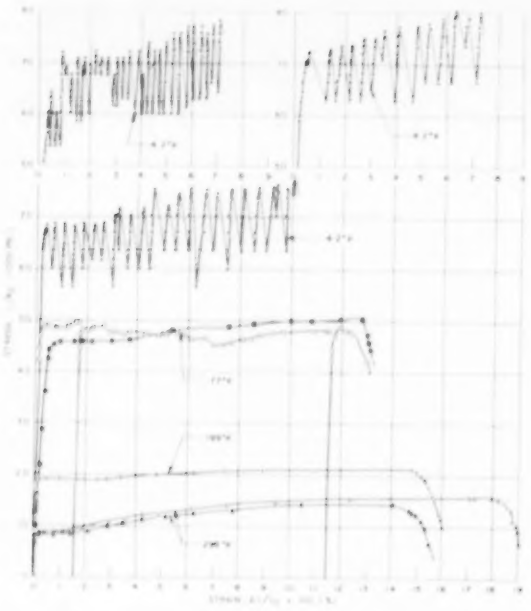

Fig. 2—Tensile properties of vacuum melted iron after zone purification, grain size ASTM No. 5 6, 10 to 20 pct of bar length

which will be referred to as *vacuum melted iron*, was prepared at the University of Pennsylvania.[3] The second, which will be called *arc melted iron*, was prepared by Rengstorff and Goodwin[4] of Battelle Memorial Institute. The impurity content of these two is given in Table I.

Because of the difficulty involved in the determination of small quantities of impurity elements, no conclusive analytical results are available for the zone refined iron. A reasonable estimate of impurity content in zone refined rods can be made from concentration profiles calculated for conditions approaching those used experimentally.[5] Table I lists these impurity estimates. These values are very small but are calculated for only five passes, whereas the ingots were given over twice this number of zone passes. Furthermore, experimental results from a previous investigation[5] checked quite well with the theoretical calculations. The experimental concentration profiles were obtained by monitoring the redistribution of radioactive tracers in zone melted bars under a known set of conditions. Of course, subsequent handling and processing, no matter how carefully performed, may introduce minor amounts of impurities, especially carbon.

After zone purification in dry hydrogen, the rods were swaged to 0.0625 in. diam and annealed in a dynamic vacuum at 900°C. The rods were then drawn to 0.031 in. diam, cut to specimens with a $^3/_4$ in. gage length, and hand polished to a four zero paper finish. They were then given a recrystallization heat treatment in the region of 600°C for various times. Some specimens were polished electrolytically. Great care was taken to avoid specimen contamination. During forming, surface material was removed by abrasion with emery paper, followed by etching, rinsing, and washing in alcohol after each operation.

The tensile tests were made in a hydraulic tensile apparatus constructed for use over a range of temperatures including that at liquid helium. The apparatus was carefully calibrated to determine the *softness* at each of the test temperatures, and from this information a correction of extension was made for each value of load. A constant rate of extension (10^{-4} sec^{-1}) was used. Crosshead motion was read directly to 5×10^{-4} in. and the load to the nearest 0.2 lb.

Since load drops were of special interest in this investigation, considerable care was taken to prevent slippage of the specimen in its grips. As an added precaution, the lengths of all specimens were measured after testing and checked against the elongations as recorded during the tests.

Results and Discussion

Conventional engineering stress-strain diagrams are shown for various irons in Figs. 1 through 4 for tests at 298°, 199°, 77°, and 4.2°K. Since the extension, rather than the diameter, was measured during the test, the region of necking strain cannot be shown on a true-stress, natural-strain basis.

All of the specimens for which tests are shown were recrystallized between 550° and 650°C in an attempt to obtain a fine grained structure. Typical structures are shown in Fig. 5. The grain size effect becomes very important at low temperatures and can easily mask the effect of purity.[7] Therefore, great care was taken to select those materials for any given series of tests that had similar structures.

Serrated Tensile Curves—It can be seen that some of the stress-strain curves have a wavy appearance due to load drops. Yield point phenomena, the occurrence of multiple necks, twinning, and discontinuous slip are all possible causes for this type of stress-strain diagram. Tests at 4.2°K on the arc melted material before zone refining showed a completely brittle behavior with fracture taking place in the elastic range. Other tests at 298° and 199°K, Fig. 3, show a well defined yield point with a smooth stress-strain curve thereafter. However, stress-strain curves at 77°K show a wavy character. This wavy behavior makes it difficult to determine whether any of the yield points are discontinuous yields due to interstitials, twinning phenomenon, localized necking, or some other reason.

A close examination of one of the tests at 77°K, Fig. 3, shows what appears to be scatter in the very early plastic region. These are very distinct and precipitous drops in stress but they occur so rapidly and the load recovers so rapidly that they are diffi-

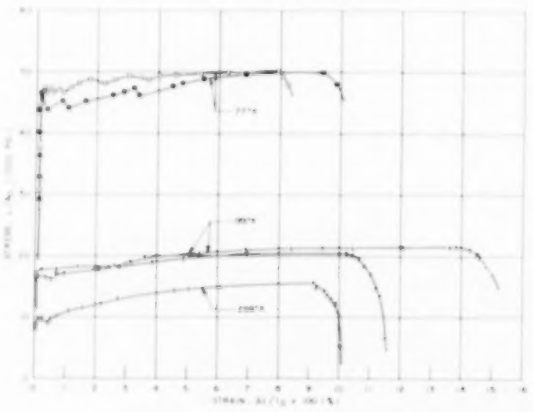

Fig. 3—Tensile properties of arc melted iron, grain size ASTM No. 3-5

cult to record. This sharp serrated type curve becomes more distinct at testing temperatures of 4.2°K, as can be seen in Figs. 2 and 4. In some cases, the stress drops are as great as 20,000 psi. The magnitude of the drop is apparently related to the stress.

Serrated tensile curves (purportedly others than those caused by strain aging) have been reported over a wide range of temperatures for a variety of materials (5 through 24). Many investigators believe that the phenomenon is caused by twinning; others think that it is caused by slip due to highly localized heating. However, it occurs for many materials under a variety of conditions and is interpreted differently by many investigators. It does not seem reasonable that one general explanation should serve in all cases.

Deformation in iron at low temperatures takes place by twinning and slip. The stress necessary for slip increases sharply with decreasing temperatures. It seems reasonable that at some low temperature, and in cases where there are favorably oriented grains, twinning will take place before slip. The onset of twinning should be accompanied by a sharp drop in load with a small amount of strain

Table I. Analyses of High Purity Irons Used in This Investigation

Elements	Arc Melted Iron,* Ppm	Vacuum Melted Iron,† Ppm	Zone Purified Iron, Calculated, Ppm
Oxygen	23	6 to 10	—
Nitrogen	<0.9*	3 to 8	—
Hydrogen	0.25	0.4 to 7	0.05
Carbon	40	X0‡	0.X (low)
Aluminum	20	X0	X
Antimony	<10	<10	<0.1
Arsenic	<10	<50	<5
Barium	—	10	<1
Beryllium	<5	<5	—
Bismuth	—	<10	—
Boron	<5	—	0.05
Cadmium	<50	<10	—
Calcium	1	<10	—
Chromium	10	<10	<1
Cobalt	40	<10	<1
Columbium	—	<100	<1
Copper	8	X0 (low)	X (low)
Gallium	<50	<10	—
Germanium	—	<10	<1
Gold	—	<100	<1
Lead	1	<5 to 10	—
Magnesium	2	<10	—
Manganese	4	X0 (low)	0.X (low)
Molybdenum	10	X0 (low)	X
Nickel	20	<5	<0.5
Phosphorous	7	—	0.07
Silicon	10	X0 (low)	X
Silver	—	<10	—
Sodium	—	<10	—
Strontium	—	<10	—
Tantalum	—	<100	—
Tellurium	—	<1000	—
Tin	5	5 to 10	1
Titanium	—	<10	<1
Tungsten	<10	—	—
Vanadium	2	X	0.X
Zinc	—	<10	<1
Zirconium	—	5 to 10	<1

* < means element not detected; figures shown indicate limit of detection.

† Metallic impurities analyzed by Sam Tour and Co. Inc., New York. For nonmetallic impurities, see reference 2.

‡ X = 1 to 9.

since the process is discontinuous. The stress then would increase elastically until the material again deforms by twinning. It can be seen in Figs. 2 and 4 that, in general, the peak stress values increase as the strain increases, indicating that twinning occurs progressively in favorably oriented grains. There may be localized heating due to the energy release so that the deformation process is adiabatic. This would allow some deformation to take place by slip in the heated, stressed area. Local heating would not be a necessary requirement for slip since twins could be regions of stress concentration from which

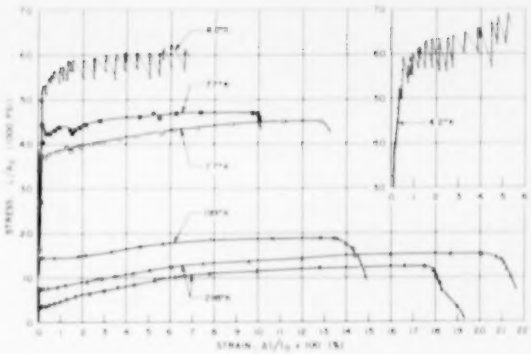

Fig. 4—Tensile properties of arc melted iron after zone purification, grain size ASTM No. 3-5, 20 pct of bar length.

slip could easily start. Although the drops in load would probably be accompanied by strain due to both slip and twinning, the primary cause of the onset of this type of discontinuous deformation in iron is most likely twinning.

A flat tensile specimen was electropolished and tested in tension at 4.2°K. The test was interrupted immediately after the first drop in load. A micrograph of the surface is shown in Fig. 6a. The surface was then polished and etched electrolytically, Fig. 6b. A comparison of these two micrographs shows that some traces remain after repolishing and etching but others disappear. This means that both twin and slip traces are present after the first drop in load. The specimen was then retested at 4.2°K until the second sharp drop in load occurred. The same area was examined and is shown in Fig. 6c. The original twin traces appear to have been broadened and a few additional slip traces have appeared. Fig. 6d shows the same area after repolishing and etching. Again some traces have disappeared indicating that they were slip lines; new twins can be seen on the right. With reference to the foregoing paragraph it is interesting to note that new slip traces appear at the ends of previously formed twins. Several areas were monitored and showed the same results.

There is a possibility that the twins could appear as a result of the load drop in the same manner that they occur at higher temperatures during impact. However, twins occurring during impact are probably due to the high stress concentration set up by the rapidly propagating crack that is caused by the impact load. Even for this type of twin formation it should be emphasized that it has not been proven that twinning does not precede slip.

Effect of Prestraining on Serrations—One of the most interesting aspects of the serrated curves is illustrated in Fig. 7. Zone melted iron from the first 5 pct of the bar length was tested at 77°K. The serrations started appearing at less than 30,000 psi.* At 45,000 psi a sharp drop occurred followed by a slow increase in stress giving the appearance of a normal discontinuous yield. The specimen was then unloaded and again brought up to room temperature and examined carefully for specimen slippage; none had occurred. The specimen was again tested at 77°K and showed another sharp drop at 49,500 psi, again followed by a slow increase in stress. It was

* Paxton and Churchman[13] showed similar sharp serrations in iron tested at 88°K at about 42,000 psi and attributed the behavior to twinning.

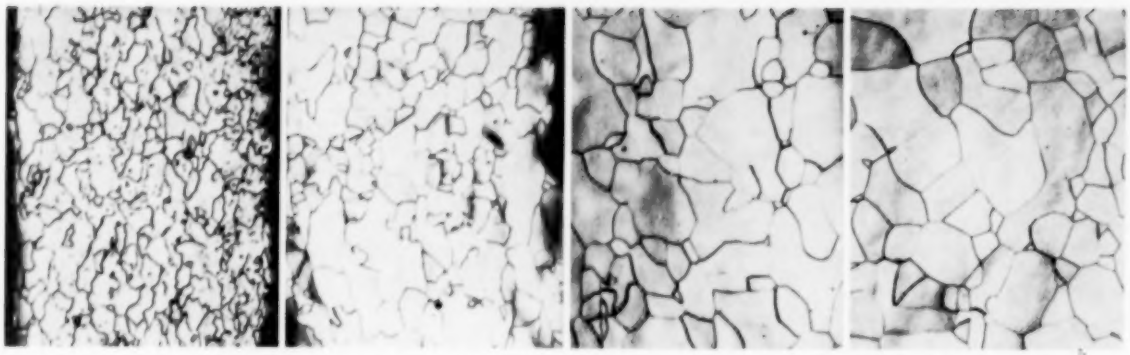

Fig. 5—Typical recrystallized structures of iron used in tensile tests, 74 pct reduction of area. LEFT TO RIGHT: a) vacuum melted iron, heat treated for 30 min at 600°C ; b) vacuum melted iron after zone purification, heat treated for 10 min at 600°C; c) arc melted iron, heat treated for 40 min at 600°C, and d) arc melted iron after zone purification, heat treated for 10 min at 600°C. X200. Reduced approximately 35 pct for reproduction.

unloaded again and brought up to room temperature and examined carefully and, finally, it was tested at 4.2°K and showed the usual serrated curve. The series was completed within 1 hr, with the total time at room temperature less than ½ hr.

If thermal instability were the cause of the serrations and a combination of high stresses, low specific heats, and thermal conductivities are necessary requirements,[20,21,22] then the marked serrations for the first test at 77°K are difficult to explain, since none of the requirements are met. In fact, the thermal conductivity is nearly two times that at room temperature. Rather, it seems more likely that in this very coarse grained material, several of the larger grains are favorably oriented so that twinning occurs before slip. The rapid increase of peak stress during subsequent load drops is merely due to the relatively few regions with orientations favorable for twinning at these stresses. The nearly elastic climb between serrations is because the stresses are not yet high enough for appreciable slip to occur. Upon retesting at 77°K, the first drop is again due to twinning and the subsequent slow increase in stress and large strains accompanying the drops are because the stress is now sufficiently high so that appreciable deformation can take place by slip. The same holds true for the third test. In the fourth test at 4.2°K, the serrations are again primarily due to twinning. The sharp drops and nearly elastic climb are further evidence that very little deformation is taking place by slip. This is because the stress necessary for slip is strongly temperature dependent and is higher at 4.2° than at 77°K.

A further consequence of this series of tests is to show that deformation by slip does not necessarily suppress twinning as postulated by Pfeil[20] and Churchman and Cottrell.[21] More conclusive proof of this is given in Fig. 8. This shows the fractured section of a zone melted specimen of intermediate purity, which has been strained 2 pct at room temperature, then immediately tested to fracture at 4.2°K. Twinning extends back from the fracture into the gage section over four diameters. This also shows that twinning is not always restricted to the immediate vicinity of the fracture.

Similar interrupted tests have been made by Churchman and Cottrell.[21] They obtained marked serrations in carburized Armco iron tested in liquid air, but did not observe serrations for carbon and nitrogen free specimens. They also noted that the behavior was eliminated by prestraining at room temperature and testing immediately in liquid air. They concluded that twinning was eliminated by removal of carbon and nitrogen or by prestraining, since the elastic limit for slip would not then depend so markedly on temperature. This conclusion does not conform to the present experimental results. The relationship between initial slip and twinning cannot be explained simply on the basis of impurities per se, but must involve such other factors as test temperatures, methods of changing impurity content, and the effect of these methods on other metallurgical variables.

Table II. Ratio of Ultimate Stress to Yield Stress

Testing Temperature, °K	Vacuum Melted Iron	Vacuum Melted Iron After Zone Purification	Arc Melted Iron	Arc Melted Iron After Zone Purification
4.2	—	1.20	—	1.23
77	1.0*	1.07	1.06	1.11
199	1.02	1.11	1.24	1.29
298	1.32	1.74	1.60	1.61

* The load continually decreases from the upper yield. Thus, the maximum load and load at yield are the same.

Flow Stresses—Figs. 9 through 12 summarize the effects of temperature on the flow properties of the various irons. Both the yield stress and ultimate* stress curves for the zone melted material fall below those for the material not zone melted. The greatest differences occur at the lowest temperatures. The comparisons of the flow stress curves must be rationalized on the basis of the differences in both purity and grain size. The vacuum melted material has the finest grain size and therefore should have the highest flow stresses at any given strain and temperature.

*In some cases the yield load or fracture load was the highest load during the test. In all cases the ultimate stress was calculated in the conventional way, i.e., maximum load divided by original area.

The effect of purification on flow properties is illustrated quite effectively by the lower tensile curve at room temperature for zone purified material, Fig. 4. This test is not a duplicate of the other room temperature test shown since it has a larger grain size, ASTM No. 2-4. The yield stress is 3,800 psi, which is unusually low.

The temperature dependence of yield stress in iron is difficult to evaluate because of the interfer-

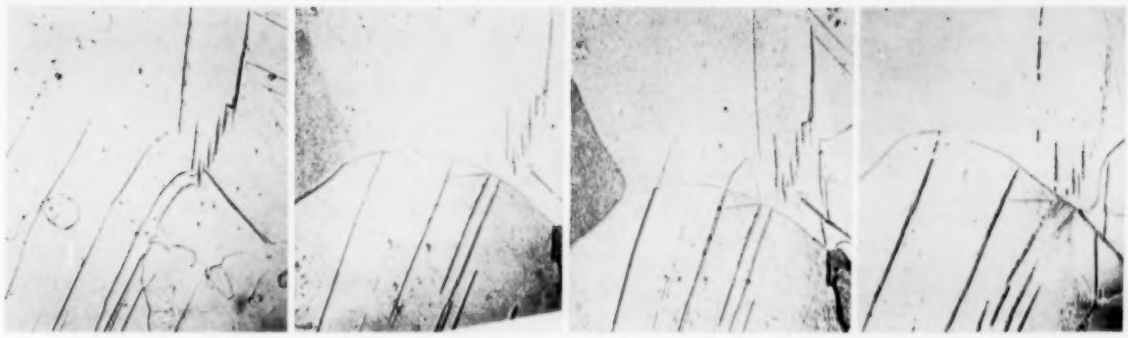

Fig. 6—Arc melted iron after zone purification, polished and etched electrolytically before testing. LEFT TO RIGHT: a) after first drop in load; b) after first drop in load, polished and etched electrolytically; c) after second drop in load; and d) after second drop in load, polished and etched electrolytically. X225. Reduced approximately 35 pct for reproduction.

ence of twinning and the significant grain size effect. A comparison of the yield stress vs. temperature curve for several metals is shown in Fig. 13. Ingot iron[26] is shown in comparison to zone purified iron of two grain sizes. A body-centered-cubic pure metal, tantalum,[27] and the body-centered-cubic alloy β brass[28] are also shown. The typical low temperature dependence of yield stress for face-centered-cubic metals is illustrated by the curve for nickel.[29]

The initial flow stress of the pure iron is not as temperature dependent as that of the ingot iron. In fact, the curve for the large grained pure iron is approaching that of β brass. This iron came from the first 5 pct of the zone purified bar but was very badly duplexed. It must be kept in mind that the low temperature points for iron are not true values of the yield stress for slip since they are most likely due to twinning. Of course, if there is slip in locally heated layers, the temperatures would be higher than that shown. This would have the effect of making the yield stress curves steeper. The primary effect of zone purification on flow stresses was to lower them. It can be seen from Figs. 9 through 12 that the temperature dependence has not changed appreciably.

It has been shown that for no yield point to be present in iron, less than 10^{-3} wt pct C is required at a dislocation density of 10^{8} lines per sq cm.[25] An estimate of the carbon present in the refined iron of about 10^{-4} wt pct leads to the expectation of a yield point. If the strain scale were compressed, the initial level portions of some of the curves would then be indicative of yield phenomena. If less than the amount of interstitials necessary for a yield were present, the curve would become perfectly smooth.

It would be of value to be able to calculate the temperature dependence of yield stress down to 0°K for a body-centered-cubic metal to compare it with experiment. Unfortunately, only crude comparisons can be made since the theory is not sufficiently advanced and the experimental data cannot be corrected for the effects of grain size, purity, and twinning. The Cottrell and Bilby analysis for temperature dependence [30] does not fit the data obtained in this work.

Strain Hardening—Because of the serrations and wavy character of the tensile curves at low temperatures, it is difficult to measure the strain hardening other than by using the ratio of the ultimate stress to the yield stress. This ratio shows a decrease in strain hardening with decreasing test temperatures down to 77°K, Table II. From 77° to 4.2°K the ratio increases.

There is no significant difference in the strain hardening characteristics of the arc melted iron before and after zone refining. The vacuum melted iron has lower ratios of ultimate stress to yield stress than the same iron does after zone melting. However, this is not a reasonable comparison because of the differences in grain size.

The increased values for specimens showing ductility at 4.2°K are also not comparable to other values since the material is probably not actually strain hardening but merely using up regions of easy twinning first.

Ductility—Reduction of area and uniform strain are used as measures of ductility and are shown in Figs. 9 through 12. The uniform strain of the mate-

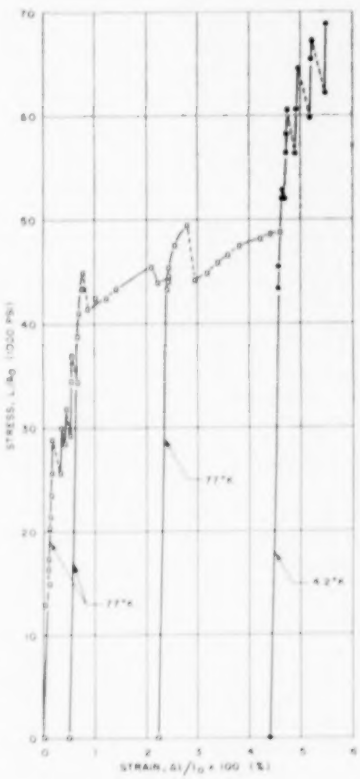

Fig. 7—Interrupted tensile test of arc melted iron after zone purification, 5 pct of bar length.

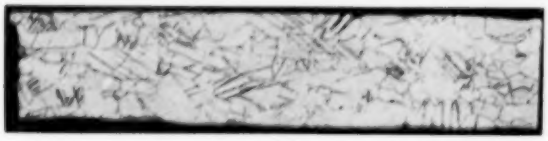

Fig. 8—End of tensile specimen tested at 4.2°K after prestraining 7 pct at room temperature, showing extent of twinning. Fractured end at left. X80. Reduced approximately 50 pct for reproduction.

rial not zone melted is zero at 4.2°K, whereas the zone purified material still retains some uniform strain at this temperature. The reduction of area of iron at low temperatures is probably more strongly dependent on grain size than any other property. It has been shown that the total strain (ln A/A) of iron at liquid air temperatures is extremely dependent on grain size.[4] A change of grain size from ASTM No. 4 to 7 changes the total strain from 0.2 to 0.9 at liquid air temperatures. This effect of grain size is independent of the heat treatment provided the material is relatively pure.

The results show that the arc melted zone purified material, Fig. 12, undergoes a very gradual decrease in both reduction of area and uniform strain. About 6 pct strain and 18 pct reduction of area remain at 4.2°K, as contrasted to the completely brittle behavior of the arc melted material which was not zone purified. Since the grain sizes were the same in both cases, the increase in ductility is due to impurity removal.

The vacuum melted material before zone melting, Fig. 9, shows a marked decrease in uniform strain with decreasing test temperatures with a complete absence of extension at 4.2°K. The reduction of area curves do not show a temperature dependence. However, it must be kept in mind that the grain size of the starting material was much finer than the zone melted material. If the starting material had a grain size of ASTM No. 5-6, it would probably have shown no reduction of area at liquid helium temperature. The vacuum melted material after zone purification, Fig. 10, showed only a gradual decrease in uniform strain with a 7 to 10 pct elongation still remaining at 4.2°K. The reduction of area curve does not show an appreciable temperature dependence.

A shadowgraph of a zone purified specimen tested at 4.2°K is shown in Fig. 14a. The high reduction of area of very fine grained material at low temperatures may in some cases be a valid measure of ductility but in others it can be very misleading. For instance, the tests at 4.2°K for the vacuum melted material before zone melting, Fig. 1, show only an elastic behavior, with fracture taking place before a yield, yet this material showed a 75 to 85 pct reduction of area. The tensile behavior was completely brittle with fracture occurring catastrophically, yet the fracture is fibrous and indicates a high ductility, as is shown in Fig. 14b. This type of fracture can occur with no observable drop in the load. It has been observed previously by one of the authors on very fine grained 1020 steel tested in liquid air. In those tests, the tensile bars were observed through glass windows. They fractured with no drop in load indicated on the Baldwin Southwark tester, yet they always showed a strongly developed neck. The neck must have formed very rapidly, since it could not be observed visually up to the instant of fracture.

The idea of a localized heating could also be utilized to explain this type of behavior. However, this does not seem logical for the same reasons discussed previously in connection with the serrated tensile curves. This behavior is probably not related to the serrations, since they can occur even in specimens that show no appreciable reduction of area. The ability of a metal to strain uniformly may be changed by alloying. Lowering the test temperature also decreases the amount of uniform strain. No clear quantitative relationship has been established between the relative changes between uniform and nonuniform strain. The phenomenon observed here is probably the end result of a continual decrease in nonuniform strain.

It can be very misleading, then, to speak of ductility in terms of reduction of area when this type of behavior is present. For example, Bechtold[5] observes that the ductility of tantalum, unlike other body-centered-cubic metals, is not highly temperature dependent. This observation is based on the relatively small temperature dependence of the reduction of area. The tensile curves show that the ductility as measured by the uniform strain decreases with decreasing test temperatures.[5, 7] Basinski[8] has reported that ultra-fine grained vacuum melted iron has about a 60 pct reduction of area at 4.2°K. However, this iron also showed a very small uniform strain at the same temperature.

It cannot be concluded that all fine grained material will show a high reduction of area at low temperatures. There must be other requirements, such as low oxygen content, minor amounts of carbon, etc. The significant ductility parameter to use as a comparison between body-centered-cubic and face-centered-cubic metals is the uniform strain. This measures the ability of the material to pass on deformation from one localized area to the next. It always decreases with decreasing test temperatures in body-centered-cubic materials, and even does so in the vacuum melted zone purified iron. The important factor to consider is that it decreases much less rapidly in this iron, and still retains a high percentage of its strain at 4.2°K. This means that minor impurities play an extremely important role in the ductile behavior of iron.

Effect of Twinning on Ductility—Interrupted tests at 77°K do not show that there are appreciably more

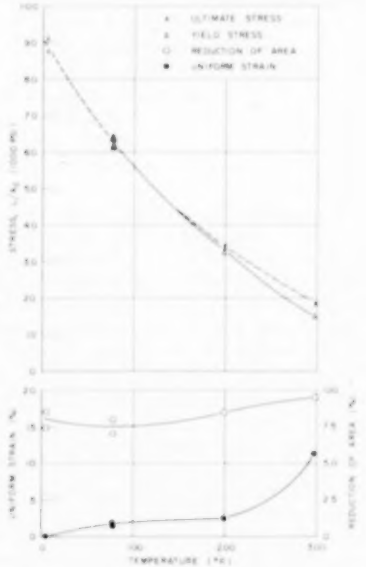

Fig. 9—Effect of temperature on properties of vacuum melted iron, grain size ASTM No. 8.

twins after fracture than there are after the first few percent strain. This is in agreement with the results of Geil and Carwile.[20] However, for interrupted tests at liquid helium, this is no longer true. Although no attempt has yet been made to determine this quantitatively, visual checks on the surface of electropolished specimens show a progressive increase in the number of new twins and the size of the first formed twins as deformation progresses. Thus, the appreciable elongation of the zone purified iron could be the result of twinning. Although most metals can deform a maximum amount of a few percent by twinning, α iron can show a maximum deformation of about 40 pct. This is for single crystals most favorably oriented.[21] In any event, the amount of elongation occurring in the iron specimens tested at 4.2°K could be attributed entirely to twinning. However, the presence of slip lines shows that at least some deformation takes place by slip.

The primary effect of purification on ductility most likely results from the lowering of the stress necessary for flow. Carbon and nitrogen in iron cause nonspherical distortions but, as pointed out by Cottrell,[22] solute atoms would not cause nonspherical distortions in a face-centered-cubic lattice. Solute atoms would anchor only edge dislocations in face-centered-cubic metals, but both screw and edge dislocations would be anchored by interstitial atoms in a body-centered-cubic lattice. Recently, Cochardt, Schoek, and Wiedersich[23] have shown that the interaction between a carbon atom and a screw dislocation in α iron has about the same strength as that between an edge dislocation and a carbon atom. This would lead to the expectation of a stronger temperature dependence of flow stress in body-centered-cubic metals than in face-centered-cubic metals. By lowering the interstitial impurities below the amount necessary to saturate all of the dislocations, the flow stress is lowered. This, in turn, enables the material to strain a greater amount before fracture occurs.

Fracture—All of the fractures not associated with high reductions of area occurred transgranularly on cleavage planes. A possible reason for this may be that certain large grains are oriented with respect to the stress direction so that they crack. This crack then propagates through cleavage planes in adjacent grains. Several investigations[18, 24, 25] have shown that the ductility in tension for single crystals of iron is strongly orientation dependent.

The idea has recently been revived that twinning may be related to brittle fracture by providing regions of stress concentrations.[27] The reason for this observation was that twins have not been observed in tantalum and this is the only body-centered-cubic metal that does not undergo a ductile-to-brittle transition. That tantalum does exhibit such a transition is shown by the marked decrease in ductility when the parameter chosen is elongation. Blewitt et al.[12] have interpreted their results as showing the presence of mechanical twins in the face-centered-cubic metal, copper, when deformed at 4.2°K, yet copper does not show a brittle behavior.

Smith, Spangler, and Brick[2] have shown that twinning does not seem to impair the ductility of iron. Specimens tested at 120°K showed appreciable twinning, yet had total natural strains of about 1.4 and uniform strains of 0.18.

Low and Feustel[26] have discussed the problem in detail and have also concluded that brittle fracture in iron is not due to twinning. They found that for iron specimens containing carbon and tested in tension at 77°K, twins occurred but did not lead to fracture. Fracture took place only long after the appearance of new twins had stopped. They suggested that no new twins form on fracture due to the prior plastic deformation. These authors pointed out that

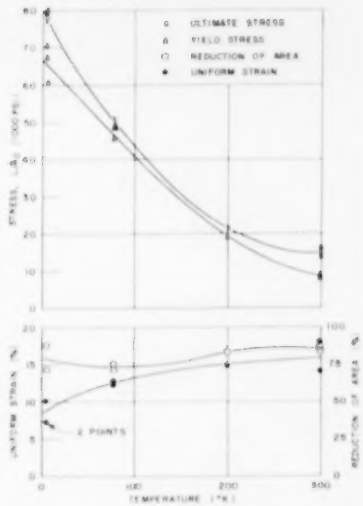

Fig. 10—Effect of temperature on properties of vacuum melted iron after zone purification, grain size ASTM No. 5-6.

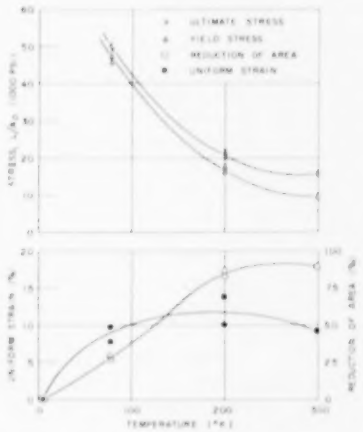

Fig. 11—Effect of temperature on properties of arc melted iron, grain size ASTM No. 3-5.

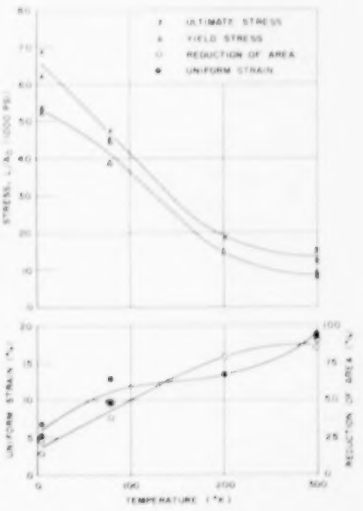

Fig. 12—Effect of temperature on properties of arc melted iron after zone purification, grain size ASTM No. 3-5, 20 pct of bar length.

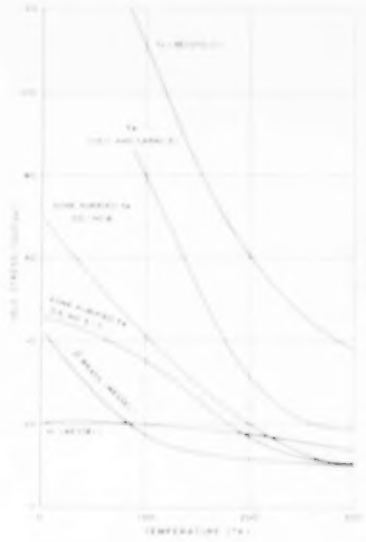

Fig. 13—Yield stress vs temperature for various metals.

it is most likely that the stress for twinning is higher than that for flow and that the stress concentration required to produce twinning is provided at the ends of slip bands temporarily held up at grain boundaries. In this work many cases show that the stress for twinning is lower than that for slip, Figs. 2, 4, and 7, and that the stress concentration required to produce slip is provided in some instances at the ends of twin traces. Fig. 6 shows slip bands propagating from old twin traces. This doesn't necessarily indicate that such stress concentration points initiate fracture. The ends of twin traces can act as regions of easy slip.

Summary and Conclusions

The foregoing results lead to the following observations and conclusions:

1) Lowering the impurity content in iron affects the tensile properties as follows:

A) The higher the purity, the lower the flow stresses. This is probably because the interaction between interstitials and screw dislocations becomes less effective.

B) The higher the purity, the better the low temperature ductility as measured by elongation. This is primarily because flow (deformation by both slip and twinning) takes place at lower stresses.

C) A comparison of the temperature dependence of ingot iron to that of relatively pure vacuum or arc melted iron shows that elimination of gross impurities decreases the temperature dependence of the yield stress. Further purification does not change the temperature dependence appreciably. Definite conclusions cannot be drawn concerning this due to the interference of twinning at low temperatures.

2) Since the zone refined iron retained an appreciable ductility at low temperatures, the following observations can be made:

A) Twins occur all during the tensile test at 4.2°K and are not restricted to the immediate vicinity of the fracture.

B) Prestraining at room temperature does not suppress twinning at 4.2°K. The primary effect of prestraining may be to raise the stress necessary for twinning.

C) The sharp serrations in the tensile curves may be attributed primarily to twinning. The waviness is most likely due to a mixture of deformation by slip and twinning.

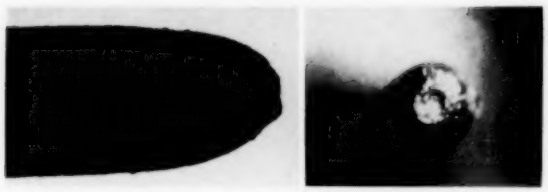

Fig. 14—Iron tested at 4.2°K: a) LEFT: zone melted iron showing 90 pct reduction of area; and b) RIGHT: nonzone melted iron showing cup fracture without elongation.

Acknowledgments

This research was supported by the United States Air Force through the Air Force Office of Scientific Research under Contract No. AF 18(600)-1581. The authors are indebted to I. G. Greenfield, M. Herman, F. E. Jaumot, Jr., and H. G. F. Wilsdorf for their assistance in preparing the micrographs and critically reviewing the manuscript. Special thanks are extended to J. W. Halley and G. W. F. Rengstorff for their cooperation in obtaining the arc melted iron, which was prepared under the sponsorship of the American Iron and Steel Institute at Battelle Memorial Institute.

References

[1] R. L. Smith and J. L. Rutherford: *AIME Trans.*, 1957, vol. 209, p. 478; JOURNAL OF METALS, April 1957.
[2] R. L. Smith, G. Spangler, and R. M. Brick: *ASM Trans.*, 1954, vol. 46, p. 973.
[3] G. W. P. Rengstorff and H. B. Goodwin: *AIME Trans.*, 1955, vol. 203, p. 467; JOURNAL OF METALS, March 1955.
[4] L. Burris, Jr., C. H. Stockman, and I. G. Dillon: *AIME Trans.*, 1955, vol. 203, p. 1017; JOURNAL OF METALS, September 1955.
[5] A. Joffé: *The Physics of Crystals*. McGraw-Hill Book Co. New York, 1928.
[6] M. Klassen-Nekludowa: *Ztsch. für Physik*, 1929, vol. 55, p. 555.
[7] R. Becker and E. Orowan: *Ztsch. für Physik*, 1932, vol. 79, p. 566.
[8] A. H. Stang, M. Greenspan, and S. B. Newman: *Journal of Research* National Bureau of Standards, 1946, vol. 37, p. 211.
[9] H. C. Doepkin: *AIME Trans.*, 1952, vol. 194, p. 157; JOURNAL OF METALS, February 1952.
[10] G. V. Nzhik: *Bulletin* Academy of Sciences, USSR, 1955, No. 1, p. 57.
[11] R. H. Kropschot: National Bureau of Standards Report No. 3517, February 1955, p. 164.
[12] F. L. Vogel and R. M. Brick: *AIME Trans.*, 1953, vol. 197, p. 700; JOURNAL OF METALS, May 1953.
[13] R. P. Steijn and R. M. Brick: *ASM Trans.*, 1954, vol. 46, p. 1406.
[14] H. W. Paxton and A. T. Churchman: *Acta Metallurgica*, 1953, vol. 1, p. 473.
[15] A. T. Churchman and A. H. Cottrell: *Nature*, 1951, vol. 167, p. 943.
[16] D. F. Gibbons: *AIME Trans.*, 1953, vol. 197, p. 1245; JOURNAL OF METALS, September 1953.
[17] T. H. Blewitt, J. K. Redman, R. A. Sherrill, and R. R. Coltman: *Bulletin* Amer. Physical Soc., 1955, vol. 30, No. 2, p. 32.
[18] G. W. Ardley and A. H. Cottrell: *Proceedings* Royal Soc., London, 1953, series A, vol. 219, p. 328.
[19] E. T. Wessel: ASM Preprint No. 3, 1956.
[20] Z. S. Basinski: AEC Conference on Solid State Physics and Metallurgy, June 1956.
[21] W. Boas and E. Schmidt: *Ztsch. für Physik*, 1949, vol. 54, p. 16.
[22] W. Spaeth: *Metalloberflache*, 1953, vol. 7A, pp. 119 and 177.
[23] W. Spaeth: *Metall*, 1953, vol. 7, pp. 34, 430, 772, and 679.
[24] C. Zener and J. H. Holloman: *Journal of Applied Physics*, 1944, vol. 15, p. 22.
[25] L. B. Pfeil: *Carnegie Scholarship Memoirs*, Iron and Steel Institute, 1926, vol. 15, p. 319.
[26] G. W. Geil and N. L. Carwile: *Journal of Research* National Bureau of Standards, 1950, vol. 45, p. 129.
[27] J. H. Bechtold: *Acta Metallurgica*, 1955, vol. 3, p. 249.
[28] A. H. Cottrell and B. A. Bilby: *Proceedings* Physical Soc., London, 1949, vol. A62, p. 49.
[29] J. W. Pugh: *ASM Trans.*, 1956, vol. 48, p. 667.
[30] G. W. Geil and N. L. Carwile: *AIME Trans.*, 1953, vol. 197, p. 213; JOURNAL OF METALS, February 1953.
[31] E. Schmidt and W. Boas: *Plasticity of Crystals*. F. A. Hughes and Co. London, 1950.
[32] A. H. Cottrell: The Yield Point in Single Crystals and Polycrystalline Metals. Symposium on the Plastic Deformation of Crystalline Solids, May 1950. Carnegie Institute of Technology and ONR.
[33] A. W. Cochardt, G. Schoek, and H. Wiedersich: *Acta Metallurgica*, 1955, vol. 3, p. 533.
[34] J. J. Cox, G. T. Horne, and R. F. Mehl: ASM Preprint No. 1, 1956.
[35] N. P. Allen, B. E. Hopkins, and J. E. McLennan: *Proceedings* Royal Soc., London, 1956, vol. 234A, p. 221.
[36] J. R. Low Jr. and R. G. Feustel: *Acta Metallurgica*, 1953, vol. 1, p. 185.

Discussion of this paper sent (2 copies) to AIME by Sept. 1, 1957 will appear in AIME *Transactions* Vol. 212, 1958, and in JOURNAL OF METALS, April 1958.

Aging in Complex Commercial Ni-Cr Alloys Hardened with Titanium and Aluminum

Four commercial Ni-Cr alloys hardened with titanium and aluminum, air melted Inconel X 550, Inco 700, and vacuum melted M-252 and Waspaloy, were studied in considerable detail for aging response. Identification of the γ' phase, Ni_3 (Al, Ti), was made in all but M-252. Quantitative determination of the various carbides was also made. Two solution treatments and two aging treatments were studied. The effect of such heat treatments on the rupture life and ductility was determined by means of creep rupture tests at 1500° and 1600°F. Metallographic studies were utilized to cross-check the findings.

by Robert F. Wilde and Nicholas J. Grant

TAYLOR and Floyd's[1,2] work in establishing phase diagrams based on the elements Ni-Cr-Ti-Al has led to an understanding of the precipitation hardening mechanism in alloys based on these elements. Nordheim and Grant[3] concluded that in simple alloys, and where the aluminum to titanium atomic ratio was such that less than three out of five aluminum atoms were replaced by titanium, the precipitate on aging is the face-centered-cubic Ni_3Al phase, called γ'. They further found that increasing amounts of hexagonal η phase, Ni_3Ti, precipitated from these alloys when the titanium content exceeded the solid solubility of both matrix and Ni_3Al. For alloys of Ni-Cr-Ti-Al, in which the titanium and aluminum contents each ranged from 0 to 4 wt pct, the titanium-rich γ' was superior for strengthening to either pure γ' or η. It was also noted that the combined titanium plus aluminum content (atomic pct) was a direct measure of the high temperature strength and overaging temperatures for these alloys.[4]

The present investigation was undertaken to extend existing data on precipitation hardening in the more complex commercial alloys containing higher titanium plus aluminum, and with significant quantities of cobalt, molybdenum, and carbon.

R. F. WILDE, Junior Member AIME, formerly Research Assistant, Dept. of Metallurgy, Massachusetts Institute of Technology, is now with Allison Div., General Motors Corp., Indianapolis, Ind. N. J. GRANT, Member AIME, is Professor, Dept. of Metallurgy, Massachusetts Institute of Technology, Cambridge, Mass.

TP 4430E. Manuscript, Feb. 17, 1956. Cleveland Meeting, October 1956.

Experimental Procedure

Reforging of As-Received Bar Stock—The alloys were received as ground, forged bar stock. Chemical analyses and the as-received bar diameters are shown in Table I along with the ASTM grain size after the various treatments. All stock except the Waspaloy was reforged to ⅜ in. diam to gain material and to facilitate machining of stress-rupture specimens. Forging was carried out at 2100°F, and discontinued when the bar temperature fell to 1800°F.

Heat Treatments—For experimental simplicity it was desirable to heat treat all of the alloys at the

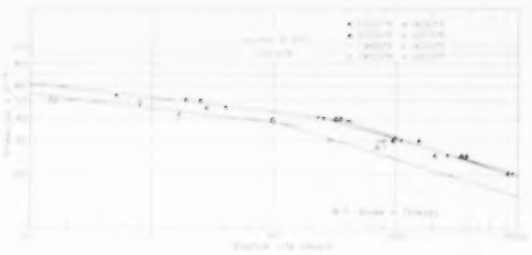

Fig. 1—Log stress-log rupture life plot at 1500°F for Inconel X 550 as a function of solution and aging treatments.

same temperatures. As a result, no attempt was made to duplicate commercial heat treatments. Instead, the temperatures used represent the usual limits of heat treatment and aging. The heat treatments were:

A) Solution at 2200°F, 2 hr, air cooled, plus aging at 1600°F, 24 hr.

B) Solution at 2200°F, 2 hr, air cooled, plus aging at 1200°F, 24 hr.

C) Solution at 1900°F, 6 hr, air cooled, plus aging at 1600°F, 24 hr.

D) Solution at 1900°F, 6 hr, air cooled, plus aging at 1200°F, 24 hr.

Electrolytically extracted residues were obtained from bars solution treated at 2000°, air cooled and aged at 1500°F, 50 and 250 hr (heat treatments A50 and A250) or solution treated at 2200°, air cooled and aged at 1600°F, 24 hr (heat treatment B).

Etching Procedure—In the aged condition, the complex alloys were electrolytically etched in a 2 pct HCl, 2 pct Cr_2O_3 solution, at 2.5 v, 30 sec. As solution treated, it was necessary to immersion etch in 97 pct HCl, 2 pct H_2SO_4, and 1 pct HNO_3, for from 30 sec to 2 min. Grain boundaries were satisfactorily defined using this etchant, but selective attack around carbide particles was sometimes severe.

Stress Rupture Tests—All tests were carried out using gage dimensions of 0.250 in. diam by 1 in. long. Specimens were held at temperature for a minimum of time and were generally loaded in about ½ hr and always in less than 45 min.

Electrolytic Extractions—The cell consisted of an alloy bar specimen as the anode, and a tantalum sheet cathode. An extraction run of 48 hr at 1.5 amp usually resulted in sufficient residue for all tests. Current density was about 1 amp per sq in. The residues were separated by centrifuging, and screened to —100 mesh.

Results

Phase Identification—*Electrolytic Extraction and X-ray Diffraction:* Ni_3Al is an intermetallic compound which is fully ordered up to its decomposition temperature with a structure analogous to the Cu_3Au type. The relative intensities to be expected from its X-ray pattern are shown in Table II.

Note that the relative intensities of the simple cubic lattice reflections, (100), (110), (210), etc., are very low compared with those of the face-centered-cubic lattice (111), (200), (220), etc., reflections. Differentiation of a Ni_3Al (γ') pattern from a γ solid solution pattern can be seen to depend on the detection of the lower-intensity lines. Unfortunately, the observed intensities of the simple cubic lattice reflections, using $CuK\alpha$ radiation, were lower than those calculated above. Only the first four of these lines appeared, see Table III. Chromium radiation increased the relative intensities of these four lines by a small factor, but they were still below those calculated.

Further, the addition of titanium to Ni_3Al decreased the intensities of the simple cubic lattice lines until only the (100) and (110) lines appeared at the composition $Ni_3(Al_{0.5}, Ti_{0.5})$, as determined from the synthetic standard, see Table III. This was to be expected, for the scattering factor of titanium is higher than that of aluminum at all angles, and the intensities of these lines depend on the difference in atomic scattering factor between the atoms occupying the two sets of lattice points in the Ni_3Al lattice.

Extracted residues were consistently high in titanium, and the effect in reducing the intensities of the simple cubic lattice lines was marked. Only the (100) and (110) lines could be identified in Inconel X 550 and Inco 700, and none of the other alloy residues showed reflections other than the (111), (200), etc., face-centered-cubic lines. These results, although consistent, make identification of Ni_3Al from its X-ray pattern difficult in commercial alloys.

Inconel X 550: Inconel X 550 was the simplest of the four commercial alloys from a chemical standpoint. As judged from its composition, Table I, $Ni_3(Al_{0.5}, Ti_{0.5})$ was expected to be the composition of the aging precipitate. Titanium carbide, nitride, or carbonitride was expected, and although columbium carbide might have appeared, due to the presence of almost 1 pct Cb, none was identified.

Extractions were made in 20 pct H_3PO_4, after aging 50 and 250 hr at 1500°, or 24 hr at 1600°F. The only phase found by X-ray diffraction of the residues was Ni_3 (Al, Ti). Table III shows a typical pattern, using copper radiation. No additional

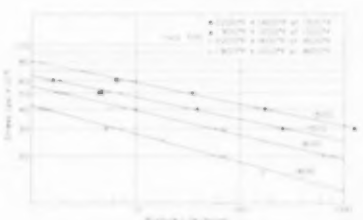

Fig. 2—Log stress-log rupture life plot for Inco 700 at 1500° and 1600°F as a function of solution and aging temperatures.

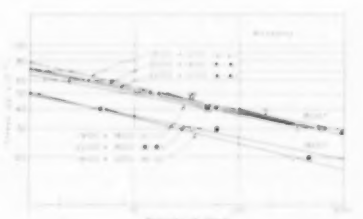

Fig. 3—Log stress-log rupture time plot for Waspaloy at 1500° and 1600°F for several heat treatments.

Fig. 4—Log stress-log rupture time plot for M-252 at 1500° and 1600°F for several heat treatments.

lower angle lines could be discerned when chromium radiation was used.

Inco 700: X-ray analyses of Inco 700 residues were made on both HCl and H_3PO_4 extractions, the H_3PO_4 extractions resulting in a γ' pattern and HCl extractions producing only the γ pattern. The Ni_3 (Al, Ti) (100) and (110) reflections appeared in the H_3PO_4 extraction of a specimen aged at 1500°F for 50 hr when chromium radiation was used (lower background intensity) but not with copper radiation.

No unidentified lines appeared in the patterns from this alloy. Phases identified were Ni_3 (Al, Ti), matrix, and TiC. No M_6C lines appeared in the residues, but this phase was prominent in microscopic observations, comprising about 70 pct of the carbides, with Ti (C, N) accounting for the remainder. Since chemical analysis of a residue reported molybdenum at 2.1 pct, the pattern from M_6C should have appeared.

Waspaloy: Electrolytically extracted residues (in H_3PO_4) were found to contain Ni_3 (Al, Ti), M_6C, and TiC when analyzed by X-ray diffraction, whereas extraction with HCl showed only matrix lines and

Table I. Alloy Analyses and Data

Element	Composition, Wt Pct			
	Inconel X 550*	Inco 700†	Waspaloy‡	M-252§
Ni	72.39	44.99	55.5	54.8
Cr	15.15	15.05	19.7	19.7
Co	—	30.73	14.1	9.6
Mo	—	3.22	4.2	9.9
Ti	2.50	2.19	3.25	2.52
Al	1.17	3.02	1.39	1.04
Fe	6.68	0.38	0.75	0.84
Mn	0.70	0.05	0.30	1.0
S	0.007	0.007	0.006	0.004
Si	0.33	0.19	0.49	0.53
C	0.04	0.13	0.09	0.12
N	#	0.015	#	#
Cu	0.04	0.02	0.1	#
Cb + Ta	0.97	—	—	—
Mg	#	#	0.01	#
Grain size, ASTM as-received	7 to 8	6 to 7	6 to 7	6 to 7, some 4 to 5
Reforge + 1900°F solution	5 to 6, some 2	5 to 6	5 to 6	5 to 6
Reforge + 2200°F solution	1	1 to 3	2 to 5	2 to 6, some 1

* Received as $^5/_8$ in. forged bar stock, air melted at Huntington, W. Va.
† Received as $^3/_4$ in. forged bar stock, air melted at Huntington, W. Va.
‡ Received as $^3/_8$ in. forged bar stock, induction vacuum melted at Utica Drop Forge.
§ Received as $^7/_8$ in. forged bar stock, induction vacuum melted at Utica Drop Forge.
# Not analyzed.

carbides. Further, the M_6C and TiC patterns were more complete in the H_3PO_4 extraction.

A consistently better extraction of the aging phase and carbide has been possible with H_3PO_4, especially when the acid concentration is kept low. The lowest acid concentration able to dissolve away the matrix at a reasonable rate is apparently to be preferred.

M-252: No Ni_3 (Al, Ti) pattern appeared from the residues of M-252. This is the only alloy in which γ' could not be found by the methods used in this work. Good identification of two carbides, M_6C and TiC, was possible, and the other microconstituents found by Beattie and VerSnyder,[5,6] $M_{23}C_6$ and σ, should not have appeared under the conditions of these tests and at the molybdenum content (10 pct) of this heat. In no case were either of the latter phases found.

Fluorescent Analysis and Chemical Analysis: Tables IV and V summarize the results of fluorescent and chemical analyses for all the alloys. Good agreement between these two methods of analysis is seen.

The difference between M-252 residues and the others is immediately evident. In M-252 the residues were predominantly matrix phase enriched with titanium carbide. It is unlikely that Ni_3 (Al, Ti) was contained in any but small quantities in M-252 residues, although failure to extract it does not positively mean that it was not present in the alloy.

Parameter Measurements: Inconel X 550 measurements were made on the high angle (420) lines from solid specimens, powdered alloy, and extracted residues, and results for this alloy and the others are given in Table VI. The parameter for the γ' phase in Inconel X 550 was 3.589A, which is 0.017A or 0.5 pct larger than the matrix. This misfit difference can be accounted for only by considering the effect of the larger titanium atoms in the intermetallic structure. The matrix parameter of 3.572A was measured after solution treating at 2200°F, obtaining filings, and vacuum annealing the filings at 1900°F for 10 min.

With Inco 700, as with Inconel X 550, the lattice parameter measurements confirm the presence of Ni_3 (Al, Ti) at aging times from 50 to 250 hr. The misfit between γ' and γ is +0.3 pct, in good agreement with presently accepted theories of precipitation-hardening. A matrix parameter measurement of between 3.571 and 3.572A was obtained from the annealed filings. The best measurement of the γ' phase was 3.583A.

Waspaloy lattice parameter measurements consistently followed the above pattern. A matrix lattice constant of between 3.578 and 3.579A was obtained both from filings and from an HCl electrolytic extraction residue. For γ' the parameter was 3.589A, a misfit of +0.28 pct.

M-252, due to its high molybdenum content, has a larger lattice than the other alloys. This may be important in considering its electrolysis extraction residues. On measuring the lattice parameters of M-252 specimens, there was no difference between extracted residues and the solid alloy matrix, suggesting that they were one and the same.

Stress Rupture Properties—In an effort to determine how large the differences in high temperature strength and ductility are among these alloys, particularly in view of the differences in aging response between M-252 and the other three alloys, creep rupture tests were run at 1500° and 1600°F for the

Table II. Calculated Intensities for Ni_3Al Lines

hkl	*FF**	*mf*	*I*	*hkl*	*FF**	*mf*	*I*
100	169	6	1020	220	1450	12	17400
110	165	12	1650	300	41	6	250
111	2075	8	16500	310	38	24	910
200	2000	6	12000	311	1100	24	26000
210	53	24	1260	222	980	8	7800

* Structure factor.
† Multiplicity.

several combinations of solution treatment and aging treatment.

Inconel X 550: Fig. 1 shows the results of stress rupture testing at 1500°F. The strength values resulting from a 2200° solution treatment were higher than those from the 1900°F treatment, as can be seen in Table VII, which summarizes the values of stress to produce rupture in specified time periods.

Ductility was significantly affected by the choice of the solution treatment temperature and aging

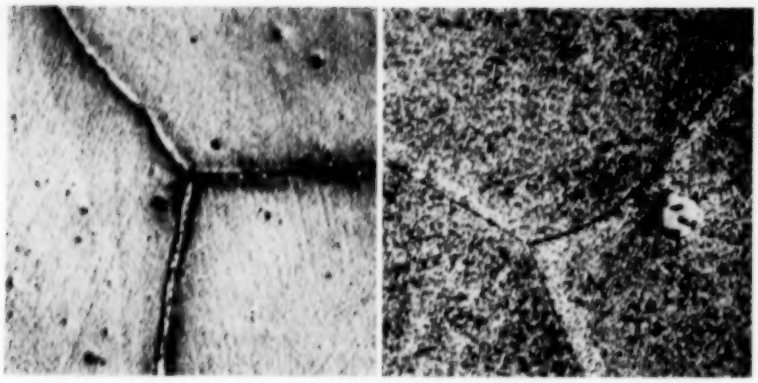

Fig. 5—Micrographs of Inconel X 550 after 2200°F solution treatment plus a) LEFT: 1200°F aging, and b) RIGHT: 1600°F aging. HCl + Cr_2O_3 electrolytic etch. X1000. Reduced approximately 20 pct for reproduction.

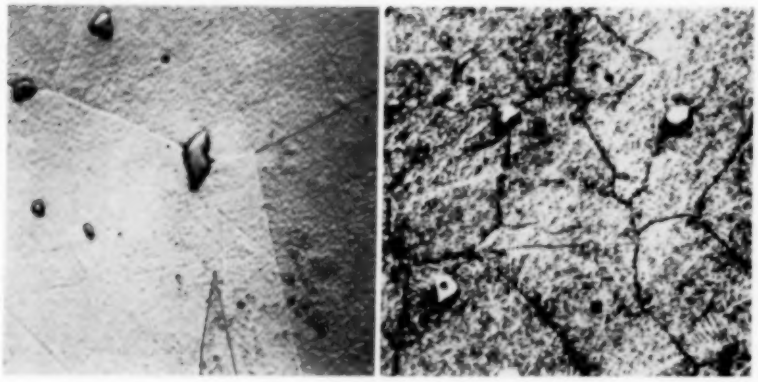

Fig. 6—Micrographs of Inco 700. a) LEFT: After 2200°F solution treatment. Pratt and Whitney etch. b) RIGHT: After 1900° solution treatment plus 1600°F aging. HCl + Cr_2O_3 electrolytic etch. X1000. Reduced approximately 20 pct for reproduction.

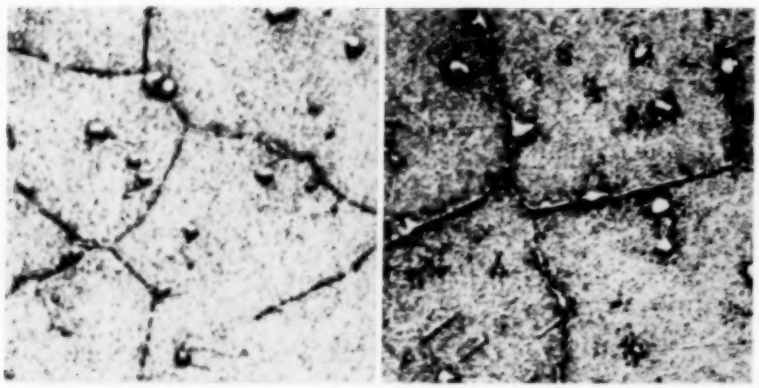

Fig. 7—Micrographs of Waspaloy. a) LEFT: After 1900° solution treatment plus 1600°F aging. b) RIGHT: After 2200° solution treatment plus 1600°F aging. HCl + Cr_2O_3 electrolytic etch. X1000. Reduced approximately 20 pct for reproduction.

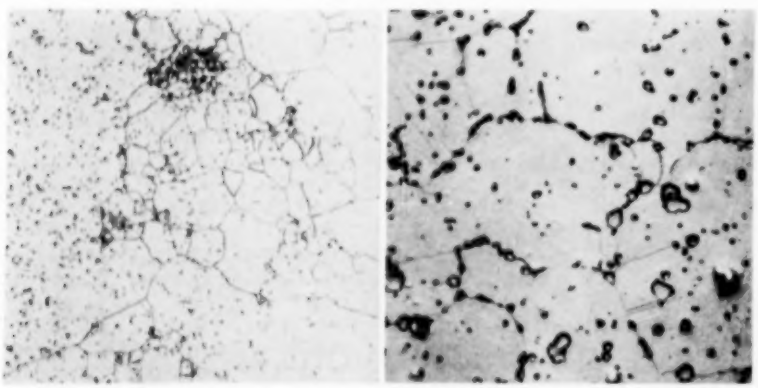

Fig. 8—Micrographs of M-252. a) LEFT: After 2200° solution treatment plus 1600°F aging. HCl + Cr_2O_3 electrolytic etch. X100. b) RIGHT: After 1900° solution treatment plus 1200°F aging. Pratt and Whitney etch. X1000. Reduced approximately 20 pct for reproduction.

Table III. Comparison of Ni_3Al and Ni_3 (Al, Ti) Patterns

	Ni_3Al, Standard		$Ni_3(Al_{0.5}, Ti_{0.5})$, Standard		$Ni_3(Al, Ti)$, Inconel X 550		$Ni_3(Al, Ti)$, Inco 700	
hkl	*d*, Observed	*I**	*d*, Observed	*I**	*d*, Observed	*I**	*d*, Observed	*I**
100	3.600	W	3.600	W	3.600	VW	3.608	VW
110	2.547	W	2.543	W	2.547	VW	2.542	VW
111	2.074	S	2.074	S	2.074	VS	2.073	VS
200	1.799	MS	1.799	S	1.793	S	1.791	S
210	1.603	W	—	—	—	—	—	—
211	1.461	VW	—	—	—	—	—	—
220	1.265	M	1.261	M	1.267	MS	1.265	MS
300	—	—	—	—	—	—	—	—
310	—	—	—	—	—	—	—	—
311	1.078	M	1.083	S	1.081	MS	1.079	MS
222	1.032	W	1.037	MW	1.035	W	1.033	W
320	—	—	—	—	—	—	—	—
321	0.819	MS	0.823	M	0.823	M	0.822	M
400	0.873	VW	0.897	MW	0.895	W	0.896	W
420	0.798	MS	0.803	M	0.803	M	0.801	M
a_o, observed	3.561		3.586		3.588		3.583	

* W stands for weak; M, medium; S, strong; and V, very.

Table IV. Chemical Analyses of Extracted Residues in Wt Pct

Alloy	Heat Treatment*	Mesh Size	Electrolyte	Ni	Cr	Ti	Al	C	Mo	Co
M-252	B	−100	H_3PO_4	57.6	12.9	7.61	2.31	0.66	—	—
	B	−325	H_3PO_4	44.8	15.8	6.75	0.87	1.47	—	—
	A250	−100	H_3PO_4	54.3	12.0	7.64	3.17	0.49	7.5	6.9
Waspaloy	A50	−100	H_3PO_4	69.0	2.56	12.5	5.08	0.45	—	—
Inconel X 550	A50	−100	H_3PO_4	62.8	2.68	9.3	4.80	0.38	—	—
Inco 700	A50	−100	H_3PO_4	52.3	3.18	6.5	7.05	0.35	2.1	26.3

* A50: solution treated 2000°F, air cooled, aged 1500°F, 50 hr; A250: solution treated 2000°F, air cooled, aged 1500°F, 250 hr; and B: solution treated 2200°F, air cooled, aged 1600°F, 24 hr.

Table V. Fluorescent Analyses of Extracted Residues in Wt Pct

Alloy	Heat Treatment*	Mesh Size	Electrolyte	Ni	Cr	Ti	Cb	Ta	Mo	Co	Fe
M-252	A50	−100	H_3PO_4	high	6	12.5	—	—	low	low	trace
Waspaloy	B	−100	HCl	low	30	18	—	—	low	low	trace
	A50	−100	H_3PO_4	high	low	—	—	—	low	low	trace
Inconel X 550	A50	−100	H_3PO_4	high	3	12.5	low	trace	trace	—	medium
Inco 700	A50	−100	H_3PO_4	high	3	9	—	—	trace	medium	trace

* A50: solution treated 2000°F, air cooled, aged 1500°F, 50 hr; and B: solution treated 2200°F, air cooled, aged 1600°F, 24 hr.

temperature, but the greater effect was due to the decreased aging temperature, see Table VII. In addition, test point scatter decreased as either the solution or aging temperature increased.

The severe embrittlement after 1200°F aging is closely associated with the observed high hardness values for this temperature.[4] This high hardness probably results in a structure which is severely notch-sensitive as evidenced by failure in the threaded portion of the test specimens. Thus, the first intercrystalline crack leads to early failure, which does not occur in the 1600°F aged structures.

Inco 700: From a strength point of view, Inco 700 responds to changes in both solution and aging temperature, the response being somewhat greater in 1600° than in 1500°F tests, see Fig. 2 and Table VII. Of greater importance, however, is the considerably smaller change in ductility at 1500°F due to a decrease in solution and aging temperatures, as compared to the behavior of the lower alloyed Inconel X 550. Tests at 1600° showed significantly higher ductilities than at 1500°F, in common with M-252 and Waspaloy.

However, Inco 700 has lower ductility at 1500°F than either Waspaloy or M-252. Since both the Waspaloy and M-252 alloys were vacuum melted, and the Inco alloy was air melted, the lower ductility of Inco 700 is not surprising.

Waspaloy: Stress rupture data on Waspaloy provided an excellent contrast with Inco 700. A complete series of heat treatments was tested at 1500°F, see Fig. 3 and Table VII. Almost all of the 1500°F test points could be fitted by a single curve with little scatter regardless of heat treatment. Thus, Waspaloy of the composition tested does not show sensitive response to the types of heat treatments used for the 1500°F tests.

The ductility behavior is different from that observed for either Inconel X 550 or Inco 700 in that the lower solution treatment resulted in somewhat higher ductility values at both 1500° and 1600°F. However, the higher aging temperature resulted in somewhat better ductility than the 1200°F aging, in line with normal behavior.

Stress rupture tests at 1600° did not indicate much difference in response to heat treatment than at 1500°F. Test point scatter was the same for both heat treatment combinations tested, but the 2200° plus 1600°F heat treatment was somewhat stronger, see Fig. 3.

M-252: As with Inco 700 and Waspaloy, testing at 1600° resulted in a more pronounced difference

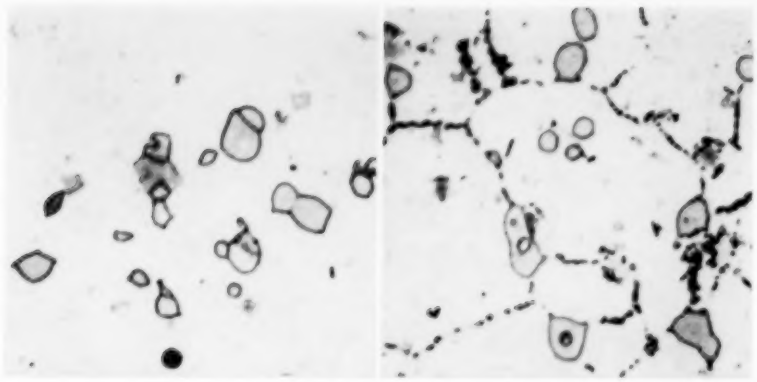

Fig. 9—Micrographs of carbides in M-252. a) LEFT: After 2200°F solution treatment. b) RIGHT: After 2200° solution treatment plus 1600°F aging. Unetched. X1500. Reduced approximately 20 pct for reproduction.

in stress rupture strength with heat treatment than at 1500°F. In M-252, as in Waspaloy, there was almost no difference between the two heat treatments tested at 1500°F. The upper pair of curves shown in Fig. 4 are drawn separated for convenience only. At 1600°F the combination of a higher solution plus aging temperature resulted in a slightly stronger alloy.

The ductility of M-252, as shown by percentage of elongation and reduction in area, Table VII, is the highest of the four alloys. Localized necking and a tendency toward transcrystalline fracture appeared at 1500°F, especially at higher stresses. However, in no case did miscroscopic examination of a fractured section show transcrystalline fracture.

Metallography—*Inconel X 550:* In the as-received condition, the matrix was uniformly fine-grained,

Table VI. Lattice Parameter Measurements*

Alloy	γ′ Misfit, Pct	Matrix, A	Residue, A	Heat Treatment‡	Electrolyte
M-252	None	3.594	3.595	B	HCl
			3.594	B	H_3PO_4
			3.593	A250	H_3PO_4
Waspaloy	+0.28	3.579	3.578†	B	HCl
			3.589	B	H_3PO_4
			3.587	A50	H_3PO_4
			3.589	A250	H_3PO_4
Inconel X 550	+0.5	3.572	3.588	B	H_3PO_4
			3.590	A50	H_3PO_4
			3.590	A250	H_3PO_4
Inco 700	+0.3	3.572	3.581	B	H_3PO_4
			3.583	A50	H_3PO_4
			3.583	A250	H_3PO_4

* For Ni_3Al, the literature showed 3.557 and 3.560A; the present work showed a standard of 3.561A. For $Ni_3(Al, Ti)$, the literature showed 3.584A, and the present work showed a standard of 3.586A.
† Undoubtedly matrix.
‡ A50: solution treated 2000°F, air cooled, aged 1500°F, 50 hr; A250: solution treated 2000°F, air cooled, aged 1500°F, 250 hr; and B: solution treated 2200°F, air cooled, aged 1600°F, 24 hr.

with a globular, fine grain boundary precipitate and a few irregular, fairly large carbides. After reforging and solution treating, heavy grain growth occurred at 2200° and a duplex grain size resulted from the 1900°F solution treatment.

The photomicrographs at X1000, Figs. 5 to 7, were made with oblique illumination and show a roughened matrix for all heat treated conditions used. If precipitate particles alone are directly responsible for this roughness, then air-cooling did not result in retention of the aluminum and titanium in solution. On the other hand, the roughness may be partially due to an etching effect. A comparison with existing electronmicrographs does not substantiate the hypothesis that the roughening noted in Figs. 5 to 7 is directly due to precipitate particles. Rather, the volume occupied by a precipitate such as Ni_3 (Al, Ti) could not account for the apparent volume in either electronmicrographs or light micrographs by a significant fraction, even if the entire theoretical amount of Ni_3 (Al, Ti) were to form.

Aging at 1200° following the 2200° or 1900°F solution treatment resulted in continuous networks of depleted matrix at the grain boundaries. Fig. 5a illustrates this type of network, which greatly decreased the alloy's ductility in stress rupture.

Stain etching was resorted to in an attempt to identify carbides optically. A successful stain etchant used before in this laboratory was a mixture of NH$_4$OH and H_2O_2. Specimens immersed in this etchant for approximately 1 hr developed a strong blue stain on M_6C, and the other carbides were not affected. This procedure was used on specimens of all four alloys. Table VIII lists the results. As was expected, none of the carbides in Inconel X 550 were stained, since there is no molybdenum or tungsten in this alloy.

Inco 700: The as-received Inco 700 stock had a uniformly fine-grained matrix, a fine grain boundary precipitate, and fairly abundant carbides of regular polyhedral shapes. After reforging, the grain size was not as uniform, and the carbides were more globular. Further, the effect of heat treatment on the reforged bars was significant. Grain growth occurred at 2200°, but the 1900°F solution treatment resulted in fine, equiaxed grains very similar to the as-received condition.

Carbides were fairly abundant for the 1900°F treatment, being small and uniformly scattered through the matrix, visible at X1000, see Fig. 6. A partial resolution of the fine carbides occurred when solution treated at 2200°F, and only larger carbide particles could be seen. This partial resolution effect was observed in M-252 and the other alloys.

Aging at 1200° resulted in a fine grain boundary precipitate after solution treatment at 2200°F, but no change seems to have taken place at the grain boundaries after solution treatment at 1900°F and aging.

Aging at 1600°F after either solution temperature caused a fine, globular grain boundary precipitate to form, and the matrix to be more readily attacked, resulting in roughness very apparent at X1500. No matrix precipitate could be seen at this magnification, however.

Microscopic examination of a stain-etched specimen which had been solution treated at 1900° and aged at 1600°F showed that approximately 70 pct

Table VII. Stress for Selected Rupture Times and Ductility Values at 1500° and 1600°F

Alloy	Heat Treatment, °F		Stress for Rupture in N Hr, Psi				Approximate 100-Hr Rupture Life Ductility	
	Solution	Aging	1	10	100	1000	Reduction in Area, Pct	Elongation, Pct
				At 1500°F				
Inconel X 550	2200	1600	52,000	43,000	31,000	20,000	9	3
	2200	1200	51,000	43,000	31,500	19,000	3	1
	1900	1600	45,000	38,000	24,000	15,000	8	2
	1900	1200	45,000		Very brittle			
Inco 700	2200	1600	80,000	58,000	42,500	31,500	8	5
	1900	1200	64,000	46,000	34,000	25,000	6	4
Waspaloy	2200	1600	71,000	53,000	40,000	29,000	12	5
	2200	1200	70,000	51,000	38,000	27,500	9	3
	1900	1600	65,000	49,000	37,000	27,500	22	8
	1900	1200	77,000	54,000	39,000	27,500	22	6
M-252	2200	1600	78,000	53,000	36,500	25,000	30	10
	1900	1200	75,000	51,000	35,000	24,000	30	14
				At 1600°F				
Inco 700	2200	1600	54,000	39,000	27,000	19,000	15	9
	1900	1200	42,000	28,000	18,000	12,000	21	14
Waspaloy	2200	1600	49,000	36,000	26,000	19,500	18	12
	1900	1200	50,000	35,000	24,000	17,000	24	13
M-252	2200	1600	50,000	35,000	24,000	16,500	25	11
	1900	1200	41,000	30,000	21,500	15,000	24	11

of the larger carbides were M_6C, and 30 pct were Ti (C, N). It is evident that electrolytic extraction procedures on this alloy dissolved much of the M_6C present, since not enough remained in the residues to appear in X-ray diffraction patterns.

Waspaloy: When received, the Waspaloy bar stock was already forged to size. It had a uniform, fine grained microstructure with medium-sized carbide particles and some clusters of very fine carbides.

When solution treated at either temperature the matrix recrystallized, but grain growth was not excessive. The carbide particles were fine and well dispersed, and there was no longer any clustering, see Fig. 7.

The grain boundaries of the solution treated specimens were clear and sharp at X1500, and aging at 1200° after a 2200°F solution treatment did not result in evident precipitation in the grains. The 2200° solution plus 1600°F aging treatment, however, precipitated an almost continuous carbide network at grain boundaries and on twinning planes. There was a smaller amount of discontinuous carbide precipitate at the grain boundaries after a 1900° solution plus 1200°F aging treatment.

When stain etched for carbide identification, three types of carbides could be distinguished. A gray, globular carbide was identified as TiC, comprising about 20 pct of the carbide phase. M_6C, stained deep blue, was almost 60 pct, and a small amount of angular pink Ti (C, N) was the remainder. These identifications were made on a specimen after a 2200° plus 1600°F heat treatment.

M-252: When the as-received M-252 bar stock was examined, it showed the characteristic microstructure of this alloy. The carbides were segregated as bands and clusters, and the irregularity of carbide distribution was severe over the cross sectional area of a ⅞ in. diam bar. The matrix grain size was duplex, medium and fine, with no grain boundary precipitate visible at X1500. Reforging this stock did not significantly alter its microstructure.

After solution treatment and aging, there was a grain boundary precipitate of what appears to be very fine carbides. Comparison of the 2200° solution treated and the 2200° solution treated plus 1600°F aged structures showed this precipitate to occur only on aging. Grain growth at 2200°F was severe, although it appeared to be inhibited by the clusters of carbides. Again, no matrix precipitate could be seen in the aged alloy, and the roughening of the matrix could not be resolved with a light microscope, see Fig. 8.

Carbides identified by stain etching were TiC and M_6C, each composing about one half of the total carbide, see Table VIII. Fig. 9 is a micrograph of the two forms of carbide precipitate at the grain boundaries resulting from solution treating at 2200° and aging at 1600°F.

Discussion and Summary

There is ample evidence that Ni_3 (Al, Ti) or γ' is the aging precipitate in Inconel X 550, Inco 700, and Waspaloy, as it was also shown to be in the more simple Ni-Cr-Ti-Al alloys[1] free of molybdenum, columbium, and cobalt, and essentially free of carbon, after aging from about 1200° to 1600°F for approximately 24 to 250 hr. The evidence for γ' in M-252 is negative, utilizing all the same tools and procedures which detected it in the other alloys.

M-252 is different from the other alloys in that it has a matrix parameter larger than that of γ', the larger size being associated with the high (almost 10 pct) molybdenum content of M-252.

Based on parameter measurements of the matrix and the Ni_3 (Al, Ti) precipitates extracted from aged alloys, there is no reason to expect significant differences during aging in Inconel X 550, Inco 700, and Waspaloy. It is likely that coherency strains may be significant at lower temperatures and for short aging periods, but growth of the precipitate is fairly rapid.

From the various measurements which have been made, it appears that air cooling of sections less than about ½ in. in diam fails to maintain all the aluminum and titanium in solution except possibly in Inconel X 550 cooled from about 1900° but not from 2200°F. It is likely that more severe quenches also fail to keep these elements in solution in Waspaloy and Inco 700.

The severe hardening and embrittlement of Inconel X 550 after the 1900° solution plus 1200°F aging and the relatively small aging response in Inco 700 and Waspaloy support these observations. The more highly alloyed Inco 700 and Waspaloy, which undergo some precipitation of γ' on cooling from the solution temperature, probably avoid embrittlement because they are somewhat overaged prior to the actual aging treatment. Similar overaging of Inconel X 550 by either the 2200° (vs

1900°F) treatment (which results in slower cooling through the aging range), or by deliberate overaging at 1600°, also avoids this embrittlement without loss of strength at 1500°F and with significant improvement in ductility.

M-252, on the other hand, did not show any evidence of γ' precipitation, although absolute proof of its absence cannot be claimed. In spite of this, the 1500°F creep-rupture properties of M-252 are better than those of Inconel X 550 and are similar to those of Waspaloy for the same heat treatments, both alloys showing a relatively poor response to solution and aging for test purposes at 1500° and 1600°F.

Table VIII. Relative Volume Percentage of Carbides, Stain Etched for Identification

		M-252	Waspaloy	Inconel X 550	Inco 700
TiC, pct	(gray)	50	30	80	—
$Ti_4C_2N_2$, pct	(pink)	—	10	20	30
M_xC, pct	(blue)	50	60	—	70
TiN, pct	(gold)	—	—	trace	trace

Definite evidence of carbide precipitation was noted instead in M-252, and this may be adequate to account for the rupture properties in an otherwise solid solution strengthened alloy. In fact, it is wondered whether M-252, Waspaloy, and Inco 700 do not all benefit to an important extent from the carbide precipitation reaction, each of these compositions having appreciable carbon. Inconel X 550, on the other hand, has the lowest carbon content and is free of the M_xC carbide. It is obvious that the results presented point to the desirability of a separate study of the role of carbon in M-252, Inco 700, and Waspaloy. These results do not minimize the importance of the γ' precipitation, but they do indicate that carbide strengthening has a greater importance than has hitherto been anticipated.

Unfortunately, the electrolytic extraction technique is fairly imperfect, both in regard to the γ' phase in certain reagents and to the inability to retain all the M_xC in Inco 700 in other reagents. Where Ni_3 (Al, Ti) has been extracted, the check between several methods of identification has been very valuable.

Acknowledgments

The authors wish to express thanks to the Navy Department, Bureau of Aeronautics, for support of this program and for permission to publish.

References

[1] A. Taylor and R. W. Floyd: The Constitution of Nickel-Rich Alloys of the Nickel-Chromium-Titanium System. *Journal* Institute of Metals, 1951-1952, vol. 80, p. 577.

[2] A. Taylor and R. W. Floyd: The Constitution of Nickel-Rich Alloys of the Nickel-Titanium-Aluminum System. *Journal* Institute of Metals, 1952-1953, vol. 81, p. 25.

[3] A. Taylor and R. W. Floyd: The Constitution of Nickel-Rich Alloys of the Nickel-Chromium-Aluminum System. *Journal* Institute of Metals, 1952-1953, vol. 81, p. 451.

[4] R. Nordheim and N. J. Grant: Aging Characteristics of Nickel-Chromium Alloys Hardened with Titanium and Aluminum. *AIME Trans.*, 1954, vol. 200, pp. 211-218; JOURNAL OF METALS, February 1954.

[5] H. J. Beattie and F. L. VerSnyder: Microconstituents in High Temperature Alloys. *ASM Trans.*, 1953, vol. 45, p. 397.

[6] H. J. Beattie and F. L. VerSnyder: Molybdenum-Dependent Phase Relationships in M-252 Type Alloys. Submitted for publication.

[7] A. H. Geisler: *Precipitation from Solid Solutions of Metals*. John Wiley & Sons, New York, 1951.

Discussion of this paper sent (2 copies) to AIME by Sept. 1, 1957 will appear in AIME *Transactions* Vol. 212, 1958, and in JOURNAL OF METALS, April 1958.

Technical Note

X-Ray Diffraction Study of the Sigma Phase in the Systems Re-Cr, Ru-Cr, and Os-Cr

by R. M. Waterstrat and J. S. Kasper

IN view of the recent findings of a pronounced ordering of atoms in σ phase alloys containing elements of the first long row of the periodic table (and including molybdenum),[1] it is of interest to resolve the question of ordering for σ phases containing second and third-row elements. Examples of the latter have been provided recently by Greenfield and Beck[2] and two of them, Re-Cr and Ru-Cr, would appear to be favorable for a study of ordering by X-ray diffraction methods because of the considerable differences in the scattering factors concerned. In addition, σ phase is found to occur in the Os-Cr system, where the difference in scattering factors is even larger. Accordingly, X-ray powder intensities have been measured in an attempt to learn the nature of the ordering, if any, in these three σ alloys. Since there is no reported work on intermediate phases in the Os-Cr system, an exploratory investigation was made in this system, and it was found that, in addition to the σ phase, the phase with the A-15 or β-W structure also occurs.

R. M. WATERSTRAT and J. S. KASPER are associated with the Research Laboratory, General Electric Co., Schenectady.

TN 399E. Manuscript, Nov. 7, 1956.

Specimen Preparation—The alloys were prepared by compressing mixed powders of −200 mesh size and sintering in an atmosphere of pure dry hydrogen. All alloys were rapidly cooled from the annealing temperature to room temperature in a stream of cold dry hydrogen in a water-cooled chamber. Table I lists the sources and purities of the starting materials, as well as the details of processing for each of the alloys investigated.

Intermediate Phases in the Os-Cr System—In the absence of information on intermediate phases in the Os-Cr system, it was suspected that this system would resemble that of Ru-Cr, where a σ phase, $RuCr_{\sim 2}$[3] and a phase with the A-15 structure, $RuCr_{\sim 3}$,[3, 4] have been identified. Both these phases were found in the Os-Cr system and at compositions

Table I. Materials Used and Method of Preparation

Alloy System	Phases Present	Temperature and Time of Sintering	Intended Composition, Atomic Pct	Chemical Analysis, Atomic Pct	Composition Reported by Greenfield and Beck[2]	Materials Used	Source	Purity, Pct
ReCr	σ	1600°C, 3 hr 1200°C, 24 hr	37 pct Cr	37.5 pct Cr	36.8 pct Cr	Chromium metal powder	Electro Metallurgical Co., Niagara Falls, N. Y.	99.9
RuCr	σ + Ru	1600°C, 1 hr* 1200°C, 3 hr	66 pct Cr	63.5 pct Cr	66 pct Cr	Ruthenium metal powder	Baker and Co. Inc., Newark, N. J.	99.9
OsCr	σ	1600°C, ½ hr 1200°C, 3 hr	63 pct Cr	65.6 pct Cr		Rhenium metal powder	Johnson-Matthey No. 830, Jarrell-Ash Co., Boston	99.99
OsCr	A-15 + Cr	1200°C, 3hr	74 pct Cr	Not analyzed		Osmium metal powder	Charles Hardy Inc., New York	99.5
OsCr	σ + A-15	1600°C, 1 hr 1200°C, 3 hr	69 pct Cr	Not analyzed				

* This alloy was found to have melted during the course of its preparation.

Table II. Os-Cr Alloy, Cr_3Os + Cr, A-15 Type Structure, Ordered; $a_o = 4.677$Å

hkl	Observed, d (A)	$I_{observed}$	$I_{calculated}$
110	3.345	M*	15
200	2.358	MS	9
210	2.101	MS	5
Cr (110)	2.068	M	
211	1.918	S	19
220	1.658	W	2
310	1.483	M	4
Cr (200)	1.463	W	
222		—	0
320	1.298	MS	2
321	1.250	VS	31
400	1.191	M	16
Cr (211)	1.172	S	

* M means medium; S, strong; W, weak, and V, very.

Table III. Comparison of Intensities

hkl	$OsCr_3$ Observed d Values	$OsCr_3$ Calculated Intensities	Observed Intensities: $OsCr_3$, $a_o = 9.107$Å, $c_o = 4.696$Å	$RuCr_3$, $a_o = 9.068$Å, $c_o = 4.704$Å	$ReCr_3$, $a_o = 9.290$Å, $c_o = 4.831$Å
110		0	—	—	—
200		0	—	—	—
101, 210	4.126	2	3	—	2
111		0	—	—	1
220		0	—	—	—
211		0	—	—	—
310		0	—	—	—
221		0	—	—	—
301, 320		0	—	—	2
311	2.472	4	8	4	8
002	2.358	13	15	9	12
400		0	—	—	—
321		0	—	—	—
112, 410	2.217	53	45	52	47
330	2.151	22	15	26*	20
202	2.092	21	15	13	20
212, 420	2.037	39	30	26	35
411	2.002	60	67	70	62
331	1.954	30	37	35	35
222	1.899	7	8	9	8

* Contains Ru (002).

that were approximately those in the Ru-Cr system. (Their X-ray diffraction patterns are given in Tables II and III.) The composition of the pure σ phase specimen corresponds quite well to the formula $OsCr_3$. The alloy with the A-15 structure contained some chromium and was not analyzed. It was presumed that its formula was $OsCr_3$, since the A-15 phases generally occur at the stoichiometric composition, A_3B. The intensity agreement for this phase, assumed to be $OsCr_3$ and ordered, is not very good even allowing for absorption effects. Further work would be necessary to ascertain the exact composition and degree of ordering, but there is no doubt that there is an A-15 phase of approximate formula $OsCr_3$. This phase is apparently stable at 1200°C, while $RuCr_3$ occurs only below 900°C.[3, 4]

It is noteworthy that the σ phases of the two neighboring elements, osmium and rhenium, differ so markedly in their chromium contents, the respective formulas being $OsCr_3$ and Re_2Cr.

X-Ray Intensities of the σ Phases—Portions of the X-ray patterns for the three σ phases, $RuCr_3$, $OsCr_3$, and Re_2Cr, are given in Table III, including the interplanar spacings of $OsCr_3$. The patterns were obtained from powdered specimens in a cylindrical camera of 5 cm radius. Intensities were estimated by visual comparison with a standard intensity scale on film. No absorption corrections were applied. The calculated intensities of Table III were made with the atomic parameters of σ Co-Cr as given in ref. 1.

The salient feature of the intensity information is that in all three cases there is little deviation of observed intensities from those to be expected for a random distribution of the component atoms. While the intensity comparisons in Table III may not be extremely good, the main point is that there is no positive indication of highly-ordered atomic distributions. Various ordered models were considered and found to give significantly larger intensity disagreements than the disordered model, particularly in calling for measurable intensities where none could be detected. The data are not accurate enough to decide whether there may be slight preferences of the respective atoms for different atomic sites, but they suffice to demonstrate that in these three cases a parallel to the ordering effects found in σ phases containing only first-row elements does not exist. Thus, since ruthenium and osmium occur in the same group as iron, they might be expected to occupy preferentially the sites of lowest coordination (coordination number 12) as does iron in σ FeCr, especially since the compositions of $RuCr_3$ and $OsCr_3$ are compatible with such a distribution. This kind of ordering would not produce a satisfactory intensity agreement.

It would seem necessary to do single crystal studies to ascertain fully the nature and degree of ordering in these three σ phases.

References

[1] J. S. Kasper and R. M. Waterstrat: Ordering of Atoms in the Sigma Phase. *Acta Crystallographica*, 1956, vol. 9, p. 289.

[2] P. Greenfield and P. A. Beck: Intermediate Phases in Binary Systems of Certain Transition Elements. *AIME Trans.*, 1956, vol. 206, p. 265; JOURNAL OF METALS, February 1956.

[3] E. Raub and W. Mahler: Die Legierungen des Chroms mit Platin, Iridium, Rhodium, und Ruthenium. *Ztsch. für Metallkunde*, 1955, vol. 46, p. 210.

[4] E. Raub: Alliages des metaux de la famille du Platine. *Revue de Metallurgie*, 1955, vol. 52, p. 429.

Diffusion in Gold and Au-Ag Alloys

The self-diffusion coefficients of gold in pure gold and alloys of gold and silver have been measured over a range of temperatures. Chemical interdiffusion coefficients have been measured on pure metal and incremental couples, but are of lower accuracy because of the development of porosity. The results are compared with earlier work and internally on the basis of Darken's equations.

by H. W. Mead and C. E. Birchenall

SELF-DIFFUSION in pure gold has been studied by Sagrubsky,[1] McKay,[2] Gatos and coworkers,[3,4] and Okkerse.[5] Sagrubsky used a sectioning technique but reported results far lower than any of the others. The work seems to be carefully done, and it appears that a factor of 60 must have been omitted in his calculations or the units misstated by an equivalent amount. McKay used a surface activity method, and Gatos and Kurtz, following Gatos and Azzam, applied autoradiography to the measurement of activity on an oblique section through the diffusion zone. These two investigations agree well with each other but give results below those reported here. Okkerse employed a very careful sectioning technique.

Chemical interdiffusion in Au-Ag alloys has been measured under several concentration conditions. Average values of the diffusion coefficient for the range of 0 to 18 atomic pct Au were obtained by Braune.[6] Since the diffusion coefficient probably varies markedly over this range, the values may not be too useful. Also, a plot of these data suggests that grain boundary contributions may have been appreciable at the lowest temperature employed. Ebert and Trommsdorff[7] give average values for 0 to 9 atomic pct Ag, and Johnson[8] reports average values for 45 to 55 atomic pct Au. Johnson also measured silver and gold self-diffusion coefficients in 49.2 atomic pct Au alloys, and self-diffusion in pure silver.[9] The self-diffusion of gold in pure silver has been determined by Jaumot and Sawatsky.[10] Other measurements which do not cover a range of temperature or are of low precision are not mentioned in this account since a review by Kubaschewski is available.[11]

This contribution reports diffusion coefficients for self-diffusion in gold, self-diffusion of gold in Au-Ag alloys, and chemical diffusion in Au-Ag alloys. Although it had been intended to obtain silver self-diffusion data in the alloys it now appears unlikely that these measurements can be done soon, so a table has been worked out for a self-consistent scheme of diffusion coefficients which should not be too far from the true values.

H. W. MEAD, Member AIME, is Technical Officer, Metals Division, Imperial Chemical Industries Ltd., Birmingham, England, and C. E. BIRCHENALL, Member AIME, is Associate Professor of Chemistry, Princeton University, Princeton, N. J.

TP 4454E. Manuscript, July 12, 1956. New Orleans Meeting, February 1957.

Experimental Details

Experiments on pure metals were conducted using fine gold of 99.99+ pct Au and silver of the same purity. Alloys were prepared by melting the two metals together in a graphite crucible in vacuo and allowing the slug to solidify in the crucible. After machining to a cylinder about 0.85 in. diam each slug formed one half of a diffusion couple. Compositions were determined later by analyzing chips taken from the extremities of the diffusion zones. The gold used in the preparation of alloys was sometimes pure gold but was normally either in the form of clean pickled alloy from previous experiments or gold recovered by oxalic acid precipitation from warm aqueous solution. Chips from the various stages of experimentation were dissolved in aqua regia and the solution taken to low bulk, diluted with water, and again taken to low bulk before diluting for the precipitation. This precipitated gold contained a small amount of silver as the only impurity detectable by spectrographic analysis. Disks for use in diffusion couples had opposite plane faces abraded on emery paper as far as zero grit, were annealed for 12 hr at 900°C in argon, and had one face of each disk polished to 000 emery paper.

Radioactive gold was plated at about 2 ma per sq cm from a small volume of cyanide solution containing 1 mg of inactive gold as a carrier. Specimens were freshly abraded on 4/0 emery paper immediately prior to plating.

In the case of the active couples disks of a similarly prepared but unplated alloy or pure metal were placed on top and welded to the active disk. With the concentration couples disks of different compositions were welded. Welding was performed after a pressure of 5,000 lb had been applied at

room temperature to *set* the couple in an apparatus and manner similar to that used by daSilva and Mehl.[12] Three strips of tantalum foil 0.002 in. thick were placed on the flat surface of one disk near the rim and these served to locate the weld interface after diffusion.

After rapid heating a time of ½ hr at 850°C was allowed for welding. A dummy run using a hollow specimen containing a thermocouple enabled the specimen temperature to be related to that of the control couple. Corrections were later applied to the time of the diffusion anneal to allow for diffusion during welding, it being assumed that diffusion commenced upon the application of pressure. The largest correction applied was one of 3 pct. Many were negligible.

Table I. Diffusion Coefficients for Gold Self-Diffusion in Au-Ag Alloys

Alloy	Diffusion Temperature, °C	Diffusion Time, Sec x 10^{-5}	D, Sq Cm per Sec
99.99+ pct Au	992	2.538	5.97×10^{-8}
	905	3.837	1.56×10^{-8}
	809	2.566	2.87×10^{-10}
	717	19.62	5.27×10^{-11}
75 atomic pct Au*	992	2.409	4.25×10^{-8}
	910	0.9306	1.26×10^{-8}
	905	3.837	1.10×10^{-8}
	897	6.992	9.28×10^{-9}
	810	5.136	2.62×10^{-9}
	809	13.58	2.06×10^{-9}
	721	10.18	3.88×10^{-11}
	717	19.62	5.44×10^{-11}
25 atomic pct Au†	910	0.9306	6.80×10^{-9}
	905	3.837	7.93×10^{-9}
	897	6.992	7.53×10^{-9}
	810	5.136	1.55×10^{-9}
	809	2.566	1.58×10^{-9}
	717	19.62	2.27×10^{-11}
	656	24.74	5.71×10^{-12}
99.99+ pct Ag	905	3.837	9.57×10^{-9}
	897	6.992	8.51×10^{-9}
	810	5.136	1.96×10^{-9}
	717	19.62	3.20×10^{-11}
	656	24.74	4.08×10^{-12}

* Couples analyzed at average of 82.94 wt pct Au.
† Couples analyzed at average of 38.08 wt pct Au.

Diffusion anneals were performed with one to four specimens placed inside a graphite crucible. One end of the crucible contained a well into which a thermocouple protection tube reached after passing through a Wilson seal on the end of the furnace tube. At the beginning of a diffusion run this tube was used to push the crucible from a cool part of the furnace to the hot zone in as short a time as was possible without danger of cracking the furnace tube. Before commencing the run the furnace was evacuated and flushed three times with argon, the last charge being allowed to remain in during the anneal at a slight positive pressure. Temperatures were taken during the heating period at least daily and more frequently during the case of short runs by means of a Pt—Pt-10 pct Rh thermocouple standardized at frequent intervals against a similar couple calibrated at the National Bureau of Standards. Diffusion temperatures were maintained to ±2°C. At the end of an anneal the Wilson seal was broken and the crucible drawn out of the furnace and allowed to cool in air.

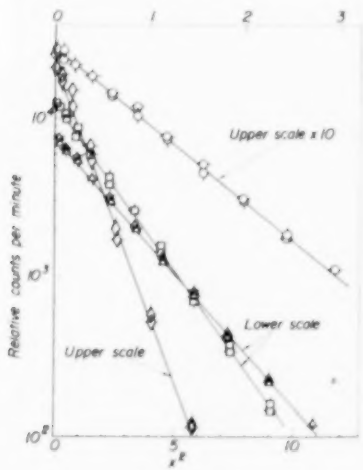

Fig. 1—Distribution of activity in four typical diffusion couples after annealing. Cross represents the distance from the weld in inches x 10^{-3}; circle, pure gold annealed 2.538 x 10^5 sec at 992°C; triangle, 75 pct Au annealed 3.837 x 10^5 sec at 905°C; diamond, 25 pct Au annealed 1.962 x 10^5 sec at 717°C; and square, pure silver annealed 3.837 x 10^5 sec at 905°C. Flags distinguish points taken from different sides of welds.

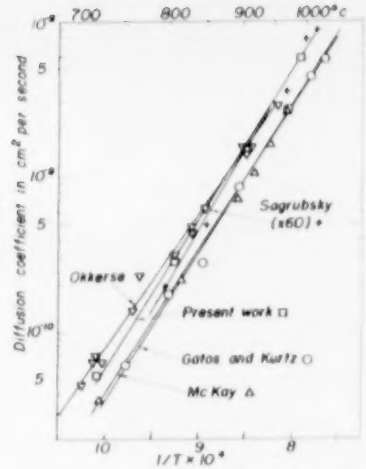

Fig. 2—Collected results of measurements of self-diffusion in pure gold.

Before aligning the specimen for machining the circumference was skimmed to a sufficient depth to expose the tantalum foils previously placed in the weld. These were observed at X40 through a microscope rigidly attached to the toolpost of the lathe after the alignment of the specimen was adjusted until, on rotating the lathe chuck, the center line of all three foils coincided with a hair line. After reducing the specimen diameter to 0.65 in. and removing sufficient material, 32 cuts of 0.002 in. or 0.003 in. thickness normal to the axis were taken for the determination of activity or chemical composition. Thickness of cuts was checked frequently by means of a depth micrometer.

Activity was determined by Geiger counting and, as the chips were too irregular to be counted directly, they were melted and rolled to foil. A circle 0.25 diam was punched from each foil, weighed, and cemented to an ashing dish suitable for insertion into an automatic sample changer. The weight of each foil was used in correcting for absorption of radiations within the sample. The correction was determined empirically. Composition was determined by standard gold assay methods carefully adapted to small samples.

Results

The raw counting data were corrected for background, coincidence, and absorption losses, and for decay, using a half-life period of 2.69 days. Under the present experimental conditions, when activity is plotted against the square of the distance from the weld, a straight line should result if the distribution of the activity is governed by volume diffusion. That this was so may be seen from Fig. 1, which illustrates four typical activity-penetration curves. The

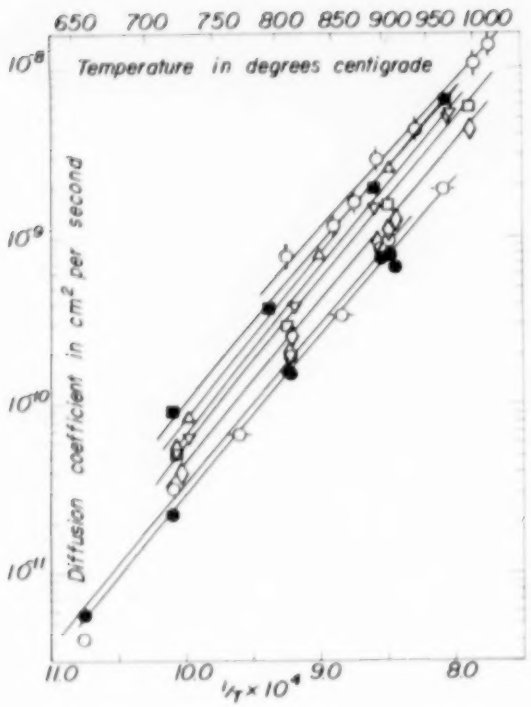

Fig. 3—Diffusion measurements in Au-Ag alloys. Open square represents self-diffusion of gold in pure gold; diamond, self-diffusion of gold in 75 pct Au; open circle, self-diffusion of gold in 99.99 + pct Ag; closed circle, self-diffusion of gold in 25 pct Au; circle with horizontal lines, self-diffusion of gold in 49.2 pct Au[5] (the last two sets of data define the same line); triangle, self-diffusion of silver in pure silver;[7] inverted triangle, self-diffusion of silver in 49.2 pct Au;[7] closed square, chemical interdiffusion in 45 to 55 pct Au;[5] and circle with vertical lines, chemical interdiffusion in 100 to 91.2 pct Au.

method of calculating diffusion coefficients from these curves has been described fully and need not be repeated here.[5] Diffusion coefficients were derived from the penetration curves of the incremental chemical diffusion couples by the method of Matano.[12]

The accuracy with which D can be determined from the curve depends upon the product Dt. For most experiments this was 10^{-7} sq cm or greater, but for experiments at the lower temperatures on pure silver and the silver-rich alloy smaller values were obtained. Inaccuracies due to temperature measurement might amount to 5 pct, and time should be less than 1 pct. In the case of alloys the possibility of variations in compositions is added. Average composition of the alloy couples varied by about 1 pct from the mean, which could introduce an error into each determination of D of up to about 3 pct, depending upon temperature.

It appears then that errors in D of up to about 10 pct may be accounted for with rather larger errors to be expected for the low temperature runs. The departures from the mean found for specimens annealed at nearly the same temperature range up to 17 pct at the lower temperatures.

The results contained in Table I have been plotted in Figs. 2 and 3 and straight lines have been drawn to represent the relationship between log D and $1/T$. The equations of these lines were determined by the method of least squares and the constants related to the equation

$$D = D_o e^{-Q/RT}$$

where Q is the activation energy, D_o the frequency factor, R the gas constant, and T the absolute temperature.

Values found for D_o and Q are presented in Table II. Standard errors in Q are near a mean of ±1.6 kcal per mole. Evidently the extra error in individual D's produced by compositional variations in the alloys was compensated for by the greater number of tests run. Errors produced in D_o by this variation in Q may alter its value by as much as a factor of two greater or smaller.

Fig. 2 is a plot of the logarithm of the diffusion coefficient vs the reciprocal of the absolute temperature for the published data on gold self-diffusion. Sagrubsky's results have been multiplied by a factor of 60, which brings them into the range of the other measurements. The present results show nearly the same slope as the Gatos and Kurtz line. It is not clear whether a constant error could have been introduced into their values by the use of the Steigman, Shockley, and Nix[13] approximation for surface activity, which neglects the fact that some of the radiation does not emerge normal to the surface. When Geiger counting with an absorbing window and small subtended angle is used this factor is negligible, but autoradiography should use oblique rays very efficiently.

Present diffusion coefficients agree best with the careful measurements of Okkerse, but his activation energy is appreciably lower. The reason for this difference in temperature dependence is not known.

Table II. Diffusion Constants for Gold Self-Diffusion in Au-Ag Alloys

Alloy	D_o in Sq Cm per Sec	Q, Kcal per Mole
Pure Au	0.14	42.9 ±1.6
75 atomic pct Au	0.041	40.7 ±1.6
25 atomic pct Au	0.064	42.8 ±1.6
Pure Ag	0.41	46.4 ±1.6

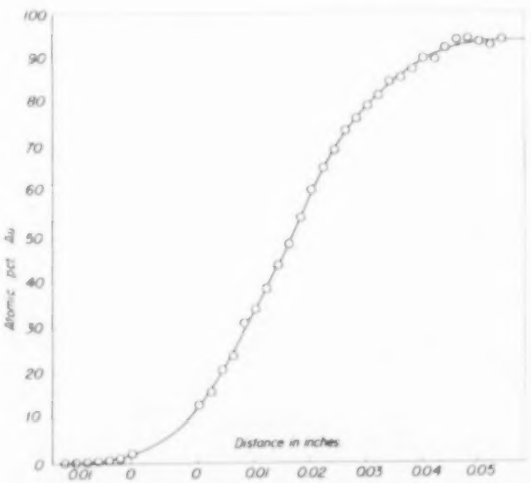

Fig. 4—Penetration curve for specimen D-3[12] for chemical interdiffusion of silver and a Ag-93.8 atomic pct Au alloy at 925°C.

The only other type of measurement to compare with the results cited above are the studies on the quenching in and annealing out of vacancies in gold wires which Kauffman and Koehler[16] followed by electrical resistance changes. They initially deduced an activation energy for self-diffusion in gold of 45.2 ±1.4 kcal per g atom. This is considerably above Okkerse's 39.4 ±0.3, but it is in reasonable agreement with the present value of 45.3 kcal per g atom. A new measurement[16] of the energy of formation of vacancies by an improved quenching procedure yields a lower value and brings the improved result into agreement with Okkerse.

Fig. 3 is a similar plot for the chemical diffusion data, for self-diffusion of gold and silver in the Au-Ag alloys and in the pure metals. Values read from this figure at 894°C are used in Fig. 4, where the diffusion coefficients are plotted against concentration. It should be noted that the new data for gold self-diffusion in the alloys fit smoothly with Johnson's point at 49.2 atomic pct Au, and that the values of 0.41 and 46.4 for D_o and Q agree well with those of 0.26 and 45.5 obtained by Jaumot and Sawatzky. Their new results[10] are indistinguishable from the lowest line in Fig. 3. The chemical diffusion data include an average value by Ebert and Trommsdorf for 91.2 to 100 pct Au and new results giving diffusion coefficients as a function of concentration

Table III. Self-Consistent Set of Diffusion Coefficients for Au-Ag Alloys at 894°C

N_{Au}	$1 + N_{Ag}\frac{d\ln\gamma_{Ag}}{dN_{Ag}}$	$D^*_{Au} \times 10^5$	$D^*_{Ag} \times 10^5$	$D \times 10^5$
1.0	1.00	1.38	(2.6)	2.6
0.9	1.11	1.25	(2.4)	{2.5}
0.8	1.25	1.08	(2.1)	{2.4}
0.7	1.40	0.93	(1.9)	{2.3}
0.6	1.58	0.78	(1.8)	{2.2}
0.49	1.76	0.67	1.6	(2.0)
0.4	1.91	0.64	{1.6}	(1.9)
0.3	1.95	0.64	{1.6}	(1.8)
0.2	1.64	0.68	{1.7}	(1.4)
0.1	1.29	0.75	{1.9}	(1.1)
0.0	1.00	0.80	2.1	(0.80)

for the ranges 35 to 60 and 0 to 100 pct Au. The last couple developed extensive porosity near the weld interface, which caused irregular machining in this region. Uncertainty in the distance measurements was introduced, so the two parts of the curve were extrapolated together on a probability plot. A sample penetration curve for specimen D-3 interdiffused at 925°C[17] is shown in Fig. 4. The nature of the curve fitting and the precision of the chemical analyses may be judged from this plot. The difficulties associated with the porous region should account for the fact that the mid-range results lie considerably below the values obtained on incremental couples.

Combining the data of Fig. 5 with the thermodynamic activities for the Au-Ag system as correlated by McCabe, Schadel, and Birchenall,[17] and using the equation derived by Darken[18]

$$D = \left(N_{Ag} D^*_{Au} + N_{Au} D^*_{Ag}\right)\left(1 + N_{Ag}\frac{d\ln\gamma_{Ag}}{dN_{Ag}}\right)$$

a reasonably self-consistent set of values of the chemical and self-diffusion coefficients has been worked out for diffusion conditions in which large amounts of porosity are not developed. In the equation D is the chemical interdiffusion coefficient,

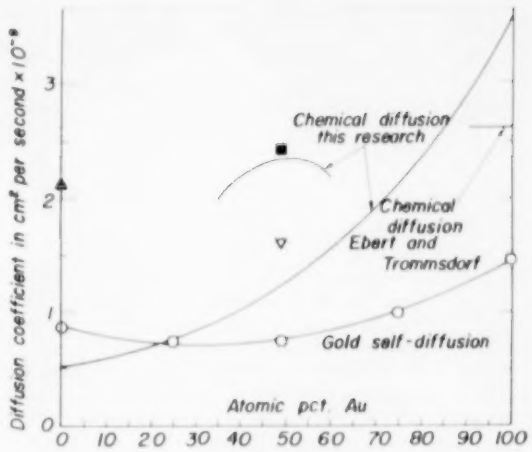

Fig. 5—Dependence of diffusion in Au-Ag alloys on concentration at 894°C. The gold self-diffusion data are from Fig. 2. Closed square represents chemical interdiffusion average for 45 to 55 pct Au,[17] inverted triangle, silver self-diffusion in 49.2 pct Au,[17] and triangle, silver self-diffusion in pure silver.[9]

D^* is the self-diffusion coefficient at atom fraction N in the alloy, and γ is the thermodynamic activity coefficient. The results of the calculations are summarized in Table III. Since the data were not complete, it was chosen to estimate those quantities for which the equation is least sensitive at the particular composition. The estimated values of D are in braces; the calculated values are in parentheses. Reasonable consistency is found. The only large deviations seem to be associated with copious porosity.

Acknowledgments

This work was done in the Metals Research Laboratory of the Carnegie Institute of Technology under the sponsorship of the Office of Naval Research. The authors appreciated discussions with R. F. Mehl in the course of the work. The Au^{198} was obtained from the Oak Ridge National Laboratory with the approval of the Isotopes Div., U. S. Atomic Energy Commission.

References

[1] A. Sagrubsky: *Physikalische Ztsch.* U.S.S.R., 1937, vol. 12, p. 118.
[2] H. A. C. McKay: *Trans. Faraday Soc.*, 1938, vol. 34, p. 845.
[3] H. C. Gatos and A. D. Kurtz: *AIME Trans.*, 1954, vol. 200, p. 616; JOURNAL OF METALS, May 1956.
[4] H. C. Gatos and A. Aztam: *AIME Trans.*, 1952, vol. 194, p. 497; JOURNAL OF METALS, April 1952.
[5] B. Okkerse: *Physical Review*, 1956, vol. 103, p. 1246.
[6] H. Braune: *Ztsch. für physikalische Chemie*, 1924, vol. 110, p. 147.
[7] H. Ebert and G. Trommsdorf: *Ztsch. für Elektrochemie und angewandte physikalische Chemie*, 1950, vol. 54, p. 294.
[8] W. A. Johnson: *AIME Trans.*, 1942, vol. 147, p. 331; METALS TECHNOLOGY, February 1942.
[9] W. A. Johnson: *AIME Trans.*, 1941, vol. 143, p. 107; METALS TECHNOLOGY, January 1941.
[10] F. E. Jaumot, Jr., and A. Sawatsky: *Journal of Applied Physics*, 1956, vol. 27, p. 1186.
[11] O. Kubaschewski: *Trans. Faraday Soc.*, 1950, vol. 46, p. 713.
[12] L. C. C. daSilva and R. F. Mehl: *AIME Trans.*, 1951, vol. 191, p. 155; JOURNAL OF METALS, February 1951.
[13] C. Matano: *Journal of Physics*, Japan, 1933, vol. 8, p. 109.
[14] J. Steigman, W. Shockley, and F. C. Nix: *Physical Review*, 1939, vol. 56, p. 13.
[15] J. W. Kauffman and J. S. Koehler: *Physical Review*, 1955, vol. 97, p. 555.
[16] J. E. Bauerle, C. E. Klabunde, and J. S. Koehler: *Physical Review*, 1956, vol. 102, p. 1182.
[17] C. L. McCabe, H. M. Schadel, Jr., and C. E. Birchenall: *AIME Trans.*, 1953, vol. 197, p. 709; JOURNAL OF METALS, May 1953.
[18] L. S. Darken: *AIME Trans.*, 1948, vol. 175, p. 184; METALS TECHNOLOGY, January 1948.

Discussion of this paper sent (2 copies) to AIME by Sept. 1, 1957 will appear in AIME *Transactions* Vol. 212, 1958, and in JOURNAL OF METALS, April 1958.

Constitution of Delta-Phase Alloys Of the System U-Zr-Ti

The ternary section between the intermediate δ-phase alloys of the U-Zr and U-Ti systems has been investigated. A constitutional diagram for the section, ranging from U-74 atomic pct Zr to U-35 atomic pct Ti, is proposed. Thermal, metallographic, and X-ray data were obtained for alloys in this composition range. The section exhibits features of a quasibinary system in that only one and two-phase regions were found at the temperatures investigated. No evidence for a three-phase region or a new phase, not found in the binary systems, was indicated. At elevated temperatures the three components exhibited complete solubility, to form the body-centered-cubic γ phase, decomposing at about 560°C to the U-Zr and U-Ti δ phases in an apparent eutectoid reaction.

by H. A. Saller, F. A. Rough, A. A. Bauer, and J. R. Doig

UNIQUE among uranium alloy systems are the U-Zr, U-Ti,and U-Mo binary systems, in that an intermediate phase, of limited solubility range, exists in each system.

These intermediate phase alloys offer a promising field of investigation, both as binary alloys and as ternary alloy combinations. While a limited amount of work has been done on the binary alloys, none has been done on ternary combinations of these alloys.

As a possible prelude to more intensive investigation of these systems, a study of the phase relationships between the δ phases of the U-Zr and U-Ti systems was undertaken.

The solid-state portions of the binary constitutional diagrams for the U-Ti,[1] Zr-Ti,[2] and U-Zr[3] systems are shown in Fig. 1. The solid to liquid transformations are not shown, as these transformations were not studied in the ternary system.

The phase designations employed are based upon those shown in the uranium constitutional diagrams. The crystal structures of the various phases are given in Table I.

Experimental Materials and Methods

The ternary section presented is based upon the results of thermal, metallographic, and X-ray analyses of a series of alloys ranging in composition between the δ phases of the U-Zr and U-Ti systems (U-74 atomic pct Zr to U-35 atomic pct Ti). After preparation of the alloys, thermal data were obtained. On the basis of these data, specimens were heat treated and examined metallographically. Specimens were then selected from those heat treated for X-ray determination of the phases present in what were considered critical phase regions.

Alloy and Specimen Preparation—Alloys for this investigation were prepared from selected as-reduced uranium and crystal-bar zirconium and titanium. For nominal compositions, see Table II.

Charges were arc melted from five to seven times under a helium atmosphere, finally being cast into wire-bar form for fabrication. A zirconium getter button was used to clean the furnace atmosphere prior to melting.

The alloys were homogenized 20 hr at 900°C and furnace cooled. A portion of each bar was then removed for thermal analysis; the remainder was saved for fabrication.

Alloys 8 through 14 were placed in steel tubes along with zirconium getter chips and, after flushing with argon, the tubes were welded shut and rolled at 1500°F to a 50 pct reduction in diam.

The remaining alloys were annealed 24 hr at 1100°F to insure transformation of the γ phase to the δ-U_2Ti phase and were then hot rolled from a salt bath.

Attempts to roll alloys 6 and 7 at 1100°F were unsuccessful. Following this, attempts were made to roll pieces of alloys 1 through 5, which had cracked rather severely during casting, at 1200°F, but these efforts were also unsuccessful. These alloys were, therefore, further treated in their cast and homogenized condition.

All alloys were pickled to remove oxide formed during rolling.

Thermal data were obtained on these alloys by conventional differential thermal analysis at a heating rate of 3°C per min, and by a high-speed heating method at rates of approximately 10°C per sec. For the latter method of analysis, a 36-gage Chromel-Alumel thermocouple is spot welded between two slivers of alloy, the sandwich being en-

H. A. SALLER, F. A. ROUGH, Associate Member AIME, A. A. BAUER, Junior Member AIME, and J. R. DOIG are associated with the Battelle Memorial Institute, Columbus, Ohio.

TP 4451E. Manuscript, Aug. 23, 1956. New Orleans Meeting, February 1957.

closed in a platinum envelope. The sandwich is then inserted in a small wire coil and is heated *in vacuo*. The heating curve is obtained on a high-speed recorder. Data were obtained on all alloys by this method.

Differential data were obtained on alloys 4 through 14. Bars of the other compositions were too badly cracked for the necessary machining to obtain a specimen.

Heat Treatment, Metallography, and Hardness Measurements—Specimens for heat treatment were cut from homogenized or homogenized and rolled bars. They were annealed at temperatures based upon the results of thermal analysis in vacuum furnaces under a vacuum of 5 x 10^{-6} mm Hg or less. All specimens examined after heat treatment appeared to be homogeneous.

Heat-treated specimens were mounted in Bakelite, ground wet through 600-grit paper, and were polished on Forstmann's cloth with Linde A abrasive and 10 pct oxalic acid solution.

Two types of etchant solutions were used for etching these alloys. Both were applied by swabbing. One solution was lactic and nitric acid plus hydrofluoric acid in the ratios 30 cu cm:30 cu cm:10 drops and 50 cu cm:50 cu cm:6 drops. Both ratios were used on alloys 6 through 14, the first concentration ratio on those alloys which were richest in zirconium and the latter concentration on those with higher titanium compositions. The other solution utilized was 100 cu cm of 10 pct oxalic acid solution plus 10 drops of HF. This etchant was used on the titanium-rich compositions, alloys 1 through 5.

A slight overlap of useful composition range of these etchants occurred.

X-Ray Analyses—Selected metallographic specimens were submitted to X-ray analysis. The specimens selected had structures which were too fine to permit identification of the phases present by metallography alone.

Each of these specimens was examined on the metallographic surface by spectrometer methods. As an additional check, some of these samples were made into sliver samples for examination in the Debye camera. These sliver specimens were rough sawed and ground to cone shape and then etched to a sharp point.

Table I. Crystal Structure of Phases in the U-Zr-Ti System

Phase Designation	Crystal Structure
α	Orthorhombic
β	Tetragonal
γ	Body-centered-cubic
δ U-Zr	Pseudocubic
δ U-Ti	Hexagonal
ϵ	Hexagonal

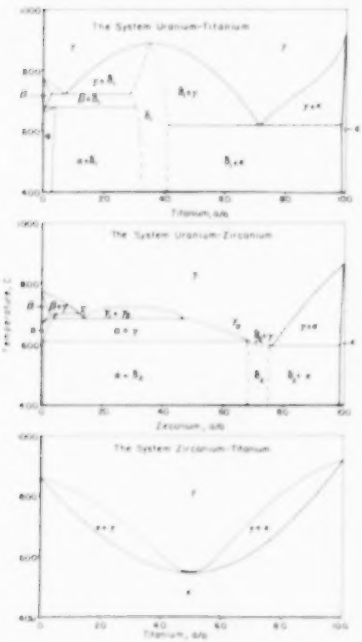

Fig. 1—Solid-state portions of U-Ti, U-Zr, and Zr-Ti binary systems.

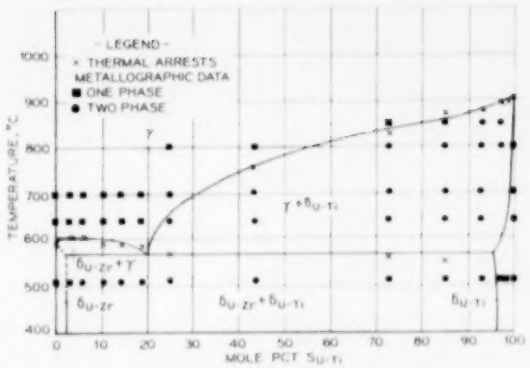

Fig. 2—Proposed ternary section between U-74 atomic pct Zr and U-35 atomic pct Ti.

Table II. Nominal Compositions and Thermal Analysis Results

Alloy	Nominal Composition (Balance Uranium), Atomic Pct: Zirconium	Nominal Composition (Balance Uranium), Atomic Pct: Titanium	Mole Pct δ U-Ti in U-35 Pct Ti	Differential Arrests, °C: Heating	Differential Arrests, °C: Cooling	High-Speed Heating Arrests, °C
1	0	35	100	—	—	908
2	1	34.5	98.7	—	—	896
3	2	34	97.3	—	—	890
4	5	32.5	93.1	—	—	878
5	10	30	85.8	879	550, 818	872
6	20	25.5	73.0	560, 846	561, 753	565, 826
7	40	16	45.8	567, 767	571, 652	577, 754
8	55	9	25.6	588	591	575
9	60	6.5	18.6	585	590	589
10	63	5	14.4	590	595	583
11	66.5	3.5	10.0	591	596	581
12	69.5	2	5.7	605	610	598
13	71.5	1	2.9	604	604	603
14	74	0	0	595	599	601

Experimental Results

The tentative ternary section between the δ phases of the U-Zr and U-Ti systems (U-74 atomic pct Zr to U-35 atomic pct Ti) is shown in Fig. 2. The section exhibits features of a quasibinary section in that only one and two-phase regions appear throughout the section. The $\gamma + \delta$ U-Zr phase region is inferred from thermal data and its occurrence in the U-Zr diagram. Metallographic and X-ray data have established the existence of the other phase fields.

The γ phases of all three systems are isomorphous at elevated temperatures, decomposing at about 560°C. Below this temperature, the two δ phases are in equilibrium with one another.

Thermal Data—The results of thermal analysis are listed in Table II. Heating data are also shown plotted in Fig. 2.

a) U-5 atomic pct Zr-32.5 atomic pct Ti at 850°C, δ U_2Ti plus γ.

b) U-20 atomic pct Zr-25.5 atomic pct Ti at 850°C, γ.

c) U-5 atomic pct Zr-32.5 atomic pct Ti at 800°C, δ U_2Ti plus γ.

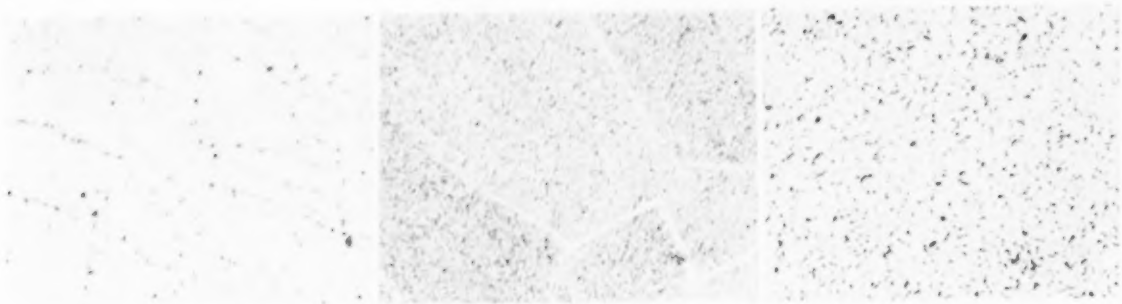

d) U-55 atomic pct Zr-9 atomic pct Ti at 640°C, δ U_2Ti plus γ.

e) U-40 atomic pct Zr-16 atomic pct Ti at 640°C, δ U_2Ti plus γ.

f) U-5 atomic pct Zr-32.5 atomic pct Ti at 640°C, δ U_2Ti plus γ.

g) U-69.5 atomic pct Zr-2 atomic pct Ti at 510°C, δ U-Zr plus δ U_2Ti.

h) U-20 atomic pct Zr-25.5 atomic pct Ti at 510°C, δ U-Zr plus δ U_2Ti.

i) U-2 atomic pct Zr-34 atomic pct Ti at 510°C, δ U_2Ti.

Fig. 3—Microstructure of heat treated and water-quenched U-Zr-Ti alloys. X250. Reduced approximately 25 pct for reproduction.

The differential data are considered more precise, with respect to the temperatures obtained for the low temperature transformation, than the data obtained by the high-speed heating method. However, where data were obtained for the higher temperature transformation, those obtained by the high-speed heating method are regarded as more reliable. The values recorded represent the end of transformation as evidenced by a sharp break in the heating curve and an increase in the rate of temperature change. The change in the differential curves was neither as pronounced nor as reproducible.

Although variations are observed in the values obtained by the two methods, these variations are quite small and the results by the two methods are in substantial agreement.

Metallographic Data—The results of metallographic examination are plotted in Fig. 2. These data were obtained for the following heat treatments, in each case followed by a water quench: 670 hr at 510°, 170 hr at 640°, 100 hr at 700°, 20 hr at 800°, and 20 hr at 850°C.

Typical structures of the γ, γ+δ U_2Ti, and the δ U-Zr + δ U_2Ti phase regions are shown in Fig. 3. All the structures are described by the captions appearing beneath them. However, a few are worthy of comment.

The second phase appearing in Fig. 3d could not be identified metallographically but was identified by X-ray diffraction methods as δ U_2Ti. Similarly, the second phase appearing in the structure shown in Fig. 3g was identified during X-ray examination as δ U_2Ti, indicating that the solubility of titanium in the U-Zr δ phase is very limited.

Fig. 3i shows single-phase δ U_2Ti, maximum solubility of zirconium in this phase being observed at this temperature.

It should be noted that a second phase, ε (α-zirconium), appeared in a number of the zirconium-rich alloys annealed at 640° and 700°C, although

these specimens are indicated as single phase in Fig. 2. However, the appearance of this phase is a result of oxygen contamination rather than titanium additions. Low levels of oxygen content are known to restrict the γ region severely, oxygen stabilizing the $\gamma+\epsilon$ phase region to higher temperatures and higher uranium compositions than those shown for the true binary alloys.

X-Ray Data—X-ray diffraction studies were made of 16 annealed and quenched specimens after metallographic examination. The results are given in Table III.

Table III. X-Ray Diffraction Data Obtained on Specimens in Ternary Section Between Composition U-74 Atomic Pct Zr and U-35 Atomic Pct Ti

Alloy	Nominal Composition (Balance Uranium), Atomic Pct		Quenching Temperature, °C	Intensities of Phase Patterns*		
	Zirconium	Titanium		U_2Ti	U_2Zr_3	γ
1	0	35	510	S	0	0
1*	0	35	510	S	0	0
3	2	34	510	S	0	0
5	10	30	510	S	0	0
6	20	25.5	510	S	0	0
6*	20	25.5	510	S	0	0
7	40	17	510	S	MF	0
8	55	9	510	S	MS	0
10	63	5	510	MS	S	0
12	69.5	2	510	VVF	S	0
14	74	0	510	0	S	0
5	10	30	640	M	0	VVF
5*	10	30	640	S	0	F
6	20	25.5	640	M	0	VF
8	55	9	640	M	0	S
8*	55	9	640	VF	0	VS
6	20	25.5	700	S	0	F
6*	20	25.5	700	0	0	S
7	40	17	700	MF	0	M+
7*	40	17	700	MS	0	S
8	55	9	700	0	0	VS
8*	55	9	700	0	0	VS
5	10	30	800	S	0	F to M
5*	10	30	800	M	0	S

* Debye camera data obtained on etched slivers of samples initially examined on spectrometer.
† F means faint; V, very; M, moderate; and S, strong.

It is seen that only two phases exist in equilibrium at any one temperature. No evidence for a new phase not appearing in the binary systems was found. However, a third phase could be present in amounts less than are required for detection, or etching of the specimens for examination in the Debye camera may remove one of the phases preferentially from the surface of the sample. It will be noted that the samples examined in the Debye camera generally exhibit relatively weaker intensities of the U_2Ti phase with respect to γ than were obtained from the same specimen on the spectrometer. This suggests the removal of U_2Ti by the etching procedure.

The coarse grain size found in some specimens also makes phase detection difficult on the spectrometer. In addition, if δ U-Zr is observed on the spectrometer, the γ phase will not ordinarily be detected because of the absence of unequivocal reflections in the γ pattern, δ U-Zr showing the same reflections as the γ phase except for additional superlattice reflections.

A relatively high solubility of zirconium in δ U_2Ti at 510°C is indicated by observation of lattice shifts. Among the alloys annealed at 510°C, alloy 5, containing 10 atomic pct Zr, had a larger lattice than alloy 3, containing 2 atomic pct Zr, placing the solubility limits between the two compositions. This agrees with metallographic data which indicate a solubility of between 2 and 5 atomic pct Zr.

Attempts were also made to estimate the approximate solubility of zirconium in δ U_2Ti at 640° and 700°C. Although lattice expansions were noted in each specimen examined on the Debye camera, they were quite variable for specimens annealed at the same temperature, and no definite trend could be established. These variations are incompatible with normal expectation. If the specimens are at equilibrium and lie in the same two-phase field, assuming composition values are correct, they should be on the same tie line and, therefore, have identical lattice constants. If they are in a three-phase field, they should also have the same lattice constants.

These variations in lattice constant have not been resolved. However, two factors probably enter into, and may account for, these variations. First, the compositions are only nominal, and some deviation from a composition tie line may be expected. Second, the majority of alloys examined in the Debye camera were titanium-rich alloys which had not been rolled. It is quite possible that the homogenization and the following heat treatment alone were insufficient to produce complete homogeneity and eliminate coring introduced during casting. A diffuseness of some of the patterns, either of δ U_2Ti or of γ, suggests that equilibrium was not reached in all cases.

An interesting orientation relationship between the U_2Ti and γ phases was observed. Alloys 5 and 6, when quenched from 700° and 800°C, respectively, showed the following coexisting planar relationships: (110), U_2Ti is parallel to the (110) γ; and (300), U_2Ti is parallel to the (211) γ. In alloy 5, quenched from 640°C, the orientation relationship was: (110), U_2Ti is parallel to (110) γ.

Observation of these special orientation relationships suggests that coherency hardening may occur in these alloys under the proper conditions.

Summary

At all temperatures investigated, a maximum of two phases was found to exist either metallographically or by X-ray. No evidence was found for the presence of a three-phase region. The proposed tentative ternary section from U-74 atomic pct Zr to U-35 atomic pct Ti is shown in Fig. 2.

The presence of U_2Ti, as determined by X-ray analysis in all specimens annealed at 510°C, except for the pure δ U-Zr composition, and the absence of any other phase but δ U-Zr and/or U_2Ti in any of the other specimens, establish the phase region at this temperature as consisting of two phases.

The two-phase $\gamma+\delta$ U_2Ti region is indicated, both metallographically and by X-ray, although the microstructures are too fine to reject unequivocally the possibility of the presence of a third phase. Similarly, a third phase may be present, but in too small an amount to detect by X-ray.

The $\gamma+\delta$ U-Zr region is inferred from its presence in the binary section and from thermal data.

Acknowledgment

This work was performed under AEC Contract No. W-7405-eng 92.

References

[1] M. C. Udy and F. W. Boulger: Uranium-Titanium Alloy System. *AIME Trans.*, 1954, vol. 200, pp. 207-210; JOURNAL OF METALS, February 1954.

[2] J. D. Fast: The Transition Point Diagram of the Zirconium-Titanium System. *Recueil des travaux chimiques des Pays-Bas*, 1939, vol. 58, pp. 973-983.

[3] H. A. Saller and F. A. Rough: Compilation of U. S. and U. K. Uranium and Thorium Constitutional Diagrams. AEC Report BMI-1060, 1954. Office of Technical Services, Washington, D. C.

Discussion of this paper sent (2 copies) to AIME by Sept. 1, 1957 will appear in AIME *Transactions* Vol. 212, 1958, and in JOURNAL OF METALS, April 1958.

Preparation of Alpha Uranium Single Crystals By a Grain-Coarsening Method

A method for preparing single crystals of α uranium is described. The method depends on grain coarsening induced by the gradual decrease in grain growth inhibiting influence of dispersed inclusions in a fine grained recrystallized matrix. The factors which influence the tendency for this phenomenon and the size of coarse grains in uranium are described first. These factors are the bases for the method. However, to prepare single crystals of round cross section it is necessary to have the grain growth inhibiting inclusions distributed in a radial gradient increasing in quantity from the rod axis. This was accomplished by diffusion penetration of small concentrations of silicon from the rod surface. The steps in the process which produced a number of single crystals 4 mm in diam by 5 to 10 mm long are outlined and discussed in the second part of the text.

by E. S. Fisher

GRAIN coarsening implies a discontinuous type of grain growth during which a few grains in a fine grained recrystallized matrix grow to large grain sizes at the expense of the matrix. Studies of this phenomenon in various metals[1-3] indicate that grain coarsening may result when continuous grain growth in a fine grained matrix is inhibited by either a dispersion of very fine inclusions or by a strong texture. In the former case a period of annealing time exists prior to grain coarsening during which grain growth inhibition is gradually decreased by dissolution or coalescence of the dispersed inclusions. This mechanism can be made to occur in α uranium during anneals at high α phase temperatures.

A study of some of the factors influencing the kinetics of grain coarsening and the coarse grain sizes in α uranium has led to a method for preparing α uranium single crystals. Previously such single crystals containing considerable substructure were prepared at this laboratory by a phase change method, similar to that described by Cahn.[5] Attempts to prepare more perfect single crystals by strain-anneal techniques were unsuccessful. Cahn[5] has reported his attempts to apply such techniques to uranium. He proposed that the failure of strain-anneal techniques is basically due to the many twins which

E. S. FISHER, Junior Member AIME, is associated with the Argonne National Laboratory, Lemont, Ill.

TP 4464E. Manuscript, Mar. 2, 1955. Chicago Meeting, February 1955.

form during slight straining of α uranium. Because of the ease of twinning, too many recrystallization nuclei are formed during annealing for successful application of strain-anneal methods.

The method for preparing single crystals which is described in this report consists of a number of steps. The purposes of some of these steps may not be obvious to the reader because they are related to experimental observations which have not been previously reported. These observations are described and discussed in the first section of this paper. The method for preparing single crystals is then described in the second section.

Table I. Typical Chemical Analyses of Uranium Used in Grain Coarsening Study and Single Crystal Preparation

Lot No.	Composition in Ppm C	N	Si	Fe	Other	Ingot Source
1	23	7	10	2	6 Al	Melted electrolytic sponge
2	17	7	5	2	10 Al, 2 Cu	Melted electrolytic sponge
3	14	—	5	5	1 Cu	Melted electrolytic sponge
4	20	19	8	3		Melted electrolytic sponge
5	20	10	5	5	10 Al, 3 Cu	Melted electrolytic sponge
6	12	—	5	5	1 Cu	Melted electrolytic sponge
7	20	12	20	30	10 Ni, 10 Al, 5 Mn, 5 Mg, 2 Cu	Remelted biscuit
8	34	—	40	15	10 Al, 5 Ni, 3 Mn	Remelted biscuit

Characteristics of Grain Coarsening in α Uranium

Experimental Procedures—During the course of investigating methods for preparing uranium single crystals, many different lots of metal were used as material, each containing different quantities of impurities. However, for the study of grain coarsening and for preparing single crystals the materials were primarily of high purity containing 10 to 25 ppm C and smaller quantities of other impurities. Some typical analyses are shown in Table I. Each lot comprises the specimens made from one ingot of high purity metal. Preparation of the ingots by high vacuum melting of electrolytically produced sponge metal is described by B. Blumenthal.[4] The chemical data showed only small differences in compositions of these ingots. Also included in this report are some results obtained using uranium of lower purity, lot Nos. 7 and 8. This material was made by remelting of sponge produced by pyrometallurgical methods at AEC contract installations.

The high purity ingots were relatively small, averaging 0.8 in. diam x 4 in. long. Preliminary studies indicated that heat treatments in the β and γ phases of uranium (660° to 760°C and 760° to 1133°C, respectively) prior to final fabrication of the α phase influenced grain growth in the α phase subsequent to final fabrication. To investigate these effects the ingots were rolled at 300°C to rods of 0.337 in. diam. The rods were cut into 1 in. lengths which were used as starting samples. These samples were electropolished in a sulfuric acid, water, and glycerine (45, 45, and 10 pct, respectively) electrolyte to a bright surface, wrapped in tantalum sheet envelopes, and sealed into evacuated fused silica capsules for γ phase heat treatments. Three different heat treating schedules were used, as designated by processes *A*, *B*, and *C* of Table II. The capsules were heated in vertical tube furnaces and quenching was effected by cutting the support wires and breaking the capsule as it fell into a bucket of water.

After the final quench the rods were reduced 77 pct in area to 0.162 in. diam specimen size by swaging at 300°C out of oil. Most of the rods were reduced using a multiple step schedule as follows: a) 10 pct reduction in area, annealed 1 hr at 600°C; b) 15 pct reduction in area, annealed 1 hr at 575°C; c) 30 pct reduction in area, annealed 1 hr at 525°C; d) 30 pct reduction in area, annealed 1 hr at 475°C; and e) 40 pct reduction in area, no anneal.

During the earlier part of this study some rods were reduced to the same final diameter without resort to intermediate recrystallization steps. The effect of the swaging schedule is discussed in the text. Unless otherwise designated, the specimens were prepared by the multiple step schedule.

Annealing of Specimens: Specimens of approximately ½ in. length were cut from the 0.162 in. diam rods, electropolished to remove surface oxide, and sealed into evacuated glass capsules. The capsules were inserted into steel tubes immersed in lead baths at various temperatures not exceeding 655°C. The anneals were carried out so as to obtain the following information:

Table II. Schedules of Processing Prior to Swaging

Step	Process *A*	Process *B*	Process *C*
1	Heated 1000°C for 5 hr	Heated 1000°C for 5 hr	Heated 1000°C for 5 hr
2	Water quenched	Water quenched	Water quenched
3	Reheated 800°C for 5 hr	Reheated 900°C for 5 hr	—
4	Water quenched	Water quenched	—

1) The induction period, or incubation period, for coarsening at a specific temperature. This period included the time necessary for primary recrystallization at this temperature.

2) The maximum stable coarse grain size resulting from an isothermal anneal.

3) The effect of multiple step annealing on the coarse grain size. Specimens were initially annealed at one temperature until coarse grain growth had virtually stopped, and were then inserted into furnaces at higher temperatures.

4) The effect of annealing in a gradually increasing temperature, 5° per hr, from 550° to 650°C, on the coarse grain size.

Examination of Specimens: The specimens were macroetched in a hot aqueous electrolyte consisting of trichloracetic acid (500 g per liter) and concentrated hydrochloric acid (20 cu cm per liter). A carbon cathode was used and the voltage varied from 5 to 20 v, depending on specimen size. A salt film produced on the specimen was removed by soaking in a dilute nitric acid bath.

Average grain sizes were estimated from micrographs at X100 of metallographic polished surfaces, using polarized light. For this purpose the surfaces were electropolished, after mechanical polishing, in an electrolyte consisting of 8 volume pct orthophosphoric acid, 5 volume pct ethylene glycol, and 5 volume pct ethanol, at 30 ma per sq cm. For inclusion studies the surfaces were electroetched in a 2 pct citric acid aqueous solution at 15 ma per sq cm.

Results—The sequence of stages in the grain coarsening in α uranium is similar to those described for Al-Mn alloy[5] and silver.[6] Subsequent to

fabrication and primary recrystallization there is an interval of annealing time at temperatures above 600°C, during which the matrix grain size is uniform and small. This is an induction or incubation period. In the second stage a few of the matrix grains begin to coarsen at the expense of the small grained matrix. Although the coarse grains appear abruptly, denoting the end of the incubation period, the rate at which these grains grow depends on the matrix grain size, the annealing temperature, and the inhibition to grain growth due to dispersed inclusions.

During both stages the matrix grain size tends to increase continuously with time. There appeared to be a threshold matrix grain size above which further significant coarse grain growth was precluded. This threshold grain size was presumably dependent on the inhibiting effect of dispersed inclusions, since it varied depending on the history of the specimen as described below.

In this study primary interest was in those conditions which produced the largest coarse grains. These conditions were found to be as follows: a) the grain size at the beginning of coarsening was uniform and small, b) the coarse grains were fewest in number, and c) these few coarse grains must have been able to grow fast enough to impinge on each other before the matrix grains grew to a threshold grain size. There remained a problem in finding a means of producing these conditions when desired. The clue to a method was observed in carrying out simultaneous experiments with different ingots of high purity metal. Although these ingots were very similar in impurity content the grain growth characteristics after rolling and annealing in the α phase differed considerably. Metallographic inspection failed to correlate the behavior with inclusion content. It was surmised that the differences observed were due to differences in the volume fraction of submicroscopic inclusions resulting from precipitation at low α phase temperatures. Subsequently, experiments were made to determine the effect of different quenching temperatures prior to α phase treatment. These experiments showed a pronounced systematic effect. It was found that very large coarse grains could be produced from any high purity ingot by quenching from some optimum temperature. The optimum temperature differed between ingots.

Effect of Final Quenching Temperature: The effect of the final quenching temperature on the character of grain coarsening is shown in Figs. 1 through 3. These curves show the grain growth as a function of annealing temperature for three different rods of lot No. 1, quenched from 800°, 900°, and 1000°C, respectively. The incubation periods increased with increase in final quench temperature. Continuous grain growth of the matrix decreased with increase in the final quench temperature. The number of coarse grains per specimen volume decreased with increase in final quench temperature and was not significantly affected by the annealing temperature.

The ability of the coarse grains to grow and impinge on each other was significantly affected by the annealing temperature. The annealing temperature necessary for ultimate disappearance of the small matrix grains increased with increase in the final quench temperature. Since the annealing temperatures were limited to below 660°C there existed an optimum final quench temperature which would produce conditions for maximum coarse grain size. In this lot the optimum quench temperature was close to 900°C.

Effect of Composition: The optimum temperature for producing the largest coarse grain size differed considerably between ingots. However, in all cases the effects of increasing the final quench temperature were the same as described above for lot No. 1. In lot No. 5 the best results were obtained from 1000°C final quench, whereas in lot Nos. 3 and 4, the optimum final quench temperatures were 860° and 800°C, respectively. It is of interest that the largest coarse grains in the lower purity lots, Nos. 7 and 8, were obtained from the 1000°C final quench. In these specimens the coarse grains did not grow larger than 4 mm in any dimension. In general, the coarse grain size decreased with significant decrease in the purity of the uranium.

Effect of Annealing Temperature: In general, the coarsest grains were formed by isothermal annealing at 640° to 655°C. Usually those specimens of a given lot which had been final quenched from an optimum temperature contained duplex structures, in which coarse grains were not impinged on each other when annealed at lower temperatures than 640°C. Some of these specimens, which had been annealed at 625° and 600°C for 65 hr, were subsequently heated at 650°C. The higher temperature had no significant effect on the grain size. A similar effect was observed in specimens which were slowly heated from 550° to 650°C. The duplex structure formed at lower temperatures was apparently stable at higher temperatures.

Effect of Fabrication Process: The coarse grains were generally longer in a direction parallel to the rolling direction than in radial directions. This shape appeared to be related to *banding* in the primary recrystallized structure, a pronounced case of which is shown in Fig. 4. This appearance is typical of microstructures in specimens which were swaged by a single step schedule. The *bands* are groups of grains somewhat similar in grain size and orientation with respect to the plane of polish (as indicated by polarized light examination). The bands appear to develop as a result of differences in the degree and types of deformation among the grains in the rods undergoing fabrication. Rods which are large grained prior to rolling, as in castings or rods heat treated in the γ phase, and are heavily rolled prior to recrystallization show this phenomenon very markedly after recrystallization. The grains in one band may be, on the average, two to three times as large as those in an adjacent band, and the bands are aligned parallel to the rolling direction. When coarsening occurs in such structures the coarse grain tends to initiate in the fine grained bands and to grow into the band in which it originated.

This banding effect was minimized by using multiple step reduction schedules. When coarsening occurred in rods reduced by the multiple step method the coarse grains still showed the tendency to grow faster in the direction of rolling. However, the anisotropy of growth was less apparent than in the heavily banded structures, i.e., the coarse grains grew larger in the radial dimensions, the lower the degree of banding.

Interpretation of Effects of Quenching Temperature—It is proposed that the grain coarsening phenomenon described in this report is dependent on the presence of very fine particles included in the uranium during annealing in the α phase. Because

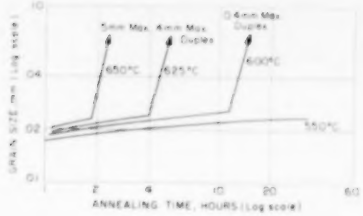

Fig. 1—Grain size vs annealing time at 550°, 600°, 625°, and 650°C for lot No. 1-A specimens. Arrow denotes grain coarsening. Maximum ultimate grain size is indicated above arrow. Duplex denotes that coarse grains did not ultimately consume matrix.

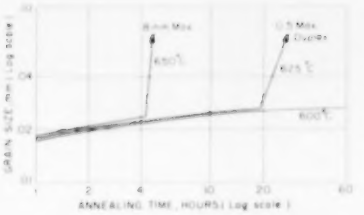

Fig. 2—Grain size vs annealing time at 600°, 625°, and 650°C for lot No. 1-B specimens. Arrow denotes grain coarsening. Maximum ultimate grain size is indicated above arrow. Duplex denotes that coarse grains did not ultimately consume matrix.

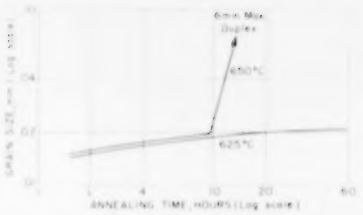

Fig. 3—Grain size vs annealing time at 625° and 650°C for lot No. 1-C specimens. Arrow denotes grain coarsening. Maximum ultimate grain size is indicated above arrow. Duplex denotes that coarse grains did not consume matrix.

of the fine particle size these inclusions are very effective for inhibiting continuous grain growth subsequent to primary recrystallization and, the larger their volume fraction, the greater the effect. During prolonged annealing these particles tend gradually to coalesce or to dissolve in the uranium. In either event the inhibiting power is decreased gradually so that at some stage of annealing some of the grains can begin to grow abruptly at the expense of the fine grains which are still inhibited. The incubation period for coarsening depends on the rate of coalescence or dissolution of the particles, which is a function of the annealing temperature, and on the volume fraction of the particles. The number of grains which start to coarsen during the initial stages of coarsening is primarily dependent on the volume fraction of particles.

The question then arises as to the source of the fine particles in the high purity uranium. Studies of binary uranium alloys indicate that most of the elements detected as impurities, Table I, have extremely small solubilities in α uranium. However, solubilities in the high temperature γ phase appear to be significantly greater. Atoms in solution in γ phase will then tend to precipitate when the metal is cooled to the α phase. The particle size of the precipitate should depend on the temperature at which precipitation occurs and on subsequent annealing. It is assumed that treatments of the rods in this study, water quenching and swaging at 300°C with intermediate recrystallization anneals, produce a precipitate of fine particle size. The volume fraction of these fine particles should depend on the number of impurity atoms in solution just before quenching. From the consistently observed correlation between quenching temperature and grain growth kinetics described in the text, the solubilities in the γ phase apparently increase with temperature, i.e., the higher the quench temperature, the longer the incubation periods for coarsening because of the greater volume fraction of fine particles produced by precipitation.

Method for Preparing Single Crystal Rods

A method for preparing single crystal rods of α uranium has been developed which is based on the conditions for obtaining a maximum coarse grain size as described above. However, it was necessary to introduce two other conditions so that the coarse grains could grow to the shape of rods with diameters approaching those of the specimens and lengths sufficient for practicable separation from other grains in the specimens. To obtain rod shaped coarse grains the distribution of fine particle inhibitor was changed from a uniform type to a radial diffusion gradient type in which the concentration of inhibitor increased with distance from the center or rod axis. Because the incubation period for grain coarsening increased with increase in inhibition, the first coarse grain in the specimen formed at the rod axis under these conditions and grew to the desired rod shape and dimensions if other conditions permitted. To obtain sufficiently long lengths the coarsening process was carried out by a special temperature gradient technique, which was also effective in limiting the number of coarse grains.

Single crystals of diameters up to 0.230 in. and lengths up to ½ in. have been prepared by this method from many different ingots of high purity material. In this report the general procedure for preparing single crystals in specimens of 0.162 in. diam and some typical results are described.

Siliconizing Process—The radial concentration gradient of inhibitor was produced by diffusing silicon into the bare uranium rods during heat treatment at 1000°C in evacuated Vycor or fused quartz capsules. An unknown reaction occurred between the uranium and silica which permitted silicon to diffuse concentrically into γ uranium in sufficient quantities to provide suitable concentration gradients within 5 to 10 hr exposure to the vapors. The time of exposure to obtain sufficient silicon varied, depending for some unknown reason on the lot of material as indicated by chemical analyses. Chemical analyses showed that a 10 to 20 ppm overall increase in silicon content was sufficient to prepare single crystals of this diameter. In some lots the depth of penetration of silicon in the uranium rod during the siliconizing process was sufficient to produce a satisfactory concentration gradient for obtaining a good yield of single crystals. In other lots it was necessary to diffusion heat treat subsequent to siliconizing.

Procedure—The general procedure for preparing single crystals was somewhat the same as the procedure described above for the study of grain coarsening characteristics. The high purity ingots, corresponding to lot Nos. 1 through 6 in Table I, were rolled to 0.337 in. diam rods, which were in turn cut into 1 in. lengths. These lengths were processed individually according to the schedule outlined below, which includes all of the steps which may have been necessary for a particular lot of uranium.

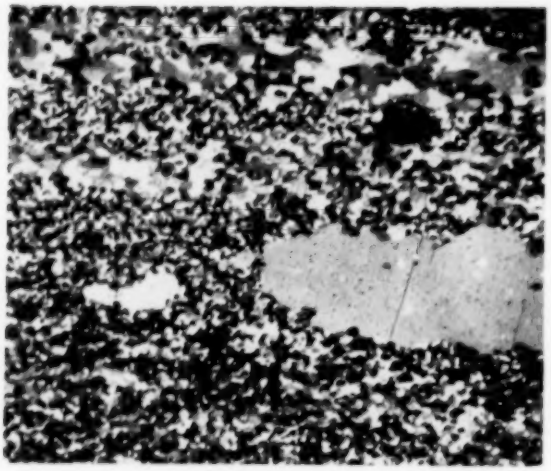

Fig. 4—Growth of long coarse grains in matrix containing pronounced longitudinal banding. Polarized light. X50. Reduced approximately 10 pct for reproduction.

1) Siliconizing Heat Treatment: The rod was electropolished, sealed into an evacuated Vycor or quartz capsule, heated at 1000°C for 5 to 10 hr, and water quenched.

2) Diffusion at 1000°C after Siliconizing: In some lots further diffusion of the silicon was found beneficial. The siliconized rod was wrapped in tantalum foil to prevent further addition of silicon, sealed in vacuum, and heated at 1000°C.

3) Final Quench Treatment: For each lot there existed a particular final quench temperature between 800° and 1000°C which produced the best final yield. The rods were heated at this temperature for 5 hr, sealed in evacuated glass capsules and protected by tantalum envelopes, and water quenched.

4) Swaging: The rods were swaged to 0.162 in. diam by the multiple step schedule outlined in the previous section.

5) Preparation of Specimens: The rod was cut into 1 in. lengths, one end of which was machined to a point with a 30° taper (pencil shape).

6) Coarsening Anneal: The pencil shape specimens were sealed in evacuated capsules, recrystallized at 475°C, and annealed for grain coarsening by a special temperature gradient procedure which was derived after investigating other methods. The capsules were first suspended vertically in a steel tube, the lower half-length of which was immersed in molten lead at 655°C, whereas the upper half was water cooled through copper tubing soldered to the steel. The height of the specimen was adjusted so that the point was at 650°C. The temperature gradient was such that the top of the 1 in. specimen was at approximately 575°C. After about 2 hr in this position the capsule was lowered abruptly to the bottom half of the tube so that the whole specimen was at 655°C for 50 to 100 hr.

After the coarsening anneal a layer of very fine grains generally existed at the cylindrical surfaces so as to form a ring about the coarse grains at a cross section, as shown in Fig. 5. This ring of grains generally could not be completely absorbed by grain growth because of the high inhibitor concentration in this area due to siliconizing. When the center of the cross section contained one large coarse grain, the outer ring of fine grains was easily removed by prolonged macroetching in the trichloracetic electrolyte, so as to leave only the one grain at the cross section. Fig. 6 shows a specimen containing five cylindrical grains after removal of the fine grained surface. This grain was then isolated from other grains attached to the ends by mechanical grinding on metallographic laps.

Method for Determining Optimum Processing Conditions: Before single crystals could be prepared from specimens of a given lot of material it was necessary to find optimum values of the siliconizing time, diffusion time, and the temperature of final quenching. Although the amount of silicon pickup by the uranium in a given time appeared to vary with the material, the effect did not complicate matters greatly because the amount of silicon was critical only to the extent of having sufficient silicon to produce an effective gradient of inhibitor. It was found that the presence or absence of sufficient siliconizing treatment could be determined from the thickness of the fine grained ring on the specimens after the coarsening anneal. When the inhibitor concentration at the surface was sufficient to form a fine grained ring of two to four grains thickness (0.05 to 0.1 mm), conditions suitable for preparing single crystals could be produced by adjustments in the other two factors. An excess of silicon over a wide range merely caused an increase in the thickness of fine grained ring and, consequently, a decrease in the single crystal diameters. Of the four lots of material only lot No. 6 required more than a 5 hr siliconizing treatment.

The total diffusion time was also apparently not too critical in its effect on single crystal yield as long as the silicon penetration was sufficiently deep. In lot No. 5, for example, the diffusion which oc-

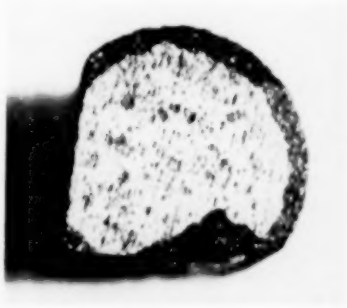

Fig. 5—Grain size distribution after grain coarsening at a cross section of a specimen containing a concentration gradient of silicon. Dark outer ring is fine grained and light area is single coarse grain. Macroetched. X7.

Fig. 6—Specimen containing five cylindrical grains after chemical removal of fine grained surface. X2.

curred during the 5 hr siliconizing time produced an inhibitor gradient which was effective in causing one coarse grain to grow from the center of the specimen cross section. However, the annealed specimens from this rod all contained an intermediate ring of smaller coarse grains between the center grain and the peripheral ring of fine grains which was two to four grains thick. Consequently, the single crystals obtained from the grain separation process were of relatively small diameter. In subsequent treatment of lot No. 5 rods an additional 5 hr diffusion time was used, subsequent to siliconizing, which was effective in permitting the single coarse grains to grow to the fine grained ring, the thickness of which was not changed significantly by the additional diffusion. In lot No. 6 the diffusion which occurred during the 10 hr siliconizing treatment was not sufficient to prevent a thin intermediate ring of relatively small coarse grains from forming between the large center grains and the surface. However, because the total thickness of the peripheral rings was relatively small, the single crystals obtained from this lot were of satisfactory diameter. An additional 5 hr diffusion in this lot caused an increase in the thickness of the fine grained ring, as shown schematically in Fig. 7.

The yield of single crystals was most significantly affected by variations in the final quench temperature. For each lot of material there was a particular range of final quench temperatures for obtaining the maximum single crystal yield. The temperatures in this range varied within an interval of approximately 50°C. In lot No. 6, a final quench temperature of 1000°C produced very good results and higher final quench temperatures were not tried. In specimens of this lot quenched from 900°C, no single crystals could be obtained. The specimen cross sections consisted of two to four large coarse grains with dispersed smaller coarse grains. The thickness of the fine grained skin did not vary significantly with final quench temperature. In lot No. 5 the mean optimum temperature was approximately 900°; the 1000°C final quench specimens consisted of a mixture of coarse grain sizes with entrapped islands of fine grains after the final anneal. Lot No. 4 specimens final quenched from 800°C produced a very good yield of single crystals, and lower final quench temperatures were not explored. However, specimens processed with a 850°C final quench were entirely fine grained after prolonged final anneals.

Because the optimum processing conditions could not be predicted from chemical analyses of a lot of material these factors had to be determined by exploration. From experience it became evident that the 10 hr total processing time at 1000°C was generally sufficient for optimum distribution of the silicon, and that the optimum final quench temperature would be between 800° and 1000°C. A procedure for finding these conditions was adopted in which the first three 1 in. lengths of a new material were processed simultaneously, using a 5 hr siliconizing time and no further diffusion. The first rod was final quenched from 1000°, the second from 900°, and the third from 800°C. After swaging and final annealing, specimens of each rod were examined to determine, first, which of the final quench temperatures produced the largest coarse grains and, second, whether further siliconizing or diffusion treatment was necessary in the processing of subsequent rods of the same lot. If the specimens contained a fine grained ring, indicating sufficient siliconizing treatment, but no single crystals of any diameter could be prepared from three or four specimens of each of the rods, further exploration of the final quench temperature was carried out. In processing the next 1 in. length from this lot, a final quench temperature 50°C above that which appeared to be the best of the first three tests was tried. If the single crystal yield from specimens of a rod was in the order of 50 pct, a 25°C variation in the final quench temperature was tried in order to obtain specimens of greater yield.

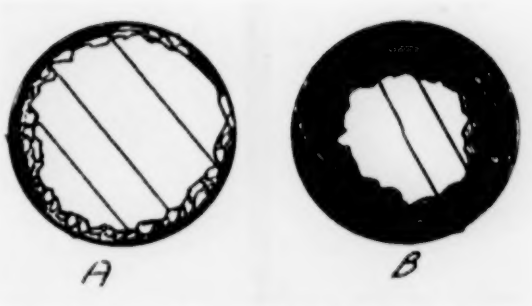

Fig. 7—Sketches showing effect of varying silicon distribution on grain size distribution after final annealing. Specimen *A* is from rod processed with 10 hr siliconizing time. Specimen *B* is from rod processed with 10 hr siliconizing plus 5 hr further diffusion. Dark areas indicate fine grains; dark lines simulate twin bands.

Table III. Processing Conditions Which Produced High Yields of Single Crystals

Lot	Siliconizing Time, Hr	Added Diffusion	Final Quench Temperature, °C
3	5	None	860
4	5	None	800
5	5	5 Hr	900
6	10	None	1000

By this method, the processing conditions necessary to prepare a high yield of single crystals from four different lots of uranium were found, which are noted in Table III. The lot numbers correspond to those in Table I.

Metallographic Observations—The inclusions observed in the specimens due to siliconizing varied in number and type depending on the lot of material. In lot No. 3, for example, a high concentration of very small gray colored inclusions was found at the periphery of the cross sections where the fine grains remained after the coarsening anneal. No inclusions were found in the isolated single crystals from this lot. In lot No. 4 no inclusions were observed even in the fine grained ring. Lot Nos. 5 and 6 contained a second type of inclusion which appeared larger, darker, and more widely dispersed than the first type. The concentrations of these inclusions decreased with distance from the cross section edge, but some were found in the coarse grained regions. The isolated single crystals from these lots contained a few of these inclusions at the edges.

Under polarized light examination the single crystals appeared free of subgrain boundaries. Seldom,

Fig. 8—Back reflection Laue pattern from well polished face of single crystal, *b* axis parallel to X-ray beam, unfiltered tungsten radiation, and 0.030 in. collimator.

however, were the crystals completely free of twin bands. If the crystal ends were not sufficiently electropolished after mechanical grinding numerous broad twin bands were observed. After prolonged electropolishing (20 to 30 min) some very thin twin bands were generally present.

X-Ray Diffraction Studies—Fig. 8 shows a typical back reflection Laue pattern taken with one end face of the crystal normal to the X-ray beam. The Laue spots were reasonably sharp, showing no evidence of significant substructure. More refined methods for detecting substructure have not been applied to these crystals.

The large grains produced by grain coarsening are generally oriented with the [010] direction almost parallel with the rod axis. In approximately 30 single crystals most of the [010] directions were within 15° of this alignment, with a maximum deviation of 25°.

Summary

A method for preparing single crystals of α uranium has been developed which depends on a discontinuous grain growth phenomenon. For grain coarsening to occur it is necessary for high purity metal to be fabricated in the α phase, so as to produce a fine grained structure after primary recrystallization. Upon further annealing at high temperatures in the α phase, 600° to 650°C, a few of the fine primary grains will grow almost abruptly to coarse grains.

The tendency for grain coarsening is significantly influenced by the variation in γ phase heat treatment prior to fabrication. This is attributed to the effect of the heat treatment on the dispersion of grain growth inhibiting inclusions in the primary recrystallized structure. These inclusions have the greatest grain growth inhibiting effect when they are finely dispersed. Grain coarsening is attributed to the gradual coalescence or dissolution of these inclusions during prolonged annealing.

The largest coarse grains are obtained when the concentration of fine inclusions is some optimum value, the primary recrystallized grains are of uniformly fine grain size, and the final annealing process is carried out at the highest permissible temperature. The fine inclusion concentration is controlled by γ phase heat treatment, the quantity increasing with increase of final quench temperature prior to fabrication. The uniformity of primary recrystallized grain size is markedly affected by the fabrication schedule; a multiple step schedule has been found for producing the greatest uniformity.

To prepare single crystals of round cross section it was necessary to introduce further processing prior to fabrication so that after fabrication the grain growth inhibiting inclusions would be distributed in a radial concentration gradient, increasing from the rod axis. This was accomplished by permitting silicon vapors to react with the surfaces of the rods during heat treatment in evacuated silica capsules at 1000°C. The diffusion penetration of the minute quantities of silicon was controlled by the time of heating. These rods were then processed so as to produce the optimum conditions for growing the largest coarse grains, as explained above, using the optimum final quench temperature, the multiple step reduction schedule, and a temperature gradient final annealing method. When appropriate processing conditions were used, which varied among different lots of high purity uranium, one coarse grain grew from the center almost to the edge of a specimen cross section. The surface of the specimen was fine grained. A number of rod shaped single crystals of 4 mm diam and 5 to 10 mm length were prepared from such specimens.

Acknowledgments

This work was performed under the auspices of the U. S. Atomic Energy Commission. The author gratefully acknowledges the interest and advice of Paul Beck in the development of the process described in this report. He is also indebted to R. Noland and C. Marzano, who developed the technique for producing high purity uranium sponge, to B. Blumenthal for preparing the high purity uranium ingots which were used in this study, and to F. Foote and H. Chiswik for advice and encouragement.

References

(1) P. A. Beck and P. R. Sperry: *AIME Trans.*, 1949, vol. 185, p. 240; Journal of Metals, March 1949.
(2) M. Cook and C. Macquarie: *AIME Trans.*, 1939, vol. 133, p. 142; Metals Technology, September 1938.
(3) R. W. Cahn: *Acta Metallurgica*, 1953, vol. 1, p. 176.
(4) B. Blumenthal: *AIME Trans.*, 1955, vol. 203, p. 1199; Journal of Metals, November 1955.
(5) P. A. Beck, M. L. Holzworth, and P. R. Sperry: *AIME Trans.*, 1949, vol. 180, p. 163; Journal of Metals, February 1949.
(6) F. D. Rost, B. H. Alexander, and C. A. Dube: *AIME Trans.*, 1952, vol. 194, p. 189; Journal of Metals, February 1952.

Discussion of this paper sent (2 copies) to AIME by Sept. 1, 1957 will appear in AIME *Transactions* Vol. 212, 1958, and in Journal of Metals, April 1958.

Elevated Temperature Phase Relationships In the Cr-Ni-Mn-N System

Austenite-austenite plus δ ferrite phase boundaries have been determined for the Cr-Ni-Mn-N system at temperatures of 2100°, 2200°, and 2300°F over the composition ranges 15 to 21 pct Cr, 0 to 3 pct Ni, 12 to 18 pct Mn, and 0.25 to 0.45 pct N. The structural diagrams permit the selection of ferrite-free stainless compositions containing little or no nickel.

by E. J. Whittenberger, E. R. Rosenow, and D. J. Carney

OVER the past two decades, the Cr-Ni stainless steels, popularly termed 18-8 steels, have been used in ever increasing amounts in the aircraft, automotive, chemical, transportation, and building industries.[1] The contribution of nickel to these steels is associated with its strong austenite forming tendencies which assure good hot and cold forming characteristics, and with its beneficial influence upon corrosion resistance, especially in oxidizing acids. The adjustment of the chromium and nickel contents has been used advantageously in controlling the rollability and the response of the mechanical properties of these steels to cold reduction.

With the advent of the jet age and the government stockpiling of nickel, considerable emphasis has been placed upon the development of satisfactory low nickel or nickel-free substitute austenitic stainless steels, especially for nonmilitary applications.[2] Ferritic 17 pct Cr (AISI Type 430) stainless steel has been effectively substituted for the austenitic grades in applications with mildly corrosive exposure. However, the limited formability and ferromagnetic behavior of this grade do not permit its satisfactory use for many applications. To achieve better formability in a nonmagnetic steel and conserve nickel, a number of low nickel substitute austenitic grades of stainless steel have been developed in recent years. In most of these steels, manganese and nitrogen have been substituted for a portion of the nickel content, for example, 17 pct Cr-4 pct Ni-6 pct Mn (AISI Type 201), 18 pct Cr-5 pct Ni-8 pct Mn (AISI Type 202), and 16 pct Cr-1 pct Ni-17 pct Mn, all of which contain approximately 0.15 pct N.[3] The precipitation of δ ferrite when large ingots of these Cr-Ni-Mn-N steels are heated to temperatures high enough for conversion to slabs on conventional universal slabbing mills has seriously affected the hot workability of these steels. This has been especially true in the case of the 16 pct Cr-1 pct Ni-17 pct Mn (sometimes referred to as 15 pct Cr-1 pct Ni-15 pct Mn) composition.[4]

Because it is possible that little, if any, nickel will be available for nonmilitary stainless steel applications in the event of a national emergency, a need has existed for a nickel-free austenitic stainless steel containing hot and cold forming characteristics similar to 18-8 steels and corrosion resistance at least comparable to the 17 pct Cr ferritic steel. The aforementioned deleterious effect of δ ferrite upon the hot working characteristics of the 16 pct Cr-1 pct Ni-17 pct Mn steel indicates the importance of establishing the austenite-austenite plus δ ferrite phase boundaries as the first step in the development of nickel-free or low nickel substitute steels. This paper presents the data collected in an elevated temperature constitutional study of the Cr-Ni-Mn-N system at the South Works of the United States Steel Corp.

Experimental Procedure

The 300 compositions used in the investigation were melted in a 26 lb induction furnace and cast in 3½ in. diam by 18 in. tall hot-topped ingot molds.

E. J. WHITTENBERGER, Member AIME, E. R. ROSENOW, and D. J. CARNEY, Member AIME, are Chief Development Metallurgist, Physicist, and Superintendent, No. 2 Electric Furnace Shop, South Works, respectively, United States Steel Corp., Chicago.

TP 4463E. Manuscript, Sept. 17, 1956. New Orleans Meeting, February 1957.

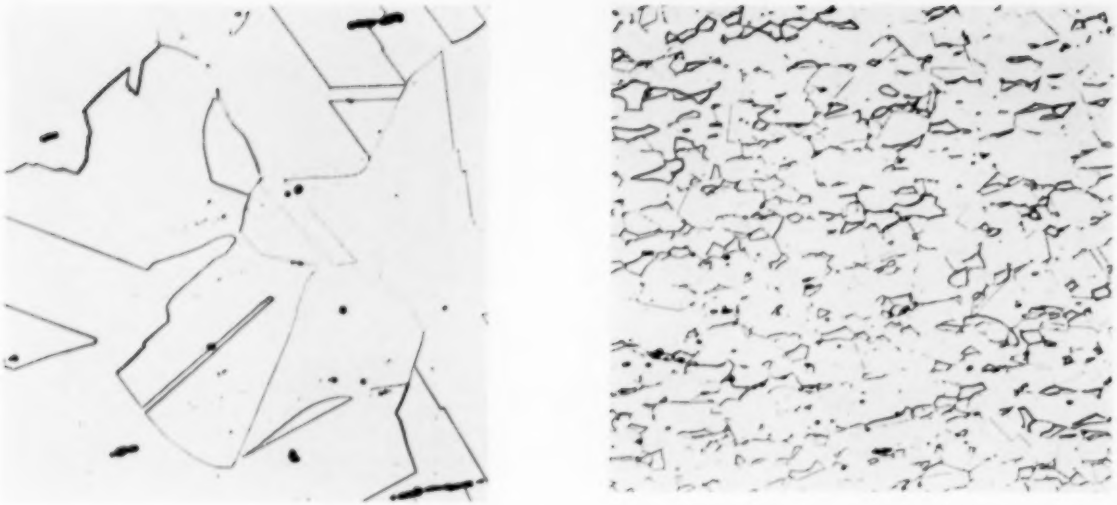

Fig. 1—Microstructure of Cr-Mn-N steels after heating forged specimens 1 hr at 2300°F and water quenching. a) LEFT: 18 pct Cr-15 pct Mn-0.45 pct N; no δ ferrite. b) RIGHT: 18 pct Cr-18 pct Mn-0.30 pct N; 5 pct δ ferrite. Note grain coarsening in absence of δ ferrite. Electrolytic chromic acid etch. X100.

The furnace charges consisted of low-metalloid scrap, low-carbon 70 pct ferrochromium, low-carbon 90 pct ferromanganese, and 75 pct ferrosilicon. Electrolytic nickel was used in melting those compositions that required nickel. To obtain the necessary nitrogen contents, either high-nitrogen (2.0 to 6.0 pct) 60 pct ferrochromium and/or high nitrogen (5.80 pct) electrolytic manganese were used. The base composition of all heats produced was approximately 0.10 pct C, 0.020 pct P, 0.015 pct S, and 0.50 pct Si.

Melting to close nitrogen limits necessitated very close control of the nitrogen bath additions. Argon gas was used over the bath in the furnace to avoid nitrogen pickup from the atmosphere. Very close visual observations were made of the ingots after casting to determine whether nitrogen gas evolution (bleeding) was evident. As-cast sections were cut from the top of the ingots (just below the hot top junction) to determine whether nitrogen gas porosity was present.

Each ingot was forged to ¾ in. x 3 in. wide plates. Samples ½ x ¾ x 1 in. were cut from the midway position of the forged plates, 6 in. from the end representing the bottom of the ingot. This location was selected to avoid the positive chemical segregation that is generally found in the top portion of these laboratory ingots.

The forged samples were annealed in a laboratory muffle furnace in the temperature range from 2100° to 2300°F at 100°F intervals for 1 hr at temperature followed by water quenching. They were sectioned and polished metallographically for determination of their ferrite content. For magnetic determination of their ferrite content, the samples were prepared by machining 1/32 in. from all surfaces to remove what appeared to be a nitrided case in which ferrite was never found regardless of the ferrite content of the interior of the sample.

The magnetic determinations of ferrite content were made with a magnetic torsion balance similar to that employed by Tisinai and Samans.[4] To assure proper calibration, standard samples were prepared by compacting homogeneous mixtures of pure iron powder and Bakelite powder in a conventional metallographic mounting press. These standards, containing from 0 to 11 pct Fe (ferrite) by volume and of a series of thicknesses ranging from 0.10 to 0.35 in., were then used to prepare a series of calibration curves relating deflection of the magnetic torsion balance to percentage of ferrite by volume. This was done for each series of sample thicknesses. To eliminate error in the magnetic torsion balance readings, the magnetic deflections of a number of the standard samples were checked against the master calibration curves before and during each set of measurements on Cr-Ni-Mn-N samples.

Discussion of Results

Typical examples of the microstructures characterizing these Cr-Ni-Mn-N steels when forged structures were solution annealed at 2300°F are shown in Fig. 1. While the two steels depicted here contained no nickel, no significant difference in microstructure was observed for the nickel-bearing steels. In general, all steels which contained no δ ferrite exhibited grain coarsening after 1 hr annealing treatments at 2200° and 2300°F. However, when δ ferrite was present, no appreciable increase in grain size occurred. This marked influence of δ ferrite upon grain coarsening behavior is demonstrated in Fig. 1. Since austenite grain size was not considered to be important in this constitutional study, no precise record of grain size vs composition and/or annealing treatment was made.

Before presenting experimental results, some recognition should be given to potential sources of error in the experimental techniques. These would be expected to be associated chiefly with precision of the chemical analyses and the ferrite measurements, as well as with the adequacy of the length of the annealing treatments in producing the equilibrium distribution of phases.

Chemical Composition—Because of the large number of laboratory heats which had to be made

to rather precise composition specifications in order to establish the elevated temperature phase boundaries, and the practical difficulties associated with precise control of the carbon, chromium, nickel, manganese, and nitrogen contents, a special bath sampling technique was developed for the purpose of obtaining chemical analyses prior to the forging of the experimental ingots. This procedure consisted of obtaining a small 1½ lb chemical sample which was representative of the bath analyses just prior to tapping of the heat. If the subsequent analyses of this tap sample indicated that the composition would be useful in establishing the elevated temperature phase relationships, the ingot was then processed as previously described. In the early stages of the experimental program, check analyses, taken adjacent to the specimens used for metallographic and magnetic determinations of the phase relationships, were obtained for comparison with the analyses of the 1½ lb tap samples. Because the metallographic and magnetic specimens were taken from locations representative of the lower portion of the ingots, the agreement between the check analyses and the tap analyses was quite good, being of the order of ±0.01 pct C, ±0.01 pct N, and ±½ pct of the total amount of chromium, nickel, or manganese present. Because of this agreement between check analyses and tapping analyses, the latter only were used in the later stages of the experimentation. The small compositional errors which may have been introduced by the omission of check analyses are not considered to have introduced any significant error into the phase relationships.

As a result of the minor deviations between the actual analyses and the aim compositions needed for precise establishment of the phase boundaries, some personal judgment was subsequently exercised in drawing the final phase boundaries.

Magnetic Determinations of Ferrite Content—The previously described procedure for preparing standards which were used in determining magnetic deflection-ferrite content relationships and for subsequently calibrating the magnetic torsion balance provided a method for establishing ferrite contents which was much more rapid and possessed greater accuracy than conventional metallographic techniques. In the early stages of the work, many comparisons were made between metallographic and magnetic determinations of ferrite content. In no case was the magnetic determination found to be significantly different from the metallographic determination.

An important contribution of the metallographic examinations, however, was that of indicating ferrite-free cases on samples whose interiors contained identifiable amounts of ferrite. This was attributed to nitrogen pickup during the solution annealing treatment in the air atmosphere of the laboratory muffle furnace. Removal of 1/32 in. of material from all surfaces of the specimens was found to eliminate the ferrite-free case. Therefore, during the entire experimental program, 1/32 in. of material was removed from all surfaces of the specimens subsequent to the annealing treatment and prior to magnetic determination of their ferrite content.

Annealing Treatment—To assure that the phase relationships determined in this work would approximate equilibrium relationships, an initial study of the influence of annealing time upon ferrite content was carried out. Specimens of unbalanced compositions, i.e., which would precipitate δ ferrite at elevated temperatures, were subjected to 2100° and 2300°F annealing treatments for various intervals of time. In every case, no detectable change in ferrite content occurred at time intervals in excess of 60 min. This was not unexpected, since forged structures were being annealed in this study and would not be expected to require the longer annealing treatment necessary for the coarser as-cast structures. Therefore, the standard annealing treatment used in this work comprised 1 hr at temperature followed by water quenching.

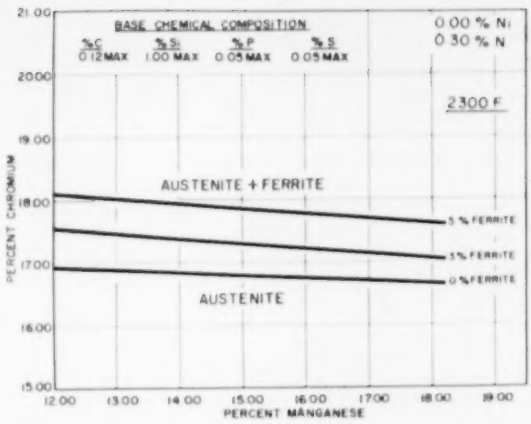

Fig. 2—Structural diagram for 0.00 pct Ni 0.30 pct N steels indicating the chromium and manganese contents providing 0, 3, and 5 pct ferrite after heating for 1 hr at 2300°F and water quenching.

The above-mentioned potential sources of error in the establishment of the austenite-austenite plus δ ferrite phase boundaries are not considered to provide a total error in excess of ±1 pct δ ferrite. This total error can best be evaluated by reference to Fig. 2, where curves representing 0, 3, and 5 pct ferrite have been drawn as a function of chromium and manganese content in nickel-free steels containing 0.10 pct C and 0.30 pct N. This diagram shows the influence of chromium as a ferrite forming element and indicates that, at 2300°F, ½ pct Cr in excess of the limit of austenitic stability will produce approximately 3 pct δ ferrite. Such relationships as depicted in the 0 pct ferrite curve were used to portray the phase boundaries in the balance of the work. It should also be pointed out that the linear nature of the phase boundary in the range from 12 to 18 pct Mn is in good agreement with the previous work of Franks, Binder, and Thompson[5] and Krainer and Mirt.[6]

Phase Relationships—While Franks, Binder, and Thompson had determined the austenite-austenite plus δ ferrite phase boundary as a function of chromium, nickel, and manganese contents, their studies were limited to nitrogen contents ranging from 0.08 to 0.15 pct N. Krainer and Mirt, on the other hand, determined this phase boundary in nickel-free steels containing chromium, manganese, and nitrogen with the nitrogen contents approximating 1/75th of the chromium content. Since neither of these investigations had determined the independent influences of chromium, manganese, and nitrogen, this became a major objective of the present experimentation.

At the outset, it was not known whether sufficient manganese and nitrogen could be added to nickel-

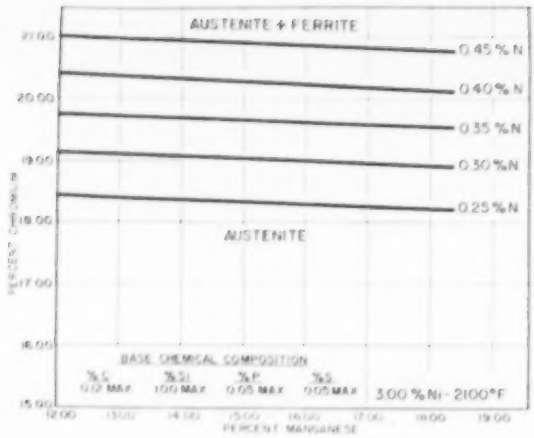

Fig. 3—Structural diagram for 3.00 pct Ni 0.25 to 0.45 pct N steels after heating for 1 hr at 2100°F and water quenching.

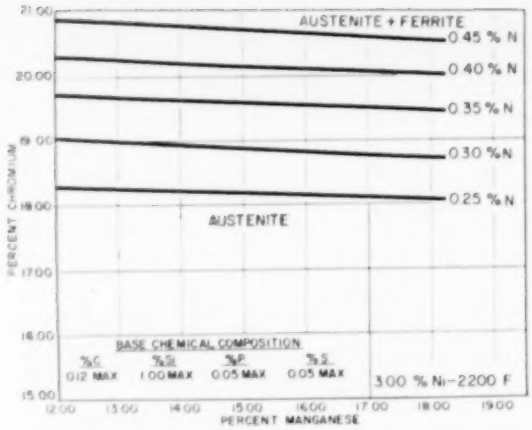

Fig. 4—Structural diagram for 3.00 pct Ni 0.25 to 0.45 pct N steels after heating for 1 hr at 2200°F and water quenching.

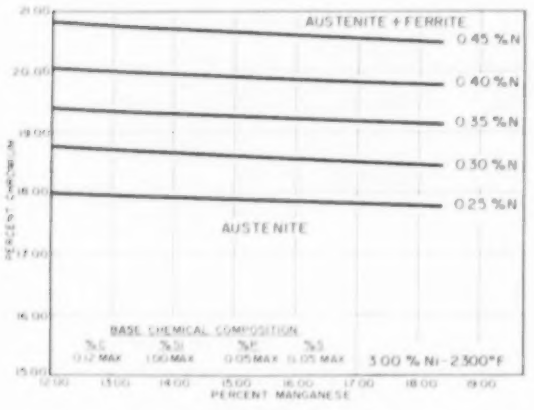

Fig. 5—Structural diagram for 3.00 pct Ni 0.25 to 0.45 pct N steels after heating for 1 hr at 2300°F and water quenching.

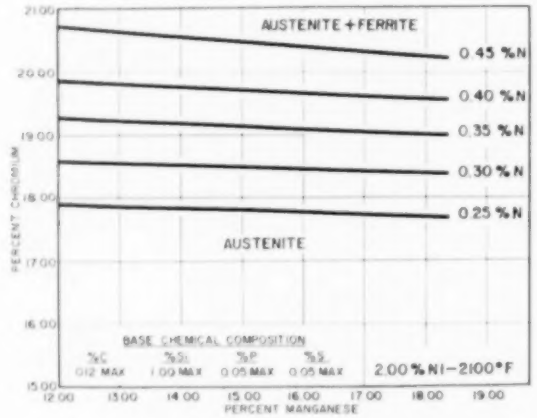

Fig. 6—Structural diagram for 2.00 pct Ni 0.25 to 0.45 pct N steels after heating for 1 hr at 2100°F and water quenching.

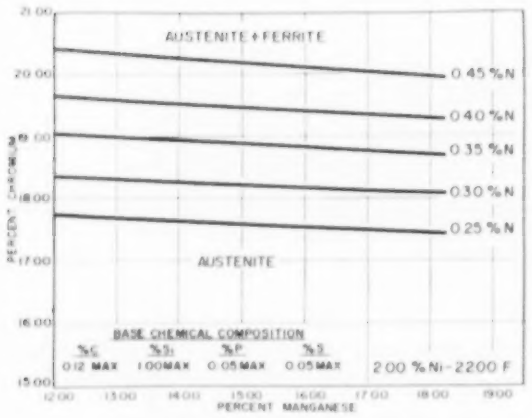

Fig. 7—Structural diagram for 2.00 pct Ni 0.25 to 0.45 pct N steels after heating for 1 hr at 2200°F and water quenching.

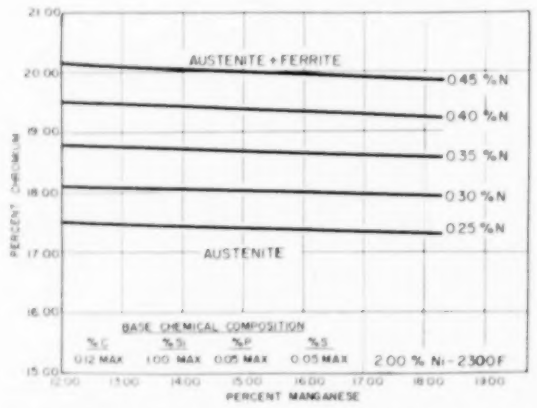

Fig. 8—Structural diagram for 2.00 pct Ni 0.25 to 0.45 pct N steels after heating for 1 hr at 2300°F and water quenching.

free steels containing 15 to 21 pct Cr to make them completely austenitic at 2300°F. Therefore, initial compositions included manganese contents up to 18 pct and nitrogen contents up to 0.50 pct. It soon became apparent that the solid solubility for nitrogen depended to a large extent upon the chromium and manganese contents. To obtain a qualitative measure of the solid solubility for nitrogen, each ingot was sectioned approximately 1 in. below the hot top junction to examine the internal structure for nitrogen gas porosity. Since nitrogen solubility was not an objective of this program and because such information is difficult to portray on the structural diagrams, only qualitative observations of the solid solubility for nitrogen are possible.

In general, an ingot containing 17.50 pct Cr and 12.50 pct Mn did not exhibit bleeding (nitrogen gas porosity) when the nitrogen content was 0.35 pct or less. Increasing the chromium and/or manganese contents appeared to increase the solid solubility for nitrogen. For example, a steel containing 17.50 pct Cr, 15.00 pct Mn, and 0.45 pct N did not exhibit nitrogen gas porosity when cast in air. Usually, compositions approaching the phase boundaries to be portrayed in the balance of this paper did not contain gas porosity. However, it should be cautioned that decreasing either the chromium or the manganese contents usually resulted in bleeding ingots.

A typical structural diagram demonstrating the chromium and manganese contents corresponding to the austenite-austenite plus δ ferrite phase boundary at nitrogen levels ranging from 0.25 to 0.45 pct in 0.05 pct increments is presented in Fig. 3. The potent influence of nitrogen as an austenite stabilizer can readily be discerned in this figure. The addition of each 0.05 pct N makes possible an increase in chromium content of approximately 0.60 pct without precipitation of δ ferrite in steels containing 3 pct Ni at 2100°F. It should also be pointed out that increasing the manganese content actually decreases the austenite stability slightly, i.e., reduces the amount of chromium which can be tolerated without the precipitation of δ ferrite. Similar relationships in 3 pct Ni steels at 2200° and 2300°F are presented in Figs. 4 and 5, respectively. Since, in the rolling of large commercial ingots, heating at 2300°F is desirable, the latter figure indicates that no difficulty from ferrite precipitation would be encountered in a steel containing 18 pct Cr, 3 pct Ni, 12 to 18 pct Mn, and 0.30 pct N.

The structural diagrams for 2 pct Ni steels at 2100°, 2200°, and 2300°F are presented in Figs. 6, 7, and 8. Comparisons of these diagrams with those for the steels containing 3 pct Ni at the corresponding temperatures (Figs. 3, 4, and 5, respectively) indicates that reduction in nickel content from 3 to 2 pct lowers the allowable chromium content for a completely austenitic structure by approximately ½ pct. On the other hand, this loss of austenite stability may be compensated for by the use of an additional 0.05 pct N.

At the 1 pct Ni level, Figs. 9, 10, and 11, austenite-austenite plus δ ferrite phase boundaries are lowered by an additional ½ pct Cr. Again, compensation for the decrease in nickel content can be made by the use of an additional 0.05 pct N. The trend of reduced austenite stability with increased manganese content has not been significantly altered by the progressive reduction in nickel content. This observation explains the commercial advantages of changing the original 16 pct Cr-1 pct Ni-17 pct Mn composition to 15 pct Cr-1 pct Ni-15 pct Mn to improve hot workability. Although these steels contained only 0.15 pct N, these structural diagrams suggest that decreasing both the chromium and manganese contents reduced or eliminated the δ ferrite present at hot rolling temperatures. Since increasing the manganese content from 12 to 18 pct consistently failed to enhance austenite formation, it follows that the only advantage found for the higher manganese contents in this study was that of increasing the solid solubility for nitrogen.

The final set of structural diagrams, Figs. 12, 13, and 14, shows the phase relationships in nickel-free steels. It can readily be seen in Fig. 14 that, at 2300°F, a steel containing 17.50 pct Cr, 14.50 pct Mn, and 0.40 pct N* would not contain δ ferrite.

* Patent applied for by the United States Steel Corp. The trade-name is USS Tenelon.

Manganese contents below 14 pct might provide nitrogen gas evolution during solidification and produce internal unsoundness. For applications where lower chromium contents can be tolerated, lower nitrogen contents, for example, 16 pct Cr and 0.30 pct N, would provide completely austenitic structures at 2300°F.

An evaluation of the influence of temperature upon the austenite-austenite plus δ ferrite phase boundary can be made by comparing the positions of the boundaries representing 2100°, 2200°, and 2300°F equilibria for each level of nickel and nitrogen investigated. This effect is important commercially, where the highest permissible heating temperatures are used in hot working operations to minimize or eliminate expensive reheating procedures. The structural diagrams, Figs. 3 through 14, indicate that, in the temperature range from 2100° to 2300°F, austenite stability is reduced the equivalent of approximately 0.25 pct Cr for each 100°F increase in temperature. This loss in austenite stability could be offset by the presence of an additional 0.02 pct N or 0.40 pct Ni. This is a graphic example of the necessity for regulating the maximum heating temperature of commercial heats of the less stable austenitic stainless steels according to chemical composition.*

The relative austenite forming abilities of nickel and nitrogen in these Cr-Ni-Mn-N steels are given in Fig. 15. This diagram shows the austenite-austenite plus δ ferrite phase boundaries at 2300°F as a function of chromium, nitrogen, and nickel content in steels containing 0.10 pct C and 15.50 pct Mn. The curves indicate that, in these steels, approximately 0.05 pct N is equivalent to 1 pct Ni in preventing δ ferrite precipitation. Certainly these results predict greater use of nitrogen as an austenite former in stainless steels of the future.

The development of these elevated temperature phase relationships in 0.10 pct C low nickel or nickel-free stainless steels permits the selection of various compositions (chromium, nickel, manganese, and nitrogen contents) which will be completely austenitic at hot working temperatures. Of course, many physical properties, such as tensile properties, weldability, formability, and corrosion and oxidation resistance of such new steels must be evaluated prior to their commercial adoption. Successful development of these new steels necessitates the close cooperation of the steel-producing, fabricating, and consuming industries.

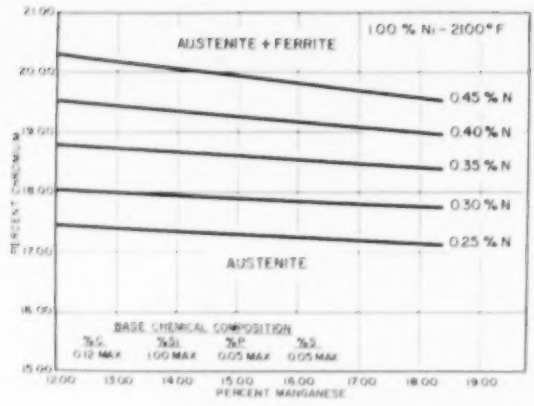

Fig. 9—Structural diagram for 1.00 pct Ni-0.25 to 0.45 pct N steels after heating for 1 hr at 2100°F and water quenching.

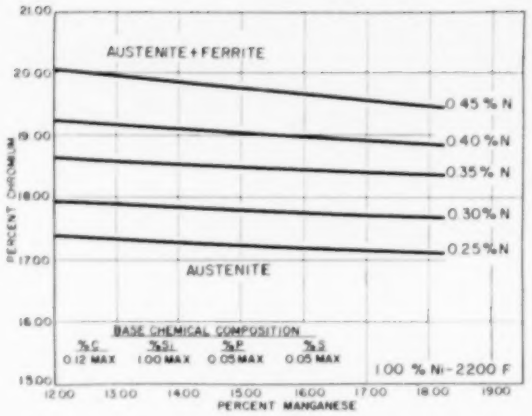

Fig. 10—Structural diagram for 1.00 pct Ni-0.25 to 0.45 pct N steels after heating for 1 hr at 2200°F and water quenching.

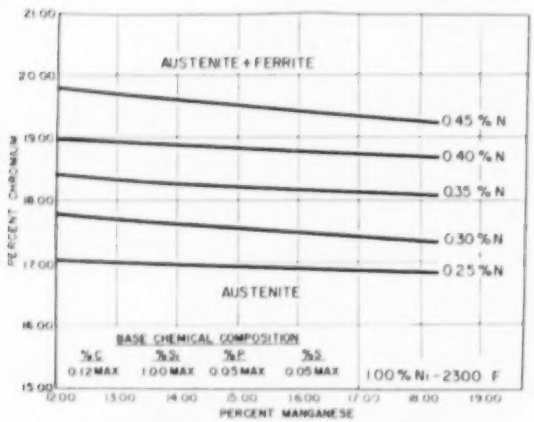

Fig. 11—Structural diagram for 1.00 pct Ni-0.25 to 0.45 pct N steels after heating for 1 hr at 2300°F and water quenching.

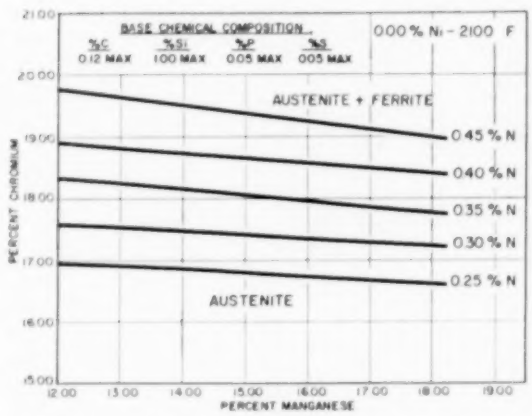

Fig. 12—Structural diagram for 0.00 pct Ni-0.25 to 0.45 pct N steels after heating for 1 hr at 2100°F and water quenching.

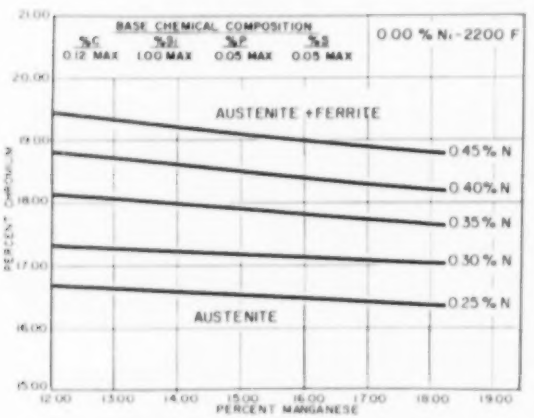

Fig. 13—Structural diagram for 0.00 pct Ni-0.25 to 0.45 pct N steels after heating for 1 hr at 2200°F and water quenching.

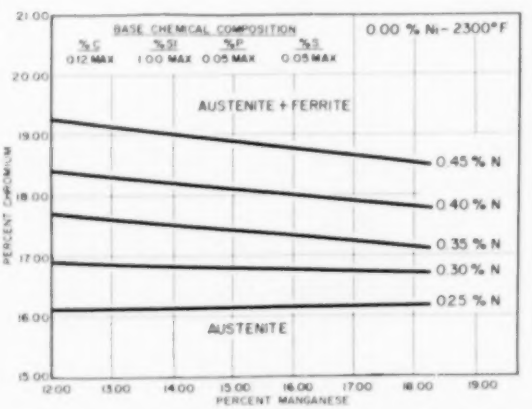

Fig. 14—Structural diagram for 0.00 pct Ni-0.25 to 0.45 pct N steels after heating for 1 hr at 2300°F and water quenching.

Summary

This elevated temperature (2100° to 2300°F) constitutional study of the Cr-Ni-Mn-N system over the composition ranges 15 to 21 pct Cr, 0 to 3 pct Ni, 12 to 18 pct Mn, and 0.25 to 0.45 pct N has shown that:

1) Increasing amounts of nitrogen and nickel contribute strongly to austenite formation, while chromium strongly promotes and manganese weakly promotes δ ferrite formation.

2) One half pct Cr in excess of the limit of austenite stability at 2300°F will produce approximately 3 pct of the δ ferrite.

3) Increasing the nitrogen content by approximately 0.05 pct is as effective as an increase of 1 pct Ni content in enhancing austenite formation at 2300°F. Either addition permits an increase in chromium content of approximately 0.60 pct without decrease in austenite stability.

4) Increasing amounts of both chromium and manganese are effective in enhancing the solid solubility of these steels for nitrogen. Since manganese mildly decreases austenite stability, the principle advantage of higher manganese content is its beneficial influence on nitrogen solubility.

5) The effect of temperature in the range from 2100° to 2300°F is to shift the austenite-austenite plus δ ferrite phase boundary to lower chromium contents, i.e., a 0.25 pct lower chromium content for each 100°F increase in temperature.

6) A nickel-free stainless steel containing 0.10 pct C, 17.50 pct Cr, 14.50 pct Mn, and 0.40 pct N is completely austenitic at hot working temperatures as high as 2300°F.

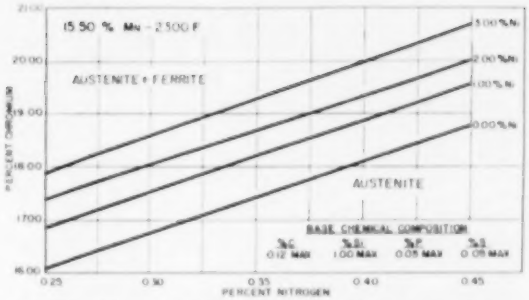

Fig. 15—Effect of nitrogen, nickel, and chromium upon the austenite stability of 15.50 pct Mn steels heated for 60 min at 2300°F and water quenched.

Acknowledgments

The authors wish to express their appreciation to J. J. Heger for constructive criticism and advice, to Mary E. Potter for the metallographic examinations, and to K. T. Rice for the magnetic ferrite ratings.

References

[1] R. H. Aborn: Modern Stainless Steels. *Metal Progress*, 1954, vol. 65, No. 6, pp. 115-125.

[2] F. P. Huddle: Nickel Conservation With High-Manganese Stainless Steels. *Metal Progress*, 1955, vol. 68, No. 6, pp. 100-103.

[3] R. H. Henke and R. A. Lula: Rare Earths Counteract Hot Rolling Defects in Stainless Steel. JOURNAL OF METALS, 1954, vol. 6, No. 8, pp. 883-888.

[4] G. F. Tisinai and C. H. Samans: Phase Relationships and Mechanical Properties of Some Iron-Chromium-Carbon-Nitrogen Alloys. *ASM Trans.*, 1956, vol. 49.

[5] R. Franks, W. O. Binder, and J. Thompson: Austenitic Chromium-Manganese-Nickel Steels Containing Nitrogen. *ASM Trans.*, 1955, vol. 47, pp. 231-266.

[6] H. Krainer and O. Mirt: Constitution Diagram of Nitrogen-Containing Chromium and Chrome-Manganese Steels. *Archiv für Eisenhüttenwesen*, 1942, vol. 15, pp. 467-472.

Discussion of this paper sent (2 copies) to AIME by Sept. 1, 1957 will appear in AIME *Transactions* Vol. 212, 1958, and in JOURNAL OF METALS, April 1958.

Electrical Resistivities and Phase Transformations Of Lanthanum, Cerium, Praseodymium, and Neodymium

The electrical resistivities of high purity lanthanum, cerium, praseodymium, and neodymium were investigated as a function of temperature over the range from room temperature to near the melting points of the metals. Transformation temperatures were observed in these metals which were confirmed by supplementary X-ray diffraction studies.

by F. H. Spedding, A. H. Daane, and K. W. Herrmann

F. H. SPEDDING, A. H. DAANE, and K. W. HERRMANN are associated with the Institute for Atomic Research and Dept. of Chemistry, Iowa State College, Ames, Iowa.

TP 4318E. Manuscript, Oct. 20, 1955. Cleveland Meeting, October 1956.

CONSIDERABLE confusion exists in the literature concerning the phase transformations exhibited by the lighter rare earth metals; namely, lanthanum,[1-9] cerium,[1,2,3,5,8,9,10] praseodymium,[8] and neodymium.[1,8,10,11] To obtain further information

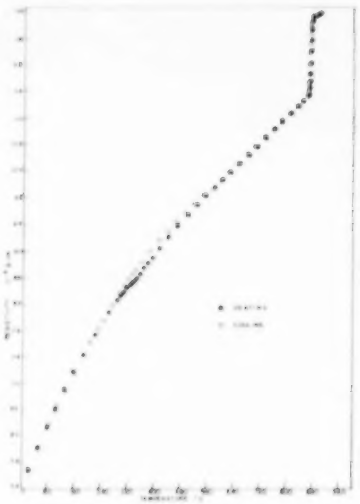

Fig. 1—Electrical resistivity of lanthanum.

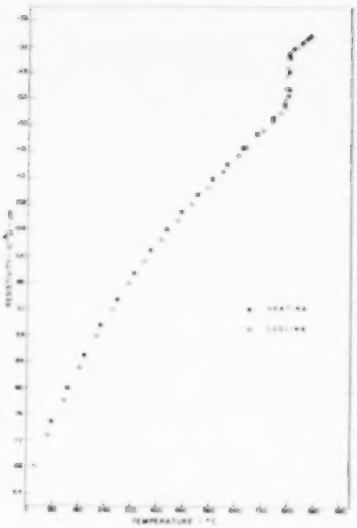

Fig. 3—Electrical resistivity of praseodymium.

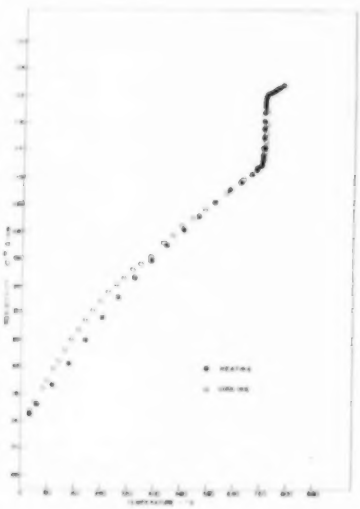

Fig. 2—Electrical resistivity of cerium.

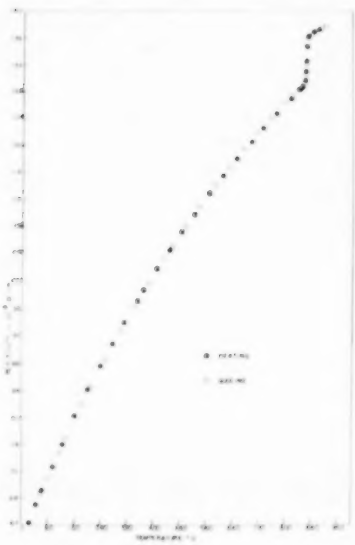

Fig. 4—Electrical resistivity of neodymium.

concerning these phenomena the electrical resistivities of the above-mentioned metals of high purity were investigated as a function of temperature. Whereas earlier resistivity work[1,12,15,25] was limited to maximum temperatures of about 750°C, this study was carried out to temperatures very close to the melting points of the respective elements.

Experimental

Sample Preparation—The metals were prepared in the Ames Laboratory by methods reported earlier.[5] After casting the metal in $\frac{3}{8}$-in. diam Ta crucibles and subsequently machining off the tantalum, the samples were reduced in size by repeated rolling and swaging. The specimens were periodically annealed in vacuo at about 300°C and cleaned with a 5 pct HNO_3 solution before and after each size reduction. The final approximate dimensions of the samples were 5 in. in length and 1/16 in. in diam.

Method—The dc potentiometric method was used for determining the electrical resistance values at various temperatures. A constant current source furnishing 100 ±0.01 ma was employed in addition to a precision potentiometer, galvanometer, and standard 1-ohm resistance. The samples were placed in a high vacuum system in which a pressure of not greater than 2×10^{-5} mm Hg was maintained and were heated in a 30-in. long Kanthal-wound resistance furnace which kept the entire specimen at a uniform temperature. Heating and cooling rates of approximately 2°C per min were employed except in regions where anomalous behavior was suspected. In these ranges the rates were decreased to about 0.5°C per min. The samples were cycled at least two times to induce homogeneity and remove the strains incurred on fabrication. All electrical connections to the rare earth metals were made with tantalum to avoid contamination. A calibrated Chromel-Alumel thermocouple was used to deter-

mine the temperature, which ranged from room temperature to within 20° to 100°C below the melting points of the metals studied. The distance, L, between potential probes was measured with a General Electric vernier scale illuminator, and a metric micrometer was used to obtain the radius, r, of the specimen. Knowing the value of the resistance, R, from the emf measurements, the resistivity, ρ, was calculated from the relationship $\rho = \frac{R \quad r^2}{L}$. An error of no greater than 1 pct was estimated for any one resistivity value. After examination the X-ray diffraction pattern of each metal was obtained with a Norelco diffractometer unit. Each specimen was also spectrographically analyzed for other rare earths and common impurities.

Table I. Electrical Resistivities and Phase Transformation Temperatures of Lanthanum, Cerium, Praseodymium, and Neodymium

Element	Purity, Pct	Resistivity at 25°C x 10^6 Ohm-Cm	Transformation Temperature, °C
La	99.8	56.8	320 to 340
			864
Ce	99.9	75.3	730
Pr	99.9	68.0	792
Nd	99.8	64.3	862

Results and Discussion

Due to strains incurred on fabrication of the metal rods the electrical resistivities during the initial heating trial were appreciably greater than those obtained on cooling and subsequent cycling. Reproducibility was achieved in the second thermal cycle and it is those values that are graphically illustrated in Figs. 1 to 4. As can be observed, cerium, praseodymium, and neodymium were found to exhibit only one phase transformation, whereas lanthanum showed two such phenomena. The discrepancy between the heating and cooling curves of cerium in Fig. 2 are due to temperature fluctuations during the cooling measurements. A subsequent recycle through the region from room temperature to 600°C gave the same results on heating and cooling as is shown on the heating curve of Fig. 2. The values of the electrical resistivities of the metals at 25°C, their purities, and their transformation temperatures are given in Table I. It is interesting to note that many of the values cited in the literature for the melting points of these elements are very close to the tabulated high temperature phase transitions.

Table II. Lattice Constants for Lanthanum, Cerium, Praseodymium, and Neodymium

Metal	Structure	Lattice Constants, A	
		a	c
La, room temperature	Hexagonal	3.770	12.159
La, above 340°C	Face-centered-cubic	5.31	
Ce	Face-centered-cubic	5.1612	
Pr	Hexagonal	3.672	11.835
Nd	Hexagonal	3.658	11.799

Lanthanum, praseodymium, and neodymium were found to have a room temperature structure that was hexagonal, with stacking sequences along the c axis of *ABAC*,[25] as has been found previously for neodymium by Ellinger[26] and Behrendt[27]. This is essentially a close-packed structure with a c/a ratio twice as large as that previously reported for lanthanum and praseodymium. Cerium was found to be entirely face-centered-cubic with a lattice constant in agreement with previous values in literature. A detailed account of crystallographic studies of the rare earth metals may be found in another paper from this laboratory.[25] The lattice constants for lanthanum, cerium, praseodymium, and neodymium are given in Table II.

High temperature crystallographic studies still in progress have shown the intermediate phase of lanthanum to be face-centered-cubic with a lattice parameter of $a_0 = 5.31$A. Cerium, praseodymium, and neodymium retain their room temperature structures up to their respective high temperature transitions. The high temperature forms of these metals that exist up to their melting points have not been identified, but from the very large resistivity anomalies exhibited at the high temperature transformations, these are expected to differ significantly from the low temperature modifications.

Acknowledgments

The authors wish to acknowledge the assistance of J. E. Powell, who prepared the rare earth oxides, and D. H. Dennison, who prepared the metals.

References

[1] F. M. Jaeger, J. A. Bottema, and E. Rosenbohm: *Recueil des travaux chimiques des Pays-Bas*, 1938, vol. 57, p. 1137.
[2] F. Trombe: *Comptes rendus*, 1934, vol. 198, p. 1591.
[3] F. Trombe and M. Foex: *Comptes rendus*, 1943, vol. 217, p. 501.
[4] P. W. Bridgman: *Proceedings* American Academy of Arts and Sciences, 1948, vol. 76, p. 55.
[5] R. Vogel and T. Heumann: *Ztsch. für Metallkunde*, 1947, vol. 38, p. 1.
[6] W. Massenhausen: *Ztsch. für Metallkunde*, 1952, vol. 43, p. 53.
[7] R. Vogel and H. Klose: *Ztsch. für Metallkunde*, 1954, vol. 45, p. 633.
[8] F. H. Spedding and A. H. Daane: JOURNAL OF METALS, 1954, vol. 6, p. 504.
[9] J. Loriers: *Comptes rendus*, 1948, vol. 226, p. 1018.
[10] R. Vogel: *Ztsch. für anorganische und allgemeine Chemie*, 1918, vol. 91, p. 277.
[11] F. Trombe: *Comptes rendus*, 1944, vol. 219, p. 90.
[12] M. Foex: *Comptes rendus*, 1944, vol. 219, p. 117.
[13] F. Trombe: *Journal des recherches* Centre National de la Recherche Scientifique, 1954, vol. 29, p. 65.
[14] J. Loriers: *Comptes rendus*, 1948, vol. 226, p. 1018.
[15] D. H. Ahmann: *Journal of Science* Iowa State College, 1953, vol. 27, p. 120.
[16] F. Trombe and M. Foex: *Comptes rendus*, 1951, vol. 232, p. 63.
[17] L. F. Bates, S. J. Leach, R. G. Loasby, and K. W. H. Stevens: *Proceedings* Physical Soc., London, 1955, vol. 68, p. 181.
[18] C. Benedicks: *Svensk Kemisk Tidskrift*, 1915, vol. 27, p. 136.
[19] C. Benedicks: *Ztsch. für Metallkunde*, 1915, vol. 7, p. 228.
[20] P. W. Bridgman: *Proceedings* American Academy of Arts and Sciences, 1921, vol. 56, p. 59.
[21] P. W. Bridgman: *Proceedings* American Academy of Arts and Sciences, 1927, vol. 62, p. 207.
[22] J. C. McLennan, J. F. Allen, and J. O. Wilhelm: *Philosophical Magazine*, 1930, series 7, vol. 10, p. 500.
[23] W. J. de Haas and J. Voogd: *Commun. Kamerlingh Onnes Lab. Univ. Leiden*, 1932, vol. 20, p. 22.
[24] N. R. James, S. Legvold, and F. H. Spedding: *Physical Review*, 1952, vol. 88, p. 1092.
[25] F. H. Spedding, K. W. Herrmann, and A. H. Daane: *Acta Crystallographica*, 1956, vol. 9, p. 559.
[26] F. H. Ellinger: *AIME Trans.*, 1955, vol. 203, p. 411; JOURNAL OF METALS, February 1955.
[27] D. Behrendt: Private communication.

Discussion of this paper sent (2 copies) to AIME by Sept. 1, 1957 will appear in AIME *Transactions* Vol. 212, 1958, and in JOURNAL OF METALS, April 1958.

Temperature Dependence of the Hardness Of Secondary Phases Common in Turbine Bucket Alloys

Representative examples of the most common types of secondary phases in turbine bucket alloys have been synthesized in bulk and their hardness measured from room temperature to 800°C. It is concluded that high hot hardness of the dispersed phase is an important factor in the high temperature strength of alloys but that other (as yet not explicitly identified) factors are also significant.

by J. H. Westbrook

UNTIL very recently the development of high temperature alloys has been strictly empirical. It is, in fact, a great tribute to the intuition, perseverance, and industry of the practicing metallurgists of this country and abroad that the amazing increases in gas turbine service temperature over the past 15 years have been achieved with so little fundamental knowledge. The result of this development has been the realization of successful but highly complex alloys possessing five, six, or more alloying elements and correspondingly complex microstructures.

Within the last few years, considerable effort has been devoted to the identification of the secondary phases in these alloys and to the correlation of the presence or absence of such phases with alloy properties. Little attention, however, has been given the problem of identification of the mechanism(s) by which such phases enhance the properties of the alloy and especially to the assessment of the particular properties of the secondary phase (either intrinsic or relative to the matrix phase) which are basically responsible for the improvement. Conceivable mechanisms which might apply include dispersion hardening and precipitation hardening. In both cases geometrical factors—particle size, dispersion, volume fraction, etc.—and agglomeration re-

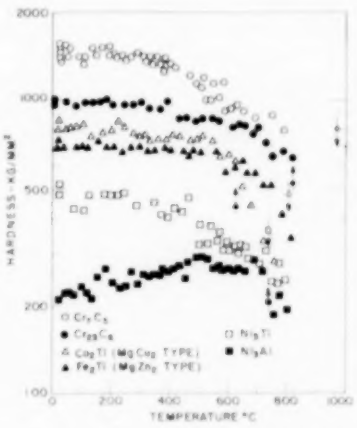

Fig. 1—Temperature dependence of the hardness of some secondary phases common in turbine bucket alloys. Arrow indicates 0.6 $T_{m.p.}$

J. H. WESTBROOK, Junior Member AIME, is associated with General Electric Co., Schenectady.

TP 4582E. Manuscript, Dec. 14, 1956. Cleveland Meeting, April 1957.

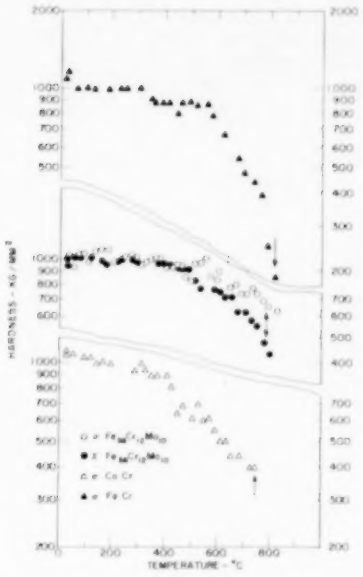

Fig. 2—Temperature dependence of the hardness of some secondary phases common in turbine bucket alloys. Arrow indicates 0.6 $T_{m.p.}$

sistance are recognized to be of major importance, yet properties of the secondary phases must also play a role whose significance cannot presently be evaluated. These properties presumably include high strength of the dispersed phase at the service temperature and, for the precipitation systems, high matrix lattice strain without loss of coherency. Data are not available, however, to assess the importance of high temperature strength of the dispersed phase to the high temperature performance of the whole alloy.

In order to fill this gap in our knowledge, it was decided to measure the temperature dependence of hardness of a large group of secondary phases in turbine bucket alloys up to and including the present service temperature. Then, according to the general hardness level and spectral distribution of hardness values, it might be decided if hardness of secondary phases at temperature is a primary, contributing, or inconsequential factor to the high temperature strength of an alloy. For example, finding that the high temperature hardness of the secondary phases was uniformly high relative to that of the matrix would be strong evidence that this is a major factor in the high temperature strength of the alloy. On the other hand, a wide spectrum of high temperature hardness values among the secondary phases would indicate that this property is only a contributing or even inconsequential factor, according to whether the range of hardness values was found to fall substantially above or approximately spanning the matrix hardness level.

Availability of high temperature hardness data on such compounds would also be of aid to those developing new cermet type compositions embodying large volume fractions of compounds of this type.[1,2]

The important secondary phases which have been identified in some of the prominent high temperature alloys are summarized in Table I. Compositions and properties of most of these alloys have recently been tabulated by Krivobok and Skinner.[3] The most frequently encountered phases can be divided into three groups and number no more than three or four types in each group. This classification and the specific compounds selected for study are shown in Table II.

Of the compounds listed in Table II, the cubic monocarbides and carbonitrides were eliminated from consideration in the present program since a detailed study of all of the cubic monocarbides is being made separately. Many variations are possible for each of the other compounds listed which were not considered in the present investigation for reasons of simplicity. These variations include both simple and high order isomorphs as well as complex solid solution compounds. Choice was made instead of representative prototypes of each structure. In addition, specimens were obtained of two actual high temperature alloys, S-816 and Jetalloy 1650, for purposes of hardness level comparison.*

* The author is indebted to T. A. Prater for these samples.

Experiment

Preparation of Samples—Approximately 100 g samples of the selected phases were prepared by cold crucible arc melting in the manner described in a previous paper.[4] Following this, all samples were given a homogenization anneal of 8 hr about 100°C below the respective melting points or temperatures at which the first liquid phase formed. Phases known to form by solid state reaction were given additional long time equilibration anneals immediately below their formation temperature. Considerable difficulty was experienced in many instances in achieving single phase materials satisfactorily even though composition control in the melting process was excellent, as indicated by chemical analysis. The root of the problem apparently lies in the extremely narrow composition range for many compounds and from uncertainties in the published phase diagrams. These difficulties were surmounted in most cases either by making up several alloys bracketing the nominal composition of the phase under consideration or by remelting a single heat with very small additions of the components as guided by metallographic examination. Special problems and observations arising from the preparation of specific phases are discussed below in reference to the individual cases. Positive identification was made for every sample by X-ray diffraction patterns. It might incidentally be pointed out that, insofar as the author is aware, this is the first time that many of the phases considered have been synthesized in bulk. The availability of these specimens will now permit measurement of other prop-

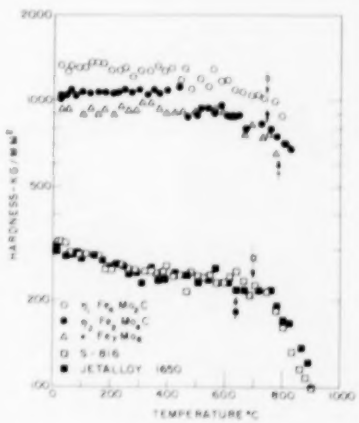

Fig. 3—Temperature dependence of the hardness of some secondary phases common in turbine bucket alloys. Arrow indicates 0.6 $T_{m.p.}$

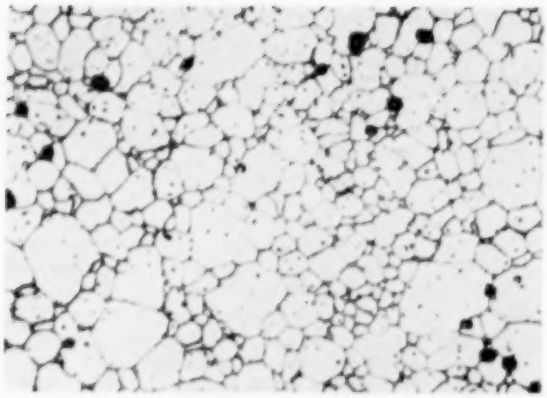

Fig. 4—Micrograph of ϵ-Fe_2Mo_3, second phase iron. Etched with acetic plus nitric acids. X500. Reduced approximately 15 pct for reproduction.

erties of interest, outside the scope of the present paper.

Hardness Testing—Indentation hardness measurements were made on all samples with a Vickers pyramidal indenter and a 200 g load on a micro hot hardness tester of modified Bergh design.[28] The testing procedure was identical to that previously employed[27] except that the indenter material was varied according to the hardness and high temperature reactivity of the compound being tested.[29] The indenter materials used included diamond, sapphire, boron carbide, and titanium diboride.

Hardness-temperature curves were run at least twice on each sample to ensure that surface work hardening effects had been eliminated.[30] The reduced data were finally plotted for convenience on a semilogarithmic scale.[30]

Results and Discussion

The principal experimental results are presented in the curves of Figs. 1 to 3 and may be compared with the behavior of typical high temperature alloys shown in Fig. 3. Representative micrographs of the phases prepared are depicted in Figs. 4 to 6. Comparison of the properties of the compounds is facilitated by the bar graphs of Fig. 7, which show the relative properties at room temperature and at 800°C, approximately the present service temperature. A number of general observations may be made, viz.:

1) At room temperature, a wide spectrum of hardness levels is found.

2) Except for Ni_3Al all compounds studied are significantly harder at room temperature than the typical high temperature alloy.

3) At 800°C the total spread in hardness values among the group is reduced considerably but distinct differences in hardness still exist between individual phases.

4) All compounds studied are significantly harder at 800°C than the typical high temperature alloy.

5) The compounds vary widely in their ability to retain their low temperature hardness at high temperatures, either absolute or homologous. However, some striking reversals emerge from such comparisons. The outstanding ability of some compounds of only moderate melting point to retain a high fraction of their low temperature hardness at high homologous temperatures, e.g., Ni_3Al and Co_3Ti, suggests further inquiry into the source of the resistance of their bonding to thermal forces. On the other hand, the high hardness at 800°C of compounds such as the chromium carbides appears to be a direct reflection of their melting point and does not seem to imply unusual temperature dependence of bond strength.

6) These results constitute some of the highest hardness values at high temperatures yet reported. A comparison of some of the harder compounds studied in this investigation with those reported for other hot-hard materials is given in Table III.

Table I. Common Microconstituents in High Temperature Alloys

Type	Alloy	Principal* Identified Microconstituents	Reference No.
Cr-Ni steels	A-286	Laves, Ni_2Ti,	10
		γ' (Ni, Ti, Si)	11
			12
	16-25-6	M_6C, $M_{23}C_6$, $CrMoN_2$,	13
		Fe_2Nb_3, Fe_7(Mo, W)$_6$	14
		$Fe_2Nb_3Si_3$	15
	G-18B	Nb(C, N), $M_{23}C_6$, M_6C	16
			17
	15-15N	Nb(C, N), Laves ($MgZn_2$ type)	16
	Cr-Mo stainless	Laves-Fe_2Ti ($MgZn_2$ type), χ	18
			19, 20
			21
			22
Cobalt base	422-19	$Cr_{23}C_6$, Cr_7C_3,	15
		Cr_3C_2, M_6C	23
			24
	H.S.-21	$Cr_{23}C_6$, Cr_7C_3, M_6C, σ,	25
		Cr_3C_2	24, 26
			15
			27
			23
	I-336	M_6C, Nb(C, N), $M_{23}C_6$	13
			24
	X-63	$Cr_{23}C_6$, Cr_2N	24
	X-40	$Cr_{23}C_6$	24
			15
	S-816	$Cr_{23}C_6$, NbC, M_6C	24
			15
			23
			14
	J-alloys	$Cr_{23}C_6$, Cr_7C_3, M_6C,	24
		TaC, Cr_3C_2	23
	E-32	M_6C, $M_{23}C_6$, NbC	28
Nickel base	Inconel X	TiN, NbN, $M_{23}C_6$,	14
		Ni_3Al	15
	Inconel X-500	Ni_3Al, M_6C	29
	Inco 700	Ni_3Al, M_6C	29
	Waspaloy	Ni_3Al, M_6C, Ti(C, N)	29
	M-252	M_6C, M_7Ti_4, Ti(C, N)	29
			13
	Nimonic 80	Ni_3Al	30
			31
	Jetalloy 1570	Ni_3Ti, M_6C, Fe_7Mo_6	32
Mixed base	N-155	Cr_7C_3, M_6C, $M_{23}C_6$,	15
		Nb(C, N), Fe_2W	23
		(Laves)	16
			14
Chromium base, developmental	60-25-15	σ, $M_{23}C_6$	33
	Cr-Mo-Fe		34, 35

* Not all compounds listed have been found by every investigator even for the same conditions of heat treatment.

Detailed discussion of the experimental results on particular phases follows.

Chromium Carbides, Cr_7C_3 and $Cr_{23}C_6$—These two chromium carbides were chosen as prototypes of the M_7C_3 and $M_{23}C_6$ type carbides, frequently found in high temperature alloys. The third chromium carbide, Cr_3C_2, while important as a new base composition for cutting tools, is not ordinarily found as a constituent of high temperature alloys. No particular difficulties were encountered in preparing these compounds by arc melting. There appears to be little to choose between these two carbides on the basis of their 800°C hardness as shown in Fig. 1. While Cr_7C_3 has the higher melting point and possibly more complex crystal structure, its hardness appears to be decreasing more rapidly at high temperatures than does that for $Cr_{23}C_6$. Lane and Grant[28] have presented evidence that during the aging of

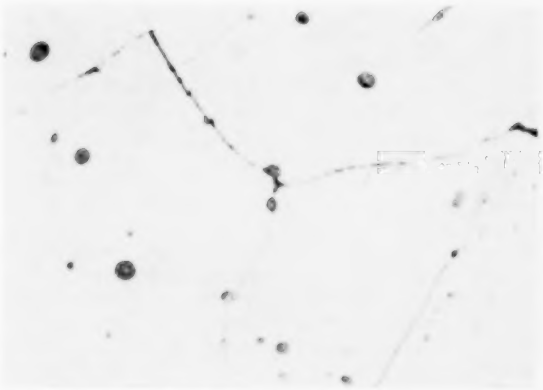

Fig. 5—Micrograph of Ni_3Ti; oxide inclusions present. Etched with HF plus HNO_3 plus water. X500. Reduced approximately 15 pct for reproduction.

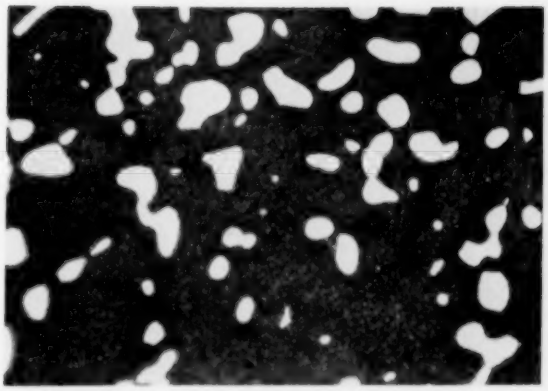

Fig. 6—Micrograph of $\eta_1 Fe_3Mo_3C$, heat tinted after mechanical polish. Second phase present, $\eta_1 Fe_3Mo_3C$. X500. Reduced approximately 15 pct for reproduction.

certain high temperature alloys primary Cr_7C_3 decomposes to $Cr_{23}C_6$ and free carbon, which in turn reacts with matrix to form more $Cr_{23}C_6$. In view of the present observation that $Cr_{23}C_6$ is not significantly harder than Cr_7C_3 at the service temperature, the improved high temperature properties observed in alloys in which this aging reaction occurs must be attributed instead to changes in the amount and/or size distribution of the carbides. There is no apparent explanation for the lack of agreement between the room temperature hardness values for the chromium carbides and those reported in the literature as shown in Table IV.

Laves Phases, Fe_2Ti and Co_2Ti—Structurally there are three types of AB_2 Laves phases distinguished by the stacking arrangements of tetrahedra of *A* atoms and designated as the $MgZn_2$, $MgNi_2$, and $MgCu_2$ types. Only the $MgZn_2$ and $MgCu_2$ types are represented among the secondary phases in high temperature alloys although it has been claimed that the $MgNi_2$ type exists as a polymorph in Co_2Ti and certain others. Recent evidence indicates that these last results were probably occasioned by the presence of impurities.[48] Fig. 1 indicates that there appears to be little difference in the hardness-temperature behavior of the two compounds tested. Co_2Ti ($MgCu_2$ type) is slightly harder at room temperature than Fe_2Ti ($MgZn_2$ type) but the reverse is true at 800°C. Although these differences are relatively small it would be interesting to know if these result from the difference in stacking arrangement or from the substitution of iron for cobalt atoms in an approximately equivalent structure. As may be noted from Fig. 1, both compounds are outstanding in their ability to retain hardness at high homologous temperatures. The room temperature hardness measured for Fe_2Ti agrees satisfactorily with the value (637 kg per sq mm) found by Arbiter.[2]

A$_3$B Compounds, Ni_3Al and Ni_3Ti—These two compounds may, in fact, be more closely related than would appear from a superficial consideration of their crystal structures. Nickel forms the cubic Cu_3Au structure not only with aluminum and silicon but also with several of the other transition metals from its own period in the periodic table. Yet when one progresses far to the left, the structure becomes first tetragonal with vanadium and then hexagonal with titanium. In addition, when both titanium and aluminum are present in nickel base alloys, these two structures are usually competitive. It will be observed from Fig. 1 that the hardness behavior of these two compounds differs radically. Ni_3Ti, although almost three times as hard as Ni_3Al at room temperature, becomes about equal to Ni_3Al at 800°C. Its hardness-temperature curve has a definite slope right from room temperature. On the other hand, the hardness curve for Ni_3Al shows an anomalous *increase* in hardness with increasing temperature, reaching a maximum at about 500°C. This surprising result was carefully checked and found to be completely reproducible. Although several possible sources of this anomaly were investigated no unequivocal explanation could be established. Further study is indicated. The conclusion of Hignett[31] and Nordheim and Grant[48] that Ni_3Al is the preferred precipitate in the case of Ni-Al-Ti alloys is supported by the present results. Guard and Prater,[31] however, have developed an outstanding high cobalt austenitic alloy strengthened by precipitation of Ni_3Ti. The improved performance may result either from strengthening of the compound by solid solution alloying with cobalt or from the effects of cobalt on some matrix-precipitate relationship. It is also of interest to note that Ni_3Ti has recently been found to be a potent hardener for zinc base alloys.[49]

Table II. Compounds Selected for Study

Group	Type	Compound Selected	Melting Point, °C
Carbides	$M_{23}C_6$	$Cr_{23}C_6$	1518
	M_6C (η)	Fe_3Mo_3C η_1	~1400
		Fe_4Mo_2C η_2	~1400
	Cr_7C_3	Cr_7C_3	1728
	$M_7(C, N)$	None, see text	
Intermetallics of base elements	σ	σ FeCr	1520
		σ CoCr	1470
Intermetallics with incongruous elements	χ	$Fe_{36}Cr_{12}Mo_{10}$	1490
	ϵ	Fe_7Mo_6	1480
	A_3B	Ni_3Ti	1378
		Ni_3Al	1395
	Laves	Fe_2Ti ($MgZn_2$ type)	1530
		Co_2Ti ($MgCu_2$ type)	1250

The σ Phases, FeCr and CoCr—A highly complex tetragonal structure, σ, essentially the same as that for β-uranium, is perhaps the most common intermetallic type among the transition metals aside from the Laves phases. The rules for its formation are as yet poorly understood. It was originally planned to study only σ-FeCr, but when difficulty

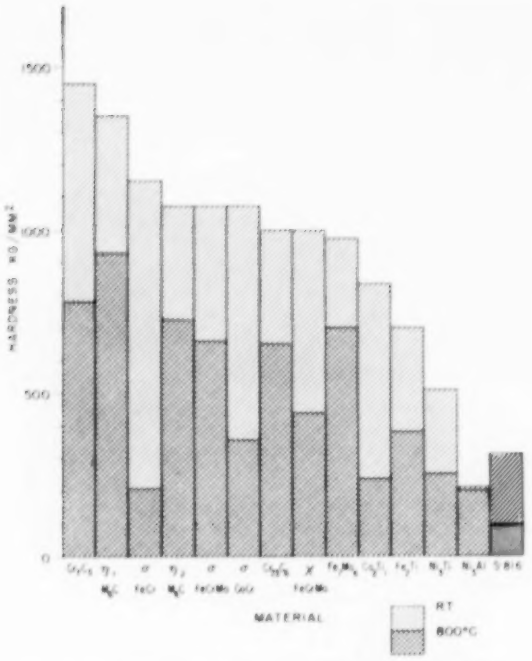

Fig. 7—Comparison of the room temperature and 800°C hardness values for representative secondary phases and a typical high temperature alloy.

was experienced in obtaining a single phase specimen (the reaction is quite sluggish at 800°C, approximately the critical temperature) σ-CoCr was added to the group of compounds under study. The σ-CoCr forms at relatively high temperatures and no difficulty was experienced in obtaining a satisfactory specimen. Ultimately, a specimen of σ-FeCr was also obtained single phase by a treatment of 200 hr at 750°C following 15 pct cold deformation. In the course of preparation of a χ phase specimen from the Fe-Cr-Mo system (see below) a satisfactory single phase was achieved. It was surprising to learn from the X-ray pattern that the sample was σ rather than χ, since the findings of McMullin et al.[7] and of Goldschmidt[6] indicate χ to be stable over a range of temperatures, at least 800° to 1000°C. The stability of σ in this composition with high annealing temperature (~1400°C) was verified and a hot-hardness run made in the σ condition. See further discussion below. As shown in Fig. 2, the three σ phases have essentially the same room temperature hardness but vary considerably in their high temperature hardness. The σ-FeCr softens quite rapidly in the 600° to 800°C range, due, no doubt, to the close approach to its critical temperature. The σ-CoCr softens somewhat more slowly and the complex σ-FeCrMo very much less. This latter result may be due to a further ordering of atoms among the five types of crystallographic positions in the structure.[6] Hardness data for the various σ phases are compared with literature values in Table IV.

The χ Phase, $Fe_xCr_yMo_z$.—The existence of a new intermetallic phase with the α-manganese structure was first reported by Andrews[7,8] and subsequently prepared by McMullin et al.[7] as an equilibrium single phase alloy in the Fe-Cr-Mo system. According to the findings of McMullin et al.,[7] verified by the structure study of Kasper,[9] the ideal composition for χ phase in this system may be written as $Fe_{36}Cr_{12}Mo_{10}$. As indicated previously, this composition as first prepared by a homogenization anneal at 1400°C was found to have the σ structure. However, a subsequent anneal of 200 hr at 815°C converted this sample wholly to χ.

This result provides an interesting sidelight on the Fe-Cr-Mo phase equilibria and may reveal a hitherto unsuspected relation between the σ and χ structures. In the Fe-Mo binary, σ is stable only above 1180°C; and in the Fe-Cr system, only below 815°C; yet σ is apparently the stable phase at about 1400°C, near the midpoint of the quasibinary; and χ in the 800° to 1000°C range. The χ must therefore intrude itself into the phase space of σ, perhaps as shown in Fig. 8, an adaptation of a figure by Bückle.[10] This result has interesting implications with respect to the relative stability of σ and χ structures, as well as with respect to the ordering of atoms in σ phase.

The temperature dependence of hardness of χ-FeCrMo is compared in Fig. 2 with that for the same composition with the σ structure. The room temperature hardness of both structures is about 1000 kg per sq mm, but the σ form is significantly harder at 800°C and appears to be softening more slowly with temperature than the χ form. There was no indication of transformation from one form to another during the course of the hardness tests. The hardness data for χ phase are compared with literature values in Table IV, together with data for σ phase of comparable composition.

M_6C Carbides, Fe_3Mo_3C and Fe_4Mo_2C.—The M_6C carbides have long been recognized as significant phases not only in high temperature alloys but also in cemented carbides and high speed steels. Recently it has become apparent that the structure is more general, and includes analogous suboxides and nitrides M_4O and M_4N. Two structural variations are now distinguished and have been designated by Kislyakova[27] as η_1 and η_2. The η_1 type has the ideal composition $M_3M_3'C$ and may extend over a composition range broad enough to include $M_4M_2'C$. On the other hand, η_2 is confined to an extremely narrow range about $M_4M_2'C$. The η_1 and η_2 phases in the Fe-Mo-C system have been identified respectively by Westgren and Phragmen[28] as $a_o = 11.08$A and by Kuo[29] as $a_o = 11.26$A. The preparation of single

Table III. Comparison of 800°C Hardness of Various Hot-Hard Materials

Material	Hardness, Kg per Sq Mm	Reference No.
WC + TiC + Co	950*	40
η_1 Fe_3Mo_3C	930	This study
WC + Co	850*	40
Cr_3C_2	780	This study
O-30 cemented oxide	750†	67
η_2 Fe_4Mo_2C	720	This study
Fe_2Mo_2	700	This study
σ-FeCrMo	660	This study
$Cr_{23}C_6$	650	This study
TiC	550	41
Synthetic Al_2O_3	500	42
Quartz	400	42
Rhenium	240	43
Nimonic 80	240	43
S-816	100	This study
Tungsten	75	43
NiAl	60	37

* Measured by a dynamic technique with a cold indenter. Therefore, these numbers may be high relative to normal Vickers values.
† Approximate conversion from Rockwell *A* value.

Table IV. Comparison of Experimental and Literature Hardness Values

	Compound	Source	Hardness, Kg per Sq Mm* Room Temperature, °C	800°C
Chromium carbides	$Cr_{23}C_6$	Synthetic binary	1000	
	$Cr_{23}C_6$	Synthetic binary	1000[55]	
	$Cr_{23}C_6$	Cemented carbide	1650[54]	
	Cr_7C_3	Synthetic binary	1450	
	Cr_7C_3	Synthetic binary	1700[55]	
	Cr_7C_3	Cemented carbide	2100[54]	
σ phases	FeCr	Synthetic binary	1150	
	FeCr	Synthetic binary	1100 to 1300[50]	
	FeCr	σFeCr + 2 pct Ni	950 to 1100[50]	
	FeCr	18-8 Mo steel	750[51]	
	FeCr	25-20 steel	500[52] ‡	
	FeCrMo-σ	Synthetic ternary	1070	660
	FeCrMo†	Synthetic ternary	870[53]	744[53]**
	FeCrMo-σ	Synthetic ternary	941[53]	
	FeCrMo-σ	Synthetic ternary	~1300[54]¶	
	Co_2Cr_3	Synthetic binary	1070	
χ phases	FeCrMo-χ	Synthetic	1000	440
	FeCrMo-χ†	Synthetic	772[53]	665[53]**
	χ‡	Molybdenum stainless steel	465[51]	
M_6C carbides	$Fe_4(Mo, W)_2C$ (η_1)	High speed steel	1500 to 1800[51]	
	Co_3W_3C (η_1)	Cemented carbide	~2000[54]	
	Cr_1Fe_2Cr§ (η_2?)	Unknown steel	1300 to 1500[52]	
	Fe_4Mo_2C (η_1)	Synthetic alloy	1350	
	Fe_2Mo_4C (η_2)	Synthetic alloy	1070	

* Superscript numbers refer to references at end of paper. Hardness numbers not followed by superscripts are from present study.
† Parke and Bens did not report any structure or metallographic determinations on their materials. Identification can be made, however, for their composition from subsequently published equilibria studies by others.[47, 48]
‡ Specific composition is unknown but probably Fe-Cr-Mo rich. Composition difference may account in part for the difference in hardness between Koh[52] on the one hand, and Parke and Bens[53] and this study on the other.
§ However, the most recent equilibria studies of this system do not show an η carbide.
‡ Low value probably due to cracking of σ under indentor.
¶ As read from reproduced micrograph.
** Test at 1600°F (871°C).

phase specimens of these two phases proved to be the most arduous portion of this investigation. This difficulty results from the narrow composition ranges, the poorly defined equilibria in this region of the Fe-Mo-C system,* and the fact that both η carbides form by very high temperature peritectic reactions. In neither case was a truly single phase specimen achieved. However, coarse grained specimens predominantly η_1 or η_2 were finally produced which were adequate to permit determination of the microhardness-temperature characteristic. The η carbides were among the hardest phases in the group when tested at room temperature, but intermediate with respect to retention of their hardness at 800°C. The room temperature data obtained on these carbides may be crudely compared with values found in the literature for other M_6C type carbides in Table IV.

* An auxiliary study[56] has resulted in a partial elucidation of this portion of the equilibrium diagram.

The ϵ Phase, Fe_7Mo_6.—This type of compound, also known as μ phase, is common particularly among the combinations of iron group elements with those of Group VI. The rhombohedral ϵ structure is somewhat similar to σ phase, especially with respect to the coordination of atoms.[57] Fe_7Mo_6 was among the hardest of the compounds tested both at room temperature and at 800°C. Since marked effects of solid solution alloying in compounds have been observed (previously in NiAl and related compounds[57] and now in σ phase) it would be interesting to explore this possibility in Fe_7Mo_6, which can be highly alloyed in certain ternary systems.[58]

Reiter and Hibbard[24] studied the high temperature properties of iron rich alloys hardened by dispersions of Fe_7Mo_6, and found a correlation between the increase in the 1200°F rupture or creep strength and the volume fraction of dispersed phase, in accordance with the prediction of Fisher, Hart, and Pry[59] from dislocation theory. Reiter and Hibbard speculated on the significance of the extrapolation of the linear log strength increment-log volume fraction plot to a 1.0 volume fraction, i.e., pure Fe_7Mo_6. This would apparently indicate a 1200°F strength for Fe_7Mo_6 of 500,000 psi, since the matrix strength can be neglected. If this value* is in turn converted to a hardness number according to the approximate relation derived by Tabor,[60] a value of 1020 kg per sq mm is obtained, in reasonable agreement with the measured 1200°F hardness of 900 kg per sq mm in this study.

* Rupture strength is assumed to be of the same order as the yield strength for the purposes of this approximation.

High Temperature Alloys, S-816 and J-1650—The hardness-temperature curves of the two conventional high temperature alloys chosen for comparative purposes as shown in Fig. 3 proved to be essentially identical. This result emphasizes one of the limitations of the hardness technique, since the long time properties of these two alloys are known to differ significantly. Jetalloy 1650 has a 100 hr, 1500°F stress rupture value of 34,000 psi, as compared to 29,000 psi for S-816.

General Conclusions

Since all phases chosen for study showed hardness values at high temperatures superior to those for

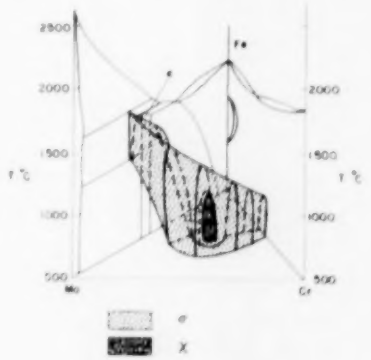

Fig. 8—Possible phase space relationship for σ and χ phases in the Fe-Cr-Mo system. Modification of a figure by Bückle.[50]

conventional high temperature alloys, high hot hardness would appear to be at least a contributing factor to the high temperature strength of these alloys. The spread in the 800°C hardness values observed for the group of compounds may indicate that other properties are also determinative with respect to the strength of the alloy. However, consideration of long time, high temperature strength properties might lead to a narrower range of strengths. Highly informative results might also be obtained from experiments on the high temperature strength of a series of synthetic alloys in which these phases were added singly to a common solid solution matrix.

The 800°C hardnesses of some of the compounds studied are among the highest values which have ever been reported for any material.

The cold crucible arc melting technique has proven particularly applicable for preparation of high purity samples of these compounds. In several instances, the first massive synthesis of the compounds was achieved.

Acknowledgments

The author is grateful for the invaluable assistance of A. J. Peat throughout the investigations. Thanks are also due J. G. McMullin, F. L. VerSnyder, R. W. Guard, and T. A. Prater for helpful discussions. R. W. Guard and J. E. Burke read and criticized the manuscript.

References

[1] W. Arbiter: New High Temperature Intermetallic Materials. WADC Technical Report No. 53-190. Amer. Electrometals Corp., 1953.

[2] W. Arbiter: New High Temperature Intermetallic Materials II. WADC Technical Report No. 53-190, Part II. Amer. Electrometals Corp., 1953.

[3] W. A. Maxwell and E. M. Grabla: Investigation of Nickel-Aluminum Alloys Containing From 14-34 Pct Aluminum. NACA Technical Note No. 3259, 1954.

[4] E. M. Grabla: Investigation of the Ni$_3$Al Phase of Nickel-Aluminum Alloys. NACA Technical Note No. 3660, 1956.

[5] H. Silverman, W. Arbiter, and F. Hodi: Effect of Sigma Phase on Co-Cr-Mo Base Alloys. *ASM Trans.*, 1957, vol. 49.

[6] R. L. Wachtell: Investigation of Various Properties of NiAl. WADC Technical Report No. 52-291, 1953.

[7] W. H. Herz: Investigation of Various Properties of NiAl II. WADC Technical Report No. 52-291-II, 1954.

[8] W. H. Herz: Investigation of Various Properties of NiAl III. WADC Technical Report No. 52-291-III, 1955.

[9] J. B. McAndrew and H. D. Kessler: Ti-36% Al as a Base for High Temperature Alloys. *AIME Trans.*, 1956, vol. 206, p. 1348; Journal of Metals, October 1956.

[10] H. J. Beattie, Jr. and F. L. VerSnyder: A-286 Alloy Phases. GE Thomson Laboratory Report No. DF55SE26, 1955.

[11] F. L. VerSnyder and H. J. Beattie, Jr.: The Laves Phase in A-286 Alloy. GE Thomson Laboratory Report No. R55TL028, 1955.

[12] C. H. Craver, G. N. Aggen, and W. W. Dyrkacz: A Study of Precipitation Hardening of A-286 Alloy. Allegheny Ludlum Steel Report No. R-H-0111-g8, 1955.

[13] H. J. Beattie, Jr. and F. L. VerSnyder: Micro-constituents in High Temperature Alloys. *ASM Trans.*, 1953, vol. 45, p. 397.

[14] L. O. Brockway and W. C. Bigelow: The Investigation of the Minor Phases of Heat Resistant Alloys by Electron Diffraction and Electron Microscopy. WADC Technical Report No. 54-589. University of Michigan, 1955.

[15] B. M. Rosenbaum: X-Ray Diffraction Investigation of 20 High Temperature Alloys. NACA Technical Note No. 1580, 1948.

[16] W. C. Hagel and H. J. Beattie: Aging Reactions in Certain Super Alloys. *ASM Trans.*, 1957, vol. 49.

[17] D. A. Oliver and G. T. Harris: The Development of a High Creep Austenitic Steel for Gas Turbines. *Journal* West of Scotland Iron and Steel Institute, 1947, vol. 54, p. 97.

[18] H. J. Beattie, Jr. and F. L. VerSnyder: The Laves and Chi Phases in a Modified 12Cr Stainless Alloy. *ASM Trans.*, 1955, vol. 47.

[19] K. W. Andrews: A New Intermetallic Phase in Alloy Steels. *Nature*, 1949, vol. 164, p. 1015.

[20] K. W. Andrews and P. E. Brookes: Chi Phase in Alloy Steels. *Metal Treatment and Drop Forging*, 1951, vol. 18, p. 301.

[21] P. K. Koh: Occurrence of Chi Phase in Molybdenum-Bearing Stainless Steels. *AIME Trans.*, 1953, vol. 197, p. 339; Journal of Metals, February 1953.

[22] J. Birtalan and R. A. Bloom: Occurrence of Chi Phase in a 16 Pct Cr-15 Pct Ni-7 Pct Mn-6 Pct Mo Alloy. *AIME Trans.*, 1956, vol. 206, p. 210; Journal of Metals, February 1956.

[23] J. Lane and N. J. Grant: Carbide Reactions in High Temperature Alloys. *ASM Trans.*, 1952, vol. 44, p. 113.

[24] J. W. Weeton and R. A. Signorelli: An Investigation of Laminar Structures and Minor Phases in Eleven Cobalt Base Alloys Before and After Heat Treatment. NACA Technical Note No. 3109, 1954.

[25] F. S. Badger and W. O. Sweeny, Jr.: Metallurgy of High Temperature Alloys Used on Current Gas Turbine Designs. *Symposium on Materials for Gas Turbine*, p. 99. ASTM. Philadelphia, 1946.

[26] J. W. Weeton and R. A. Signorelli: Effect of Heat Treatment upon Microstructures, Microconstituents, and Hardness of a Wrought Cobalt Base Alloy. *ASM Trans.*, 1955, vol. 47, p. 815.

[27] R. L. Beck, E. E. Fletcher, A. R. Elsea, A. B. Westerman, and G. K. Manning: Alloys for High Temperature Service. *Metal Progress*, 1954, vol. 66, No. 1-A, p. A191.

[28] G. T. Harris and H. C. Child: Development of a High Temperature Alloy for Gas Turbine Rotor Blades. *Symposium on High Temperature Steels and Alloys for Gas Turbines*. Iron and Steel Institute. London, 1952.

[29] R. F. Wilde and N. J. Grant: Aging in Complex Commercial Nickel-Chromium Alloys Hardened with Titanium and Aluminum. *AIME Trans.*, 1957, vol. 209, p. 865; Journal of Metals, July 1957.

[30] R. Nordheim and N. J. Grant: Aging Characteristics of Nickel-Chromium Alloys Hardened with Titanium and Aluminum. *AIME Trans.*, 1954, vol. 200, p. 211; Journal of Metals, February 1954.

[31] H. W. G. Hignett: *High Temperature Alloys in British Jet Engines*. International Nickel Co. New York, 1951.

[32] R. W. Guard and T. A. Prater: Austenitic Alloy for High Temperature Use. *ASM Trans.*, 1957, vol. 49.

[33] R. M. Parke and F. P. Bens: Chromium Base Alloys. *Symposium on Materials for Gas Turbines*, p. 80. ASTM. Philadelphia.

[34] J. P. Hammond: An Investigation of Microconstituents in Cr Base Cr-Fe-Mo Alloys and their Behavior with Heat Treatment. Ph.D. dissertation. Yale University, 1949.

[35] J. P. Hammond, A. B. Westerman, and H. C. Cross: Microconstituents in Cr Base Cr-Fe-Mo Alloys and their Behavior with Heat Treatment. *AIME Trans.*, 1952, vol. 184, p. 1329; Journal of Metals, December 1952.

[36] V. N. Krivobok and E. N. Skinner: Composition and Strength of Heat Resisting Alloys. *Metal Progress*, 1955, vol. 68, p. 120B.

[37] J. H. Westbrook: Temperature Dependence of Hardness of the Equi-atomic Iron Group Aluminides. *Journal* Electrochemical Soc., 1956, vol. 103, p. 54.

[38] J. H. Westbrook: Microhardness Testing at High Temperatures. ASTM. To be published.

[39] J. H. Westbrook: Temperature Dependence of the Hardness of Pure Metals: *ASM Trans.*, 1953, vol. 45, p. 221.

[40] E. Ammann and J. Hinnüber: The Development of Hard Metal Alloys in Germany. *Stahl und Eisen*, 1951, vol. 71, p. 1081.

[41] J. H. Westbrook: Note on the Temperature Dependence of Hardness of the Transition Metal Monocarbides. *Acta Metallurgica*, 1955, vol. 3, p. 104.

[42] J. H. Westbrook: Unpublished research.

[43] G. A. Geach and J. E. Hughes: The Alloys of Rhenium with Molybdenum or with Tungsten and Having Good High Temperature Properties. *Proceedings* Second Plansee Seminar. Reutte, 1955.

[44] J. Hinnüber: Cemented Carbides with Special Chemical and Physical Properties: *Technische Mitteilungen Krupp*, 1954, vol. 12, p. 1.

[45] J. H. Westbrook: Unpublished research.

[46] J. C. Holzworth and A. L. Boegehold: Gmoodie, a Low-Cost Die Material. *Metal Progress*, 1956, vol. 69, p. 49.

[47] J. G. McMullin, S. F. Reiter, and D. G. Ebeling: Equilibrium Structures in Fe-Cr-Mo Alloys. *ASM Trans.*, 1954, vol. 46, p. 799.

[48] H. J. Goldschmidt: Discussion of Ref. 47. *ASM Trans.*, 1954, vol. 46, p. 807.

[49] J. S. Kasper: Atomic and Magnetic Ordering in Transition Metal Structures. *Crystal Structure*. ASM. Cleveland, 1955.

[50] A. T. Grigorev, N. M. Gruzdeva, and I. A. Bondar: The Chemical Nature of the Sigma Phase in the Iron-Chromium System. *Izvestia Sektora Fiziko-Khimicheskogo Analiza*, 1954, vol. 21, p. 132.

[51] E. J. Dulis and G. N. Smith: Identification and Mode of Formation and Resolution of Sigma Phase in Austenitic Chromium-Nickel Steels. *Symposium on the Nature, Occurrence and Effects of Sigma Phase*, p. 3. ASTM. Philadelphia, 1950.

[52] J. J. Gilman, P. K. Koh, and O. Zmeskal: Delta Ferrite Formation and its Influence on the Formation of Sigma in a Wrought Heat Resisting Steel. *ASM Trans.*, 1949, vol. 41, p. 137.

[53] J. W. Putnam, N. J. Grant, and D. S. Bloom: Sigma Phase in Chromium-Molybdenum Alloys with Iron or Nickel. *Symposium on the Nature, Occurrence and Effects of Sigma Phase*, p. 61. ASTM. Philadelphia, 1950.

[54] H. Bückle: The Contribution of Microhardness to the Study of Solid State Reactions. *Proceedings* International Symposium on Reactivity of Solids, p. 133. Gothenburg, 1952.

[55] J. S. Kasper: The Ordering of Atoms in the Chi Phase of the Fe-Cr-Mo System. *Acta Metallurgica*, 1954, vol. 2, p. 456.

[56] H. Bückle: Discussion of paper by E. M. Onitach-Modl. Microhardness as a Tool in the Investigation of the Sintering Process in Complex Systems. *Proceedings* First Plansee Seminar, p. 184. Reutte, 1952.

[57] E. N. Kislyakova: Determination of the Structure and the Composition of the Double Carbides in the System W-Co-C by Means of Investigation on the Relative Intensities of Debye Lines. *Journal of Physical Chemistry* USSR, 1943, vol. 17, p. 108.

[58] A. Westgren and G. Phragmen: The Double Carbide of High Speed Steel. *Trans.* Amer. Soc. for Steel Treating, 1928, vol. 13, p. 539.

[59] K. Kuo: The Formation of η Carbides. *Acta Metallurgica*, 1953, vol. 1, p. 301.

[60] J. H. Westbrook: Unpublished research.

[61] P. Leckie-Ewing: A Study of the Microhardness of the Major Carbides in Some High Speed Steels. *ASM Trans.*, 1952, vol. 44, p. 348.

[62] R. Kieffer and P. Schwartzkopf: *Hartestoffe und Hartmetalle*, p. 517. Springer. Wien, 1953.

[63] D. K. Das, S. P. Rideout, and P. A. Beck: Intermediate Phases in the Mo-Fe-Co, Mo-Fe-Ni, and Mo-Ni-Co Systems. *AIME Trans.*, 1953, vol. 194, p. 1071; Journal of Metals, October 1953.

[64] S. F. Reiter and W. R. Hibbard: High Temperature Properties of Iron Rich Fe-Mo Alloys. *AIME Trans.*, 1955, vol. 203, p. 655; Journal of Metals, May 1955.

[65] J. C. Fisher, E. W. Hart, and R. H. Pry: The Hardening of Metal Crystals by Precipitate Particles. *Acta Metallurgica*, 1953, vol. 1, p. 336.

[66] D. Tabor: A Simple Theory of Static and Dynamic Hardness. *Proceedings* Royal Soc., London, 1948, vol. A192, p. 247.

[67] H. J. Siekman, E. W. Goliber, and K. W. Stalker: Tomorrow's Cutting Tools. *American Machinist*, 1956, vol. 100, p. 160.

[68] W. Köster and F. Sperner: The Ternary System Cobalt-Chromium-Carbon. *Archiv für das Eisenhüttenwesen*, 1955, vol. 26, p. 555.

Discussion of this paper sent (2 copies) to AIME by Sept. 1, 1957 will appear in AIME *Transactions* Vol. 212, 1958, and in Journal of Metals, April 1958.

Shear Along Grain Boundaries In Aluminum Bicrystals

Aluminum bicrystals 99.99 pct pure having a pure tilt boundary about the <110> axis were subjected to creep stresses along their boundary at various temperatures. The initial rate of grain boundary gliding was found to be almost linear and a plot of the logarithm of the initial rate for various stresses vs the reciprocal of the absolute temperature resulted in a series of parallel straight lines. The usual rate equation was used to calculate the activation energy for grain boundary shear. It was found to increase continuously as the boundary angle increased, and approached a maximum value for the maximum angle of misorientation. The mechanism for grain boundary shear is considered to be a combination process involving slip and grain boundary self-diffusion.

by S. K. Tung and R. Maddin

SUCCESS of the dislocation theory in formulating the transitional lattice theory proposed by Hargreaves and Hill in 1929[1] is well established for low angle grain boundaries. The theoretical work of Burgers[2] and Read and Shockley,[3] together with the experimental observations of Aust and Chalmers[4] and Parker and colleagues,[5] leaves little doubt as to the structure of grain boundaries with differences of orientations up to between 15° and 20°. Beyond these angles, the structure of the boundary is not so clear, and is still a matter for conjecture.

There have been notable experiments devised from which the data could be used to calculate energetics for possible arrangements of atoms in forming a large angle boundary.[6] Most of these experiments deal with diffusion through and along the grain boundary.

The recent work of Rhines and Cochart[7] and Rhines, Bond, and Kissel[8] was concerned with the relative movement of grains in aluminum bicrystals under constant tensile loads with their boundaries aligned at 45° to the tension axis. The gliding along the grain boundary was cyclic and began after an incubation period. The velocity of gliding increased with the sum of the angular difference, θ, between the operative slip direction in the conjugate crystals and the angular difference between the active slip planes as measured between their traces upon the grain boundary. The initial gliding rate varied with temperature, and the logarithm of the average gliding taken over a considerable period was a linear function of the reciprocal of the absolute temperature: the slope gave an activation energy of 11,000 ±1,000 cal per mole.

Since the rate of grain boundary shear is sensitive to the misorientation of the grains themselves, as shown by several workers,[7,8] it is suggested that further work of this type might be fruitful in adding information regarding the behavior of boundaries under stress. The techniques devised by Chalmers[9] added impetus to the facility for observing grain boundary behavior, in that they provided a simple means for producing bicrystals of predetermined orientation so that the angle of the boundary could be controlled.

S. K. TUNG, Student Member AIME, and R. MADDIN, Member AIME, are Graduate Student and Professor of Metallurgy, respectively, School of Metallurgical Engineering, University of Pennsylvania, Philadelphia.

TP 4478E. Manuscript, July 26, 1956. New Orleans Meeting, February 1957.

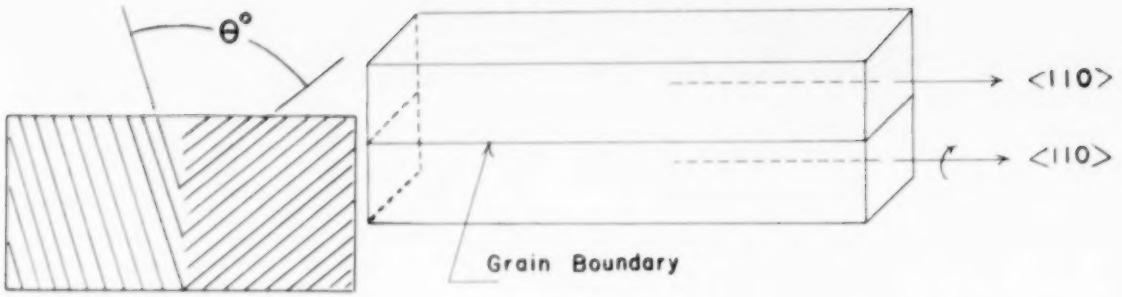

Fig. 1—a) LEFT: misorientation angle relationship between two single crystals, and b) RIGHT: orientation relationship of aluminum bicrystals.

The present investigation was undertaken in order to determine the activation energy for grain boundary shear as a function of the grain boundary angle. If the stresses necessary to activate grain boundary gliding are known as a function of both the angle of misfit and the temperature, it is likely that a plot of activation energy for shear vs grain boundary angle may add information about the structure of the boundary as it changes from a pure dislocation boundary to one of some other structure. This plot could also shed some light on the mechanism of grain boundary shear, which plays an important role during creep.

Growth of Aluminum Bicrystals

The material chosen for the investigation was aluminum since it can be obtained with fairly high purity. This eliminates somewhat the influence of relatively large amounts of impurities, which always exist, particularly in the grain boundary. Also, aluminum can be seeded relatively easily to produce the desired boundary angles.

Single crystals of aluminum obtained previously were used as seed crystals to grow a master seed having a specimen axis orientation located at a <110> direction. The single crystal seeds were rotated to obtain various bicrystal master seeds from which the final specimens were obtained, Fig. 1a and 1b. The Laüe back reflection X-ray technique was employed to check the crystal orientation of the master seed bicrystals and those of the final specimens.

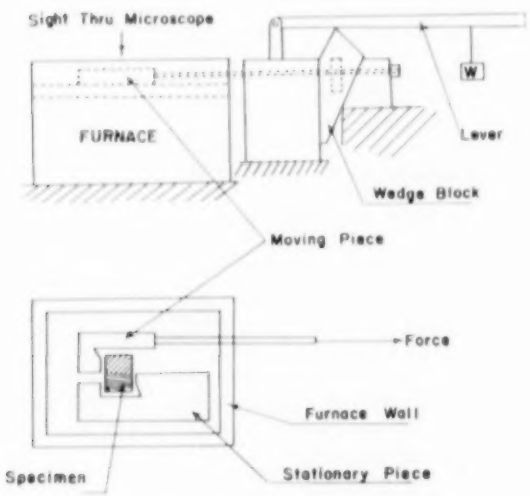

Fig. 2—Schematic drawing of shearing equipment.

Experimental Procedure

Specimen Surface Preparation—Each specimen had a cross section approximately 12.5 x 5 mm. The specimens were annealed 8 hr at 620°C in order to relieve any strains. Laüe X-ray back reflection patterns were made at this time to determine the actual orientation difference, since a slight variation from the preset orientation might have resulted. This was so because of the inherent slight error of positioning the seed crystal.

The specimens, imbedded in paraffin in a wooden trough, were cut with the aid of a jeweler's saw into a series of samples 12.5 x 5 x 10 mm. They were next heavily etched with *aqua regia* for 2 min and chemically polished for 20 to 30 min using Alcoa R-5 bright dip solution.

Using a razor blade, a light scratch was made perpendicular to the grain boundary approximately in the center of each specimen. The dimensions of the specimen were again measured so that the boundary area could be computed precisely.

Shear Apparatus—The shearing apparatus is shown schematically in Fig. 2. The shear stress, acting along the grain boundary, is produced by a suspended dead weight, which presses on a wedge block through a lever mechanism. A block moved horizontally, thus producing a shear force acting on the specimen. Consequently, a constant shear stress was available. All energy losses due to friction at contact surfaces were determined experimentally and compensated for in the applied stress.

The furnace was constructed by using a length of Nichrome wire wound around transite board, the overall dimensions of which were 7.6 x 15.9 x 7.6 cm. A stationary piece along with a moving piece made of stainless steel having the shape shown in Fig. 2 were placed above a stainless steel floor and set above the furnace. For operation, the specimen was held by the stationary piece, which was fixed to the floor, and the moving piece was controlled by a mechanism as described above.

The temperature was controlled by a Chromel-Alumel thermocouple operating through a Wheelco controller, with the couple held on the stainless steel floor of the furnace against the specimen.

It is considered that temperature measurement was accurate to ±8°C. (There was a large heat loss through a special glass ceiling window.) The max-

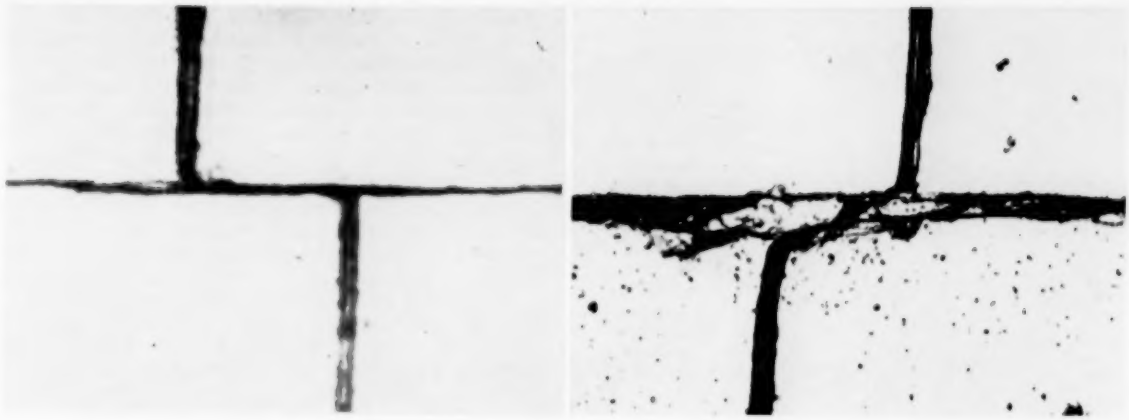

Fig. 3—a) LEFT: macroscopically homogeneous shear, and b) RIGHT: two stage shearing and boundary migration. Grain boundary is horizontal. X200. Reduced approximately 10 pct for reproduction.

imum operating temperature of the furnace was 600°C.

Displacement of the fiducial scratch was measured by a normal bench-type microscope using a calibrated eyepiece and a reflecting objective. The total arrangement operated as a simple hot-stage microscope yielding a magnification of X80. The low magnification was due partly to the long working distance maintained between the specimen and objective. The addition of an air cooling device permitted the use of the objective at the maximum temperature desired.

Experimental Results

The relative displacement of the grain boundary was observed in more than 100 specimens tested at different shear stresses and temperatures. In general, the two grains separated cleanly along the boundary during the early state of creep. Fig. 3a illustrates a typical displacement observed during the macroscopically uniform displacement period. In many cases, there was ample evidence of boundary migration during the later shearing period, particularly at higher temperature and under higher applied stresses. In almost all of these cases, an initial macroscopically uniform displacement was observed. A two-stage nonuniform shear was observed during which the boundary migrated irregularly in a direction perpendicular to the original boundary trace. This was accompanied by a shearing displacement occurring at the new boundary region during the migration period.

Fig. 3b shows a typical result of nonuniform displacement. It is of interest to note that the fiducial mark, after the shearing period, was curved in the vicinity of the grain boundary. This suggests that displacement at the boundary was taking place continuously as the boundary advanced.

In the main, tests were carried out on specimens having reasonably straight boundaries. Initial displacements were generally the same at all points along the grain boundary. Displacements were measured on a few specimens having three or more fiducial scratches to check the uniformity of the displacement at the various points. In many cases the boundary displacements were found to differ markedly from point to point. It appears likely that in these cases deformation of the crystals them-

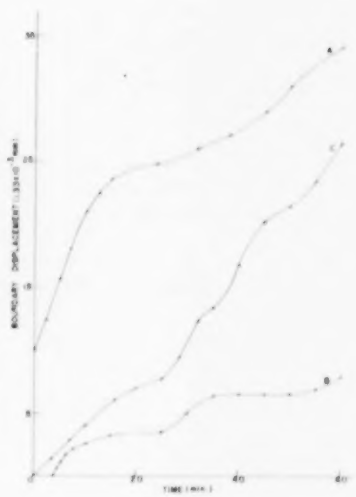

Fig. 4—Three types of grain boundary displacement vs time curves. Curve *A*: Specimen No. 53; temperature, 550°C; stress, 45 g per sq mm; and boundary angle, 20°. Curve *B*: Specimen No. 96; temperature, 450°C; stress 45 g per sq mm; and boundary angle, 85°. Curve *C*: Specimen No. 37; temperature, 500°C; stress, 45 g per sq mm; and boundary angle, 55°.

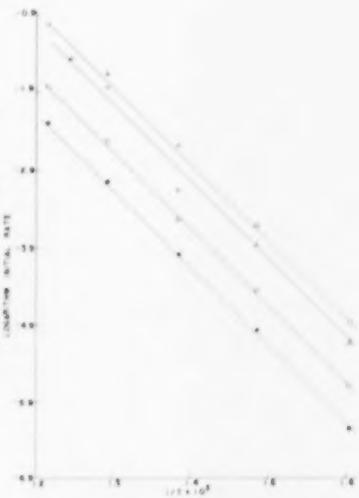

Fig. 5—Log of creep rate vs 1/T for grain boundary misorientation angle θ equal to 55°. Square represents stress equal to 75.5 g per sq mm; triangle, stress equal to 60 g per sq mm; open circle, stress equal to 45 g per sq mm; and closed circle, stress equal to 30 g per sq mm.

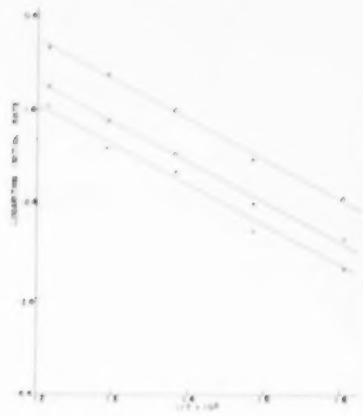

Fig. 6—Log of creep rate vs $1/T$ for grain boundary misorientation angle θ equal to 20°. Triangle represents stress equal to 60 g per sq mm; square, stress equal to 45 g per sq mm; and circle, stress equal to 30 g per sq mm.

selves, in addition to sliding past one another, must have occurred between these points. In the cases where nonuniform displacements were observed, the data were not used in calculating energies.

The specimens with constant orientation angle difference were subjected to different creep stresses at temperatures of 350° to 550°C. Three different types of grain boundary displacement vs time curves were obtained. Curve *A* in Fig. 4 shows a behavior typical for the higher temperatures. There was an initially high linear rate of flow which was followed by a rate gradually decreasing to zero. After a certain amount of time, creep began again at a rate which was in some cases larger and in other cases smaller than the initial rate. The creep curve exhibited a cyclic variation when observed over a long period. Curve *B* in Fig. 4 shows a creep curve typical of relatively low temperatures. In these cases, an incubation period was often observed. However, the existence of an incubation period was strongly orientational-dependent. These curves were also cyclic in nature. Curve *C* in Fig. 4 shows the third type of displacement vs time curve characteristic of intermediate temperatures. As in the case of the curves at high temperatures, no incubation time was observed. There was always an initially linear rate of flow. The succeeding gliding rates were also cyclic. It is considered, however, that only two types of displacement-time curves were present in that the third type could always be thought of as either the first or second type by assuming that the initial displacement was either too small or the incubation time too short to be observed. Both cases were possible considering the uncertainty in the experimental measurements.

Table I. Activation Energy for Different Boundary Angles

Orientation Difference, θ, Degrees	Stress, G per Sq Mm	Activation Energy, Q, Cal per Mol	Average Activation Energy, Q, Cal per Mol
20	60	8,800	
	45	8,600	
	30	8,600	8,670
55	75.5	20,140	
	60	20,200	
	45	20,000	
	30	20,100	20,100
80	30	28,700	28,700
85	70	29,200	
	50	34,600	
	45	39,400	34,400
88	90	38,400	
	60	40,400	39,400

The creep curves obtained herein exhibited the same characteristics obtained by Rhines, Bond, and Kissel[7] and Chang and Grant.[10] All of the curves showed cyclic variation. Chang and Grant divided the cyclic curves into two periods, i.e., an active boundary gliding period and a boundary migration period (rest portion of the curve).

The present experimental work showed no evidence of boundary migration during the rest period. On the contrary, the cyclic curve was evident even when no grain boundary migration occurred over the entire testing time. This is in agreement with the observations of Rhines, Bond, and Kissel.

The initial rate was always selected as the rate observed immediately after a sudden shearing displacement or incubation time. In either case it is interesting to note that this rate was almost always linear within a short period of time. When the logarithms of the initial rates for the various stresses were plotted against the reciprocal of the absolute temperatures, a series of parallel straight lines was obtained.

The resulting plots are shown in Figs. 5, 6, and 7 for θ angles of 55°, 20°, and 85°, respectively. The theoretical treatment of boundary slip, as proposed by Kê[11,12] and Mott,[13] suggests that the rate of boundary slip could be determined by a rate-reaction equation. Consequently, assuming a relation of the type

$$r = Ae^{-Q/RT}$$

where r is initial rate of grain boundary displacement, A is a constant which may be a function of stress and/or boundary angle, Q is the activation energy for grain boundary displacement, R is gas constant, and T is absolute temperature, the activation energies, Q, for the different grain boundary angles, θ, were obtained from the slopes of the curves. The results are shown in Table I.

The constant, A, in the rate equation was partly evaluated by plotting the logarithms of the rates vs $1/T$, and extrapolating to $1/T$ equal to zero. The values of rate obtained by these extrapolations were plotted in a number of ways in an attempt to evaluate the rate constant, A.

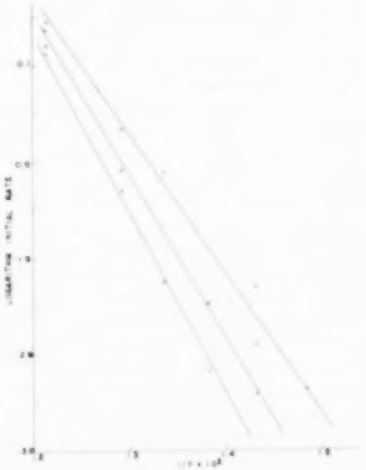

Fig. 7—Log of creep rate vs $1/T$ for grain boundary misorientation angle θ equal to 85°. Circle represents stress equal to 70 g per sq mm; triangle, stress equal to 50 g per sq mm; and square, stress equal to 45 g per sq mm.

The present data were insufficient for analyzing the rate constant completely. Nevertheless, since the plot of ln A against $1/\sigma$ was nearly linear with a negative slope, it may be suggested that the rate constant is of the form $A = Be^{-\sigma_o/\sigma}$, in which case the rate equation is of the form

$$r = Be^{-\sigma_o/\sigma}\, e^{-Q/RT}$$

where σ_o is an index of the strength of the grain boundary, and B is a constant which may be a function of boundary misorientation angle θ.

The plot of activation energy for grain boundary shear vs boundary misorientation angle θ is shown in Fig. 8. The curve appears to be continuous and approaches a maximum value for a boundary angle of 90°, which is the maximum misorientation between two grains rotated about the <110> direction.

The wide variation in the activation energy observed for specimens with θ value of 85° probably results from the steeply rising values of Q for specimens with these misorientations. An error of 2° in θ (which is likely from orientation determinations by the Laüe back reflection method) would account for a variation of 8 kcal per mol. Consequently, the plots of the logarithm of rate vs $1/T$ are not all parallel.

Table II. Orientation Difference of 55°

Stress, G per Sq Mm	Temperature, °C	Incubation Time, Sec	Q, Shear, Kcal per Mol	Q, Induction, Kcal per Mol
45	350	8700		
45	400	1800		
45	450	900		
45	500	500		
45	550	—		
			20	22.6
60	350	3300		
60	400	900		
60	450	300		
60	500	—		
60	530	—		
			20.2	22.5
75.5	350	1800		
75.5	400	600		
75.5	450	120		
75.5	500	—		
75.5	550	—		
			20.14	22.4

The induction times for grain boundary displacement for boundaries of $\theta = 55°$ at different stresses were plotted vs $1/T$, Fig. 9, and resulted in straight, parallel lines. An activation energy was obtained as 22 kcal per mol. This value is to be compared with the activation energy for boundary shearing, 20.1 kcal per mol, for the same boundary angle.

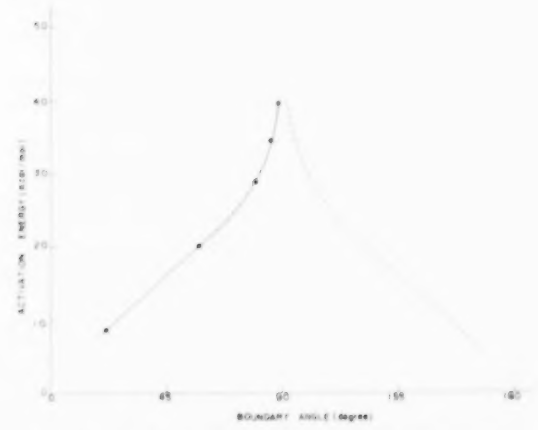

Fig. 8—Plot of activation energy for grain boundary shear vs boundary misorientation angle θ.

Fig. 9—Plot of induction times for grain boundary displacement at different stresses vs $1/T$. $\theta = 55°$. Circle represents stress equal to 45 g per sq mm; triangle, stress equal to 60 g per sq mm; and square, stress equal to 75.5 g per sq mm.

Unfortunately, the data for induction time for other angles were meager and consequently analysis was not possible. The data are listed in Table II.

It is interesting to note that the activation energy for an average misfit angle, 55°, is approximately equal to grain boundary self-diffusion (one half volume diffusion), according to Turnbull.[14] It is also of interest to note that for $\theta = 55°$, the sum of the activation energies for shear and incubation is approximately equal to the bulk diffusion activation energy.

Discussion

The theory of grain boundaries proposed by Mott[10] is based on the idea that a grain boundary can be pictured as a sequence of islands of good atomic fit separated by areas of misfit. Based on Mott's model, the basic mechanism for gliding along a grain boundary is thus a transfer of groups of atoms from the disordered boundary layer to the crystalline lattice and the reverse (i.e., the transformation is somewhat analogous to melting and solidification).

Consider a group of n atoms in each island to form a layer of boundary between the grains. Mott assumed that the free energy F necessary to cause boundary slip will be given by

$$F = nL\,(1 - T/T_m)$$

where L is latent heat of fusion, and T_m is melting temperature. The expression proposed by Mott was

$$r = Ae^{-(nL/kT)}$$

where $A = \dfrac{\nu a^2 n\omega\sigma}{kT} e^{nL/kT} = e^{nL/kT}$; ν, the frequency of atomic vibration; a, the distance that each island moved in the direction of stress; n, the number of atoms each island contains; ω, the area each island covers; σ, stress; k, Boltzmann's constant; and T, absolute temperature. Here Mott concluded that the activation energy for grain boundary slip is equal to nL, and proposed $n = 14$.

The interesting feature of Mott's theory lies in the value of n. It is hard to imagine n to be fixed

for all boundaries as considered by Mott. On the contrary, n should depend strongly on the relative orientation of the two grains across the boundary.

Using Mott's expression $F = nL\ (1 - T/T_m)$ and along with Mott neglecting T/T_m, the data reported herein are used to calculate the value of n. Here, L is taken as 2.55 kcal per mol (the latent heat of solidification for aluminum) and F is taken as the value of Q measured in the above data. The values of n for the various boundaries used are shown in Table III.

It should be noted that the number of atoms per island calculated here applies only to the simple tilt boundary. In polycrystalline aluminum the boundaries would, in general, be both tilt and twist types. The misorientation would then be larger using these 2 degrees of freedom and hence it would be expected that the value of n for boundaries in a polycrystalline specimen would be larger than that proposed by Mott.

Table III. Values of n for Boundaries Used

θ, Degrees	n
20	3.4
55	7.9
60	11.5
65	13.5
88	15.5

Turnbull's idea[14] that the large angle boundary is composed of an array of atoms and holes is only slightly different from Mott's theory in that the regions between the holes could be both good and bad fit regions. It is quite possible then that slip along grain boundaries may take place by the migration of vacant sites (holes). This is essentially a process of self-diffusion, and can occur at temperatures for which self-diffusion is appreciable. Nabarro has discussed this mechanism in detail,[15] and shows that the process involves the transport of atoms with the creation of vacancies on one face and destruction on the other face. Since the large angle grain boundary acts freely as both a source and a sink for vacancies, it can be assumed that this mechanism occurs quite readily at large angle grain boundaries.

For any displacement occurring along the grain boundary (as is likely, due to the activation of dislocation sources in the vicinity of the boundary by externally applied stresses), the bad fit region would constitute an effective barrier to continued displacement. A form of bulk diffusion would then be called into play to permit further displacement. Thus, for large displacements, boundary slip may be considered to be a diffusion controlled process.

The uniform initial gliding rate can be considered to be governed by two processes, i.e., slip and diffusion. The maximum shear stress resolved along the {111} planes occurs in the one which is 90° from the {110} plane whose pole is both the specimen axis and the slip direction. Hence it is reasonable to assume that some slip will occur along this plane. As the angle θ increases, the slip plane will rotate accordingly and go through a maximum at θ equal to 90°. Consequently, the applied shear stress acting along the grain boundary will have a component resolved along the slip plane which will decrease according to a cosine function as the angle θ increases. This means that the greater the angle θ the higher will be the applied shearing force to cause slip. However, it is considered that the slip process contributes only one part of the shear displacement of the boundary. After the initial displacement occurring over a relatively short distance, the structure inside the boundary is altered to produce a barrier to further glide. Since the barrier can be overcome only by diffusion, displacement comes gradually to a halt as the effectiveness of the barrier increases. Diffusion which is time dependent permits a readjustment of the barriers to allow further displacement.

Nonuniform shear is observed in some cases and has an effect in causing lateral boundary movement. As suggested in the discussion of the boundary model, atoms in a strained configuration constituting a barrier to further glide along the boundary would be expected to realign themselves by diffusion. This process would produce a boundary migration as described by Beck.[17] It is to be expected that, subsequent to the initial grain boundary displacement, the strain becomes progressively larger, and hence there should be migration perpendicular to as well as along the grain boundary. In fact, Aust, Harrison, and Maddin[18] have observed the rate of grain boundary migration as a function of the boundary angle. They obtained the activation energy for boundary migration of aluminum bicrystals for $\theta = 55°$ as 22 ± 3 and 10 ± 3 kcal per mol, respectively. These data are qualitatively in agreement with those reported herein if a low activation energy for boundary migration can be associated with a highly misoriented boundary. This would require a high energy for shear along this boundary. Conversely, a high energy for migration is associated with a boundary of small misorientation which would require a small energy for shear along this boundary.

Acknowledgments

This work was supported by the Office of Naval Research. The paper is based on a portion of a thesis by S. K. Tung submitted to the Graduate School of Engineering, University of Pennsylvania, in partial fulfillment of the requirements for the degree of Master of Science.

References

[1] F. Hargreaves and R. J. Hill: *Journal* Institute of Metals, 1929, vol. 41, p. 257.
[2] J. M. Burgers: *Proceedings* Koninklijke Nederlandse Akademie van Wetenschappen, 1939, vol. 42, p. 293.
[3] W. Shockley and W. T. Read: *Physical Review*, 1950, vol. 78, p. 275.
[4] K. T. Aust and B. Chalmers: *Proceedings* Royal Soc., London, 1950, vol. A204, p. 359.
[5] J. Washburn and E. R. Parker: *AIME Trans.*, 1952, vol. 194, p. 1076; JOURNAL OF METALS, January 1952.
[6] R. Smoluchowski: *Bulletin* American Physical Soc., 1952.
[7] F. N. Rhines and A. W. Cochart: *NACA Report No. 2746*, July 1952.
[8] F. N. Rhines, W. E. Bond, and M. A. Kissel: *ASM Trans.*, 1955, vol. 48, p. 919.
[9] B. Chalmers: *Proceedings* Royal Soc., London, 1949, vol. A196, p. 64.
[10] H. C. Chang and N. J. Grant: *AIME Trans.*, 1952, vol. 194, p. 619; JOURNAL OF METALS, June 1952.
[11] T. S. Ke: *Physical Review*, 1947, vol. 72, p. 41.
[12] T. S. Ke: *Journal of Applied Physics*, 1948, vol. 19, p. 285.
[13] N. F. Mott: *Proceedings* Physical Soc., 1948, vol. 60, p. 391.
[14] D. Turnbull: *AIME Trans.*, 1951, vol. 191, p. 661; JOURNAL OF METALS, August 1951.
[15] D. Turnbull: *Atom Movements*, p. 129. ASM. Cleveland, 1951.
[16] F. R. N. Nabarro: Report on Conference on Strength of Solids, p. 75. Physical Soc. London, 1948.
[17] P. A. Beck: *Metal Interfaces*, p. 208. ASM. Cleveland, 1952.
[18] K. T. Aust, E. H. Harrison, and R. Maddin: *Journal* Institute of Metals, 1956, vol. 85, p. 15.

Discussion of this paper sent (2 copies) to AIME by Sept. 1, 1957 will appear in AIME *Transactions* Vol. 212, 1958, and in JOURNAL OF METALS, April 1958.

Intermetallic Compounds In Titanium-Hardened Alloys

Aging reactions in 26 pct Ni-15 pct Cr alloys of the *A*-286 type have been investigated using light and electron microscopy, X-ray and electron diffraction. Maximum dispersion hardening is provided by aluminum-poor γ'; η platelets are observed above 1400°F; *G* phase is a globular nickel-titanium silicide resulting from grain-boundary segregation; bulky Laves or σ phases appear depending on whether there is an excess of titanium or aluminum. Cellular precipitation involving a new phase occurs in vacuum-melted *A*-286 of negligible silicon content. Calculated Patterson-Harker sections show that the interatomic distances in *G* phase are not short.

by H. J. Beattie, Jr. and W. C. Hagel

DURING an earlier examination of high-temperature alloy, *A*-286, the presence of an unknown intermetallic compound was verified by X-ray diffraction. Owing to its prominent appearance at grain boundaries, the arbitrary name of *G* phase was assigned.[1] Low-silicon, vacuum-melted heats were found to contain no *G* phase, and this investigation was initiated to determine the influence of silicon on *G*-phase formation; additional work was undertaken to extend existing data on other intermetallic compounds and the aging reactions in this group of alloys.

Taylor and Floyd[2-4] observed that the Ni_3Al phase (γ') and the Ni_3Ti phase (η) are the only equilibrium intermetallic compounds in nickel ternary alloys containing up to 25 pct Cr and 10 pct Ti or Al. They found that γ' can dissolve considerable nickel, chromium, and titanium, although the stoichiometric composition of η remains fixed. Nordheim and Grant[5] confirmed that age hardening of 80 pct Ni-20 pct Cr alloys of the Nimonic-80 type is due to precipitation of γ', where aluminum is partially replaced by titanium. They suggest that optimum hardness and ductility result from increasing the titanium to aluminum ratio toward the end of the γ' solubility range and from increasing total titanium and aluminum content to the maximum limit permitted by processing. Such information is necessary for those seeking to improve the service-temperature range and long-time structural stability of high-temperature components.

H. J. BEATTIE, JR. and W. C. HAGEL, Junior Member AIME, are associated with the Materials and Processes Laboratory, Large Steam Turbine-Generator Dept., General Electric Co., Schenectady.
TP 4472E. Manuscript, Sept. 12, 1956.

Experimental Methods

Compositions of materials studied are listed in Table I. Alloys *D*, *E*, and *F* possess representative *A*-286 analyses; silicon increases from less than 0.02 to 1.75 pct in alloys *A* to *H*; in alloys *I* to *K*, titanium decreases from 2.24 to 0.39 pct, and aluminum increases from 0.16 to 2.40 pct. Alloys *A* and *D* were solution heat treated for 4 hr at 1700°F, oil quenched and aged for 0.5, 2, 6, 12, 30, 70, 200, and 1000 hr at 1200°, 1300°, 1400°, and 1500°F. Therefore, a total of 33 specimens was required for each

Table I. Composition of Alloys Investigated

Alloy Designation	Alloy Content, Wt Pct									
	C	Mn	Si	Cr	Ni	Mo	Ti	Al	V	Fe
A*	0.05	Nil	<0.02	14.60	25.14	1.24	1.83	0.20	0.27	Balance
B	0.05	1.14	0.10	14.82	26.09	1.12	1.91	0.15	0.35	Balance
C*	0.03	1.32	0.14	14.54	25.83	1.60	1.86	0.28	0.30	Balance
D	0.05	1.29	0.67	14.67	25.51	1.11	1.83	0.20	0.24	Balance
E	0.03	1.23	0.88	14.73	25.59	1.10	1.98	0.19	0.32	Balance
F	0.04	1.17	0.92	14.66	25.16	1.12	1.86	0.14	0.31	Balance
G	0.04	1.21	1.32	14.68	26.09	1.28	1.98	0.13	0.32	Balance
H	0.04	1.23	1.75	14.46	26.81	1.44	1.84	0.09	0.12	Balance
I	0.04	1.50	0.87	13.77	24.37	1.37	2.24	0.16	0.26	Balance
J	0.05	1.60	0.54	14.76	25.71	1.35	1.50	2.40	0.32	Balance
K	0.04	1.68	0.68	15.34	26.25	1.34	0.39	2.28	0.30	Balance

* Vacuum melted.

Table II. X-Ray Data on New Phase Extracted from Alloy A Aged 1000 Hr at 1400°F After Solution Treatment for 4 Hr at 1700°F; Cobalt K α Radiation

d, A, Observed	Intensities*	(hkl)†	$\sin^2\theta$ Observed	$\sin^2\theta$ Calculated†
3.340	M	004	0.0679	0.0719
2.455	MW	105	0.1331	0.1335
2.225	S	006	0.1616	0.1620
2.082	MW	222	0.1847	0.1858
1.954, broad	MW	310	0.2096	0.2098
1.866	MW	303	0.2298	0.2293
1.822	W	224	0.2410	0.2398
1.598	MW	323	0.3135	0.3132
1.545	MW	400	0.3351	0.3356
1.502	MW	?	0.3555	—
1.134	MW	408	0.6218	0.6235
1.010	MW	534	0.7846	0.7851
		4, 0, 10		0.7855

* S represents strong; M, medium; and W, weak.
† Tentative body-centered-tetragonal lattice; a = 6.180A, and c = 13.344A.

of these two alloys. Alloys *B*, *C*, *E*, *F*, *G*, and *H* were solution heat treated for 1 hr at 1800°F, oil quenched and double aged for 16 hr at 1325°F, followed by 256 hr at 1600°F. The same heat treatment was used for alloys *I*, *J*, and *K*, except that the latter double-aging temperature was 1500°F. Furnaces were at temperature on specimen insertion, and the time period of heating was considered to commence after the small specimen disks cut from hot-rolled bar stock had been exposed for 0.1 hr. At least ten Rockwell *A* hardness impressions were made on each specimen of alloys *A* and *D*, and the resulting average reading was converted to Bhn.

After mechanical polishing on an intermediate Carnauba-wax wheel and Gamel cloth with fine alumina, specimens were chemically etched with 92 pct HCl-5 pct H_2SO_4-3 pct HNO_3. More than two etching times were used to evaluate the effect of etch depth on structural appearance. After light-microscopic examination, specimens possessing unique or representative structures were selected for electron microscopy. Negative replicas were prepared by the direct stripping of parlodion, and they were chromium shadowed at angles of 15 to 25°.

X-ray diffraction patterns of electrolytically extracted residues were obtained from selected specimens. The most successful electrolyte was 10 pct HCl in ethyl alcohol, and a current of 0.1 to 0.2 amp per sq in. was passed for 48 hr at a dc potential of 1.0 v. The more noble phases remaining were separated by suction filtration, washed, dried, and preserved under 0.00025-in. Mylar sheet. Residues underwent diffractometer recordings using filtered cobalt radiation, and a few were examined photographically in a cylindrical powder camera of 5-cm radius using filtered copper radiation. Lattice parameters were determined by least-squares analyses of $\sin^2\theta$ values.

Specimens were prepared for reflection electron diffraction by etching with an aqueous solution of $FeCl_3$ and HCl, rinsing with 10 pct HCl in ethyl alcohol, and degreasing successively with anhydrous acetone and benzene before mounting in an electron-diffraction unit. Magnesium-oxide and lithium-chloride standards were used to establish electron wave length.

Experimental Results

The only interstitial compound found in these alloys is TiC; this stable carbide remains relatively unaffected by heat treatment and was observed in all specimens in the form of lavender particles possessing the directionality given them by hot working. A preliminary check of solution heat treatments for 1, 4, and 8 hr at 1600°, 1700°, 1800°, and 2000°F showed that holding for 4 hr at 1700°F is sufficient for solutioning of γ' and η. Although *G* phase progressively dissolves on increasing time at temperature above 1800°F, a small trace of *G* phase still remains after 8 hr at 2000°F. Hardness data are plotted in Figs. 1 and 2 as a function of aging time at temperature. The presence of undissolved *G* phase at the grain boundaries of alloy *D* retards high-temperature grain growth and provides a higher short-time hardness level than that measured when *G* phase is not present in alloy *A*. Otherwise, the general shape of both curves shows that *G* phase does not take part in the principal aging reactions; some overaging appears after 200 hr at

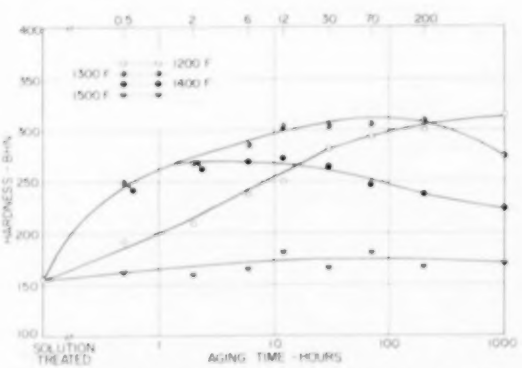

Fig. 1—Change in hardness of alloy *D* during aging at 1200° to 1500°F after solutioning 4 hr at 1700°F.

Table III. X-Ray Phase Identification of Alloys *A* and *D* Aged 1000 Hr After 4 Hr Solution Treatment at 1700°F

Alloy Designation	Aging Temperature, °F, 1000 Hr	Lattice Parameters, A, and Abundances*						
		TiC, Cubic	*G* Phase, Cubic	Ni_2Ti, Hexagonal		$MgZn_2$ Type Laves Phase, Hexagonal		New Phase
				a_0	c_0	a_0	c_0	
A	1200	4.325, A						MR
	1300	4.325, A						MR
	1400	4.325, A						M
	1500	4.325, A		5.109	8.326, A			R
D	1200	4.327, M	11.198, MA					
	1300	4.327, M	11.198, A			4.765	7.697, MR	
	1400	4.324, MR	11.198, A	5.100	8.304, MR	4.753	7.704, M	
	1500	4.324, VR	11.198, A	5.104	8.311, M	4.751	7.696, M	

* A means abundant; M, medium; R, rare; and V, very.

1300°F and within less time at 1400° and 1500°F.

The typical electron micrographs shown in Figs. 3 to 9 are mounted so that the direction of shadowing is from the top of the page; chromium then fell on the lower side of replica craters, signifying that the outlined particles received less etchant attack than the matrix. Initial hardening occurs during those early stages of nucleation and growth when well-defined precipitate particles cannot be observed, Fig. 3. Maximum age hardening is associated with a fine dispersion, Fig. 4, of aluminum-poor γ'; some overaging has occurred when relatively larger platelets of η are seen, as in Fig. 5, interspersed in local regions when titanium concentration exceeds the allowed solubility ratio of γ'. While the nucleation of cubic γ' requires only the segregation and ordering of aluminum and titanium atoms, an additional restacking of layers from the face-centered-cubic (*ABCA*) to hexagonal (*ABACA*) arrangement must proceed for η nucleation. Longer times and/or higher temperatures, Fig. 6, cause further coalescence of *G* phase and spherical γ', additional growth of η, and formation of Laves phase at grain interiors.

Vacuum-melted alloy *A* with a negligible amount of silicon was entirely lacking in *G* and Laves phases. However, the cellular precipitation of lamellae of a new phase was observed at grain boundaries. This reaction was most prominent at 1400°F, as shown in Fig. 7. X-ray diffraction data on this new phase are given in Table II together with an indexing on a tentative body-centered-tetragonal lattice. All lines are listed except those due to TiC. At 1500°F the new phase appears at early stages, but it later gives way to η. Fig. 8

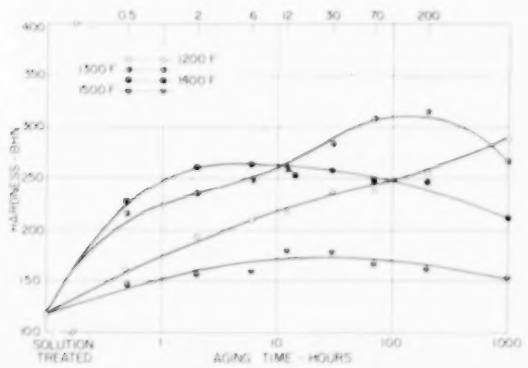

Fig. 2—Change in hardness of alloy *A* during aging at 1200° to 1500°F after solutioning 4 hr at 1700°F.

Table IV. X-Ray Data on Alloy *D* Aged 1000 Hr at 1500°F After Solution Treatment for 4 Hr at 1700°F; Cobalt $K\alpha$ Radiation

d, A, Observed	Intensities*	TiC, *hkl*	*G* Phase, $h^2+k^2+l^2$	Ni_2Ti, *hkl*	Laves Phase, *hkl*	$\sin^2\theta$ Observed	$\sin^2\theta$ Calculated†
2.79	MS		16			0.1028	0.1022
2.57	W		19			0.1215	0.1214
2.495	M	(111)	20			0.1296	0.1278
2.37	MW				110	0.1428	0.1420
2.28	S		24			0.1539	0.1534
2.21	W			200		0.1634	0.1641
2.18	W				103	0.1687	0.1691
2.153	VVS	(200)	27			0.1733	0.1725
2.078	MS			004		0.1853	0.1856
2.022	MS				112	0.1963	0.1961
1.977	VVS		32			0.2047	0.2045
1.950	MS			202		0.2104	0.2105
1.890	VS		35			0.2240	0.2237
1.863	S		36			0.2306	0.2300
1.808	W				202	0.2440	0.2435
1.768	MW		40			0.2561	0.2556
1.727	M			203		0.2684	0.2685
1.705	MS		43			0.2754	0.2748
1.686	M		44			0.2824	0.2812
1.613	W		48			0.3070	0.3067
1.528	VW	220					
1.513	W			204		0.3496	0.3497
1.456	M		59			0.3773	0.3770
1.397	MW		64			0.4106	0.4097
1.329	M			(205)	213	0.4529	0.4532
1.318	S		72			0.4606	0.4601
1.291	S		75		(302)	0.4800	0.4793
1.276	MW			220		0.4913	0.4922
1.232	MW				205	0.5271	0.5276
1.227	S		83			0.5314	0.5304
1.221	MS		84			0.5375	0.5368
1.187	MW				220	0.5679	0.5681
1.173	S		91	(206)		0.5817	0.5815
1.141	S		96			0.6142	0.6134
1.124	VS		99			0.6326	0.6326
1.120	M		100			0.6378	0.6390
1.097	MW		104			0.6644	0.6646
1.087	MS				206	0.6767	0.6764
1.082	MS		107			0.6841	0.6837
1.077	MS		108			0.6897	0.6901
1.067	MW			402		0.7034	0.7026
1.046	MW		115			0.7340	0.7349
1.040	M		116			0.7401	0.7412
1.008	MW		123			0.7868	0.7860
0.9885	MS		128			0.8181	0.8179
0.9772	S		131			0.8379	0.8371
0.9739	MS		132			0.8435	0.8435
0.9604	W		136			0.8675	0.8690
0.9457	S		140			0.8946	0.8946
0.9326	MS		144			0.9198	0.9202
0.9235	MW		147			0.9382	0.9393
0.9199	M		148			0.9447	0.9457

* S represents strong; M, medium; W, weak; and V, very.
† Where two phases have coinciding d-spacings, the one with indices enclosed in parentheses was weaker and therefore not used in calculating $\sin^2\theta$ values.

shows spherical particles of γ' and platelets of new phase and/or η are present, according to the X-ray evidence. After 1000 hr, Fig. 9, η predominates, although traces of the new phase are still evident in the X-ray data.

Table III lists the lattice parameters and relative abundances of phases separated electrolytically in alloys *A* and *D* after 1000 hr at 1200° to 1500°F; Table IV is an example of X-ray data on a single

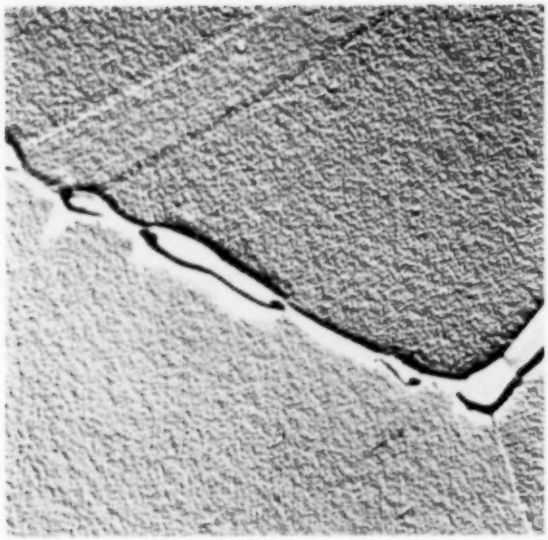

Fig. 3—Alloy *D* aged 2 hr at 1200°F after solutioning 4 hr at 1700°F. Some undissolved *G* phase is present at grain boundaries; no matrix precipitation is yet detectable. X8000.

Fig. 4—Alloy *D* aged 200 hr at 1200°F after solutioning 4 hr at 1700°F. A fine dispersion of aluminum-poor γ' causes maximum hardening. X8000.

Fig. 5—Alloy *D* aged 200 hr at 1400°F after solutioning 4 hr at 1700°F. Initial formation of η platelets can be observed within γ' dispersion. X8000.

Fig. 6—Alloy *D* aged 200 hr at 1500°F after solutioning 4 hr at 1700°F. Overaged structure contains globular *G* phase, spherical γ', and Widmanstätten platelets of η. X8000.

specimen. Relative abundance from X-ray line intensities is designated as abundant (*a*), medium abundant (*ma*), medium (*m*), medium rare (*mr*), rare (*r*), and very rare (*vr*). In these alloys, $MgZn_2$-type Laves phase can consist of (Mo, Ti) (Cr, Mn, Fe, Si)$_2$, but it is essentially $TiFe_2$. The low manganese and silicon content of alloy *A*, as well as increased γ' and η precipitation consuming titanium, appears to inhibit Laves-phase formation.

Representative electron-diffraction data for alloys *I* and *K*, identifying γ' and η, are listed in Table V. Calculated *d*-spacings and intensities are also shown for alloy *I*; these were obtained from the relationship:

$$I_{hkil} \sim \frac{p_{hkil} E^2_{hkil}}{\sin^2 \theta} \qquad [1]$$

where p_{hkil} is the multiplicity of equivalent planes, and E_{hkil} is the electron-scattering structure factor assuming hexagonal-close-packing with stacking sequence of form, *ABACA*. The (00*l*) reflections which normally appear in X-ray patterns are absent in the electron-diffraction data, resulting from the characteristic platelet shape of the η particles pro-

Table V. Electron-Diffraction Data for Alloys Aged 256 Hr at 1500°F After Solution Treatment for 1 Hr at 1800°F

Alloy *I*					Alloy *K*†		
d, A. Observed	*d*, A. Calculated*	Observed Intensities‡	Calculated Intensities*	*hkl**	*d*, A. Observed	Observed Intensities‡	*hkl*
2.22	2.21	MS	141	200	2.04	S	111
2.12	2.13	S	553	201	1.74	W	200
1.95	1.95	VS	1000	202	1.25	MS	220
1.73	1.727	MS	171	203	1.07	MS	311
1.52	1.516	MW	38	204	1.02	W	222
1.395†	—	MW	—	—	0.817	M	331
1.325	1.330	W	38	205	0.793	MW	420
1.279	1.275	MS	85	220	0.721	MW	442
1.182	1.175	VW	61	206	0.680	W	333-511
1.089	1.088	MS	71	224	0.597	W	531
0.824	0.827	M	16	422			
0.694	0.694	VW	6	604			
0.610	0.610	VW	5	2, 2, 12-444			

* Hexagonal η; $a_0 = 5.10$A and $c_0 = 8.33$A.
† Cubic γ′, $a_0 = 3.54$A.
‡ Due to γ-Al_2O_3.
§ S represents strong; M, medium; W, weak; and V, very.

truding from the matrix. With the basal plane of the lattice coinciding with the platelet planes, the only particles favorably oriented for diffraction from the (00*l*) planes are platelets at grazing incidence to the electron beam. Since diffracted electrons arise solely from transmission through thin sections of particles, diffraction from the (00*l*) planes is impossible. Observed intensities for planes (205) and (206) are lower than calculation indicates because the Widmanstätten η platelets contributing to these lines are inclined at small angles to the electron beam, and hence even the thin edges present relatively long path lengths. Since atomic configurations in the basal planes of η and the octahedral planes of austenite are almost identical, it can be understood why η possesses a plate-like morphology. Large, unsuitably shaped particles merely absorb or scatter electrons incoherently. Therefore, the *G*, Laves, and σ phases in these alloys could only be detected by X-ray diffraction.

The increasing silicon content of alloys *A* to *H* caused an increase in *G* and Laves phases and a decrease in grain size that is most striking under a light microscope. The high titanium content of alloy *I* achieved the same effect at a lower silicon content, except that η platelets were in greater abundance. In higher silicon and titanium alloys, *G* phase also surrounds TiC particles, as shown in Fig. 10: scratch hardnesses taken on these specimens showed *G* phase to be softer than TiC but harder than the matrix. The higher aluminum content of alloys *J* and *K* caused the formation of σ instead of *G* and Laves phases; a fluorescent X-ray analysis of σ phase in alloy *K* gave the approximate composition as 47 pct Fe-26 pct Cr-17 pct Mo-10 pct Ni, and the lattice parameters are $a_0 = 8.796$Å and $c_0 = 4.572$A.

A large quantity of alloy *D* was aged for 48 hr at 1500°F and electrolytically digested to give a high yield of residue. A density separation removed any attached matrix, γ′ and η. The remainder was held in hot 50 pct HNO_3 to dissolve TiC, since *G* phase is resistant to all acids except HF; 5 pct Na(OH) was added to eliminate silica. About 12 to 14 g of *G* phase remained for chemical analysis; removal of TiC and silica was verified respectively by X-ray diffraction and infrared spectroscopy. Although not as precise as desired, the separation indicated that the stoichiometric composition of *G* phase is Ni_2TiSi or $Ni_3Ti_2Si_3$. A subsequent attempt by Westbrook[6] to synthesize *G* phase showed that the composition, Ni_2TiSi, consists mostly of *G* phase as determined by

Table VI. Intensities and $|F|^2$ Values of *G*-Phase Powder, Cu*K*α Radiation

hkl	*d*, A	Intensity, Counts per Sec	$\|F\|^2$
200	5.604	14	5
220	3.983	34	13
400	2.803	66	109
420	2.499	79	42
422	2.285	134	87
333-511	2.154	635	332
440	1.977	556	1000
531	1.890	162	82
442-600	1.865	101	85
620	1.770	34	40
533	1.708	66	84
622	1.688	45	60
553-731	1.458	21	14
800	1.399	16	137
660-822	1.320	86	139
555-751	1.292	56	61
911-753	1.229	43	41
842	1.220	23	33
931	1.174	23	36
844	1.142	34	109
755-771-933	1.125	79	88
773-951	1.082	22	52
666-10, 2, 2	1.077	23	119

X-ray diffraction. With further refinement, an essentially homogeneous *G* phase occurred at the composition $Ni_{16}Ti_6Si_7$ with a density of 6.27 g per cu cm. This gives 108 atoms per unit cell, which is more consistent with the formula $Ni_{16}Ti_6Si_7$. Systematic absences are limited to those of face-centered symmetry. Hence, the possible space groups are *F*23, *Fm*3, *F*432, *F*43*m* and *Fm*3*m*.

Patterson-Harker Sections

As a preliminary step toward determination of atomic arrangements within *G* phase, the Patterson function can be used

$$P_{(uvw)} = \sum_h \sum_k \sum_l |F_{(hkl)}|^2 \cos 2\pi (hu + kv + lw) \quad [2]$$

which is a non-stochastic device for obtaining partial information about an unknown structure directly from X-ray data. This treatment has been used occasionally for determining metallic structures; e.g., by Tucker[7] in solving the crystal structure of β-uranium. The integers *hkl* are Miller indices; the parameters *uvw* are coordinates within the unit cell expressed as fractions of unit-cell axes; the quantities $F_{(hkl)}$ are structure factors whose magnitudes are calculated directly from X-ray intensities. The function $P_{(uvw)}$ can be evaluated at every point within the unit cell; any vector from the origin to a maximum of $P_{(uvw)}$ represents an interatomic vector.

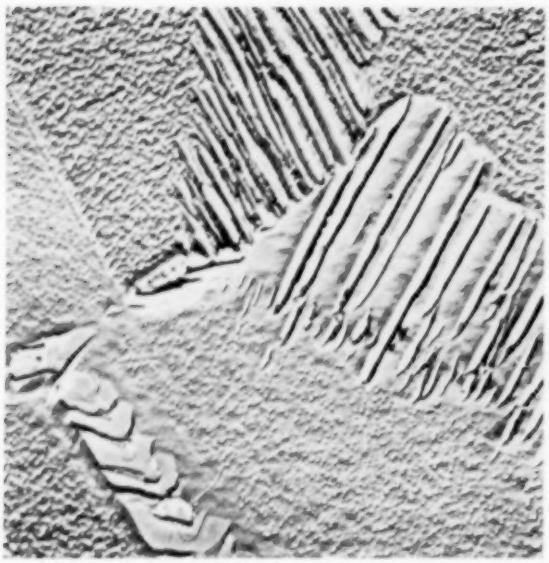

Fig. 7—Alloy *A* aged 1000 hr at 1400°F after solutioning 4 hr at 1700°F. No *G* phase is present, and cellular precipitation involving new phase has occurred at grain boundaries. X8000.

Fig. 8—Alloy *A* aged 200 hr at 1500°F after solutioning 4 hr at 1700°F. Larger particles of γ' and platelets of new phase and/or η are observable. X8000.

Fig. 9—Alloy *A* aged 1000 hr at 1500°F after solutioning 4 hr at 1700°F. X-ray diffraction shows abundant presence of η_1, little of new phase. X8000.

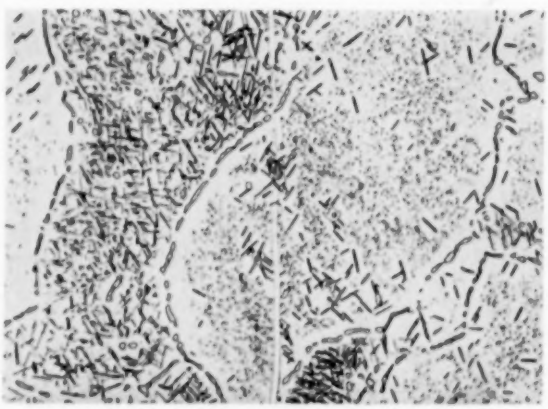

Fig. 10—Optical micrograph of alloy *D* aged 200 hr at 1400°F after solutioning 4 hr at 1700°F. Bierbaum scratch has passed over TiC particle surrounded by *G* phase. X750.

The magnitude of a maximum is proportional to the product of atomic numbers of an interatomic-vector pair and also to the multiplicity of equal interatomic-distance vectors in the structure.[8]

Table VI lists values of $|F_{(hkl)}|^2$ which were calculated from intensities by the relation

$$I \sim \frac{(1 + \cos^2 2\theta)}{\cos\theta \sin^2\theta} p\,|F_{(hkl)}|^2 \qquad [3]$$

where p is the multiplicity of planes of equal spacing. This assumes that $|F_{(hkl)}|$ is the same for all permutations of a given set of integers (hkl) and that $|F_{(hkl)}| = |F_{(\bar{h}\bar{k}\bar{l})}|$; both assumptions are valid for the space groups possible in *G* phase. The above relation also assumes that $|F_{(hkl)}|$ is the same for two or more sets of indices having the same $(h^2 + k^2 + l^2)$ value, such as (333) and (511). While this assumption is not strictly valid and must be made in absence of single-crystal data, the fidelity of the treatment is not seriously impaired.

From Eq. 2, the form of the two-dimensional Patterson-Harker section giving vectors parallel to the cube face is

$$P_{(uv0)} = \sum_h \sum_k c_{(hk)} \cos 2\pi hu \cos 2\pi kv - \sum_h \sum_k c_{(hk)} \sin 2\pi hu \sin 2\pi kv \quad [4]$$

where $c_{(hk)} = \sum_l |F_{(hkl)}|^2$. Since $|F_{(hkl)}| = |F_{(\bar{h}\bar{k}\bar{l})}|$, the second term involving sines vanishes, meaning that the borders of the quadrant bounded by $u = 0$, ½ and $v = 0$, ½ are mirrors of symmetry. Therefore, only one quadrant is shown in Fig. 11.

The equation for the one-dimensional Patterson-Harker section plotted in Fig. 12 is

$$P_{(x)} = \sum_n B_{(n)} \cos 2\pi nx \quad [5]$$

where x is the distance along the [111] axis, expressed as a fraction of the cube diagonal, and $B_{(n)} = \sum_{hkl} |F_{(hkl)}|^2$ summed over the nth-layer line of the [111] axis; all (hkl) of the nth-layer line of this axis have the property that $h + k + l = n$.

Table VII summarizes the positions of maxima in both Patterson-Harker sections. There are vectors of essentially equal magnitude in the [100] and [111] directions. The smaller one (2.62A) has about equal multiplicity in both directions. The larger one (4.85A) has higher multiplicity along the cube diagonal than along the cube edge and stands at a position (¼, ¼, ¼) from its neighbor. These sections are significant because they show that the interatomic distances in G phase are not short.

Table VII. Interatomic Distance Information from Patterson-Harker Sections of G Phase

Type	Position Parameter, u	Interatomic Distance, A	Wt. Arbitrary Scale
uoo	0.234	2.62	6
	0.434	4.85	3+
uuo	0.171	2.71	5
	0.250	3.96	9
uuu	0.137−	2.65	5
	0.250	4.85	6
	0.385	7.47	8
	0.475	9.22	1

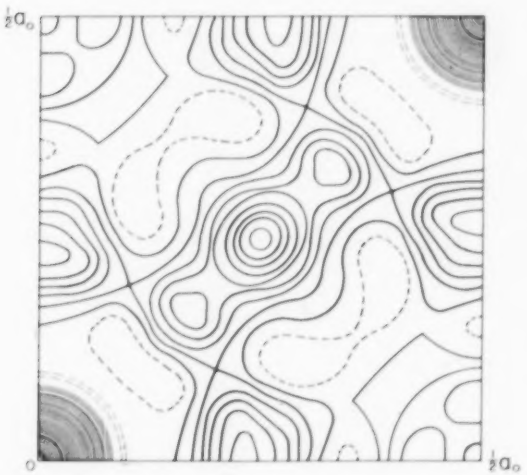

Fig. 11—Two dimensional Patterson-Harker section of G phase showing interatomic vectors parallel to cube face only.

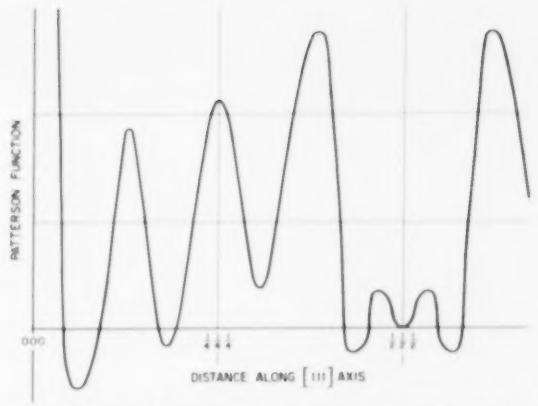

Fig. 12—One dimensional Patterson-Harker section of G phase in [111] direction.

Conclusions

Phase relationships in 26 pct Ni-15 pct Cr alloys of the A-286 type appear to result from the tendency of excess nickel to leave the matrix and combine with aluminum-poor γ', η, and G phases. Such depletion is controlled by time, temperature, and relative concentrations of silicon, titanium, and aluminum. Presumably owing to the incompressibility of its nearly saturated 3d shell, nickel tends not to take part in such phases as Laves and σ which possess abnormally short interatomic distances. Neither γ' nor η has short interatomic distances; calculated Patterson-Harker sections show that G phase is not characterized by short interatomic distances involving nickel. Laves phase appears only after most of the excess nickel in high-titanium alloys combines with γ', η, and G phases. Similarly, σ phase forms in high-aluminum alloys when excess nickel combines with γ'. While γ' is responsible for dispersion hardening in a normal manner, G phase of probable stoichiometric composition, $Ni_{16}Ti_6Si_7$, forms an additional sink for nickel segregation and thus promotes Laves-phase formation in grain interiors. Vacuum-melted A-286 of negligible silicon content has essentially the same aging characteristics based on γ' and η phases, but instead of G or Laves phases there is cellular precipitation involving a new phase.

Acknowledgments

Alloys B, C, and E through K were supplied by the Allegheny-Ludlum Steel Corp. at the request of F. L. VerSnyder, who engaged in the early stages of this investigation. Chemical analyses of separated G phase were performed by R. L. Barnard.

References

[1] H. J. Beattie, Jr. and F. L. VerSnyder: A New Complex Phase in a High-Temperature Alloy, *Nature*, 1956, vol. 178, p. 208.

[2] A. Taylor and R. W. Floyd: The Constitution of Nickel-rich Alloys of the Ni-Cr-Ti System, *Journal* Institute of Metals, 1951-1952, vol. 80, p. 577.

[3] A. Taylor and R. W. Floyd: The Constitution of Nickel-rich Alloys of the Ni-Cr-Al System, *Journal* Institute of Metals, 1952-1953, vol. 81, p. 451.

[4] A. Taylor and R. W. Floyd: The Constitution of Nickel-rich Alloys of the Ni-Ti-Al System, *Journal* Institute of Metals, 1952-1953, vol. 81, p. 25.

[5] R. Nordheim and N. J. Grant: Aging Characteristics of Ni-Cr Alloys Hardened with Titanium and Aluminum, *AIME Trans.*, 1954, vol. 200, p. 211; JOURNAL OF METALS, February 1954.

[6] J. H. Westbrook: Private communication.

[7] C. W. Tucker, Jr.: The Crystal Structure of the β Phase of Uranium, *Acta Crystallographica*, 1951, vol. 4, p. 425.

[8] R. W. James: *The Optical Principles of the Diffraction of X-rays*, pp. 371-385, Bell and Sons Ltd. London, 1948.

Discussion of this paper sent (2 copies) to AIME by Sept. 1, 1957 will appear in AIME *Transactions* Vol. 212, 1958, and in JOURNAL OF METALS, April 1958.

Hydrogen Distribution in Heat-Treated Titanium as Established by Autoradiography

The duplex heat treatment of the two phase titanium alloys containing relatively large amounts of β-stabilizing elements frequently produces a dark-etching phase at the grain boundaries. An investigation of this phase was conducted on an alloy containing Ti-3 pct Mn-1 pct Fe-1 pct Cr-1 pct Mo-1 pct V in the annealed and in the heat-treated condition. Autoradiography, using tritium as a tracer element, and electron microscopy showed the intergranular phase to be a hydrogen-rich material.

by O. J. Huber, J. E. Gates, A. P. Young, M. Pobereskin, and P. D. Frost

HYDROGEN effects in titanium alloys have been the subject of extensive research in recent years. Lenning, Craighead, and Jaffee[1] showed that hydrogen embrittles α titanium and, at the same time, elevates the temperature at which the transition from brittle to ductile failure occurs during impact testing. In later work,[2] the same investigators concluded that several all-β alloys tolerate large amounts of hydrogen without serious damage to mechanical properties, but two-phase alloys suffer varying degrees of embrittlement, depending upon the specific β-stabilizing addition used and whether or not an α stabilizer is also present.

The mechanism of hydrogen embrittlement has not been clearly established. Strain rate has been shown to be an important factor and, therefore, a strain-aging phenomenon is suspected to cause the effects that hydrogen has produced on mechanical properties.[3-5] Ripling[6] has pointed out that ductility damage varies inversely with strain rate in α-β alloys and directly in α alloys. This effect in α alloys can be associated with transition-temperature behavior, but the embrittlement mechanism in two-phase alloys remains in question.

During the course of research conducted for the U. S. Air Force, a dark-etching phase has been observed at the grain boundaries of certain two-phase titanium alloys after duplex (solution plus aging) heat treatments.[5-7] An example of the dark-etching interface phase is shown in Fig. 1. Decrease in ductility accompanies the appearance of the minor phase but has not always been attributable solely to the presence of the phase. Although the dark-etching phase has been observed in alloys under a rather narrow range of heat-treatment conditions, it is of general interest since it is always associated with the presence of hydrogen. The known embrittling effect of hydrogen makes any facet of its behavior of particular importance.

The intergranular phase has been observed in titanium-base alloys with relatively high amounts of the β-stabilizing elements. Specific examples of such alloys include Ti-5 pct Mn-2.5 pct Cr, Ti-3.5 pct Cr-3.5 pct V, Ti-8 pct Mn, and Ti-3 pct Mn-1

O. J. HUBER, Member AIME, J. E. GATES, A. P. YOUNG, M. POBERESKIN, and P. D. FROST, Member AIME, are Principal Metallurgical Engineer, Light Metals Div.; Principal Chemist, Radioisotopes and Radiation Div.; Principal Physicist, Structural Chemistry Div.; Assistant Chief, Radioisotopes and Radiation Div.; and Chief, Light Metals Div., respectively, Battelle Memorial Institute, Columbus, Ohio.

TP 4480E. Manuscript, Apr. 17, 1956.

pct Cr-1 pct Fe-1 pct V-1 pct Mo.[7] Alloys of this type are amenable to heat treatments of the duplex type. Solution treatment in the two-phase ($\alpha + \beta$) region followed by an aging treatment in the 800° to 1100°F temperature range produces improvements in mechanical properties which are highly desirable for many applications. However, such heat treatments also result in increased susceptibility to embrittlement when the hydrogen content is excessive. The actual level of tolerance has been shown to be dependent upon the strength level produced by the heat treatment, at least in the case of the Ti-3 pct Mn-1 pct Cr-1 pct Mo-1 pct Fe-1 pct V alloy.[8] The dark phase appears to be produced by heat treatments which yield a relatively high α to β ratio in the structure. Vacuum annealing decreases the relative amount of the dark phase, and the degree of degassing necessary to carry a particular alloy to the point where the phase is undetected depends upon the temperature of the solution and aging treatments.

Recent research has established that the dark-etching phase described above is titanium hydride or at least a hydrogen-rich phase. The present paper describes autoradiographic experiments in which tritium, the radioactive isotope of hydrogen, was used as a tracer element to reveal the location of hydrogen in the titanium alloys studied. Not only was the nature of the dark-etching phase revealed in this research, but some visual evidence of the tendency of hydrogen to partition to the β phase rather than the α phase was observed.

Experimental Work and Results

Although the dark-etching interface phase can be associated with the presence of hydrogen, it was not possible to identify or even detect evidence of hydrogen in situ using X-ray or electron diffraction. The most logical explanations accounting for this are 1) there was such a minor amount of the material present that it was undetected or 2) the phase is actually a modification of one of the phases present (more probably the α) in which the hydrogen concentration does not cause sufficient lattice distortion for the phase to be observed. The former is an entirely adequate explanation and there is no known relation between α phase and hydrogen to support the latter.

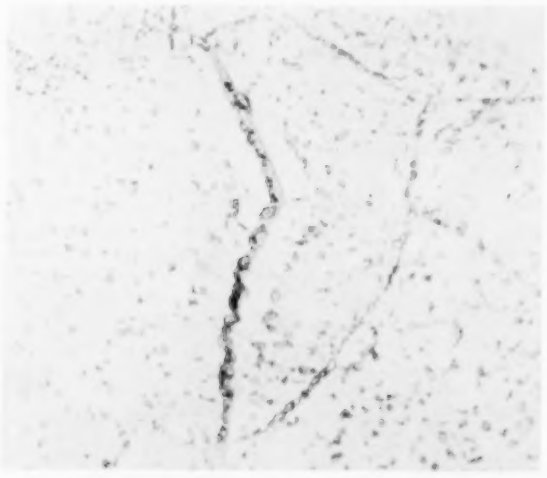

Fig. 1—Ti-3 pct Mn-1 pct Fe-1 pct Cr-1 pct Mo-1 pct V alloy with 260 ppm H rolled and solution treated in the α-β phase region and aged 48 hr at 800°F.[8] Etchant used was 1½ parts HF-3½ parts HNO_3-95 parts H_2O. The dark phase is hydride or hydrogen-rich. A heavier etch shows the matrix phase to be β with α precipitate dispersed throughout. X1000. Reduced approximately 20 pct for reproduction.

Fig. 2—Autoradiograph of Ti-3 pct Mn-1 pct Fe-1 pct Cr-1 pct Mo-1 pct V alloy before heat treatment. Specimen was outgassed at 1800°F and charged with 600 ppm tritium-bearing hydrogen; 30 hr exposure. Etchant used was 1½ parts HF-3½ parts HNO_3-95 parts H_2O. The general distribution of exposed silver grains igdicates that a reaction took place between the specimen and the emulsion. X750. Reduced approximately 20 pct for reproduction.

The correlation of the dark-etching material with hydrogen can be more convincingly established by use of autoradiography and electron metallography. A series of specimens for this purpose was prepared from a Ti-3 pct Mn-1 pct Fe-1 pct Cr-1 pct Mo-1 pct V alloy which, for other experiments, also contained 0.1 pct C. The presence of carbon is not related to nor does it affect the formation of the dark-etching hydride phase.

Specimens were prepared to provide duplicate series, one of which consisted of hydrogen-free (degassed) samples, the other of material charged with hydrogen or tritium-bearing hydrogen. Calculations indicated that 0.1 millicurie* tritium per g Ti would be sufficient to produce autoradiographs with approximately 30 hr exposure time. The tritium was purchased from the Oak Ridge National Laboratories as a gas. Hydrogenation with either pure or mixed gases was accomplished in a Sievert's apparatus, producing an overall gas content of 600 ppm. A degassing period of 10 hr at 1800°F preceded charging and a homogenization treatment of 25 hr at 1400°F followed.

* A millicurie is defined as the amount of a radioactive substance which produces the same amount of radiation as 0.001 g Ra in a unit time.

The specimens were sealed in evacuated Vycor during heat treatment. Both solution and aging treatments were followed by breaking the capsules under iced brine as rapidly as possible to effect a quench.

Autoradiography

Autoradiographic or tracer techniques can be used in many systems to determine the distribution or location of a particular component which is radio-

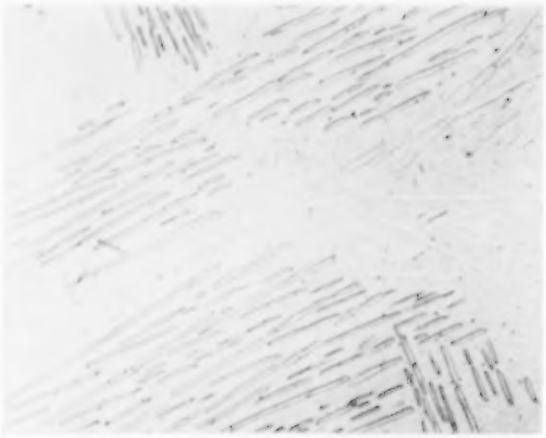

Fig. 3—Autoradiograph of Ti-3 pct Mn-1 pct Fe-1 pct Cr-1 pct Mo-1 pct V-0.1 pct N alloy. Specimen was charged with 600 ppm H and heat treated ½ hr at 1300°F followed by water quench; 168 hr exposure. Etchant used was 1½ parts HF-3½ parts HNO_3-95 parts H_2O. The low number of exposed silver grains indicates no reaction between the specimen surface and the emulsion and no radioactivity in the specimen. X1000. Reduced approximately 25 pct for reproduction.

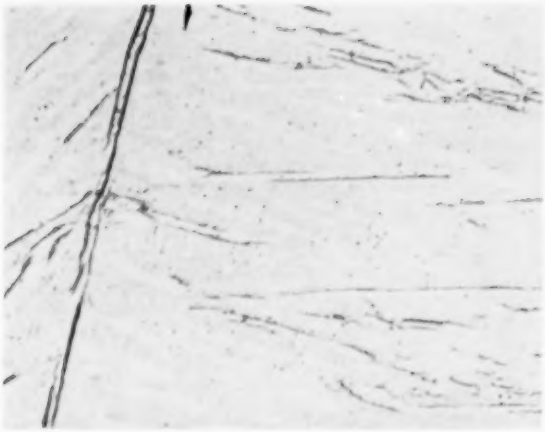

Fig. 4—Autoradiograph of Ti-3 pct Mn-1 pct Fe-1 pct Cr-1 pct Mo-1 pct V-0.1 pct N alloy. Specimen was charged with 600 ppm H and heat treated ½ hr at 1300°F followed by water quench; then aged 24 hr at 900°F; 168 hr exposure. Etchant used was 1½ parts HF-3½ parts HNO_3-95 parts H_2O. The low number of exposed silver grains provides a control to validate results using tritium-bearing hydrogen. X1000. Reduced approximately 25 pct for reproduction.

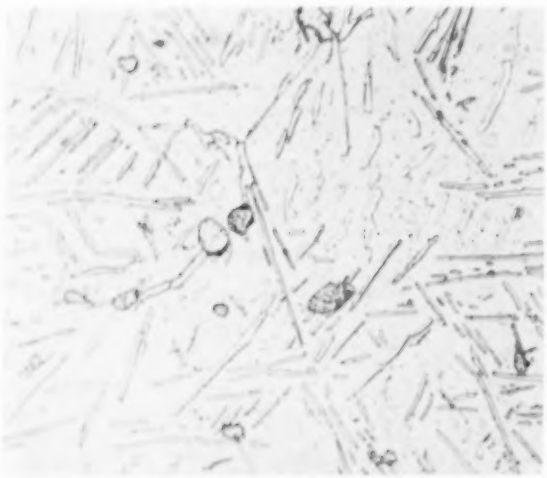

Fig. 5—Autoradiograph of Ti-3 pct Mn-1 pct Fe-1 pct Cr-1 pct Mo-1 pct V-0.1 pct C alloy. Specimen was degassed 10 hr at 1800°, loaded with 600 ppm tritium-bearing hydrogen, and homogenized 25 hr at 1400°F. Etchant used was 1½ parts HF-3½ parts HNO_3-95 parts H_2O. The matrix β phase contains white needles of primary α phase and gray spheriods of titanium carbide. The exposed silver grains indicate concentration of tritium in the carbide phase and rather universal distribution in the β phase, but relatively little in the α phase. X1000. Reduced approximately 15 pct for reproduction.

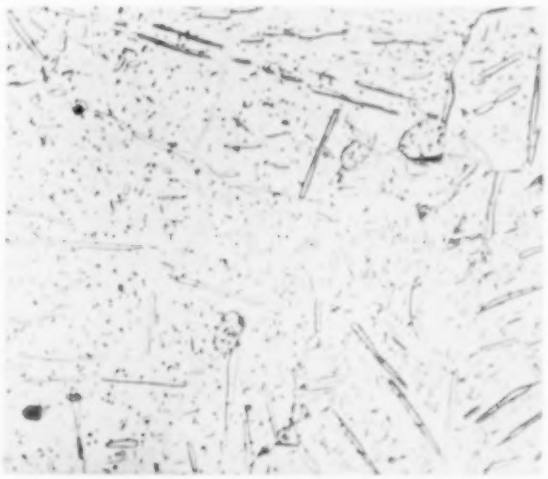

Fig. 6—Autoradiograph of Ti-3 pct Mn-1 pct Fe-1 pct Cr-1 pct Mo-1 pct V-0.1 pct C alloy. Specimen was degassed 10 hr at 1800°, loaded with 600 ppm tritium-bearing hydrogen, homogenized 25 hr at 1400°, then solution treated for ½ hr at 1300°F and quenched. Etchant used was 1½ parts HF-3½ parts HNO_3-95 parts H_2O. The matrix β phase contains needles of primary α phase and gray spheroids of carbide. Exposed silver grains indicate the tritium is distributed about as shown in Fig. 5. X1000. Reduced approximately 15 pct for reproduction.

active. In heat-treatment studies, it is possible to use tritium, the radioisotope of hydrogen, to show the distribution of the contained hydrogen. The physical and chemical properties of tritium are the same as those of hydrogen. However, the three-fold greater mass of tritium might make its reaction rate slower than that of hydrogen in some cases.

The tracer techniques, as applied in metals, allow direct comparison of the metallographic structure and the distribution pattern as revealed by the radiation pattern in a photographic emulsion. An excellent review of this technique has been published by H. J. Gomberg.[5] The technique used in the present research is as follows: The metal containing the radioactive constituent is polished and etched as for conventional metallography. A photographic emulsion is applied directly to the polished surface. The emulsion is optically clear after development so

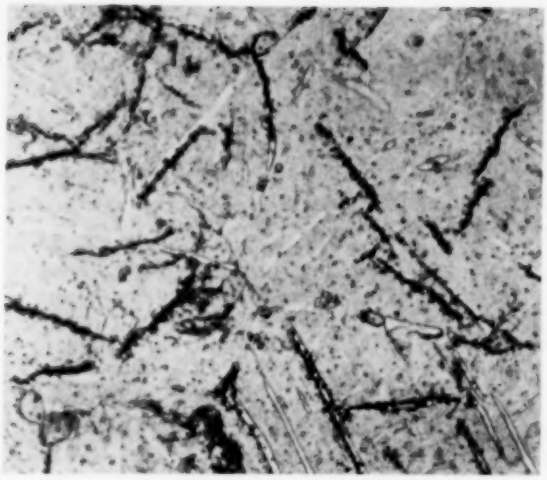

Fig. 7—Autoradiograph of Ti-3 pct Mn-1 pct Fe-1 pct Cr-1 pct Mo-1 pct V-0.1 pct C alloy. Specimen was degassed 10 hr at 1800°F, loaded with 600 ppm tritium-bearing hydrogen, homogenized 25 hr at 1400°, solution treated for ½ hr at 1300°, quenched, and given an aging heat treatment of 24 hr at 900°F. Etchant used was 1½ parts HF-3½ parts HNO_3-95 parts H_2O. The matrix β phase contains white needles of primary α phase and unresolved precipitated α, as well as the gray carbide spheroids. The exposed silver particles are concentrated over a dark phase located at the α-β interface. This indicates a high tritium concentration in this interface phase. X1000. Reduced approximately 15 pct for reproduction.

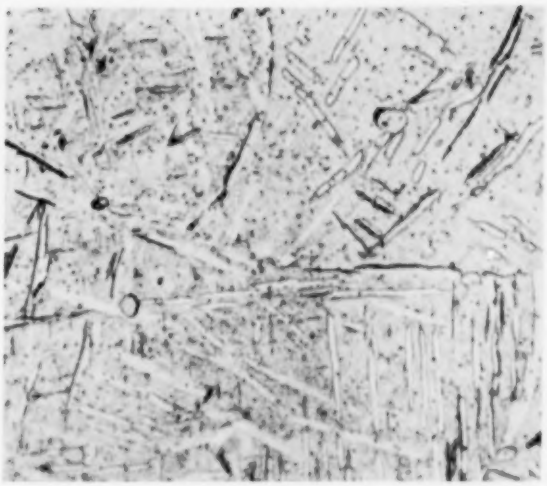

Fig. 8—Autoradiograph of control specimen, which was degassed 10 hr at 1800°, loaded with 600 ppm H (containing no tritium), homogenized 25 hr at 1400°, solution treated for ½ hr at 1300°, quenched, and given an aging heat treatment of 24 hr at 900°F. Etchant used was 1½ parts HF-3½ parts HNO_3-95 parts H_2O. The white needles of α phase and spheroids of carbide phase lie in a matrix field of β and α precipitate phases. A dark-etching interface appears along the α needles. The few dispersed, developed silver grains are artifacts resulting from such effects as pressure or corrosion at the interface between the specimen and the emulsion. X1000. Reduced approximately 15 pct for reproduction.

that exposed silver grains appear superposed on the microstructure. Under ideal conditions, an autoradiographic resolution of several μ is possible. The major factors influencing the resolution are 1) the degree of proximity between the emulsion and the metal surface and 2) the energy of radiation emitted by the radioactive material. In the case of tritium, very good resolution is possible since the energy of the 0.019 mev β radiation is so low that only the β particles emitted from the tritium in the surface layers reach the photographic emulsion.

The very low energy radiation level which makes tritium so attractive from a resolution standpoint, however, leads to many practical difficulties in its use for autoradiography because the radiation is so easily absorbed. In biological systems where high concentrations of tritium may be achieved, high resolution autoradiography may be used to show compound distribution in cell structures. Although there are many metallurgical systems in which the behavior of hydrogen is of particular importance, the application of tritium as an autoradiographic tracer has not been very successful. Low concentrations of hydrogen, as well as extreme mobility and exchange of hydrogen atoms, are severe handicaps in many systems. In titanium, however, relatively high concentrations of hydrogen are retained and fixed, probably as the hydride.

In this research early autoradiographic exposures with metallic specimens were unsuccessful as a result of reaction between the photographic emulsion and the freshly polished metal surfaces. An example of this is shown in Fig. 2. In nearly all such cases, a thin protective film, usually plastic, may be used to separate the emulsion and the surface. A film thickness of 1 μ is the minimum thickness practicable for such isolation but the average energy of the β radiation from tritium is too low to penetrate even this thin a film. Exposure of the titanium alloy to the atmosphere apparently produces a corrosion film. It was found that the emulsion did not react with the specimen after the latter had been permitted to stand in the air for a few hours prior to application of the emulsion. Actually, this type of handling produces the highest resolution in the autoradiographs by elimination of all intermediate materials.

It was calculated that satisfactory autoradiographs could be obtained from the tritium-bearing specimens during a 30-hr exposure period. This proved to be the case for specimens which were not heat treated after being charged with tritium. However, the heat-treated samples required an exposure time of seven days. The difference is probably the result of hydrogen and tritium loss during heat treatment in evacuated Vycor capsules. Sealing the specimens in an inert atmosphere might have prevented partial degassing and probably would have been equally satisfactory for protection from contamination.

After the specimens had been heat treated, they were mounted in Bakelite for metallographic polishing and etching. Each mount was arranged to hold degassed, hydrogen loaded, and hydrogen plus tritium loaded specimens. This effectively provided two nonradioactive control specimens in each mount. Comparison of the autoradiographs of the two controls established whether or not the dark-etching phase was reacting with the emulsion and producing exposed silver grains in the emulsion. Examples of such control specimens are shown in Figs. 3 and 4.

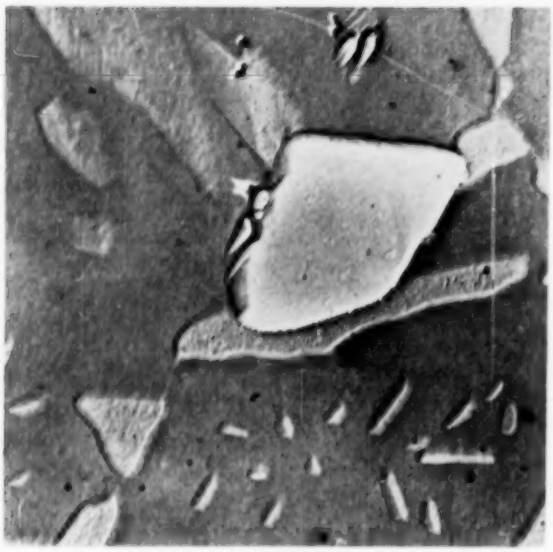

Fig. 9—Negative plastic replica electron micrograph of Ti-3 pct Mn-1 pct Fe-1 pct Cr-1 pct Mo-1 pct V-0.1 pct C alloy. Specimen was loaded with 600 ppm H plus tritium and solution treated ½ hr at 1300°F. Etchant used was 1½ parts HF-3½ parts HNO_3-95 parts H_2O. The large light particle is carbide which is standing in relief on the specimen. The gross structure is a β matrix containing primary α. X7500. Reduced approximately 35 pct for reproduction.

Fig. 10—Negative plastic replica electron micrograph of Ti-3 pct Mn-1 pct Fe-1 pct Cr-1 pct Mo-1 pct V-0.1 pct C alloy. Specimen was loaded with 600 ppm H plus tritium, solution treated ½ hr at 1300°, and given an additional heat treatment of 24 hr at 900°F. Etchant used was 1½ parts HF-3½ parts HNO_3-95 parts H_2O. The light phase is the hydrogen-rich material which has formed largely at the interfaces between the primary α and the β matrix. The latter contains a fine precipitate of the α phase. X7500. Reduced approximately 35 pct for reproduction.

Fig. 3 shows an autoradiograph of a Ti-3 pct Mn-1 pct Fe-1 pct Cr-1 pct Mo-1 pct V-0.1 pct N alloy specimen loaded with 600 ppm H before heat treatment of ½ hr at 1300°F followed by water quench. Relatively few exposed silver grains are scattered through the autoradiograph. These grains were probably exposed by radiation from cosmic sources, atomic bomb fall-out, or naturally occurring radioisotopes. Such effects are evident to some degree in any sensitive emulsion, the degree varying according to the age of the emulsion. Fig. 4 shows an autoradiograph of a specimen charged with 600 ppm H and heat treated to precipitate the dark-etching phase. Again only a light scattering of exposed silver grains is evident. The absence of significant numbers of exposed silver grains in the emulsion demonstrates the fact that there was no chemical interaction between either the metal substrate or the dark-etching phase and the emulsion during either the 168 hr exposure time or the development processes. If such reaction had occurred, the autoradiographs would have shown much heavier concentrations of exposed silver grains.

Some autoradiographs from one series of specimens loaded with hydrogen and tritium are shown in Figs. 5 through 8. The alloy is nominally Ti-3 pct Mn-1 pct Fe-1 pct Cr-1 pct Mo-1 pct V-0.1 pct C. The alloy is shown in Fig. 5 after hydrogenation but before heat treatment. The exposed silver grains are rather evenly distributed over the β phase, are relatively absent from the α, and are somewhat concentrated over the carbide spheroids. This indicates that hydrogen tends to partition into the titanium carbide and offers some visual indication that hydrogen partitions to the β in preference to the α phase. Solution treatment in the two-phase region (½ hr at 1300°F) produced little change in either the microstructure or the autoradiographic results, as is shown in Fig. 6. This is as would be expected, since the cooling rate is the main difference between the treatments. After solution treatment, the material was quenched in iced brine, while the post-hydrogenation homogenizing treatment was followed by cooling in the apparatus. In Fig. 7, the effect of aging for 24 hr at 900°F is immediately obvious. There is a concentration of exposed silver grains directly over the dark-etching material as a result of the concentration of radioactive tritium in this phase.

A control specimen was carried through the entire procedure just described except that it was initially loaded with pure hydrogen and contained no radioactive tritium. The control specimen is shown in Fig. 8 in the same condition of heat treatment as for Fig. 7. It is apparent that there are few exposed silver grains scattered over the surface and that the dark-etching phase at the α-β interfaces is sharply defined as contrasted to the appearance of the phase shown in Fig. 7. The few developed silver grains result from radiation from cosmic source or naturally occurring radioisotopes.

It would appear from this research that the dark-etching phase which formed at the α-β interfaces is TiH or at least a hydrogen-rich phase.

Electron Metallography

Upon completion of the autoradiographic work, the same series of specimens was examined in the electron microscope, using shadowed, negative plastic replica techniques.[7] The structure resulting from a solution treatment of ½ hr at 1300°F appears in

Fig. 9. The material was loaded with 600 ppm tritium-bearing hydrogen before this heat treatment. The structure is predominantly a β matrix with primary α, i.e., α which is present at the solution temperature. The large spheroid is a titanium carbide particle. The solution treatment described above followed by aging 24 hr at 900°F produced the microstructure shown in Fig. 10. The matrix is β containing a fine dispersion of precipitated α. The phases in relief are primary α and the hydrogen-rich phase. The α appears darker and the hydride is light and is located at the interface between primary α and the matrix. Since in the electron micrographs both the hydride and the carbide phases appear as light areas (thin areas in replica), other regions in the same sample which showed carbide particles were also examined to confirm the differences in their appearance.

Fig. 11 is an electron micrograph of a specimen which received the same heat treatment as that of Fig. 10 but which was previously degassed. The obvious difference between Figs. 10 and 11 is that the hydride phase present in Fig. 10 does not exist in the degassed material.

The appearance of the α phase throughout this series is interesting, although the effect is probably not connected with the presence of hydrogen. There are varying degrees of attack by the etchant on the the various α islands. In Fig. 11 particularly, some of the α phase appears to be relatively unattacked and, therefore, it stands in relief above the matrix material. Other areas have been more seriously attacked and are recessed. Compositional variations in the α phase are possible in the heat treatment of complex alloys, and they could also account for the observed variations. The effect need be a relatively minor one to be visible at the magnification used, X7500.

Some speculation on the mechanism of hydrogen embrittlement is possible based on the observations made in this paper. The autoradiographs indicate a tendency for hydrogen to partition to the β phase during a solution treatment. During subsequent aging the hydrogen comes out of solution and diffusion to the α-β interfaces takes place. The hydrogen forms the titanium hydride compound with the α phase. The same diffusion and compound formation could conceivably be produced by strain aging as well as by thermal aging. Since it is known that titanium hydride is brittle, this mechanism of formation of the hydride phase at α-β interfaces might be the one which produces strain embrittlement in high-hydrogen titanium alloys.

Summary

In two-phase titanium alloys containing relatively large amounts of the β-stabilizing elements, a minor phase has been observed at the β-α interfaces after duplex heat treatments involving aging (isothermal anneal) in the 800° to 1100°F range. The dark-etching phase appears where the ratio of α to β phase is relatively high and it increases in quantity with increasing hydrogen content. Crystallographic evidence has not been obtained, but the formation of the intergranular phase has been established by light and electron metallography and its high hydrogen content has been proven by autoradiographic tracer techniques, using samples charged with tritium-bearing hydrogen. Autoradiography has also provided some evidence for the tendency of hydrogen to partition to the β phase in preference to the α phase in titanium alloys.

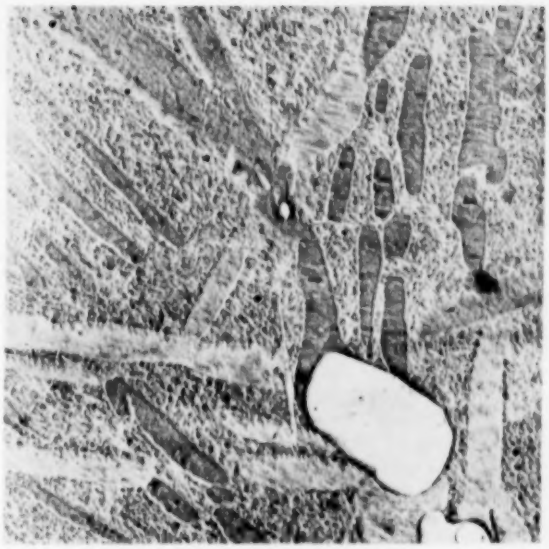

Fig. 11—Negative plastic replica electron micrograph of control specimen of degassed material solution treated ½ hr at 1300° and aged 24 hr at 900°F. Etchant used was 1½ parts HF-3½ parts HNO_3-95 parts H_2O. The large light area is a carbide particle. Primary α needles and fine α precipitate appear throughout the β matrix. No hydrogen-rich phase is present. Note that the degree of etchant attack on the α phase areas varies. X7500. Reduced approximately 35 pct for reproduction.

Acknowledgments

This research was conducted under Air Force contracts administered by the Materials Laboratory, WADC. Permission to publish the results of this work is gratefully acknowledged. Other Battelle personnel who contributed to the research include H. A. Robinson, G. B. Engle, M. W. Mallett, and W. M. Parris.

References

[1] G. A. Lenning, C. M. Craighead, and R. I. Jaffee: Constitution and Mechanical Properties of Titanium-Hydrogen Alloys. *AIME Trans.*, 1954, vol. 200, p. 367; JOURNAL OF METALS, March 1954.

[2] C. M. Craighead, G. A. Lenning, and R. I. Jaffee: Hydrogen Embrittlement of Beta-Stabilized Titanium Alloys. *AIME Trans.*, 1956, vol. 206, p. 923; JOURNAL OF METALS, August 1956.

[3] R. J. Kotfila and E. F. Erbin: Hydrogen Embrittlement of a Titanium Alloy. *Metal Progress*, 1954, vol. 66, p. 129.

[4] H. M. Burte, E. F. Erbin, G. T. Hahn, R. J. Kotfila, J. W. Seeger, and D. A. Wruck: Hydrogen Embrittlement of Titanium Alloys. *Metals Progress*, 1955, vol. 67, p. 115.

[5] H. A. Robinson, W. M. Parris, and P. D. Frost: Development of Improved Titanium-Base Alloys. WADC Report No. 54-205, Part II. Battelle Memorial Institute, Columbus, 1954.

[6] E. J. Ripling: Hydrogen Embrittlement of a Commercial Alpha-Beta Titanium Alloy. *AIME Trans.*, 1956, vol. 206, p. 502; JOURNAL OF METALS, May 1956.

[7] W. M. Parris, P. D. Frost, and J. H. Jackson: Heat Treatment of High Strength Titanium-Base Alloys. *ASM Trans.*, 1954, vol. 46, p. 568.

[8] H. J. Gomberg et al.: High Resolution Autoradiography for Study of Grain Boundaries in Metals. Engineering Research Institute Report No. 2029-1-F, University of Michigan, Ann Arbor, 1954.

[9] C. M. Schwartz, A. E. Austin, and P. M. Weber: A Positive Replica Technique for Electron Microscopy. *Journal of Applied Physics*, 1949, vol. 20, pp. 202-205.

Discussion of this paper sent (2 copies) to AIME by Sept. 1, 1957 will appear in AIME *Transactions* Vol. 212, 1958, and in JOURNAL OF METALS, April 1958.

Blister Formation in Rolled Aluminum

Blister raising discontinuities have been located in sheet ingots and followed by means of nondestructive testing methods through the various stages of sheet production to the formation of blisters. The relative importance of gas content and ingot discontinuities has been determined. The use of a fabricating technique based on at least 40 pct cold reduction of the *as cast* ingot prior to the application of normal hot and cold rolling procedures has been shown to eliminate blisters. An explanation for this is offered.

by J. H. O'Dette

BLISTER formation on wrought aluminum products has been a matter of concern to aluminum fabricators for many years.

The fact that blisters make their appearance during the final stages of fabrication means that much time and effort have been expended before it is evident that the material must be scrapped. This and the loss of production are ample reasons for embarking on a research program to find out more about blistering and possible methods of control.

Many excellent papers on this subject have appeared in the technical literature in the last few years. In one of the more recent papers, Kostron[1] gives a fairly complete review of the problem of gas in aluminum and blistering in general. From the work of the various investigators, a general mechanism for the formation of blisters has evolved and may be summarized briefly as follows: Hydrogen gas is usually present in the cast ingot, in the atomic or ionic state, in excess of the solid solubility. At room temperature the gas atoms are relatively immobile, but at elevated temperatures they become mobile and diffuse to free surfaces where they associate to form molecules. If these free surfaces are discontinuities within the ingot then the associated gas molecules collect and build up considerable pressure until equilibrium is reached with the dissolved gas around the discontinuity. Since the solubility of the gas is proportional to the square root of the partial pressure it is evident that large pressures may be built up at the discontinuities. When the metal is rolled to sheet the pressure of the gas in these discontinuities is sufficient to deform the surface of the sheet and form a blister, particularly when the strength of the material is reduced during the annealing.

Although the mechanism of the formation of blisters was fairly well known, the actual importance of the individual roles played by the gas and the discontinuities was not so well established that positive methods for control of blistering were at hand. It was the object of the investigation to learn more about the nature of the discontinuities giving rise to blistering and to develop methods of control.

The investigation was carried out in three stages as follows:

a) A study of the more commonly used methods of removing hydrogen from aluminum, such as fluxing and holding, and their effects on blistering.

b) Location of the discontinuities giving rise to blistering.

c) A study, by indirect methods, of the movement of gas in the metal and its effect on blistering, and the development of methods of blister control during fabrication.

Removing Gas and Reducing Blistering by Fluxing or Holding—The work of removing gas and reducing blistering by fluxing or holding was carried out on metal of Alcan 2S (1100) composition with an artificially high gas content. The high gas content was obtained by introducing water into the melt prior to casting; the water reacted with the aluminum forming Al_2O_3 and hydrogen. The procedure was to raise the gas content by introducing water into an aluminum melt and using half the melt to cast one ingot immediately. The remaining metal was treated again with water to make up for the reduction in gas content during holding, while the first ingot was being cast, and then given a fluxing or holding treatment and cast into an ingot. Samples for gas determination were cast from the molten metal before and after the *gassing* operation; before, after, and during fluxing, and while casting. Samples were also cut from sections of the ingots. Gas determinations were made on these samples using the well known vacuum fusion technique. All ingots were hot rolled at 500°C to 0.250-in. slab which, in turn, was cold rolled to 0.040 in. sheet. The sheet was coiled and annealed for 2 hr at 500°C and then cut into 5-in. squares which were inspected for

J. H. O'DETTE is Research Metallurgist, Aluminium Laboratories Ltd., Kingston, Ont., Canada.

TP 4460E. Manuscript, Sept. 13, 1956.

blisters. One or more blisters on either surface of a square was sufficient to classify it as scrap.

Invariably the initial ingots cast from the melts just after the *gassing* operation had a high level of gas (in the order of 1.7 to 2.7 ml per 270 g) and an extremely high tendency to blister (100 pct scrap). Fluxing the melts with chlorine, nitrogen, or argon in the temperature range 680° to 750°C was effective in reducing the gas content to a low level (in the order of 0.20 to 0.50 ml per 270 g) and the blistering to a low level (0 to 4 pct scrap). Fluxing tools that gave multiple streams of small fluxing gas bubbles were also more effective than tools that emitted a single stream of larger bubbles. Solid fluxes, such as hexachlorethane, acted similarly to gaseous fluxes in reducing both gas and blistering.

Although without exception it was possible to reduce the gas content of the melts to a low level it did not always follow that the blistering would be entirely eliminated. In seeking the reason for this it was found that in cases where the gas was reduced to a low level and there was still some blistering, the ingot contained an appreciable amount of shrinkage porosity. In the cases where the blistering was eliminated there was very little, if any, shrinkage porosity in the ingot.

Identification of Ingot Discontinuities Giving Rise to Blistering—Microsections of blisters, Fig. 1, from annealed sheet were prepared and showed the blisters to be expanded lamellar discontinuities lying in a plane parallel to the surface of the sheet.

The appearance of these discontinuities suggested that they had their origin in shrinkage cavities or in entrapped oxide particles in the ingot. Sections of tilt mold and direct chill cast sheet ingots were examined using radiography and ultrasonic reflectoscope techniques and following this a metallographic examination was carried out in areas indicated to contain defects. In nearly all cases where ingots had a high tendency to blister many discontinuities were located in the nondestructive testing, and metallographic examination showed them to be shrinkage cavities. In ingots with little tendency to blister very few discontinuities could be located. It was also noted that in the case of tilt mold ingots the shrinkage cavities were usually quite large and the blisters on the sheet produced from these ingots were large. On the other hand, direct chill cast ingots had, on the whole, much smaller shrinkage cavities, and the resulting blisters on the sheet rolled from these ingots were quite small. This relationship between ingot porosity and blistering is shown in Fig. 2.

Table I. The Effect of Preheating Time and Temperature on Gas Content and Blistering of Alcan 2S (1100) Aluminum Alloy

Time at Temperature, Hr	Preheating Temperature, °C		
	500°	550°	600°
6*	1.35	1.65	1.63
†	1.55	1.11	0.35
‡	89.0	93.0	34.0
12*	1.32	1.51	1.50
†	1.22	1.23	0.19
‡	87.0	100.0	17.0
18*	1.53	1.38	1.90
†	1.27	0.87	0.14
‡	80.0	94.0	33.0
24*	1.43	1.39	1.70
†	1.28	0.42	0.28
‡	84.0	64.0	27.0

* Original ingot gas content in ml per 270 g.
† Gas content of ingot after preheating in ml per 270 g.
‡ Pct blister scrap.

During the examination of the ingot sections very few oxide inclusions were observed and it appeared that shrinkage cavities in the ingot were the main blister-raising discontinuities. However, oxide inclusions could not be discounted completely because the methods used to examine the sections were such as to detect readily shrinkage cavities, whereas oxide inclusions were more difficult to detect. The X-ray method, in particular, located shrinkage cavities but was practically useless in locating oxide, unless it had associated porosity. This is because the X-ray absorption coefficients for aluminum and its oxide are almost identical.

To go a step further in this part of the investigation, sections of tilt mold and direct chill cast ingots were tested by means of ultrasonics and radiography and porosity in the ingots was accurately located. Using the same testing methods it was possible to trace the ingot porosity through the various stages of sheet production and to observe blisters forming during annealing at the site of the porosity, which had, during the course of fabrication, become a lamellar discontinuity.

While the examination of production ingots to identify the blister-raising discontinuities was under way, a separate investigation to evaluate the effect of the variables in the direct chill casting process on the quality of sheet ingot and, in particular, the blistering was completed. An examination of sections of ingot from this program was carried out to determine the reasons for the variation in blistering. Nondestructive testing methods failed in this case to locate the discontinuities, and it was necessary to use density determinations to locate the porosity in the sections. The measurements were made on 3/4 in. x 3/16 in. x 6 in. sections cut side by side across the width of the ingot. Density patterns were plotted for the individual sections and ingots which had a high tendency to blister had regions of low density that corresponded with the source of the blister-raising discontinuities. Metallographic examinations were then carried out on the sections with low density and considerable microshrinkage was found in most cases to account for this low density.

At this stage in the investigation of blistering the relative importance of gas in the ingot and shrinkage porosity was considered to have been established. The findings agreed with the generally accepted view that both gas and internal discontinuities were required for the formation of blisters, but in addition went a step further and pointed out the marked importance of the discontinuity (in this case microshrinkage) factor in controlling blistering. Ingots with widely varying gas content gave various

Fig. 1—Cross section of typical blister in Alcan 2S (1100) aluminum sheet. Note the expanded lamellar discontinuity resulting in the raised portion on the surface of the sheet. As-polished. X40. Reduced approximately 25 pct for reproduction.

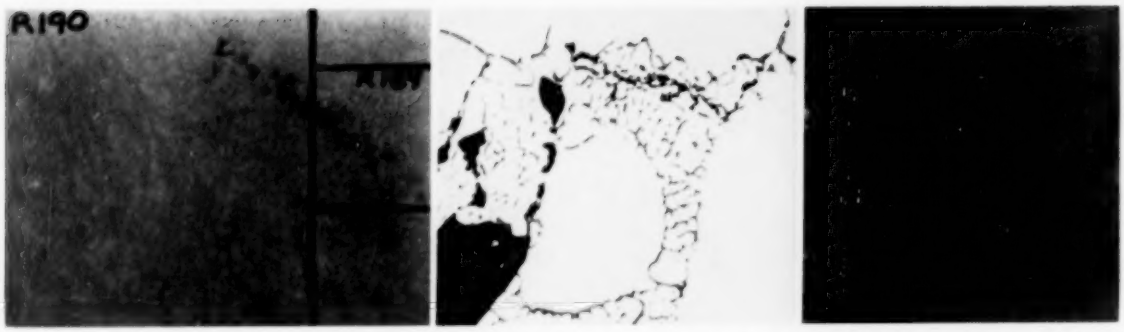

Fig. 2—LEFT: Radiograph of section of ingot showing porosity and the location of rolling ingot R-190 and microsection R-189 in relation to the discontinuity. CENTER: Micrograph R-189 as-polished, showing details of porosity. X100. RIGHT: Photograph of section of sheet rolled from ingot R-190 showing the blistering. X1.

levels of blistering depending on the soundness of the ingot. An ingot could have the lowest possible gas level it was practicable to obtain and still have a tendency to blister because of ingot unsoundness. On the other hand, an ingot with a much higher level of gas could have a slight tendency to blister due to a very sound ingot structure, free from coarse microshrinkage. A large measure of control could also be exerted over the extent, size, and distribution of the ingot microshrinkage by changes in the casting conditions.

Gas Diffusion and Methods of Blister Control During Fabrication—The third stage of the investigation was concerned with a study of gas diffusion in an ingot by determining the effect of fabrication variables, such as preheating and interannealing, on the gas content and the blistering. Admittedly, this was an indirect way of studying gas diffusion, but then no direct method exists whereby the actual movement of gas through a metal can be observed. Eborall and Swain[7] showed that it was possible to remove hydrogen from brass ingots during preheating and annealing. In this case the hydrogen gas was caused to diffuse out of the ingot prior to the stage in which the ingot was rolled to light gage sheet and blistering was prevented. It seemed reasonable to expect that similar treatments might be effective in reducing the gas content of aluminum and possibly the blistering. Eborall and Ransley[7] demonstrated (in their work on the Al-Mg alloys) that hydrogen diffused readily in aluminum. However, there was another consideration in attempting to diffuse hydrogen out of aluminum and that was the barrier to diffusion which existed at the surface of the metal, in the oxide film. Smithells and Ransley[8] and Russell[9] showed the marked effect of the surface oxide film in retarding the permeation of hydrogen through aluminum.

Table II. The Effect of Slab Annealing Time and Temperature on the Gas Content and Blistering of Alcan 2S (1100) Aluminum Alloy

Time at Temperature, Hr	Annealing Temperature, °C			
	400°	450°	500°	550°
1*	2.43	2.35	2.83	2.59
†	1.74	1.35	1.72	1.36
‡	50.0	65.0	76.5	58.7
3*	2.37	2.64	2.62	2.45
†	1.61	1.65	1.69	1.15
‡	55.5	82.0	73.7	30.3
6*	2.45	2.45	2.36	2.08
†	1.59	1.26	1.12	0.78
‡	84.5	11.4	22.1	0.0
9*	2.21	2.17	2.50	2.35
†	1.13	1.66	1.21	1.17
‡	62.0	25.0	45.0	5.2

* Gas content of slab before annealing in ml per 270 g.
† Gas content of slab after annealing in ml per 270 g.
‡ Pct blister scrap.

Each experimental lot consisted of four ingots. Two gas samples were taken from each ingot prior to preheating and two after preheating. In the case of the interannealing experiments eight gas samples were taken at various positions in the slab from each ingot before and after annealing.

Typical results for the preheating and the interannealing experiments are presented in Tables I and II, respectively.

Considering first the results of the preheating experiment it is apparent that, although preheating reduced the gas content up to 17 pct at 500°C, it had little effect on blistering. It was not until a temperature of 550°C was reached and the loss in gas was of the order of 70 pct that the blistering was reduced. At a temperautre of 600°C, when the reductions in gas were of the order of 80 to 90 pct, the blistering was reduced considerably. It is evident that at temperatures of 550°C and less the diffusion of gas from the ingot is slow and that only at temperatures of about 600°C can the ingot gas content be reduced in a reasonable length of time. Since a reduction in blistering takes place it would also indicate that there is a reduction in gas content at the discontinuities; that is, if gas has separated at free surfaces in the ingot it now dissociates and diffuses out of the ingot.

Preheating and Interannealing—Experiments were designed to determine the effect of preheating and interannealing on the gas content and blistering of 3¾ in. x 9 in. x 36 in. direct chill cast ingots in Alcan 2S (1100) alloy composition. All ingots were cast from metal with a high gas content to ensure a marked tendency to blister. The high gas content was produced, as in the work on fluxing, by introducing water into the melt. The procedure was to hot roll the ingots at 500°C to 0.250 in. slab, cold roll the slab to 0.040 in. sheet, coil the sheet and anneal it for 2 hr at 500°C, and then to cut it into 5 in. squares (there were approximately 70 5 in. squares of sheet from each ingot) which were subsequently inspected for blisters. One or more blisters on either side of a sheet was sufficient to classify it as scrap. In the case of the preheating experiments, the ingots were preheated before hot rolling; in the case of the interannealing experiments, the ingots were hot rolled and the interanneals carried out on the hot mill slab.

The results of the interannealing experiments were similar to those of the preheating experiments inasmuch as it was possible to reduce the gas content and the blistering of the slab by annealing. However, the time at temperature was shorter and the temperature lower for any specific reduction in blistering. This could be reasonably accounted for on the basis of the shorter path over which the gas was required to diffuse to reach the atmosphere. There was also the possibility that the oxide film on the hot mill slab was more porous than that on a cast ingot and offered less of a barrier to the diffusion of the gas from the slab.

Cold Reduction of Ingots Prior to Heating—In production, increased blistering had been experienced after preheating. An explanation for this could be found if the gas in the cast ingot were considered to be in solid solution and not separated on internal free surfaces as suggested by Ransley.[6] Under these conditions, any heating of a cast ingot into the temperature range 450° to 500°C, where gas diffused readily through the aluminum lattice, would allow the gas to separate on the internal discontinuities (these should be free of any oxide film on their surface). At the same time the gas would tend to diffuse out of the ingot, but this would be a much slower process due to the longer path over which the gas would have to diffuse and the resistance to diffusion offered by the external oxide film. This being the case, an ingot preheated 8 hr at 535°C would have much the same total gas content as an as-cast ingot but, instead of the gas being in solid solution, part of it would now be separated as molecular gas at internal free surfaces. The gas separated at discontinuities would prevent the discontinuities from being welded shut during rolling and result in a lamellar gas-filled discontinuity in the finished sheet which would form a blister during annealing.

The blister-raising discontinuities had been identified as mainly shrinkage cavities in the early stages of the investigation. This being the case, and considering the above mechanism of gas diffusion to be operative, the possibility of removing these discontinuities by cold rolling prior to any heating suggested itself. If, as postulated, the cavities were gas-free, they could be expected to weld shut during a cold rolling operation.

To test this theory an experiment was conducted in which cold rolling of an ingot was compared with hot rolling. One half of a *high gas* ingot was cold rolled and the other half hot rolled at 500°C. The cold rolled ingot was reduced 85 pct and the resulting sheet contained no blisters. The sheet from the hot rolled ingot, which was also reduced 85 pct, had approximately 1000 blisters. Since gas analysis on the ingots before cold rolling and on the slab after rolling showed the same gas content the experiment indicated that the cold rolling had removed the sites where gas separation normally took place and resulted in blistering. A further proof of this was supplied by ultrasonic inspection tests which were carried out during the course of the experiments. Internal defects were detected in both ingots prior to rolling. They disappeared in the ingot which was cold rolled, but persisted in the ingot which was hot rolled through to the sheet stage and resulted in blistering.

A series of experiments was conducted to determine the amount of cold reduction necessary to reduce blistering. In these tests high gas ingots were used and were given varying cold reductions. After the cold reduction, the ingots were hot rolled at 500°C to 0.250 in. slab, which was in turn cold rolled to 0.040 in. sheet, annealed, and inspected for blisters. The results of these experiments are shown in Fig. 3.

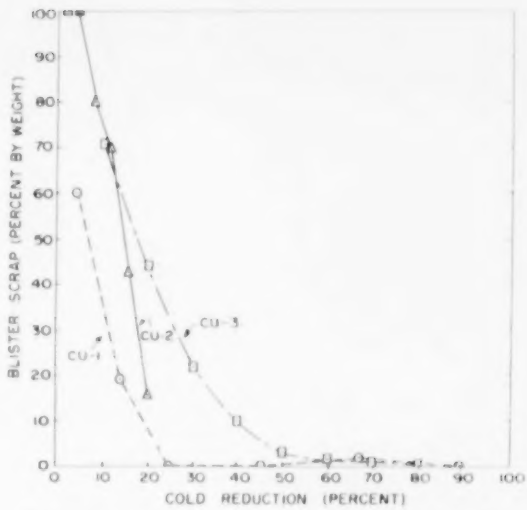

Fig. 3—Relationship between cold reduction and blistering for Alcan 25 (1100) aluminum alloy.

During the course of this work two gas samples were taken from each cast ingot, four from the slab after cold reduction and four from the slab after hot rolling. On analysis of these samples it was found that the gas content of the material did not change during fabrication.

The tests showed quite clearly that cold reductions of the order of 40 pct were sufficient to reduce blistering to a very low level. This reduction in blistering was attributed to a closing up of ingot shrinkage cavities during cold rolling, with the resultant removal of free surfaces on which gas might separate from solid solution. The gas analysis results ruled out any possibility that the reduction in blistering was due to a drop in the gas content during fabrication.

To complete this phase of the investigation a series of tests was carried out in which ingots were heated to 500°C for ½ hr and then cooled to room temperature, before being given cold reductions varying from 10 to 80 pct. In these tests the cold reductions had no effect in reducing blisters. It appeared that in as short a time as ½ hr at 500°C gas separated at internal discontinuities and that cold reduction, after this gas separation had taken place, was no longer effective in welding shut the cavities. The film of gas between the two surfaces of the cavity probably prevented them from welding during the rolling.

Since cold rolling (rolling with the ingots at room temperature, approximately 25°C) produced no blistering and hot rolling at 500°C produced a great deal of blistering, it was to be expected that in this temperature range (25° to 500°C) there would be a transition temperature below which little blistering would occur and above which appreciable blistering would occur. This temperature would correspond to that at which the diffusion of gas to internal shrinkage cavities becomes rapid and the cavities would be filled in a short period of time.

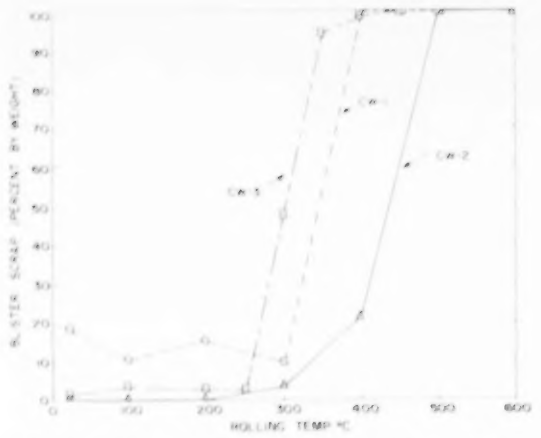

Fig. 4—Relationship between rolling temperature and blistering of Alcan 2S (1100) aluminum alloy.

Tests were conducted to determine this transition temperature. In these tests the ingots were rolled, at temperatures from 20° to 500°C, as indicated in Fig. 4, to 0.250-in. slab. The slab was then cold rolled to 0.040-in. sheet, annealed, and inspected for blisters. The results of these tests are presented in Fig. 4.

The graph shows quite clearly that in the temperature range 300° to 400°C there is a marked increase in blistering. As mentioned previously this is attributed to the fact that, at these temperatures, the gas in solid solution in the metal is diffusing to the internal shrinkage cavities at such a rate that the cavities become filled with gas in the short time required to bring the ingot to these temperatures (½ to 1 hr). Eborall and Ransley[5] report rapid gas diffusion in Al-Mg alloys at a temperature of 400°C and it appears quite probable from these results that for Alcan 2S (1100) alloy, internal gas diffusion proceeds very rapidly at temperatures even below 400°C. The blister scrap figure for curve CW-1 is higher than that for curves CW-2 and CW-3 up to a temperature of 300°C. In determining the reason for this it was found that the ingots used in this test had, in addition to normal shrinkage porosity, some gas porosity very close to the surface. This porosity was in the form of spherical cavities. Since these cavities contained gas precipitated during casting it was not to be expected that rolling at low temperatures would have any effect on reducing blistering from this source. This curve shows a rapid rise in blistering when the temperature is reached where gas precipitation to shrinkage cavities takes place. In this respect it is very similar to curves CW-2 and CW-3.

Summary and Discussion

The initial investigation of the problem of blistering, which consisted of experiments using conventional fluxing techniques for the removal of gas and reduction of blistering, gave results that were in agreement with previously published work on this subject. It was possible to reduce greatly the amount of gas in the liquid metal prior to casting and, in so doing, to reduce markedly the tendency to blister. In addition, it was observed that, although fluxing reduced the gas content of the molten metal to a very low level, it did not necessarily follow that the blistering would be reduced to zero. The reason for this became apparent during the second part of the investigation when the blister-raising discontinuities in the ingot were identified as shrinkage cavities. It was observed that ingots with quite low gas contents would blister if there was microshrinkage to act as a center for gas separation. On the other hand, ingots with quite high gas content had little tendency to blister if they were free of microshrinkage, particularly near the surface.

The later stages of the investigation, which were directed toward the development of remedial measures to be used during fabrication, proved to be the most rewarding from the point of view of offering new methods of blister control and a fairly clear explanation of the process of blister formation.

In the development of a theory to explain the process of blister formation there is a limitation in the fact that the all important movement of the hydrogen through the metal lattice cannot be observed directly. Indirect indications of the movement of the gas, such as a change in total gas content or changes in blistering, must be relied upon.

The results of the experimental work support the generally accepted theory of blister formation, based on gas diffusion and separation on free surfaces within an ingot where large pressures are built up, which result in blistering during annealing. Moreover, the free surfaces on which gas separates in the ingots have been identified as shrinkage cavities and special fabricating techniques have been devised to overcome blistering.

It is quite often assumed that the direct chill casting process allows appreciable gas to escape from the liquid metal to become entrapped as gas bubbles in the solidifying casting. As mentioned previously, Ransley[5] has suggested that this is not the case and the results of this work would substantiate his views. Although the gas is much less soluble in the solid metal than in the liquid metal, it does not follow that it is rejected automatically to the liquid on freezing. It is held in the solid initially and whether or not it passes to the liquid and leads to porosity depends on the rate of diffusion of the gas in the solid in relation to the rate of advance of the freezing front. For Alcan 2S (1100) aluminum alloy it appears that under normal direct chill casting conditions the greater part of the gas is in solid solution in the as-cast ingot.

Given an as-cast ingot with hydrogen in solid solution and with some shrinkage porosity to act as a free surface for gas separation it would appear from the results of this work that the mechanism of the formation of blisters would be that, during the preheating of the ingot or during heating for hot rolling, the hydrogen in solid solution diffuses to shrinkage cavities and separates, probably as molecular gas. This diffusion and separation takes place rapidly at a temperature of 300° to 400°C, as indicated by the experiments to determine the effect of hot rolling temperature on blistering. Prolonged heating in this temperature range merely allows more gas to separate and increase the blistering in the final sheet. During the hot rolling the gas-filled shrinkage cavities are rolled out into gas-filled lamellar discontinuities in the slab. The film of gas between the two surfaces of the discontinuities is sufficient to prevent the welding of the two surfaces during rolling. The cold rolling of the slab to sheet serves to reduce the thickness of the material and in effect to bring the lamellar gas-filled discontinuity closer to the surface of the sheet. When the

sheet is annealed the gas in this discontinuity, which is under high pressure, is expanding and at the same time the strength of the material is falling. This results in deformation outward of the surface of the cavity and formation of a blister on the surface of the sheet. As stated previously in the introduction, this is a conventional theory of blister formation, which is supported by the results of this work, inasmuch as the ingot discontinuities were located nondestructively and followed through the various stages of sheet production to the actual formation of the blisters.

Additional indirect support for this theory of blister formation was also obtained in the experiments on cold rolling of as-cast ingots and its effect on blistering. If the mechanism of blister formation was as presented above it was reasoned that the removal of the internal free surfaces, where gas might separate, would prevent the separation of the gas and reduce blistering. Since the initial work had shown these internal free surfaces to be shrinkage cavities the problem became one of removing them at some temperature below that at which gas would readily diffuse to them. Rolling of ingots at room temperature proved to be a successful method of removing the cavities and of reducing blistering. The actual closure and disappearance of the cavities during rolling was followed with the ultrasonic reflectroscope and also by means of sectioning and microradiography. The reduction in blistering was dependent on the amount of cold reduction given to the ingot up to approximately 40 pct reduction, at which point the blistering was reduced to approximately zero.

The immediate explanation of the effect of this cold reduction on blistering is a simple one, based on the observed fact that the shrinkage cavities in the ingot were being removed by the cold reductions and this prevented blistering. The gas-free shrinkage cavities apparently cold welded and thus removed free surfaces where gas might precipitate and cause blistering.

The later tests to observe the effect of rolling temperature on blistering indicated that at temperatures up to 300°C the diffusion of gas to shrinkage cavities was slow and that it might not be necessary to give the ingots heavy reductions at room temperature, but that rolling at temperatures up to 300°C might be satisfactory. However, no experiments were conducted to investigate cold rolling effects in the temperature range 30° to 300°C.

The concept of essentially gas-free shrinkage cavities in an as-cast ingot was further supported by the experiment to determine the effect of cold reductions on blistering on a preheated ingot. In this case the short time required to raise the temperature of the ingot to 500°C was sufficient to allow the gas to diffuse and separate to the cavities. Once the gas had separated no amount of cold reduction would then remove the cavities since the film of gas presumably prevented cold welding of the adjacent faces of the laminate. This left the slab with free surfaces on which gas had separated and on which more gas could separate, giving rise to blisters.

Although the above explanation for the effect of cold reduction of as-cast ingots on blistering has been presented as being the most probable from the observed facts, another explanation is being considered and experiments are under way to obtain some experimental data to support it.

This alternative explanation takes into account the fact that cold rolling has introduced many dislocations in the metal and, possibly, for this material has also introduced the maximum number of dislocations in the region of 40 pct cold reduction. The dislocations are considered as sites where gas separation may take place from solid solution, possibly to the extent of one or two gas molecules per dislocation. The extremely large numbers of dislocations in the material could conceivably accept all the gas from solid solution. A situation could thus exist in which the gas in the metal could be precipitated at a large number of sites in amounts too small to be of consequence in the formation of blisters. In such a case other free surfaces in the ingot would not play a part in blistering, since the gas would be tied up at the dislocations and would not be free to move to alternative free surfaces. This theory would not require the removal of the free surfaces presented by shrinkage cavities during rolling in order to explain the disappearance of blisters. The introduction of a large number of dislocations during rolling would suffice. If the above theory of gas separating on dislocations is correct, the precipitated gas molecules could be expected to hinder the movement of dislocations. This problem is at present under study.

This work has indicated the importance of the roles played by gas and shrinkage cavities in the formation of blisters in rolled aluminum and has shown the rate of lattice diffusion of gas atoms to be very high. Conventional methods for the removal of gas from metals by fluxing have been found to be effective in reducing blistering. However, the effectiveness of such methods has been shown to depend not only upon the removal of gas from the metal but also on the soundness of the ingot subsequently cast from the treated metal. Ingots with microshrinkage, particularly near the surface, are prone to blistering even at low gas levels, unless special techniques are employed during fabrication. Such techniques are:

1) Preheating of ingots for 24 hr and longer at temperatures above 550°C. This has the effect of lowering the gas content.

2) Interannealing hot mill slab at temperatures above 500°C for periods of 6 hr or longer. This also lowers the gas content.

3) Reducing the ingots 40 pct at or near room temperature, followed by normal fabrication procedures. This has the effect of removing the free surfaces where gas may separate in the ingot.

The last method proved to be the most effective in reducing blisters.

In searching for an explanation of the effectiveness of the cold rolling treatment in reducing blistering, the possibility of dislocations playing a role in the process has been suggested. This point will bear further investigation.

References

[1] H. Kostron: Aluminum and Gas. *Ztsch. für Metallkunde*, 1952, vol. 43, pp. 8-11, 269-284, and 373-387.

[2] A. J. Swain and R. Eborall: Hydrogen Blisters in Brass Sheet. *Journal* Institute of Metals, 1953, vol. 81, p. 499.

[3] R. Eborall and C. E. Ransley: The Reaction of Aluminum-Magnesium Alloys with Water Vapour, and the Absorption of Hydrogen. *Journal* Institute of Metals, 1945, vol. 71, p. 525.

[4] C. J. Smithells and C. E. Ransley: *Proceedings* Royal Soc., London, 1935, vol. A152, p. 706.

[5] A. S. Russell: Diffusion of Hydrogen through Aluminum Tubes. *Metal Progress*, 1949, vol. 55, p. 827.

[6] C. E. Ransley: Discussion, The Control of Quality in the Production of Wrought Non-Ferrous Metals and Alloys. I—The Control of Quality in Melting and Casting. *Journal* Institute of Metals, 1952-1953, vol. 81, p. 708.

Discussion of the paper sent (2 copies) to AIME by Sept. 1, 1957 will appear in AIME *Transactions* Vol. 212, 1958, and in JOURNAL OF METALS, April 1958.

Abrupt Yielding and the Ductile-to-Brittle Transition in Body-Centered-Cubic Metals

The relationship of brittle fracture to the early stages of plastic deformation, particularly pronounced yielding, was examined in detail. Both abrupt yielding and brittle fracture are preceded by appreciable amounts of nonelastic strain. Abrupt yielding and the transition from a ductile-to-brittle behavior are shown to be closely related to one another and to a common origin. A mechanism for abrupt yielding and the ductile-to-brittle transition which is in good agreement with experimental data is presented.

by E. T. Wessel

UNEXPECTED brittle failures of metals in practical applications are a serious problem to many industries and to the nation as a whole. Considerable effort has been devoted to studies of the brittle behavior in metals. However, the major portion of this effort has been directed at developing techniques and apparatus for the purposes of determining the susceptibility of metals to brittle failure and of making various types of observations of the phenomena. Relatively minor effort has been made to understand the basic mechanisms involved in initiating brittle failures. A more complete understanding of the nature and mechanism of the brittle failure problem would be very helpful in efforts directed toward predicting and avoiding brittle failure and toward the development of suitable materials and designs that are not susceptible to a brittle behavior. The intent of the present investigation is to acquire this basic understanding.

The pronounced transition from a ductile-to-brittle behavior is most prevalent in metals having the body-centered-cubic lattice structure, primarily because metals of this structure exhibit a strong dependence of yield strength upon temperature and the rate of straining. The generally recognized qualitative concept of the ductile-to-brittle transition is that brittle (cleavage) failure occurs when the yield strength exceeds the cleavage fracture strength. This condition can apparently be achieved by decreasing temperature or increasing strain rate. Likewise, a normally ductile metal can be made to fracture in an apparently brittle manner by the introduction of triaxial stresses (notches) where the ratio of normal to shear stresses can be increased to such an extent that the normal stress exceeds the fracture strength before the critical shear stress for plastic flow is achieved. Neither of these concepts require any prior plastic deformation or explain why the observed fracture strengths are so much less than the theoretical cohesive strength.

The results of several investigations of the ductile-to-brittle transition in body-centered-cubic metals illustrate rather conclusively that measurable amounts of nonelastic deformation do precede cleavage fracture, even at extremely low temperatures. These studies suggested that the early stages of plastic flow, particularly abrupt yielding, and their relationship to brittle fracture should be examined

E. T. WESSEL is a Research Engineer, Metallurgy Dept., Westinghouse Research Laboratories, Churchill Borough, Pittsburgh.

TP 4501E. Manuscript, Aug. 31, 1956.

Table I. Identification of the Metals Studied

Fig. No.	Metal	Composition, Wt Pct	Condition
1	Rimmed structural steel[1]	0.24 C, 0.45 Mn, 0.02 Si, 0.013 P, 0.043 S, 0.12 Ni, 0.08 Cr, 0.21 Cu	As rolled 250 grains per sq mm, ASTM No. 5
2	Molybdenum	0.007 C 0.012 N 0.002 O	Annealed ½ hr at 1250°C in hydrogen 1000 grains per sq mm, ASTM No. 7
3	Tantalum,[2] Lot No. 1	0.010 C, 0.010 N 99.9 Ta (estimated)	Annealed 1 hr at 1700°C in a vacuum of 5×10^{-5} mm of Hg 500 grains per sq mm, ASTM No. 6
4	Columbium	0.10 C, 0.50 Ta, 0.04 Ti, 0.02 Si, 0.01 Fe * 0.012 C 0.012 N 0.020 O †	Annealed 2 hr at 1200°C in a vacuum of 1×10^{-6} mm of Hg 4 grains per sq mm, ASTM No. 00

* Supplier analysis.
† Westinghouse analysis.

in more detail. The present paper summarizes the results of such studies and relates the various factors involved in the early stages of plastic deformation, particularly abrupt yielding, with the transition from a ductile-to-brittle behavior. Basic concepts which are in good agreement with the experimental data are developed using dislocation theory.

Experimental Data—To understand the fundamentals of the ductile-to-brittle transition, it is necessary to consider such factors as the temperature dependence of the yield and flow stresses, the mechanism of the sharp discontinuous yield behavior, and the nature of the pre- and postyield plastic flow. Data illustrating these pertinent factors concerning the early stages of plastic flow for some body-centered-cubic metals exhibiting a sharp yield and a ductile-to-brittle transition are presented in Figs. 1 to 4. The various properties shown in Figs. 1 to 4 are defined in Figs. 5 and 6. The various symbols, Figs. 1 to 4, are altered in the temperature range below the sharp break in the curves (transition temperature) to denote brittle fracture. A more complete presentation of other data on two of these metals, steel, Fig. 1, and tantalum, Fig. 3, may be found in the literature.[1,2] The testing techniques and apparatus used in these experiments have previously been reported.[1,2,4] Pertinent information regarding the metal's condition, composition, etc. is shown in Table I.

Description of Mechanisms—The increased resistance to initial plastic deformation with decreased temperature as illustrated by the pronounced temperature dependence of the yield strength has probably been best explained as being due to the anchoring of dislocations by impurity atmospheres, as described by Cottrell[5-7] and elaborated on by Fisher.[8] Certain detailed aspects of the temperature dependence of the yield and flow strengths of body-centered-cubic metals cannot be adequately explained by the dislocation anchoring concept. However, a complete understanding of the exact mechanism governing the initial movement of dislocations through the lattice is not essential to the abrupt yield and fracture concepts to be developed in this paper.

The original Cottrell[5,6] concept of abrupt yielding assumes that stresses aided by thermal fluctuations enable small dislocation loops to break away from anchoring impurity atmospheres and that the nucleation of the first dislocation loop is the beginning of pronounced yielding. During the subsequent extension of a loop or loops, other dislocations are caused to break away from their atmospheres, resulting in catastrophic yielding. Since thermal fluctuations decrease with decreasing temperature, greater external stresses are required to tear the dislocations away from their anchoring atmospheres; hence, the temperature dependence of the yield strength. This concept of sharp yielding as being a breaking away of dislocations from their anchoring atmospheres requires no prior plastic strain except, possibly, that extremely small amount when the initial small dislocation loops are tearing away from their atmospheres. The possibility of some additional very small amount of nonelastic strain prior to pronounced yielding has been suggested by Cottrell,[7] Fisher,[8] Stroh,[9] and others. Some experimental evidence substantiating the existence of small amounts ($\sim 10^{-4}$) of preyield plastic strain has been reported in the literature. The delayed yield experiments of Vreeland, Clark, and Wood[10] indicate that measurable amounts of both anelastic and plastic strain occur before abrupt yielding. Other observations of these small amounts of plastic strain prior to an upper yield point have also been reported.[11-13] The data given by Geil and Carwile[13] illustrate fairly appreciable amounts of plastic strain occurring before the upper yield point in ingot iron. However, the experimental data presented in Figs. 1 to 4 and summarized in Fig. 7 show that a considerable amount of plastic strain (~ 0.1 to 1.0 pct, 10^{-3} to 10^{-2}) precedes the sharp yield (upper yield point) in an assortment of body-centered-cubic metals.

To account for the large amounts of preyield plastic strain observed in the current experiments, it is necessary to assume that many dislocations must be moved through the lattice prior to a sharp yield. It is probable that dislocations are originally pinned by a Cottrell[6] atmosphere, but some start to tear away at stresses which are even lower than currently measurable elastic limits. As the stress rises above the elastic limit, increasing numbers of dislocations move through the lattice. These dislocations propagate until they are piled up at grain boundaries or other barriers, i.e., subgrain boundaries, hard particles or phases, other dislocation groups, etc.

The amount of preyield plastic strain observed is about that which could be associated with the accumulated effect of many dislocations moving through the lattice and subsequently being piled up at grain boundaries or other barriers. Based on the

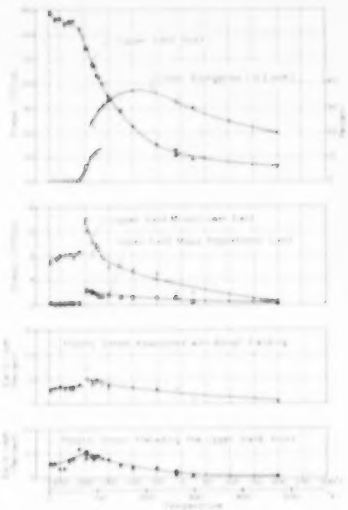

Fig. 1—Factors involved in the early stages of plastic flow. Mild steel[5] tested in tension; strain rate, 2.1 x 10^{-4} sec^{-1}.

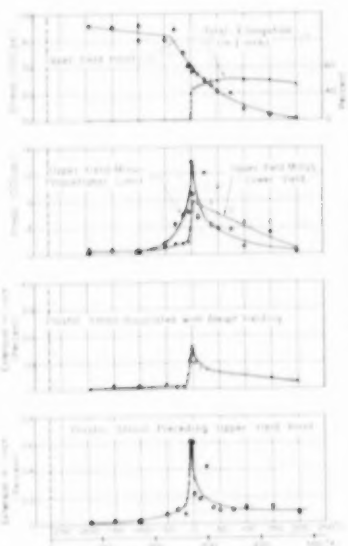

Fig. 2—Factors involved in the early stages of plastic flow. Recrystallized molybdenum tested in tension; strain rate, 1.8 x 10^{-4} sec^{-1}.

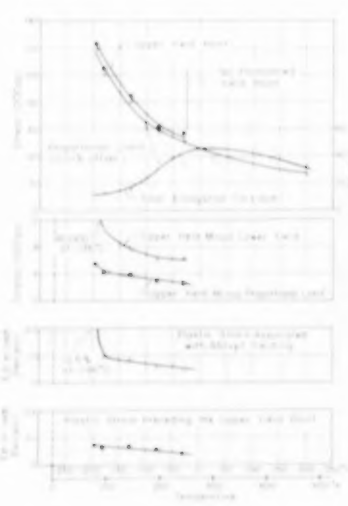

Fig. 3—Factors involved in the early stages of plastic flow. Annealed tantalum[5] tested in tension; strain rate, 2.8 x 10^{-4} sec^{-1}.

expression[6] $\epsilon = \rho L b$, with ϵ equal to observed plastic strain; ρ, dislocation density; L, length over which the dislocations move, assumed to be one half the grain diameter; and b, Burgers' vector; it appears that, on the average, about 1000 piled-up dislocations per grain would be necessary in the case of the mild steel to account for the amount of preyield strain which was obtained at −196°C. Assuming approximately 300 dislocations per source, the observed preyield plastic strains indicate that an average of from one to three dislocation groups per grain are piled up at barriers prior to abrupt yielding. On the basis of current dislocation theory, these approximations appear reasonable.

As a result of the piling up of dislocation groups at barriers and the accompanying increase in the general applied stress level, high stress concentrations are developed in the regions of the pile-up. The abrupt yield now becomes associated with the relaxation of these stresses at piled-up groups by the activation of new dislocation sources in adjoining material and, to a lesser extent, the continued propagation of the piled-up dislocations. The achievement of the necessary critical stress concentration in the immediate vicinity of a piled-up dislocation group and the resulting activation of plastic flow in adjoining material are given the descriptive terminology of being a *breaking through* or a *breaking away* of the piled-up dislocation group from its barrier. Once this break-through occurs in a few localized regions, the relaxation in the vicinity of the break-through causes higher microstresses in neighboring piled-up groups, triggering a general cataclysmic yielding and the associated drop in load. A schematic illustration of the early stages of plastic flow for temperatures above the transition temperature is given in Fig. 5. The rounded upper yield point which is shown slightly exaggerated in Fig. 5 is believed to be indicative of the incubation or conditioning period where a few piled-up dislocation groups are starting to break away from their barriers. The abrupt catastrophic yield then occurs after sufficient break-through momentum has been developed during this conditioning period. The degree of rounding (or sharpness) of the upper yield point has been observed to vary considerably, depending upon the particular metal, its chemical and metallurgical condition, and the temperature and stress levels at which the yielding occurs. However, in nearly all cases of pronounced yielding which have been observed, some degree of rounding of the upper yield point is present. Exception is made in a few cases where very sharp upper yield points were obtained in some metals tested at 4.2°K.[14] Stress-strain curves obtained in an earlier investigation[14] illustrate that the degree of rounding (or sharpness) of the upper yield point is not a unique function of the test machine or recording apparatus.

At low temperatures where cleavage failure is observed to occur during yielding, the mechanism involved in yielding must be somewhat different from that just described for the higher temperatures. A schematic representation of the subtransition temperature behavior is given in Fig. 6. At these lower temperatures, higher stresses are necessary to cause the movement of dislocations both in the first and subsequent grains or regions to yield. Likewise, because of the increased resistance to plastic deformation, higher localized stresses are required to enable piled-up dislocations to break through or away from barriers (upper yield point).

As a result, very high localized stresses can exist in front of some groups of piled-up dislocations. These stresses can be sufficiently high to exceed the fracture (cohesive) strength and to open up a crack in unfavorably oriented and adjoining material much in the manner described by Zener,[15] Petch,[16] Stroh,[17] and recently by Alers.[18] Prior to and simultaneously with the formation of these microcracks, many of the piled-up dislocation groups will initiate plastic flow rather than cracks in regions where the adjoining material is more favorably oriented for flow. The initiation of one or more microcracks together with some plastic flow is believed to trigger the abrupt yielding. During the subsequent drop in load (abrupt yielding) the microcracks grow in size and number and develop into a larger, more continuous network until, at some point during the abrupt yielding, the Griffith conditions[19,20] for brittle crack propagation are achieved.

Stroh[17] has recently described, in mathematical terms, a theoretical model for abrupt yielding and brittle fracture in which he suggests that piled-up dislocations initiate abrupt yielding at temperatures above the transition temperature and brittle cracks at subtransition temperatures. In this work the necessity for some unknown amount of preyield nonelastic strain is implied (model begins with piled-up dislocations present), but is not treated in any detail. The model and mechanisms for abrupt yielding and brittle fracture derived by the experimental approach in the present paper are similar, in that both approaches utilize the generally known concept of piled-up dislocations to initiate flow or fracture. In the present paper, however, the nature and magnitude of the preyield plastic strain is paramount. Particular emphasis is directed at a determination of the physical picture of what occurs in a static tension test prior to and at the upper yield point (beginning of fracture at subtransition temperatures), as well as during the drop in load which is associated with abrupt yielding. In general, the concepts developed by the two approaches are in good agreement.

Discussion of Experimental Results—The experimental data in Figs. 1 to 4 appear to confirm the concepts of yielding and brittle fracture developed above. As temperature decreases, the stress required to cause the initial movement of dislocations increases. Likewise, the stress (upper yield point) required to cause piled-up dislocation groups to activate flow and/or fracture in adjoining material also increases, but to a much greater extent, as is illustrated by the increasing difference in stress level between the proportional limit (0.01 pct yield strength) and the upper yield point, Figs. 1 to 4. It is believed that the difference in stress level between the upper yield point and the true elastic limit even increases to a much greater extent. The necessity for these higher stresses to cause abrupt yielding results in the formation of a more extensive and more dense accumulation of piled-up dislocations with an associated increase of potential energy. Hence, as temperature decreases down to the transition temperature, more preyield plastic strain precedes abrupt yielding, as shown in Figs. 1 to 4 and 7. When the break-through of these high potential piled-up groups does occur (abrupt yield), it is reasonable to expect that greater amounts of plastic deformation and larger drops in load would also occur, as was observed experimentally, Figs. 1 to 4. As temperature decreases, this occurrence

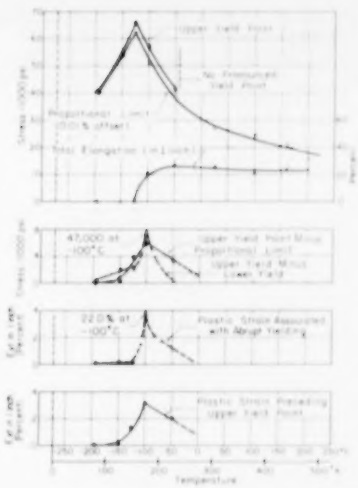

Fig. 4—Factors involved in the early stages of plastic flow. Annealed columbium tested in tension; strain rate, 1.0×10^{-3} sec^{-1}.

of larger drops in load and larger amounts of plastic strain during the abrupt yield could arise from several sources: the presence of a more extensive and higher potential network of piled-up dislocations, the associated activation of larger numbers of other dislocation sources during the abrupt yielding, and the apparently decreased ability of the material to strain harden at the lower temperatures.[8,14]

At temperatures at or below the transition range, cracks are initiated by piled-up dislocations and brittle fracture occurs during subsequent yielding. The increased ability with decreased temperature of piled-up dislocation groups to initiate microcracking and, in effect, to promote premature abrupt yielding, results in a decreased amount of preyield plastic strain, as shown in Figs. 1, 2, and 4. While tantalum, Fig. 3, did not undergo a ductile-to-brittle transition at the lowest test temperature (−196°C), its behavior for the temperature range examined conforms to the general pattern established. The development of total fracture during yielding also results in a decrease in the magnitude of the drop in load and the associated plastic strain which occurs during yielding. The relative effectiveness of piled-up dislocations in opening microcracks and initiating brittle fracture at or below the transition temperature varies considerably between materials as well as with decreasing temperature for a given material. The variation between materials may be seen by comparing the subtransition data of mild steel, Fig. 1, with that for molybdenum and columbium, Figs. 2 and 4. It is apparent from the mild steel data that, even at the very low temperatures, considerable plastic deformation is still associated with the brittle fracture both in terms of the preyield plastic strain and the plastic strain which occurs simultaneously with crack formation during abrupt yielding. The data for columbium, Fig. 4, and molybdenum, Fig. 2, show that relatively smaller amounts of plastic strain occur prior to or during the abrupt yield-fracture process. It is believed that this difference in behavior below the transition temperature arises primarily from the inherent differences in the ability of the different materials to deform or fracture in the presence of the stress concentrations which exist in front of piled-up dislocation groups. For any given material, decreasing temperature below the transition temperature results in decreased amounts of preyield

Fig. 5—Factors involved in the early stages of plastic flow at temperatures above the transition temperature (tension).

and abrupt yield plastic strain. The decrease in plastic strain at subtransition temperatures is quite rapid at first (in the lower transition range) and tends to become relatively constant at temperatures below the transition range. It is believed that this increased ability for piled-up dislocations to initiate brittle failure at subtransition temperatures is in large part due to development of increased stress concentrations at the heads of piled-up dislocation groups. Because of the increased resistance to plastic flow and the associated rise in the general stress level, higher local stress concentrations can prevail after a relatively small pile up of dislocations.

The preyield behavior (above the transition temperature) can also vary considerably in different lots of any one metal, as can be seen in the case of the two lots of tantalum in Fig. 7. This marked difference in behavior is undoubtedly related to variations of impurity content, grain size, microstructure, etc., with particular reference to the influence of these factors on the propagation of dislocations. The two lots of tantalum are currently being studied with particular reference to variations in the size, shape, and distribution of dislocation barriers.

The abruptness of the transition from an all plastic deformation to a crack initiating type of yielding (ductile-to-brittle transition) is dependent to a large extent upon the particular metal and its chemical and metallurgical condition. For instance, the total elongation data for mild steel, Fig. 1, illustrates that the ductile-to-brittle transition occurs gradually over the temperature range of —160° to —200°C. In this temperature range (upper transition range), plastic flow and some microcracks may be initiated during abrupt yielding. However, if formed, the microcracks do not achieve the critical conditions necessary to cause failure during initial abrupt yielding. Nevertheless, during subsequent postyield plastic deformation, the critical conditions for brittle failure are achieved, either by the merger and/or growth of existing yield-produced microcracks and/or by the initiation and growth of new cracks. In this temperature range, the elongation data, Fig. 1, indicate that either a ductile or a brittle behavior is possible.

If plastic flow is considered to be the result of the propagation of dislocations, it is quite conceivable that, after a sufficient amount of deformation which, in some cases, may also be associated with some strain hardening, some groups of dislocations could be piled up and could develop sufficiently high localized stress concentrations to initiate brittle cracks in much the same manner as previously described. Such would also be the case for metals which do not normally exhibit pronounced yielding but do fail in a brittle manner. Naturally, the physical makeup of the metal, with particular reference to the location, size, shape, and distribution of the barriers, would exert considerable influence on the relative ability of dislocations to pile up and to cause microcracking.

In general, most body-centered-cubic metals exhibit a greater tendency for pronounced (sharp) yielding at lower temperatures, as illustrated by the experimental data for columbium, Fig. 4, and tantalum,[2] Fig. 3, which do not exhibit a sharp yield point at room temperature, but yield emphatically at lower temperatures. The stress-strain curves for columbium, Fig. 8, markedly illustrate the various degrees of yielding which can be obtained over a rather narrow range of temperatures. At +25°C, no pronounced yielding occurs. At —50°C, a modest yield point is observed. A very pronounced yield occurs at —100°C with no well defined lower yield point. This accounts for the large values, Fig. 4, for the difference in stress between the upper and lower yield points and the amount of plastic strain occurring during the abrupt yield. The stress-strain curve for this particular test shows a continuous drop in load after initial pronounced yielding and fracture was taken as the lower yield point. This pronounced yield was accompanied by a 22 pct extension in length and a reduction in area of 85 pct, illustrating an appreciable capacity for plastic flow with considerable localization of strain. However, during the next lower temperature test at —125°C, microcracks were apparently formed by piled-up dislocations resulting in premature abrupt yielding and brittle cleavage failure during the early stages of this yielding.

Some explanation of the criterion used for determination of the lower yield point seems necessary at this time. In the present paper the lower yield point was taken as that point in the stress-strain curve subsequent to abrupt yielding, where the load first showed any indication of rising. If no rise was observed, as in columbium at —100°C, fracture was considered as the lower yield point. It might appear more reasonable in the case of the low temperature tests of tantalum and columbium to con-

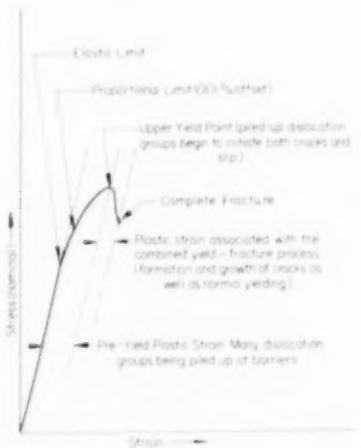
Elastic Limit
Upper Yield Point (piled up dislocation groups begin to initiate both cracks and slip)
Complete Fracture
Plastic strain associated with the combined yield + fracture process (formation and growth of cracks as well as normal yielding)
Pre-Yield Plastic Strain Many dislocation groups being piled up at barriers

Fig. 6—Factors involved in the early stages of plastic flow at subtransition temperatures (tension).

sider the flat portion of the stress-strain curve subsequent to abrupt yielding as the lower yield point. If this latter option is chosen, appropriate reductions should be made in the values for the difference in stress between the upper and lower yield point and the plastic strain asspciated with the abrupt yielding for the −196°C test of tantalum, Fig. 3, and the −100°C test of columbium, Fig. 4. Such changes would not affect the concepts presented in the paper. However, the author prefers the lower yield point criterion used in the presentation of the data, for experience has demonstrated that large precipitous drops in load and associated plastic strain continuous to fracture do occur during abrupt yielding in some metals, particularly at low temperatures.

Undoubtedly, the influence of notches in promoting brittle failure (raising transition temperature) is in large part the result of a piling up of a concentrated network of dislocations in the highly localized regions undergoing deformation at the root of the notch. A recent investigation[1] illustrates the role of plastic strain in promoting brittle fracture in the presence of notches.

Summary and Conclusions

The relationship of brittle fracture to the early stages of plastic deformation, particularly pronounced yielding, was examined in detail for body-centered-cubic metals. It is concluded that some nonelastic deformation is a necessary prerequisite for brittle failure in metals. Abrupt yielding and the transition from a ductile-to-brittle behavior are shown to be closely related to one another and to a common origin. A mechanism for abrupt yielding and the ductile-to-brittle transition which is in good agreement with experimental data is described. The general mechanism is briefly summarized as follows:

1) Prior to an abrupt yield or brittle fracture, many dislocations move through the lattice but are subsequently piled up at barriers. An appreciable amount of plastic strain is associated with the piling up of these dislocation groups. The magnitude of this plastic strain increases with decreasing temperature, reaching a maximum at the transition temperature, below which the plastic strain decreases with decreasing test temperature.

2) At temperatures above the transition temperature, abrupt yielding occurs when the stress concentrations that are present in the vicinity of piled-up dislocation groups become sufficiently high to overcome the resistance to deformation and activate

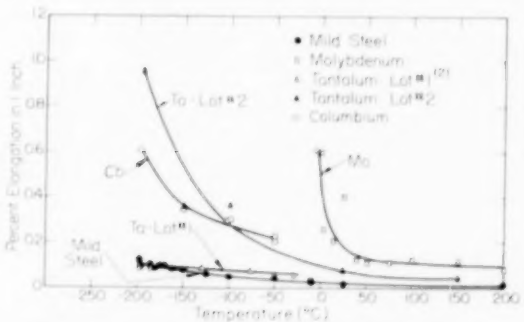

Fig. 7—Plastic strain preceding abrupt yielding (tension).

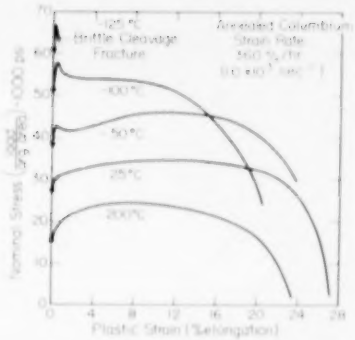

Fig. 8—Effect of temperature on the stress-strain curves of annealed columbium.

other sources in the adjoining material, triggering a general catastrophic yielding.

3) At temperatures below the transition temperature, the resistance to plastic deformation is so great that the stress concentrations in some of the regions of piled-up dislocation groups become sufficiently high to initiate microcracks in these areas. The achievement of these high localized stresses and the resulting formation of some microcracks together with some plastic deformation triggers a combined general catastrophic yielding and crack formation, terminating in complete brittle fracture.

Acknowledgments

The author is indebted to his associates at the Westinghouse Research Laboratories for interesting and enlightening discussions of the subject matter. He is especially indebted to W. H. Pryle for his contribution in the experimental phases of the investigation, and to J. H. Bechtold and C. Zener for their interest and support of this work.

References

[1] E. T. Wessel: A Tensile Study of Brittle Behavior of a Rimmed Structural Steel. *Proceedings* ASTM. To be published.
[2] J. H. Bechtold: Tensile Properties of Annealed Tantalum at Low Temperatures. *Acta Metallurgica*, 1955, vol. 3, No. 2, p. 249.
[3] E. T. Wessel and R. D. Olleman: Apparatus for Tension Testing at Sub-Atmospheric Temperatures. Bulletin No. 187, p. 56. ASTM. Philadelphia, 1953.
[4] E. T. Wessel: Tension Testing Apparatus for the Temperature Range of −320°F to −452°F. Bulletin No. 211, p. 40. ASTM. Philadelphia, 1956.
[5] A. H. Cottrell and B. A. Bilby: Dislocation Theory of Yielding and Strain Aging in Iron. *Proceedings* Royal Soc., London, 1949, vol. A62, p. 49.
[6] A. H. Cottrell: *Dislocations and Plastic Flow in Crystals*. Oxford Press. Clarendon, England, 1953.
[7] A. H. Cottrell: The Yield Point in Single-Crystal and Polycrystalline Metals. Symposium on the Plastic Deformation of Crystalline Solids. Mellon Institute. Pittsburgh, 1950.
[8] J. C. Fisher: Applications of Cottrell's Theory of Yielding to Delayed Yield in Steel. *ASM Trans.*, 1955, vol. 47, p. 451.
[9] A. N. Stroh: Brittle Fracture and Yielding. *Philosophical Magazine*, 1955, vol. 46, p. 968.
[10] T. Vreeland, Jr., D. S. Wood, and D. S. Clark: A Study of the Mechanism of the Delayed Yield Phenomenon. *ASM Trans.*, 1953, vol. 45, p. 620.
[11] C. S. Roberts, R. C. Carruthers, and B. L. Averbach: The Initiation of Plastic Strain in Plain Carbon Steels: *ASM Trans.*, 1952, vol. 44, p. 1150.
[12] B. L. Averbach and H. Muir: Discussion of paper by T. Vreeland, Jr., D. S. Wood, and D. S. Clark: A Study of the Mechanism of the Delayed Yield Phenomenon. *ASM Trans.*, 1953, vol. 45, p. 632.
[13] G. W. Geil and N. L. Carwile: Effect of Tensile Strain at Low Temperatures and Deformation Twinning in Ingot Iron. *AIME Trans.*, 1953, vol. 197, p. 213; JOURNAL OF METALS, February 1953.
[14] E. T. Wessel: Some Exploratory Observations of the Tensile Properties of Metals at Very Low Temperatures. *ASM Trans.*, 1957, vol. 49.
[15] C. Zener: The Micro-Mechanism of Fracture. *Fracturing of Metals*, p. 3. ASM. Cleveland, 1948.
[16] N. J. Petch: The Cleavage Strength of Poly-crystals. *Journal* Iron and Steel Institute, 1953, vol. 174, p. 25.
[17] A. N. Stroh: The Formation of Cracks as a Result of Plastic Flow. *Proceedings* Royal Soc., London, 1954, vol. A223, p. 404.
[18] G. Alers: To be published.
[19] A. A. Griffith: The Phenomena of Rupture and Flow in Solids. *Philosophical Trans.* Royal Soc., London, 1920, vol. A221, p. 163.
[20] A. A. Griffith: Theory of Rupture. *Proceedings* First International Congress of Applied Mechanics, 1924, p. 55.

Discussion of this paper sent (2 copies) to AIME by Sept. 1, 1957 will appear in AIME *Transactions* Vol. 212, 1958, and in JOURNAL OF METALS, April 1958.

Diffusion of Magnesium, Silicon, And Molybdenum in Nickel

Diffusion rates of magnesium, silicon, and molybdenum were measured in nickel as a function of temperature. Activation energies, *Q*, and values of the frequency factor, D_0, were calculated for each system. The activation energies obtained were found to be close to that for self-diffusion in nickel with the exception of magnesium, for which the value was found to be about 10 kcal per g-atom less. The results are interpreted in accordance with Lazarus' theory of solute diffusion and with a model proposed by one of the authors.

by R. A. Swalin, Allan Martin, and R. Olson

IN this paper, the results of an investigation concerning the diffusion of three elements, magnesium, silicon, and molybdenum, in nickel are presented. The work represents a continuation of a diffusion program relating to solute diffusion in nickel. The program has the dual aim of obtaining useful diffusion data and of yielding insight into the factors governing solute diffusion in close-packed metals. The first paper of this series has been published earlier.[1] In both investigations, in agreement with recent results from other laboratories, the activation energies for solute diffusion were found to be close but not identical to that of self-diffusion in the pure solvent in question.

In order to obtain valid diffusion data, certain experimental pitfalls recognized only in recent years had to be avoided. Chief among these were the necessity for minimizing short-circuiting diffusion paths such as grain boundaries and the necessity for using low solute concentration gradients. In this series of investigations the following precautions were taken in an attempt to minimize such errors.

R. A. SWALIN is Asst. Professor of Metallurgy, Dept. of Metallurgy, University of Minnesota, Minneapolis. A. MARTIN is with Vanadium Corp. of America, Cambridge, Ohio. R. OLSON, formerly with Dept. of Metallurgy, University of Minnesota, is now with the U. S. Army, Tokyo, Japan.

TP 4508E. Manuscript, Dec. 10, 1956.

1) Samples with large grain sizes, 0.5 to 10 mm, were prepared.

2) The diffusion coefficients were measured at relatively high temperatures, since imperfections such as dislocations play a less important role at such temperatures than at lower temperatures.

3) Alloys containing less than 1 atomic pct were chosen for study.

Experimental Work

Materials—A diffusion couple technique was employed in the experimental investigation. Briefly, this technique consisted of the following. A diffusion couple was fabricated by placing a flat face of a cylindrically shaped alloy disk against a similar face of a pure nickel disk, and a bond was formed at an intermediate temperature under pressure. The diffusion couple thus fabricated was subjected to a diffusion anneal at higher temperatures for a measured period of time and then sectioned perpendicular to the direction of diffusion. After analyzing the sections for solute concentration the diffusion coefficient was determined from a probability plot of concentration vs distance from the diffusion interface.

Vacuum melted Mond nickel was used in the experimental program. The chemical analysis of this nickel is listed in Table I. Alloys used were prepared

by vacuum melting and casting in the form of cylindrical ingots 1 in. in diam and about 4 in. in length.

Fabrication of Diffusion Couples—Cylindrical disks about ¼ in. thick were cut from the ingots and deformed slightly by passing through rolls in a direction parallel to the planar faces. The disks were then recrystallized at 1300°C for the purpose of obtaining large grain size. This treatment yielded a final grain size varying from 0.5 to 10 mm.

A diffusion couple was made by placing a polished face of the desired alloy disk against a polished face of a pure nickel disk (or a disk containing less solute than the former) and forming a bond between the two disks by application of a pressure of 12,000 psi at 1000°C in an atmosphere of hydrogen. Several tungsten wires 0.001 in. in diam were placed at the interface before welding.

Diffusion Treatment—A diffusion couple thus fabricated was sealed under argon in a fused silica tube and heated to the desired diffusion anneal temperature. Upon completion of this treatment, the diffusion couple was mounted on a precision lathe and aligned accurately by using a cathetometer to sight on the ends of the tungsten wire markers. The markers were made visible by removing material from the cylindrical surface and polishing and etching the surface. The machining treatment removed material which might have been affected by surface diffusion. Extraneous material outside the diffusion zone was removed and 1 mil thick slices were cut in the diffusion zone. About 40 slices were removed altogether. In some couples slices 2 mil thick were taken.

Determination of Solute Concentration—The concentration of the solute in the slices was determined by use of spectrophotometric methods of analysis in the Ni-Si and the Ni-Mo diffusion system and by the spectrographic method in the Ni-Mg system. The spectrophotometric method used for the silicon determinations was based on the reaction between silicon ion and molybdate forming silicomolybdic acid in acid solution upon the addition of stannous chloride.[2] Since the amount of silicon in any one slice was very small, on the order of 50 μg, the possibility of contamination of solutions by the silicon in laboratory glassware was an important consideration. To minimize this source of error, redistilled water which had been distilled in a Pyrex glass apparatus and subsequently stored in polyethylene bottles was used in the analytical work. Silicon-free ammonium hydroxide was prepared by bubbling air through concentrated ammonium hydroxide and passing the ammonia saturated air into redistilled water. The resulting purified ammonium hydroxide was stored in polyethylene bottles rather than in glass to avoid silicon contamination. Similar precautions were taken with all other reagents used in the chemical work.

In the case of molybdenum a spectrophotometric method based on the formation of a yellow thiocyanite complex with Mo(IV) was adapted to use.[3] The details of the methods used for silicon and molybdenum are given in refs. 2 and 3.

The standard spectrographic method was employed for magnesium. Suitable samples were prepared by dissolving the Ni-Mg sections in nitric acid, evaporating the liquid, and igniting to form the oxides.

Since the spectrographic method cannot distinguish between magnesium present dissolved in the nickel lattice, magnesium present as MgO particles, and magnesium present as $MgNi_2$, it was necessary to avoid the formation of the latter two types of magnesium both in the formation of the magnesium alloy and in the diffusion process itself. Otherwise the measured concentration gradient after diffusion could not have been used to measure the diffusion coefficient of magnesium in the lattice. The presence of $MgNi_2$ particles was avoided by using alloys with less than the solubility of magnesium in nickel, 0.24 atomic pct.[1] The formation of MgO particles during the formation of the magnesium alloy was minimized by the prior deoxidation of the nickel melt with aluminum. The formation of MgO particles during the diffusion process was minimized by the use of nickel disks which had been deoxidized by the same amount of aluminum, 0.2 pct.

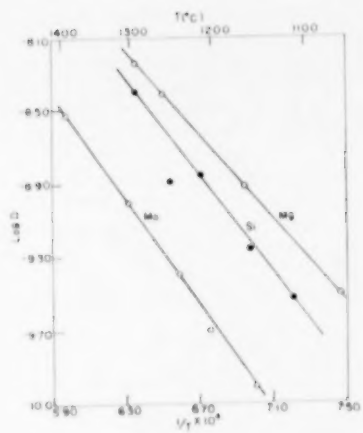

Fig. 1—Log D vs reciprocal of absolute temperature for the Ni-Mg, Ni-Si, and Ni-Mo systems.

Since silicon also would react with dissolved oxygen to form SiO_2, the considerations discussed above apply in this connection also. Upon addition of silicon to molten nickel, most of the dissolved oxygen would probably react with silicon, leaving a low concentration of dissolved oxygen. The pure nickel component of the diffusion couple might have a considerably higher oxygen concentration. During the diffusion anneal, there could have been a net flow of dissolved oxygen toward the diffusion interface, whereupon it would react with silicon, resulting ultimately in an erroneous result for the diffusion coefficient. To compensate for this potential source of error silicon was added to both components. The alloy disks contained 1.25 atomic pct Si and the other component contained 0.21 atomic pct Si.

This problem encountered with magnesium and silicon was not present in the Ni-Mo diffusion system since molybdenum is not a strong deoxidizer. Accordingly, alloy disks containing 0.93 atomic pct were placed in contact with pure nickel disks.

Experimental Results

The Grube solution to Fick's second law of diffusion was found to be applicable in all cases. The solution is

$$\frac{2\,(C_i - C_o)}{C_\infty - C_o} = 1 - \text{erf}\left[\frac{X_i}{2\sqrt{Dt}}\right] \qquad [1]$$

where C_i is the solute concentration at a distance X_i from the diffusion interface, C_∞ is the solute concentration in the alloy disk at time, $t = 0$, C_o is the solute concentration in the *nickel* disk, and D is the

diffusion coefficient. The necessary conditions to be fulfilled in order for the above solution to be valid are the following: 1) diffusion is unidirectional; 2) the couple can be considered as an infinite solid; and 3) D is independent of concentration. The first two conditions were met by suitable experimental design. The third condition was shown to be valid when straight line plots of $C_x - C_o/C_m - C_o$ vs X, on probability paper were obtained. If D had been a function of C in the concentration range employed in the experiments, nonlinear plots would have been obtained. The diffusion coefficient for each couple was obtained by comparison with Eq. 1.

Table I. Analysis of Nickel

Element	Pct	Element	Pct
Cu	0.0225	Si	0.002
Pb	0.001	Mg	0.001
Fe	0.001 to 0.01	Ca	0.001
Al	0.0003	Cr	0.001
Mn	0.001	Co	0.01 to 0.05

The diffusion coefficients for each system exhibited the usual temperature dependence, namely

$$D = D_o \exp [-Q/RT] \qquad [2]$$

where D_o is the frequency factor, Q is the activation energy, R is the gas constant, and T is absolute temperature. In Fig. 1, the experimental values of log D are plotted vs the reciprocal of the absolute temperature for the three systems. From these curves the diffusion parameters were obtained using the method of least squares and are given in Table II. The real accuracy of the experimental data is not apparent from Fig. 1. The scatter of points on the probability plots is more significant. Considerable scatter occurred for the magnesium data due to analytical difficulties so the error of Q is probably about ±4 kcal per g-atom whereas that for molybdenum is about ±1 kcal per g-atom. The scatter on the probability plots in the case of silicon was in between the two giving an error of ±2 or ±3 kcal per g-atom.

Discussion of Results

The results obtained in this investigation are consistent with the results obtained in the previous investigation[1] insofar as values of D_o and Q are concerned. The values of Q in both investigations are in the vicinity of that for self-diffusion in nickel, reported to be 66.8 kcal per g-atom,[3] giving support to the vacancy mechanism of solute diffusion. The highest activation energy reported out of the seven solutes investigated was for tungsten, 76.8 kcal per g-atom, while the lowest was for magnesium, reported here to be 56 kcal per g-atom. The results for the other five solutes fall between 61.4 and 68.9 kcal per g-atom, all very close to Q for nickel. The high value reported for tungsten and the low value reported for magnesium are probably correct since, in the temperature range of the investigation, tungsten was found to diffuse considerably slower than the other elements, which would lead to the expectation of a high value for Q. Likewise, magnesium diffused considerably faster than the other solutes, which would lead to a low value of Q. At 1200°C, the value of D for tungsten is about 0.45×10^{-10} sq cm per sec, D for magnesium is about 19.3×10^{-10} sq cm per sec, and D for the other solutes ranges from about 2.0×10^{-10} to 12.4×10^{-10} sq cm per sec.

The results reported in the earlier paper were analyzed with respect to the theory of solute diffusion proposed by Lazarus.[4] In this theory an inverse correlation between solute activation energy and extra valence relative to the solvent is predicted. The choice of proper valence for nickel as well as for some of the transition element solutes is open to question. In the previous paper,[1] good agreement between theory and experiment was found if the following choice of valence was made: nickel (0), aluminum (+3), titanium (+4), manganese (−1), and tungsten (−2). The valence of 0 for nickel is the Hume-Rothery valence. Moving to the left in Period IVA, cobalt and iron would also have a valence of 0 using this reasoning. Manganese would, therefore, have a valence of −1 and chromium −2. Since molybdenum and tungsten are directly below chromium in Periods V and VI, respectively, they would also be assigned valences of −2. Aluminum and titanium were assigned their chemical valences of +3 and 4, respectively. It is interesting to analyze the data presented in the present paper with the theory. The assigned valences using the above reasoning are the following: magnesium (+2), silicon (+4), and molybdenum (−2). Since titanium and silicon have the same valence, they would be expected to have the same value of Q. This condition is fulfilled, since Q was found to be 61.4 and 61.7 for titanium and silicon, respectively.

Table II. Diffusion Parameters

Solute	D_o, Sq Cm per Sec	Q, Kcal per G-Atom
Mg	0.44	56
Si	1.5	61.7
Mo	3.0	68.9

On the same basis, molybdenum and tungsten should have the same value of Q. This condition is not met very well since Q is 68.9 for molybdenum and 76.8 for tungsten. The most serious discrepancy, however, occurs for magnesium. According to the above reasoning a value of 64.0 would be predicted for the activation energy for magnesium, which does not agree with the experimental value of 56.

It appears, therefore, that Lazarus' theory has some success in rationalizing the solute diffusion results in nickel if the Hume-Rothery valence scheme is used. A serious discrepancy, however, is found for two solutes, namely, magnesium and molybdenum. The choice of valences needed to obtain the agreement, however, casts considerable doubt on the applicability of Lazarus' theory to the cost of diffusion in nickel. For example, ferromagnetic studies with nickel indicate the valence to be 0.6, not 0. Also, valence values for some of the solutes when dissolved in nickel are equally open to question and, hence, perhaps the agreement observed could be fortuitous, since it is not on strong ground from a theoretical standpoint.

Many of the features of the solute diffusion results in nickel can be explained in terms of an alternative model proposed by one of the authors in which the size of the impurity ion is considered.[7] In this model, the solute ion is considered to behave as a compressible sphere and part of the energy of

jumping is considered to result from the hydrostatic compression of the solute ion and part from the dilation of the solvent lattice. Using this model the following equation has been derived for diffusion in face-centered-cubic lattices.[7]

$$Q_{\text{solute}} = 0.6\,Q_{\text{self}} + \frac{1.29\,(r'_o + r)^3\,r'_o\,B_s}{45\,\pi\,B_s\,r'_o} \qquad [3]$$
$$1 + \frac{}{13.3\,(\sqrt{3}\,r'_o - 0.27\,r)\,C}$$

where Q_{self} is the activation energy for self-diffusion in the pure solvent; r is the Goldschmidt atomic radius of the solvent ion; B_s, the bulk modulus of the solute ion; C is related to the shear modulus of the solvent lattice; N is Avagadro's number; and r'_o is given by

$$r'_o = \frac{\mathrm{Br}^3 + 2\,B_s\,r_o^3}{Br + 2\,B_s\,r_o} \qquad [4]$$

where r_o is the Goldschmidt atomic diameter for the solute ion and B is the bulk modulus of the solvent.

The comparison between theory and the experimental results for the seven solutes in nickel is shown in Table III. The agreement appears to be quite good except for titanium, where the difference between theory and experiment is considerably larger than expected on the basis of experimental error. These calculations are considered in more detail in ref. 7. It appears, therefore, that solute diffusion in nickel can be interpreted satisfactorily in terms of a size factor model without the necessity of invoking valence differences.

Table III. Comparison Between Theory and Experiment

Solute	Q, Experiment	Q, Theory
Mg	56 kcal per g-atom	56* kcal per g-atom
Si	61.7	65.1
Mo	68.9	73.8
Al	64.0	64.8
Ti	61.4	70.5
Mn	67.1	68.9
W	76.8	75.5

* Used to obtain geometrical constants in theory.

Summary

Diffusion rates of magnesium, silicon, and molybdenum have been measured as a function of temperature. The usual exponential temperature dependence of D was found, and values of the activation energy were found to be close to that for self-diffusion in nickel with the exception of that for magnesium, which is about 10 kcal per g-atom less.

The results obtained are generally consistent with those of an earlier investigation of solute diffusion in nickel. These results have been analyzed in accordance with Lazarus' theory and with a model proposed by one of the authors.

Acknowledgment

This work was performed under Bureau of Ships Contract No. NO bsr - 6 3172.

References

[1] R. A. Swalin and A. Martin: *AIME Trans.*, 1956, vol. 206, p. 567; JOURNAL OF METALS, May 1956.
[2] C. L. Luke: *Analytical Chemistry*, 1953, vol. 25, p. 148.
[3] C. E. Crouthamel and C. E. Johnson: *Analytical Chemistry*, 1954, vol. 8, p. 1284.
[4] *Metals Handbook*, ASM, Cleveland, 1948.
[5] R. E. Hoffman, F. W. Pikus, and R. A. Ward: *AIME Trans.*, 1956, vol. 206, p. 483; JOURNAL OF METALS, May 1956.
[6] D. Lazarus: *Physical Review*, 1954, vol. 96, p. 610.
[7] R. A. Swalin: *Acta Metallurgica*, 1957, vol. 5.

Discussion of this paper sent (2 copies) to AIME by Sept. 1, 1957 will appear in AIME *Transactions* Vol. 212, 1958, and in JOURNAL OF METALS, April 1958.

Technical Note

Determination of Orientation in Magnesium By Polarized Light Examination

by S. L. Couling and G. W. Pearsall

MOTT and Haines[1] have summarized the available techniques for the examination of aluminum and some anisotropic metals under polarized light. Many of these techniques are rather complicated and cumbersome. This note presents a simplified procedure for using polarized light to obtain information about the crystallographic orientation of any particular grain in a magnesium alloy. Since other hexagonal metals are more anisotropic than magnesium, similar methods might well be applied to them.

Ernst and Laves[2] produced a double-refracting layer on magnesium alloy specimens by successive etches in solutions of perchloric acid in alcohol, magnesium perchlorate in perchloric acid and alcohol, and calcium and magnesium carbonates in water. They examined their specimens under polarized light and were able to determine the direction of the hexagonal axis in any particular grain from a measurement of the extinction behavior of that grain. The disadvantages of their technique were the complexity of the etching procedure and the explosive hazard of the perchloric acid-alcohol solutions.

Results equivalent to those of Ernst and Laves were obtained in this investigation after etching specimens for 6 to 8 sec in an acetic picral solution containing 100 parts 6 pct picral, 10 parts distilled water, and 5 parts acetic acid. A similar etch has been used by George[3] in earlier metallographic

S. L. COULING and G. W. PEARSALL, Junior Member AIME, are associated with the Metallurgical Laboratory, Dow Chemical Co., Midland, Mich.

TN 418E. Manuscript, Feb. 11, 1957.

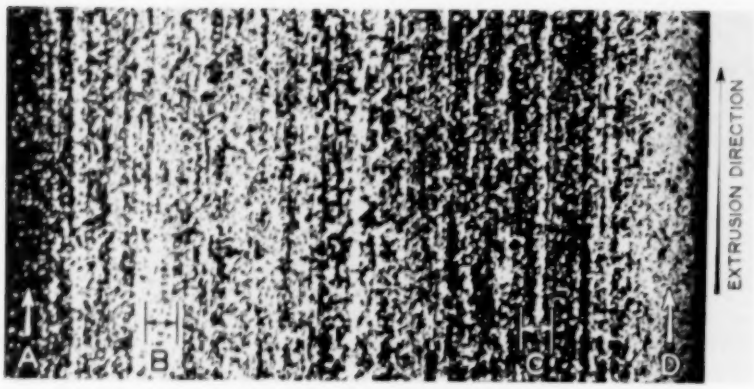

Fig. 1—Distribution of preferentially oriented grains in Mg-3.1 pct Th alloy extrusion. Polarized light with a Corning 2-62 filter (No. 25). X50. Reduced approximately 25 pct for reproduction.

studies of magnesium. For examination under polarized light, the metallograph used was one permitting the insertion of an adjustable full-wave retardation plate between the specimen and polarizer. The retardation plate permits selective wave-length extinction to occur, causing the color of a grain to change sharply with every 90° rotation of the specimen. Using a large-grained sample in which the orientations of several grains had been determined by the standard X-ray Laue technique, it was found that the *trace* of the basal plane in any grain was exactly parallel to a vertical cross hair in the eyepiece of the metallograph when, on stage rotation, the color of that grain changed abruptly from blue to orange. The amount of basal plane tilt in any grain could be estimated roughly from the magnitude of the intensity change; the greatest change occurs when the basal plane is perpendicular to the surface and no change occurs when it is parallel. Without the wave plate, extinction was observed but there were no color changes. Hence, there was a twofold ambiguity in determining the direction of the hexagonal axis.

This technique has proved valuable in several applications. It has been used to determine the local reorientations caused by inhomogeneous deformation and it is currently being employed to study the changes in preferred orientation that result from heavy twinning and annealing. The results of these investigations will be reported in the near future. An application described briefly here concerns a study of preferred orientation in an extruded magnesium alloy. The preferred orientation of most extruded magnesium strip is such that two maximum basal pole densities are present throughout most of the extrusion thickness. These maxima are usually rotated in opposite directions from the normal to the extrusion surface in a plane containing the surface normal and the extrusion direction.

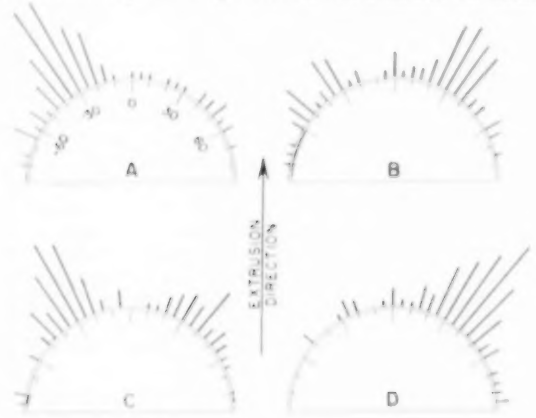

Fig. 2—Preferred orientation profiles for positions *A*, *B*, *C*, and *D* in Fig. 1.

The material used in this investigation was a Mg-3.1 pct Th alloy extruded at 900°F as 1/8 in. x 1¼ in. strip. X-ray measurements have shown that this alloy has a double peak at ±35° throughout most of the thickness.[4] When a longitudinal cross section of this material was etched in acetic picral and examined under polarized light, the distribution of the grains making up the two peaks was immediately apparent, Fig. 1. The dark grains appear blue under polarized light and the basal traces of these grains are rotated counter-clockwise from the extrusion direction; the light grains appear orange under polarized light and their basal traces are rotated clockwise from the extrusion direction. It is seen that on the left surface, *A*, almost all grains are tilted counter-clockwise, while on the right surface, *D*, almost all are tilted clockwise. Between the surface layers, elongated clusters of grains of both orientations are present, the two orientations alternating in a laminar fashion. At positions *A*, *B*, *C*, and *D* across the thickness of the extrusion, the basal plane tilts of 100 consecutive grains were measured (to the nearest 5°) and the results are shown as profile plots in Fig. 2. The length of a profile line at any angle is proportional to the number of grains in which that particular basal tilt was measured. It is seen that the profile plot for each surface (*A*, *D*) shows a single orientation while the plots for the positions in the interior (*B*, *C*) show double orientations. In each case, the maxima occur at approximately ±35°, which agrees with the X-ray results.[4]

Preliminary results on other extruded alloys indicate that the laminar distribution observed here is fairly typical. It is hoped that an explanation for the observed effects can be obtained by studying extrusion butts to see how grains change their orientation as they deform and recrystallize while flowing toward the die opening.

Acknowledgment

This work was sponsored by Wright Air Development Center under Contract No. AF 33(616)-2337.

References

[1] B. Mott and H. Haines: *Research*, 1951, vol. 4, p. 63.
[2] T. Ernst and F. Laves: *Ztsch. für Metallkunde*, 1949, vol. 40, p. 1.
[3] P. F. George: *ASM Trans.*, 1947, vol. 38, p. 686.
[4] WADC Technical Report No. 55-160, Part 3. Dow Chemical Co. Midland, Mich., 1955.

Appreciation is gratefully acknowledged to the following organizations whose support has helped to make possible AIME's extensive publications program of metallurgical research:

Aerojet-General Corp.
Allis-Chalmers Mfg. Co.
Aluminum Co. of America
American Brake Shoe Co.
American Cast Iron Pipe Co.
American Iron & Steel Institute
American Metal Co. Ltd.
American Metallurgical Products Co.
American Smelting & Refining Co.
American Zinc, Lead & Smelting Co.
Anaconda Co.
Apex Smelting Co.
Arnold Engineering Co.
Atom Energy of Canada, Ltd.
Avco Manufacturing Corp.
Battelle Memorial Institute
Bridgeport Brass Co.
Budd Co.
Bunker Hill Co.
Calumet & Hecla, Inc.
Cerro de Pasco Corp.
Clevite Corp.
Climax Molybdenum Co.
Consolidated Coppermines Corp.
Consolidated Mining & Smelting Co. of Canada Ltd.
Copper Range Co.
Cornell Aeronautical Laboratory Inc.
Crane Co.
Cyprus Mines Corp.
Detroit Testing Laboratory Inc.
Dow Chemical Co.
Driver-Harris Co.
Wilbur B. Driver Co.
Eagle-Picher Co.
Eaton Mfg. Co.
Electro Metallurgical Co., Div. of Union Carbide & Carbon Corp.
Engineering Foundation
Esso Research and Engineering Co.
Ford Motor Co.
Freeport Sulphur Co.
General Electric Co.
General Motors Corp.
Handy & Harman
E. F. Houghton & Co.
Howe Sound Co.
Hudson Bay Mining & Smelting Co. Ltd.
International Nickel Co. Inc.
Janney Cylinder Co.
Kennecott Copper Corp.
Leeds & Northrup Co.
Magma Copper Co.
Mallinckrodt Chemical Works
P. R. Mallory & Co., Inc.
Mallory-Sharon Titanium Corp.
Metal Hydrides, Inc.
Miami Copper Co.
Molybdenum Corp. of America
Mueller Brass Co.
National Lead Co.
New Jersey Zinc Co.
Newmont Mining Corp.
Noranda Mines, Ltd.
Olin Mathieson Chemical Corp.
Owens-Corning Fiberglas Corp.
Owens-Illinois Co.
Phelps Dodge Corp.
Quigley Co. Inc.
Raytheon Mfg. Co.
Rem-Cru Titanium Inc.
Revere Copper & Brass Inc.
Reynolds Metals Co.
Richfield Oil Corp.
Scovill Mfg. Co.
Alfred P. Sloan Foundation, Inc.
Southwestern Engineering Co.
Steel Improvement & Forge Co.
St. Joseph Lead Co.
Superior Tube Co.
Texas Gulf Sulphur Co.
Thompson Products Inc.
Titanium Metals Corp. of America
U. S. Smelting, Refining & Mining Co.
Vanadium Corp. of America
S. K. Wellman Co.

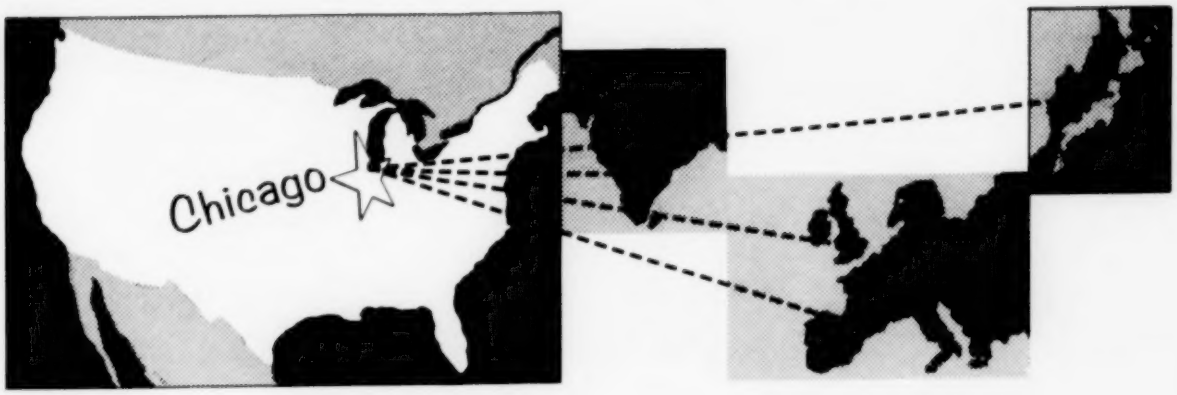

39th National Metal Exposition
2nd World Metallurgical Congress

In the whole, wide, wonderful world of metals, for one fast-moving, action-packed week, Chicago will be world headquarters for metal men.

From wherever metals are made . . . from wherever metals are used . . . from all parts of the United States and around the free world, the responsible men of metals will move into Chicago the week of November 4, 1957.

Engineers and scientists . . . executives and production metal engineer experts . . . the responsible men of metals will be in Chicago to see the 39th National Metal Exposition — the best, the biggest, the most important Metal Show of them all. Hundreds of manufacturers will place their best products and operating processes and equipment on display in the vast International Amphitheatre and New Exposition Halls. This great Exposition will make show history . . . will make metals history.

And this is only half the story. World authorities on metals . . . outstanding scientists from the United States . . . again, the responsible men of metals will be speakers at the 2nd World Metallurgical Congress and at the 39th National Metal Congress. Technical and practical sessions will begin on Saturday, November 2, and run continuously through Friday, November 8. Never before has such an array of metal engineering and scientific talent been assembled on so vast a scale . . . engineering developments of world-wide impact will be presented for all to hear and digest and discuss.

You will want to attend this great event, this world metals week in Chicago. Your organization may well wish to have management, engineering and sales representatives in Chicago this important week. Make the first move now — make the hotel reservations you will need for full representation. Or write for further details now to —

AMERICAN SOCIETY FOR METALS

The Engineering Society for the Metal Industry

7301 Euclid Avenue — Cleveland 3, Ohio

Cooperating Societies: Metals Division, American Institute of Mining, Metallurgical and Petroleum Engineers . . . the Society for Non Destructive Testing . . . the Industrial Heating Equipment Association.

Exhibit Space Available

Hundreds of manufacturers have reserved Metal Show space, but there are good locations still available in the vast new exposition halls of the International Amphitheatre. If the metalproducing or metalworking industries are your market, don't miss this show — write for display information now.